Effects of the Nanostructure and the Chemistry of Various Oxide Electrodes on the Overall Performance of Dye-Sensitized Solar Cells

Tammy Ping-Chun Chou

A dissertation
submitted in partial fulfillment of the
requirements for the degree of

Doctor of Philosophy

University of Washington

2006

Program Authorized to Offer Degree:
Materials Science and Engineering

INFORMATION TO USERS

The quality of this reproduction is dependent upon the quality of the copy submitted. Broken or indistinct print, colored or poor quality illustrations and photographs, print bleed-through, substandard margins, and improper alignment can adversely affect reproduction.

In the unlikely event that the author did not send a complete manuscript and there are missing pages, these will be noted. Also, if unauthorized copyright material had to be removed, a note will indicate the deletion.

ProQuest Information and Learning Company
300 North Zeeb Road
P.O. Box 1346
Ann Arbor, MI 48106-1346

University of Washington
Graduate School

This is to certify that I have examined this copy of a doctoral dissertation by

Tammy Ping-Chun Chou

and have found that it is complete and satisfactory in all respects,
and that any and all revisions required by the final
examining committee have been made.

Chair of the Supervisory Committee:

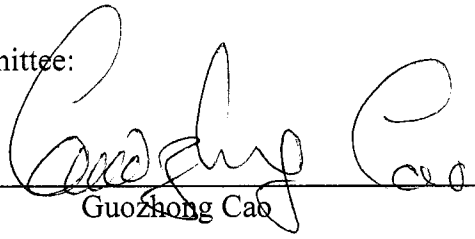

Guozhong Cao

Reading Committee:

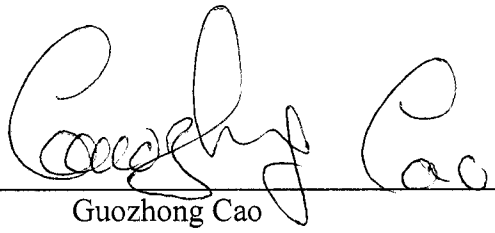

Guozhong Cao

Glen Fryxell

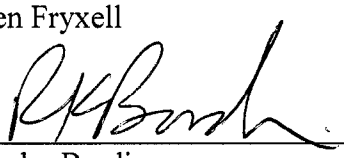

Rajendra Bordia

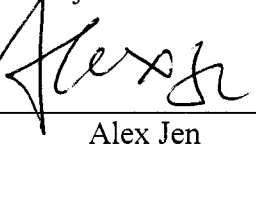

Alex Jen

Date: 08/11/06

In presenting this dissertation in partial fulfillment of the requirements for the doctoral degree at the University of Washington, I agree that the Library shall make its copies freely available for inspection. I further agree that extensive copying of the dissertation is allowable only for scholarly purposes, consistent with "fair use" as prescribed in the U.S. Copyright Law. Requests for copying or reproduction of this dissertation may be referred to ProQuest Information and Learning, 300 North Zeeb Road, Ann Arbor, MI 48106-1346, 1-800-521-0600, to whom the author has granted "the right to reproduce and sell (a) copies of the manuscript in microform and/or (b) printed copies of the manuscript made from microform."

Signature 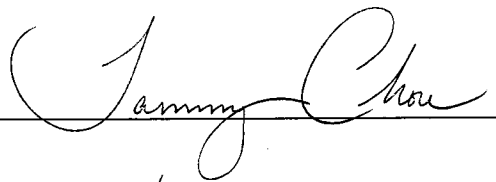

Date 08/18/06

University of Washington

Abstract

Effects of the Nanostructure and the Chemistry of Various Oxide Electrodes on the Overall Performance of Dye-Sensitized Solar Cells

Tammy Ping-Chun Chou

Chair of the Supervisory Committee:
Associate Professor Guozhong Cao
Materials Science and Engineering

With the need for alternative energy resources, solar cell research utilizing solar energy to produce electrical energy has emerged as an important area of research with great potential. In this dissertation, various oxide nanostructures are explored to improve the overall performance of dye-sensitized solar cells. This study examines the solar cell performance of: 1) TiO_2 nanoparticle film with varying particle sizes, 2) TiO_2-ITO nanocomposite films with various nanoparticle and nanorod structures, and 3) ZnO nanostructures consisting of nanoparticles and nanowires. Additional investigation in the dye loading of TiO_2 and ZnO nanoparticle films are also reported. From this study, it was found that the TiO_2 nanoparticle film with larger particles ~ 18nm in diameter resulted in a higher efficiency ~ 5.2%, possibly due to 1) better crystallinity, 2) larger contact points, and 3) better dye adsorption. The addition of ITO nanoparticles to the TiO_2 nanoparticle film also improved the overall efficiency from ~ 4.7% to ~ 5.6%, possibly due to the increase in the overall electron mobility and reduced recombination losses in the TiO_2-ITO system. In addition, the ZnO nanoparticle film prepared by sol-gel processing had a higher overall efficiency of ~ 3.5%, as compared to commercially-obtained ZnO nanoparticle film. This is most likely due to the hierarchical structure of sol-gel-derived ZnO consisting of primary nanoparticles ~ 20nm in size and secondary colloidal spheres ~ 300nm in size, giving rise to 1) a higher surface area and 2) a greater light scattering ability. It was also found that the manner of dye loading for both TiO_2 and ZnO had two competing processes: 1) complete surface adsorption and 2) surface dissolution. A higher and lower concentration of dye required a shorter and longer amount of time, respectively, for adequate dye adsorption and complete surface coverage.

Table of Contents

List of Figures viii

List of Tables xiv

1 Introduction to solar cells 1

1.1 Introduction 1

1.2 Solar cell devices for conversion of solar energy to electricity 6

1.2.1 Solid-state inorganic solar cells 7

1.2.2 Organic solar cells 9

1.3 Dye-sensitized solar cells 12

1.3.1 TiO_2 nanocrystalline film 13

1.3.2 Synthesis of TiO_2 nanocrystalline film 15

1.3.3 Mechanism of light conversion in dye-sensitized solar cells 16

1.3.4 Alternative materials for dye-sensitized solar cells 22

1.3.4.1 ZnO-based dye-sensitized solar cells 23

1.3.5 Current state of dye-sensitized solar cells 25

1.4 Rationale and motivation for this work 27

1.5 Scope 31

Notes to Chapter 1 33

2 Dependence of solar cell performance on TiO_2 particle size in dye-sensitized solar cells 43

2.1 Introduction 43

2.2 Experimental procedure 46

2.2.1 TiO_2 sol preparation 46

2.2.2 Hydrothermal crystallization of TiO_2 47

2.2.3 Fabrication of TiO_2 nanoparticle film 49

2.2.4 Solar cell assembly 50

2.2.5 General analysis techniques 51

2.2.5.1 X-Ray Diffraction (XRD) 51

2.2.5.2 Scanning Electron Microscopy (SEM) 52

2.2.5.3 UV/VIS/IR Spectrometry 52

2.2.6 Solar cell analysis 52

2.2.6.1 Current-Voltage (I-V) measurements 55

2.2.6.2 Characterization of I-V behavior 56

2.3 Results and discussion 57

2.3.1 Hydrothermal treatment of TiO_2 58

2.3.1.1 TiO_2 particle size dependence on varying temperature 58

2.3.1.2 TiO_2 particle size dependence on varying time 61

2.3.2 Solar cell performance of TiO_2 nanoparticle film obtained by hydrothermal treatment at various temperatures 63

2.3.2.1 Open-circuit voltage 65

2.3.2.2 Short-circuit current density 66

2.3.2.3 Fill factor 70

2.3.2.4 Overall light conversion efficiency 71

2.3.3 Solar cell performance of TiO_2 nanoparticle film obtained by hydrothermal treatment at various times 75

2.3.3.1 Open-circuit voltage 76

2.3.3.2 Short-circuit current density 78

2.3.3.3 Fill factor 81

2.3.3.4 Overall light conversion efficiency 82

2.3.4 Characterization of TiO_2 nanoparticle films 85

2.3.4.1 TiO_2 film obtained by hydrothermal treatment at various temperatures 85

2.3.4.2 TiO_2 film obtained by hydrothermal treatment at various times .. 88

2.3.5 Dye loading in TiO_2 nanoparticle film 90

2.3.6 Comparison of data obtained from prepared TiO_2 nanoparticle film with values found in literature 94

2.4 Conclusions 95

Notes to Chapter 2 96

3 TiO_2-ITO nanocomposite films for dye-sensitized solar cells 97

3.1 Introduction 97

3.2 Experimental procedure 99

3.2.1 Formation of ITO nanostructures 99

3.2.1.1 ITO sol preparation 100

3.2.1.2 ITO nanoparticles 101

3.2.1.3 ITO nanorods 101

3.2.2 Fabrication of TiO_2-ITO nanocomposite films 103

3.2.2.1 TiO_2 nanoparticle film with ITO nanoparticles 104

3.2.2.2 TiO_2 nanoparticle film with ITO nanorods 105

3.2.2.3 ITO nanorod arrays with TiO_2 coating 105

3.2.3 Analysis techniques 106

3.3 Results and discussion 106

3.3.1 Characterization of ITO nanostructures 107

3.3.1.1 ITO nanoparticles 107

3.3.1.2 ITO nanorods 110

3.3.2 Solar cell performance of TiO_2-ITO nanocomposite films on conductive FTO substrates 113

3.3.2.1 Open-circuit voltage 114

3.3.2.2 Short-circuit current density 116

3.3.2.3 Fill factor 117

3.3.2.4 Overall light conversion efficiency 119

3.3.3 Solar cell performance of TiO_2-ITO nanocomposite films on conductive ITO substrates 120

3.3.3.1 Open-circuit voltage 122

3.3.3.2 Short-circuit current density 123

3.3.3.3 Fill factor 125

3.3.3.4 Overall light conversion efficiency 126

3.3.4 Comparison of I-V characteristics using FTO and ITO substrates 128

3.3.4.1 Open-circuit voltage 128

3.3.4.2 Short-circuit current density 129

3.3.4.3 Fill factor 130

3.3.4.4 Overall light conversion efficiency 131

3.3.5 Characterization of TiO_2-ITO nanocomposite films 133

3.3.5.1 TiO_2 nanoparticle film with ITO nanoparticles 133

3.3.5.2 TiO_2 nanoparticle film with ITO nanorods 135

3.3.5.3 ITO nanorod arrays with a layer of TiO_2 coating 136

3.3.6 Comparison of data to examine improvement in solar cell performance ...138

3.4 Conclusions ...139

Notes to Chapter 3 ... 140

4 Dye-sensitized solar cells with ZnO nanoparticles and nanowires ... 141

4.1 Introduction ...141

4.2 Experimental procedure ...144

4.2.1 Formation of ZnO nanostructures ...144

4.2.1.1 ZnO nanoparticle film ... 145

4.2.1.2 ZnO nanowire film ... 147

4.2.2 Analysis techniques ...148

4.3 Results and discussion ...148

4.3.1 ZnO nanostructures ...148

4.3.1.1 ZnO nanoparticles ... 149

4.3.1.2 ZnO nanowires ... 150

4.3.2 Comparison of solar cell performance of ZnO film with various nanostructures ...151

4.3.2.1 Open-circuit voltage ... 153

4.3.2.2 Short-circuit current density ... 155

4.3.2.3 Fill factor ... 158

4.3.2.4 Overall light conversion efficiency ... 159

4.3.3 Solar cell performance of ZnO nanoparticle film sensitized with N3 dye at various concentrations ...161

4.3.3.1 Open-circuit voltage ... 164

4.3.3.2 Short-circuit current density ... 165

4.3.3.3 Fill factor 169

4.3.3.4 Overall light conversion efficiency 170

4.3.4 Solar cell performance of ZnO nanoparticle film sensitized with N3 dye for various times 173

4.3.4.1 Open-circuit voltage 176

4.3.4.2 Short-circuit current density 177

4.3.4.3 Fill factor 180

4.3.4.4 Overall light conversion efficiency 182

4.3.5 Dye loading of ZnO nanoparticle film 184

4.3.6 Comparison of data obtained from prepared ZnO nanoparticle and nanowire film with values found in literature 189

4.4 Conclusions 190

Notes to Chapter 4 191

5 Future work 192

5.1 Solar cell performance of TiO_2 nanoparticle film fabricated by way of combining hydrothermal crystallization and electrophoretic deposition 193

5.2 Comparison of solar cell performance of TiO_2 and ZnO nanoparticle films by incorporating various amounts of ITO 195

5.3 Fabrication of ITO-TiO_2 and ZnO-TiO_2 nanocomposite structures for dye-sensitized solar cells 196

5.4 Other considerations 200

Notes to Chapter 5 202

Bibliography 204

Appendix A: Other Pertinent Information 218

Appendix B: Corrosion Resistance of Sol-Gel-Derived Organic-Inorganic Hybrid Coatings on Stainless Steel 220

Appendix C: Adhesion of Sol-Gel-Derived Organic-Inorganic Hybrid Coatings on Polyester 223

Appendix D: TiO_2 Nanoparticle Film 226

Appendix E: TiO_2 Nanorods 233

List of Figures

Figure 1.1. Examples of solar panels used in space exploration 2

Figure 1.2. Examples of solar panel use 3

Figure 1.3. Schematic of the operation of photoelectrochemical cells 4

Figure 1.4. Depiction of the band bending 5

Figure 1.5. Examples of the types of solar cells 6

Figure 1.6. Schematic of the inorganic solar cell devices 8

Figure 1.7. Schematic of the inorganic solar cell devices 8

Figure 1.8. Depiction of an inorganic solar cell device 9

Figure 1.9. Schematic of 11

Figure 1.10. SEM image of TiO_2 nanocrystalline film 14

Figure 1.11. Schematic of the light conversion process in dye-sensitized solar cells 17

Figure 1.12. Schematic of the metal-to-ligand charge transfer 18

Figure 1.13. Schematic of the rate constants 19

Figure 1.14. Schematic of the interconnected nanoparticle network 20

Figure 1.15. Schematic of the band edge 22

Figure 1.16. The band gap of various semiconducting materials 24

Figure 1.17. Absorbance spectra of 26

Figure 2.1. Schematic of the advantages associated with using larger particles. 44

Figure 2.2. Schematic of the advantages associated with using smaller particles. 45

Figure 2.3. Schematic of the steps and procedures involved in sol-gel processing 47

Figure 2.4. Image of the equipment used for hydrothermal crystallization 48

Figure 2.5. A schematic of the doctor-blading process 49

Figure 2.6. Schematic showing the assembly and configuration of 51

Figure 2.7. Schematic of the equipment used for solar cell analysis 53

Figure 2.8. Schematic of 54

Figure 2.9. Comparison of the solar irradiance spectrum 55

Figure 2.10. Representation of the ideal I-V curve for a highly efficient solar cell 56

Figure 2.11. XRD peaks showing the crystallinity of hydrothermally-treated TiO_2 59

Figure 2.12. Plot of particle size as a function of temperature. 60

Figure 2.13. XRD peaks showing the crystallinity of hydrothermally-treated TiO_2 61

Figure 2.14. Plot of particle size as a function of time. 62

Figure 2.15. Plot and comparison of the I-V characteristics for each solar cell 64

Figure 2.16. Plot of the open-circuit voltage 65

Figure 2.17. Plot of the short-circuit current density 67

Figure 2.18. Plot of the difference in particle size 68

Figure 2.19. Plot of the total difference in particle size 70

Figure 2.20. Plot of the fill factor as a function of 71

Figure 2.21. Plot of the overall efficiency as a function of 72

Figure 2.22. Plot of the difference in particle size 73

Figure 2.23. Plot of the total difference in particle size 74

Figure 2.24. Plot and comparison of the I-V characteristics for each solar cell 76

Figure 2.25. Plot of the open-circuit voltage as a function of 77

Figure 2.26. Plot of the short-circuit current density as a function of 78

Figure 2.27. Plot of the difference in particle size 80

Figure 2.28. Plot of the total difference in particle size 80

Figure 2.29. Plot of the fill factor as a function of 81

Figure 2.30. Plot of the overall efficiency as a function of 82

Figure 2.31. Plot of the difference in particle size 83

Figure 2.32. Plot of the total difference in particle size 84

Figure 2.33. SEM images of TiO_2 nanoparticle film 86

Figure 2.34. SEM images of TiO_2 nanoparticle film 89

Figure 2.35. Plot of overall efficiency as a function of dye immersion time 92

Figure 2.36. Plot of the highest overall efficiency 93

Figure 3.1. Schematic of the ideal TiO_2-ITO nanocomposite films 98

Figure 3.2. Schematic of the steps and procedures involved in sol-gel processing 100

Figure 3.3. Depiction of the EPD process 102

Figure 3.4. SEM images of ITO nanoparticles 108

Figure 3.5. XRD plot obtained from ITO nanoparticles 108

Figure 3.6. Plot of resistivity as a function of sintering temperature 109

Figure 3.7. SEM images of ITO nanorod arrays attached to an ITO substrate 110

Figure 3.8. SEM images of ITO nanorod arrays attached to an ITO substrate 111

Figure 3.9. XRD plot comparing 112

Figure 3.10. EDS plot of a single ITO nanorod 112

Figure 3.11. Plot and comparison of the I-V characteristics for each solar cell 114

Figure 3.12. Comparison of the open-circuit voltage 115

Figure 3.13. Comparison of the short-circuit current density 116

Figure 3.14. Comparison of the fill factor 118

Figure 3.15. Comparison of the overall efficiency 119

Figure 3.16. Plot and comparison of the I-V characteristics for each solar cell 121

Figure 3.17. Comparison of the open-circuit voltage 123

Figure 3.18. Comparison of the short-circuit current density 124

Figure 3.19. Comparison of the fill factor 126

Figure 3.20. Comparison of the overall efficiency 127

Figure 3.21. Comparison of the open-circuit voltage 129

Figure 3.22. Comparison of the short-circuit current density 130

Figure 3.23. Comparison of the fill factor 131

Figure 3.24. Comparison of the overall efficiency 132

Figure 3.25. SEM images of TiO_2 nanoparticle film 134

Figure 3.26. SEM image of TiO_2 nanoparticle film 134

Figure 3.27. SEM image of TiO_2 nanoparticle film 135

Figure 3.28. SEM images of ITO nanorod arrays 136

Figure 3.29. SEM image 137

Figure 4.1. Schematic of 143

Figure 4.2. Schematic of the process involved in sol-gel processing 146

Figure 4.3. Schematic of the steps and procedures 147

Figure 4.4. SEM images of the sol-gel-derived ZnO nanoparticles 149

Figure 4.5. SEM images of the sol-gel-derived ZnO nanoparticles 150

Figure 4.6. SEM images of the sol-gel-derived ZnO nanoparticles 150

Figure 4.7. SEM images of the solution-grown ZnO nanowires 151

Figure 4.8. Plot and comparison of the I-V characteristics for each solar cell 153

Figure 4.9. Plot of the open-circuit voltage 154

Figure 4.10. Plot of the short-circuit current density 155

Figure 4.11. Absorption spectra comparing 157

Figure 4.12. Plot of the fill factor 158

Figure 4.13. Plot of the overall efficiency 160

Figure 4.14. Plot and comparison of the I-V characteristics for each solar cell 163

Figure 4.15. Plot and comparison of the I-V characteristics for each solar cell 163

Figure 4.16. Plot of the open-circuit voltage 165

Figure 4.17. Plot of the short-circuit current density 166

Figure 4.18. Plot of the total difference in short-circuit current density 167

Figure 4.19. Plot of the total difference in short-circuit current density 168

Figure 4.20. Plot of the fill factor 169

Figure 4.21. Plot of the overall efficiency 171

Figure 4.22. Plot of the total difference in overall efficiency 172

Figure 4.23. Plot of the total difference in overall efficiency 173

Figure 4.24. Plot and comparison of the I-V characteristics for each solar cell 175

Figure 4.25. Plot and comparison of the I-V characteristics for each solar cell 175

Figure 4.26. Plot of the open-circuit voltage 177

Figure 4.27. Plot of the short-circuit current density 178

Figure 4.28. Plot of the total difference in short-circuit current density 179

Figure 4.29. Plot of the total difference in short-circuit current density 180

Figure 4.30. Plot of the fill factor 181

Figure 4.31. Plot of the overall efficiency 182

Figure 4.32. Plot of the total difference in overall efficiency 183

Figure 4.33. Plot of the total difference in overall efficiency 184

Figure 4.34. Plot of overall efficiency 187

Figure 4.35. Plot of the highest overall efficiency 188

Figure 5.1. SEM images of TiO_2 nanoparticle film 194

Figure 5.2. Schematic of TiO_2 film formation on a conducting substrate 195

Figure 5.3. Schematic of the ideal nanocomposite structures 198

List of Tables

Table 2.1. Summary of TiO_2 particle sizes 59

Table 2.2. Summary of TiO_2 particle sizes 62

Table 2.3. The measured and calculated values 64

Table 2.4. The open-circuit voltage values 65

Table 2.5. The short-circuit current density values 68

Table 2.6. The fill factor values 71

Table 2.7. The overall efficiency values 72

Table 2.8. The measured and calculated values 76

Table 2.9. The open-circuit voltage values 77

Table 2.10. The short-circuit current density values 79

Table 2.11. The fill factor values 81

Table 2.12. The overall efficiency values 83

Table 2.13. The measured and calculated values 91

Table 3.1. The measured and calculated values 113

Table 3.2. The open-circuit voltage values 115

Table 3.3. The short-circuit current density values 116

Table 3.4. The fill factor values 118

Table 3.5. The overall efficiency values 120

Table 3.6. The measured and calculated values 121

Table 3.7. The open-circuit voltage values 123

Table 3.8. The short-circuit current density values 124

Table 3.9. The fill factor values 126

Table 3.10. The overall efficiency values 127

Table 4.1. The measured and calculated values 152

Table 4.2. The open-circuit voltage values 154

Table 4.3. The short-circuit current density values 155

Table 4.4. The fill factor values 158

Table 4.5. The overall efficiency values 160

Table 4.6. The measured and calculated values 162

Table 4.7. The measured and calculated values 162

Table 4.8. The open-circuit voltage values. 165

Table 4.9. The short-circuit current density values 166

Table 4.10. The fill factor values 170

Table 4.11. The overall efficiency values 171

Table 4.12. The measured and calculated values 174

Table 4.13. The measured and calculated values 174

Table 4.14. The open-circuit voltage values 177

Table 4.15. The short-circuit current density values 178

Table 4.16. The fill factor values 181

Table 4.17. The overall efficiency values 183

Table 4.18. The measured and calculated values 185

Acknowledgements

The author would like to thank members of her PhD Committee – Guozhong Cao (MSE advisor), Glen Fryxell (PNNL), Donald Janssen (GSR), Rajendra Bordia (MSE), Alex Jen (MSE), and Younan Xia (Chemistry) – for their time and effort during the process of examination. The author also wishes to express sincere appreciation to Professor Guozhong Cao for his knowledge, dedication, mentorship, and patience during the completion of this dissertation. In addition, the author would like to thank previous and current group members and visiting professors for their help; the faculty and staff in the Department of Materials Science and Engineering for their support; the Joint Institute for Nanoscience and Nanotechnology, funded by Pacific Northwest National Laboratory and the University of Washington, for three years of financial support; and the Intel PhD Foundation for one year financial support. The author would also like to acknowledge Shari Li from Pacific Northwest National Laboratory for her help in initial BET analysis; Jeff Zhang (postdoc) for his help with the ZnO study; Professor Samson Jenekhe from the Department of Chemical Engineering for the use of his lab and equipment; and Abhishek Pradeep Kulkarni (ChemE), for his help with solar cell analysis.

Dedication

To my grandparents, who passed away before the completion of this dissertation and could not be here to celebrate my achievement of earning a doctorate degree. To my parents, for I would not be who I am today without them. To my Mom, for her continued support and dedication to my success and well-being. To my Dad, for his continued support and understanding in all my endeavors. To my brother and his wife, who have blessed me with a niece this year, as commemoration to completing this dissertation. To my friends and family, who have stood by and supported me in all my struggles and challenges to complete this dissertation. To the love of my life, who is and always will be my best friend and someone I can confide in and depend on for the rest of my life.

1 Introduction to solar cells

1.1 Introduction

The increase in research activity surrounding the development of solar cells emphasizes the need for a higher light conversion efficiency of solar energy to electrical energy. This rise in interest has emerged due to current circumstances involving reduced energy resources that have lead to higher energy production costs on a global scale[1,2]. As a result, the utilization of the sun's solar energy to produce electrical energy to supply the everyday energy need has emerged as an important area of research with great potential.

With the need for alternative energy sources, extensive solar cell research has resulted in the development of three generations of photovoltaics, or solar cells. First generation photovoltaics consist of single-layer p-n junction silicon diodes; second generation photovoltaics consist of multiple layers of p-n junction inorganic diodes; third generation photovoltaics consist of dye-sensitized oxides, organic polymers, and quantum dots. The general mechanism of light conversion involve 1) the absorption of photons, 2) the generation of electron and hole pairs, 3) the separation of electron and hole pairs, 4) the collection of electrons at the semiconductor electrode (photoanode), and the collection of holes at the counterelectrode (cathode). Various solar cell devices have been extensively studied and the most studied devices have consisted of solid-state p-n junction or heterojunction materials, which have dominated this area of research for efficient light conversion, achieving highest efficiencies close to 35%[3,4].

The fabrication of individual solar cells into a large array of solar cells has resulted in the development of solar panels. These solar panels have been widely used in

space exploration to power space stations, satellites and space vehicles. Figure 1.1 shows the solar panels used for space exploration and telecommunication. The International Space Station[5] from NASA has solar panels along the exterior of the wings to provide energy from the sun's energy to power the station. The Mariner 5 satellite[6] from NASA has solar panels running across the span of the extensions to power the satellite with the sun's energy. The Sojourner vehicle[7] from NASA also has solar panels on top to operate the vehicle in space and allows for easy recharging from the sun's energy.

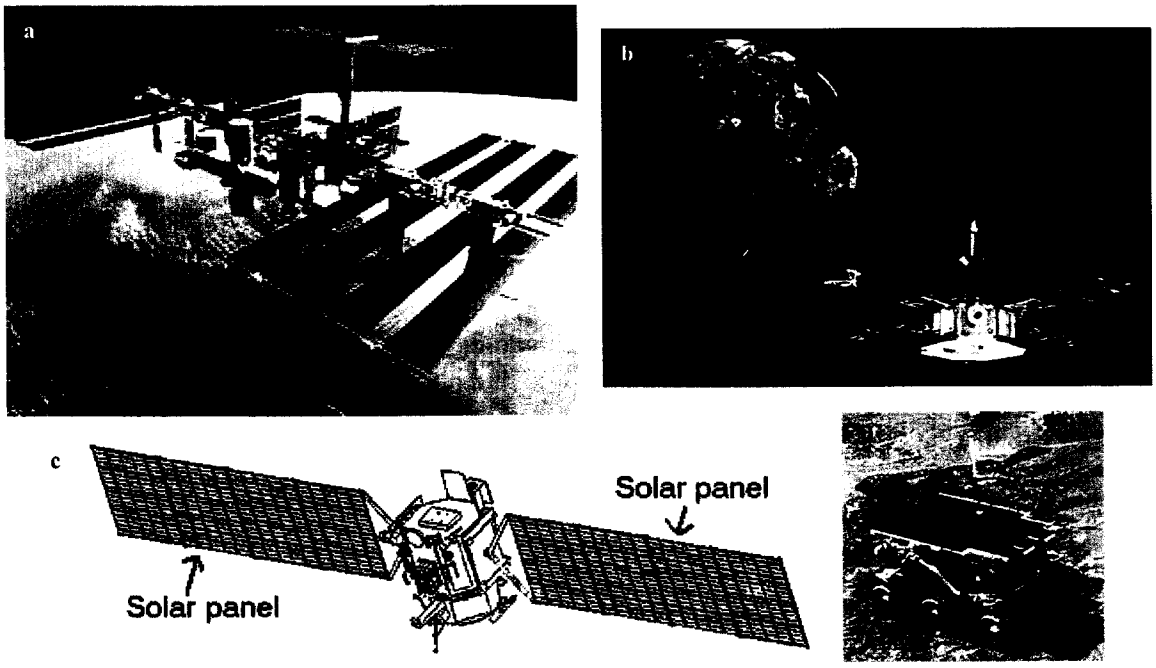

Figure 1.1. Examples of solar panels used in space exploration, showing a) the International Space Station from NASA, b) the Mariner 5 Satellite from NASA, c) the wing of the space station and satellite, and d) the Sojourner Vehicle from NASA. [Ref 5,6,7]

Additionally, solar panels have become more prevalent on the ground, as a means to provide power to buildings, houses, and cars, as well as a means for energy storage. Figure 1.2 shows a few examples[8,9,10] of where solar panels have started to be utilized. It can be seen that solar panels have been placed on the roofs of houses and buildings for

power as an alternative means to obtain electricity. Hybrid vehicles that run on electricity also have solar panels for quicker recharging, and energy storage through the use of solar panels is also prevalent.

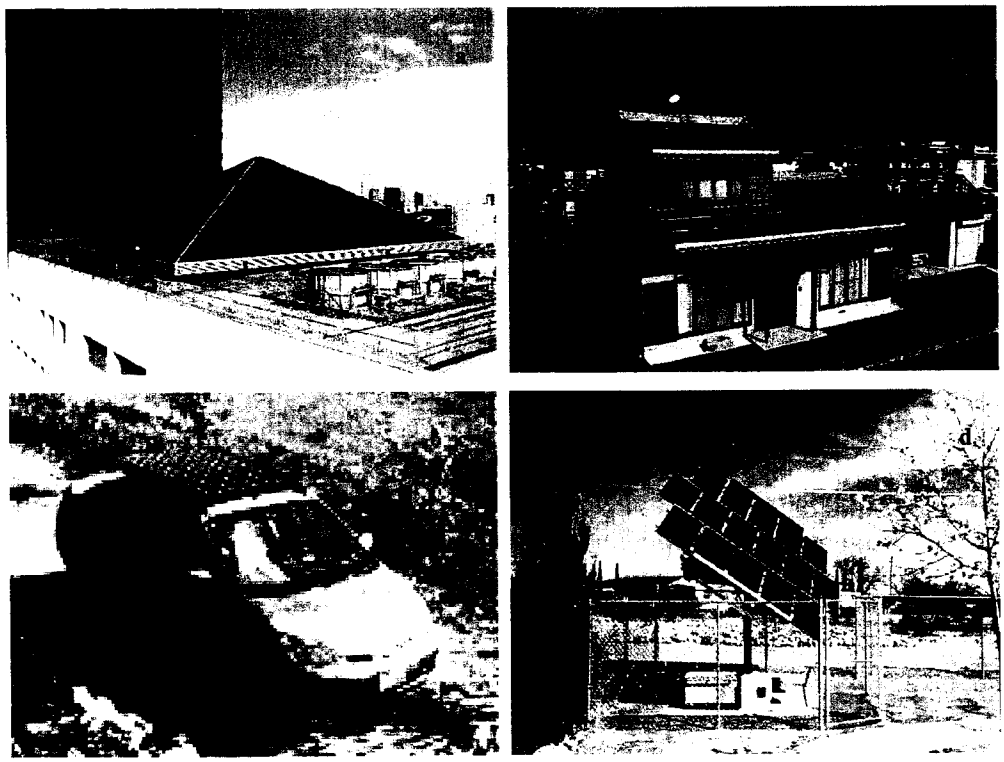

Figure 1.2. Examples of solar panel use, showing a) a building with solar panels on the roof, b) a house in Japan mainly powered by solar panels, c) a hybrid car with solar panels for recharging, and d) a solar panel station for energy storage. [Ref 8,9,10]

Solar cell devices are also referred to as photoelectrochemical cells[11], which convert photon energy of light to electrical energy and/or chemical fuels. Photon absorption and conversion to electron and hole pairs take place at the interface of a semiconductor layer or thin film, and the resultant electrons and holes are quickly collected in opposite electrodes adjacent to the interface before recombination can take place. Such devices[12,13] typically consist of a working semiconductor electrode or photoanode, a counter electrode with a catalyst layer or cathode, and an electrolyte layer

sandwiched in between the two electrodes. Figure 1.3 shows the device configuration used for the process of water cleavage and current generation from sunlight in an n-type semiconductor electrode.

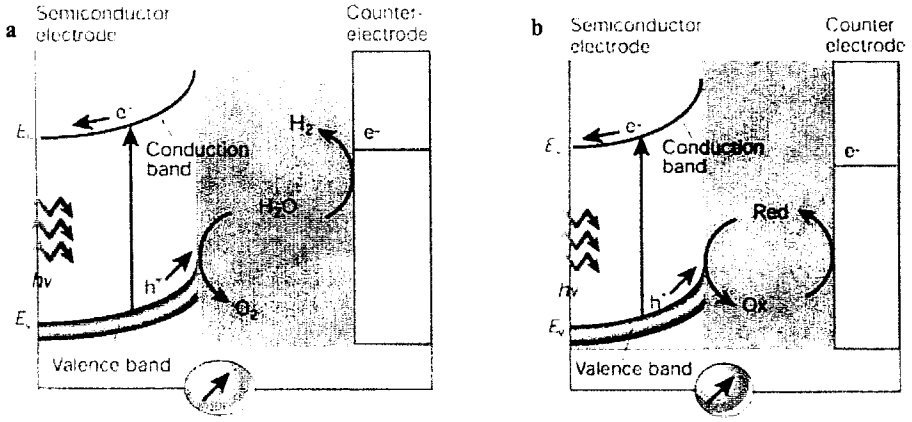

Figure 1.3. Schematic of the operation of photoelectrochemical cells consisting of n-type semiconductors, showing a) hydrogen generation and b) electric current generation from sunlight. [Ref 11]

There are two types of photoelectrochemical cells that have been extensively studied, where one type utilizes water as the electrolyte and one type utilizes a redox electrolyte, as shown in Figure 1.3. The first type of cell converts solar energy to chemical fuels, most notably hydrogen, by photo-cleavage of water[11,14]. The second type of cell converts solar energy to electrical power by generating electrical current from photon absorption. Both types of cells utilize photons of energy from sunlight to generate electron-hole pairs. In this process, photons of energy exceeding that of the band gap of the semiconductor electrode generate electron-hole pairs, which are separated by an electric field present in the space-charge layer. This space-charge layer develops when the transfer of electric charge produces a region with a difference in charge distribution at the semiconductor-electrolyte junction as compared to the bulk. Figure 1.4 shows the

band bending associated with an accumulation of electrons at the semiconductor-electrolyte junction, which represents the process involved in an n-type semiconductor.

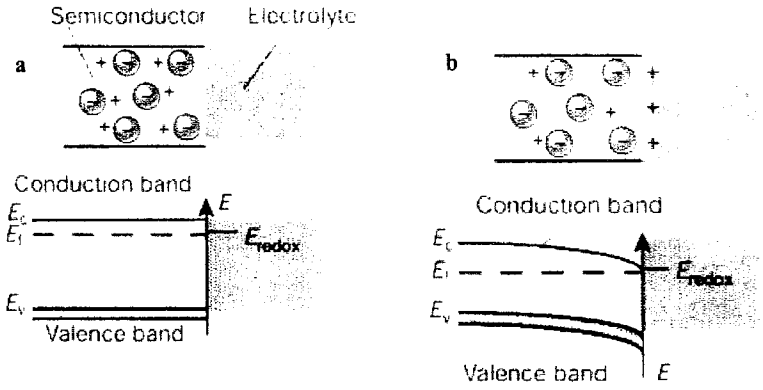

Figure 1.4. Depiction of the band bending associated with n-type semiconductors, showing a) a flat band potential with no space charge layer, and b) an accumulation layer from excess electrons in the solid at the semiconductor-electrolyte junction. [Ref 11]

In the first type of cell, also called a photosynthetic cell[15,16], water is used as the electrolyte. After the generation of electron and hole pairs, generated holes are accumulated at the surface of the semiconductor electrode and water is then oxidized, producing oxygen. At the counterelectrode, generated electrons are accumulated at the surface and water is then reduced, producing hydrogen[17,18].

In the second type of cell, also called a regenerative cell[19,20], a redox electrolyte is used. The generated holes accumulate at the semiconductor-electrolyte junction, oxidizing the redox molecules in the electrolyte. The generated electrons migrate through the bulk of the semiconductor electrode to the current collector and move through the external circuit, producing current. The generated electrons that re-enter into the cell from the external circuit reduce the oxidized form of the electrolyte to restart the entire process all over again from the beginning.

Although the highest efficiencies so far have been obtained using solid-state inorganic p-n junction or heterojunction materials, the high cost of production, expensive equipment, and necessary clean-room facilities associated with the development of these devices has directed the field of converting solar energy to electrical energy to cheaper semiconducting materials and devices.

1.2 Solar cell devices for conversion of solar energy to electricity

Many types of solar cells using metallic, ceramic, and polymeric materials have been extensively studied to convert solar energy to electrical power, including 1) solid-state inorganic solar cells[21], 2) polymer-based organic solar cells[22], and 3) oxide-based dye-sensitized solar cells[23]. Figure 1.5 shows a) a monocrystalline silicon solar panel[24], b) a bendable organic solar cell[25], and c) a dye-sensitized solar cell module[26].

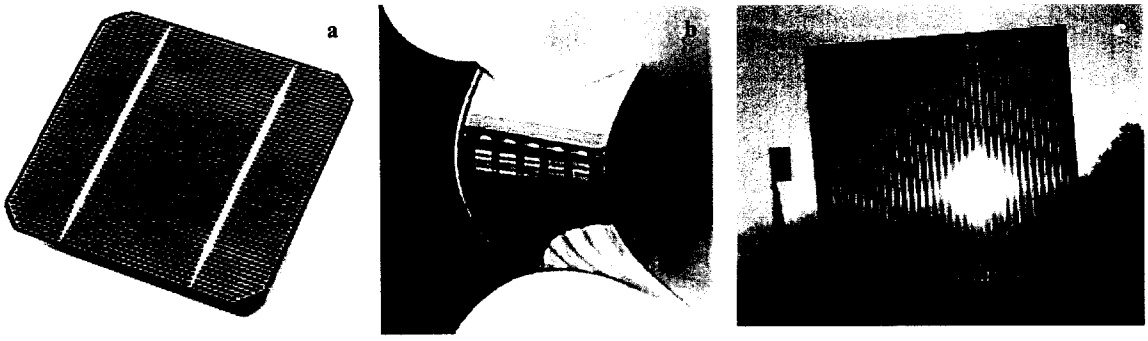

Figure 1.5. Examples of the types of solar cells, showing a) a monocrystalline silicon solar panel, b) a bendable organic solar cell, and c) a dye-sensitized solar cell module. [Ref 24,25,26]

Solar cells based on semiconducting heterojunctions[3] have so far dominated the research area of converting solar energy to electrical power, and have obtained the highest efficiencies, but other solar cells utilizing polymeric and oxide materials have emerged to reduce the cost of production, and to eliminate the complicated fabrication

processes involving elevated temperatures, high vacuum, and numerous lithographic steps, as experienced in the semiconductor industry[27].

1.2.1 Solid-state inorganic solar cells

The fabrication of solar cell devices was initially instigated by the well-known production process of solid-state inorganic materials in the semiconductor industry[3]. The experience and material availability of doped forms of crystalline or amorphous silicon initiated the use of compound semiconductors, most notably the III-V compounds or the copper-indium-sulphide or selenide (CIS) thin films[28], to produce devices to convert solar energy to electrical power. Initial research started with single-junction devices[3], most notably solar cells consisting of crystalline silicon, amorphous silicon, cadmium telluride (CdTe), and copper-indium-gallium-selenide [$Cu(In,Ga)Se_2$], for the efficient conversion of light to electrical power.

Figure 1.6 shows the solar cell designs consisting of crystalline silicon and amorphous silicon. The highest efficiency obtained for crystalline silicon[4,29] has been ~ 24% using a passivated emitter, rear locally diffused (PERL) cell on a Czochralski growth (CZ) wafer. In this device, local diffusion is used near the rear point contact to provide a minority carrier-reflecting region between the contact and the substrate, and to reduce contact resistance. The highest efficiency obtained for amorphous silicon[3,4] has been ~ 13% using an n-p (or "tunnel") junction in combination with an undoped amorphous silicon-germanium alloy (a-SiGe:H) layer on the second p-layer and an amorphous silicon (a-Si) layer on the second n-layer. The "tunnel" junction functions as a recombination junction connecting the two p-i-n junctions in the series tandem cell.

Figure 1.7 shows the solar cell designs consisting of CdTe and $Cu(In,Ga)Se_2$. In the case of CdTe, the highest efficiency obtained for a CdTe homojunction[3,4] device is ~ 11%, but using n-type cadmium sulfide (CdS) in conjunction with p-type CdTe to form a heterojunction[3,4] increased the efficiency to ~ 16%. A solar cell with a heterojunction[4,30] consisting of CdS and $Cu(In,Ga)Se_2$ obtained the highest efficiency of ~ 19%.

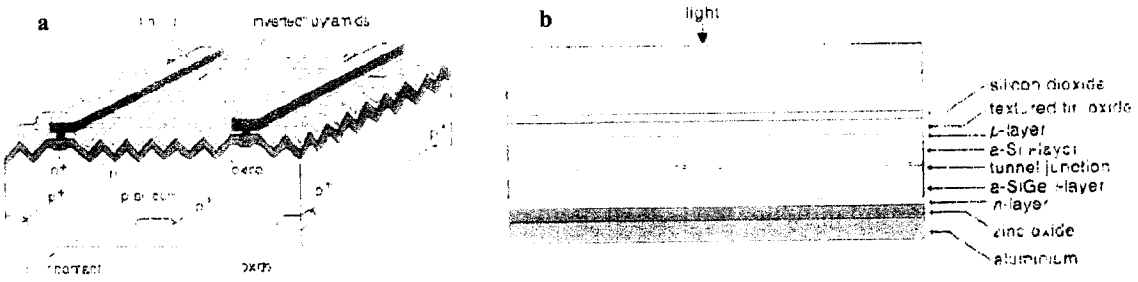

Figure 1.6. Schematic of the inorganic solar cell devices consisting of a) crystalline silicon, and b) amorphous silicon. [Ref 3]

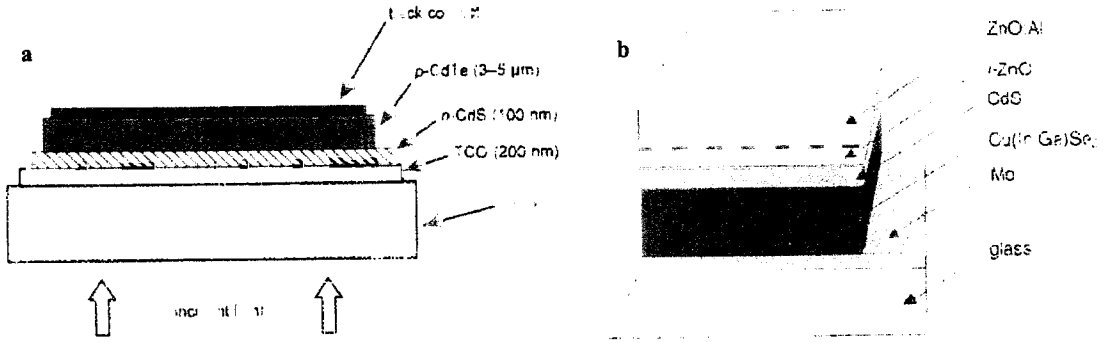

Figure 1.7. Schematic of the inorganic solar cell devices consisting of a) cadmium-telluride (CdTe), and b) copper-indium-gallium-selenide [$Cu(In,Ga)Se_2$] materials. [Ref 3]

Further exploration moved to the use of super-high efficiency III-V tandem and multi-junction cells[3,31]. There was great potential in earlier studies which showed that the use of single-junction solar cells consisting of a homojunction[3] of indium-phosphide (InP) or a heterojunction[32] of gallium-arsenide (GaAs) and gallium-indium-phosphide (GaInP) resulted in efficiencies close to 22% and 26%, respectively. As a result, solar

cells with multi-junctions[4,33] consisting of III-V compounds have obtained the highest efficiencies greater than 30%. Figure 1.8 depicts a solar cell with gallium-indium-phosphide (GaInP) in tandem with gallium-arsenide (GaAs) with the addition of an indium-gallium-phosphide (InGaP) tunnel junction layer and an aluminum-indium-phosphide (AlInP) barrier layer. Although the four-junction solar cell device has obtained the highest efficiency, the fabrication process is too complicated and the production cost is too high for commercial use. In addition, in order to widely utilize these solar cell devices, materials cost needs to be reduced.

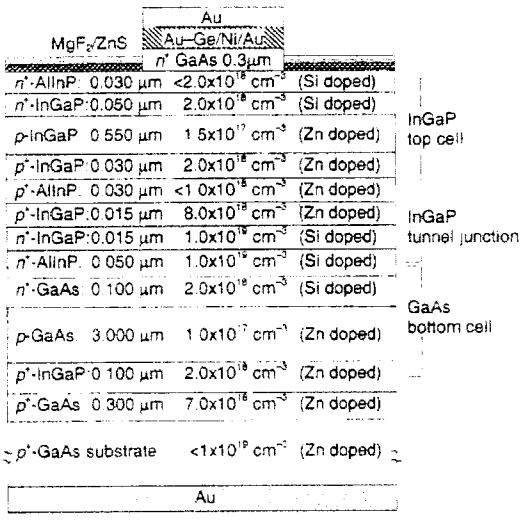

Figure 1.8. Depiction of an inorganic solar cell device with four-junctions, consisting of gallium-indium-phosphide (GaInP), gallium-arsenide (GaAs), indium-gallium-phosphide (InGaP), and aluminum-indium-phosphide (AlInP). [Ref 32]

1.2.2 Organic solar cells

The inexpensive and easy fabrication, as well as the versatility of polymeric materials, initiated the emergence of organic solar cell devices[34,35] that can be utilized on flexible substrates and complex shapes, and can be modified to accommodate specific

applications. Polymeric materials[22] are versatile for solar cell devices in that they can be synthesized and tailored to function at a specific region of the solar spectrum. Many of the materials used in organic solar cells exhibit high coloration to absorb strongly in the visible region of the spectrum and good stability under illumination in air and moisture. In addition, these materials can be prepared in thin-film form to reduce the bulk resistance, can be chemically "doped" to enhance the conductivity, and can exhibit photoconducting behavior.

Research in the area of organic solar cells has been based on flat-junction organic solar cells[34] consisting of interpenetrating polymer networks[35], polymer/fullerene blends[36], and halogen-doped organic crystals[37]. Newer devices with bulk donor-acceptor heterojunctions[38] formed by blending two organic materials, where one material serves as the electron donor (p-type conductor) and one material serves as the electron acceptor (n-type conductor) emerged to reduce the probability of surface charge recombination at the interface of the two materials. Figure 1.9 depicts a p-n organic solar cell showing the movement of electrons and holes after exciton separation.

In this type of composite structure, the electron-hole pair produced by the absorption of sunlight can reach the junction and dissociate into two free charge carriers before recombining since the distance the electron-hole pair has to travel within the structure is at most a few nanometers before reaching the interface. Typically, electron-hole pairs diffuse only a few nanometers before recombining. Thus, it was found that these composite structures have efficient photo-induced charge separation[39]. The disadvantage with solar cells consisting of only organic materials is the low electron mobility associated with conjugated polymers due to the presence of electron trapping

species, specifically oxygen[27]. The presence of two different organic materials provides an interface for charge transfer via percolation pathways, but the efficiency is limited due to inefficient transport by charge hopping and the presence of structural traps associated with an incomplete network of percolation pathways[40]. Therefore, the highest light conversion efficiency[4] obtained so far for organic solar cells is ~ 3%.

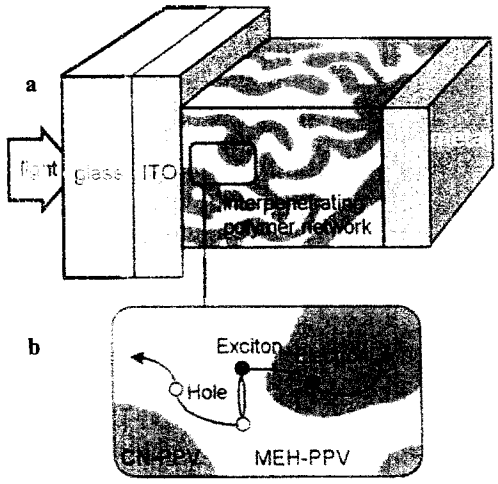

Figure 1.9. Schematic of a) an organic solar cell consisting of an n-type polymer and a p-type polymer interconnected to form a heterojunction, and b) the electron and hole migration through the polymer network after exciton generation. [Ref 3]

Additional organic solar cell devices have utilized hybrid structures[41] to improve the electron mobility and the light conversion efficiency, where a combination of solid-state electron-conducting materials and polymeric hole-conducting materials function together to convert solar power to electrical power. For example, the Alivisatos group[40,42] incorporated semiconducting nanorods of cadmium selenide (CdSe) into a hole-conducting conjugated polymer, poly-3(hexylthiophene) or P3HT, to fabricate a working solar cell with light conversion efficiency ~ 6.9%. The combination of inorganic and organic materials to fabricate hybrid solar cell devices is thought to correlate the

advantages of both types of materials. The presence of inorganic semiconductor materials utilizes the high intrinsic carrier mobility to reduce current loss from recombination by quicker charge transport, and the advantage of using polymeric materials is the ease in incorporating organics by solution methods to provide an interface for charge transfer, which is typically favored between high electron affinity inorganics and relatively low ionization potential organics[40,43]. It is found that charge transfer rates in organics that are chemically bound to nanocrystalline and bulk inorganic semiconductors with a high density of electron states can be very fast[42,44].

1.3 Dye-sensitized solar cells

One of the major reasons for the shift in solar cell exploration to oxide-based materials is the expensive and complicated fabrication process associated with solid-state inorganic p-n junction or heterojunction devices, as demonstrated in the semiconducting industry[3]. Although polymeric materials are easy to fabricate and have shown to have great potential in the development of solar cell devices, oxide-based semiconducting materials have been the material of choice in the exploration of cheaper solar cell devices due to better electron mobility and faster charge transfer rates than conjugated conducting polymers[23]. However, oxide-based semiconductors with band gaps narrow enough for efficient light absorption that are stable against photocorrosion are not available[12]. The semiconducting materials that are stable have wide band gaps, only absorb in the ultraviolet region of the spectrum, and are insensitive to visible light[23], which is not desirable for use in solar cells.

To resolve this issue, O'Regan and Grätzel[12] introduced an idea of separating the light absorption process and the charge-generating functions in the development of dye-sensitized solar cells. This type of device incorporates an electron transfer sensitizer that absorbs in the visible spectrum to inject charge carriers across the semiconductor-electrolyte junction. The electron carriers would be transported through the wide band gap semiconducting oxide material to the conducting substrate and the hole carriers would be transported through the electrolyte layer for subsequent sensitizer regeneration.

In order to take advantage of as much of the visible spectrum as possible, the nanostructure of the broad-band semiconductor oxide material in dye-sensitized solar cells was modified to possibly absorb more of the incident light. As a result, the development of mesoscopic semiconductor materials[12,45] that were minutely structured to obtain high internal surface area evolved. Films made of mesoporous oxide material consisted of arrays of nanometer-sized crystals that were interconnected to enable electron conduction. Semiconducting or conducting material for hole carrier transport, specifically a p-type semiconductor, a polymer, or an electrolyte, would be incorporated within the pores to form a junction between the two interpenetrating materials with large contact area and high internal surface area, enabling the continuous network of mesoscopic particles to provide a percolation pathway for both types of charge carriers.

1.3.1 TiO_2 nanocrystalline film

Much of the research in dye-sensitized solar cells has surrounded the use of porous nanocrystalline titania (TiO_2) film in conjunction with an efficient light-absorbing dye, and have shown an impressive energy conversion efficiency[4,12] of > 11% at lower

production costs. The TiO_2 semiconducting oxide[11] functions as a suitable electron-capturing and electron-transporting material with a conduction band at 4.2eV and an energy bandgap of 3.2eV, corresponding to an absorption wavelength of ~ 387nm. Typical TiO_2 film[11,46] thickness for solar cells with the highest light conversion efficiency ranges from 8μm to 12μm with a porosity of ~ 50%. It is also estimated that the size of the nanocrystals are ~ 20nm in diameter. Figure 1.10 is an SEM image of the typical TiO_2 mesoporous nanostructure used in the electrode for dye-sensitized solar cells.

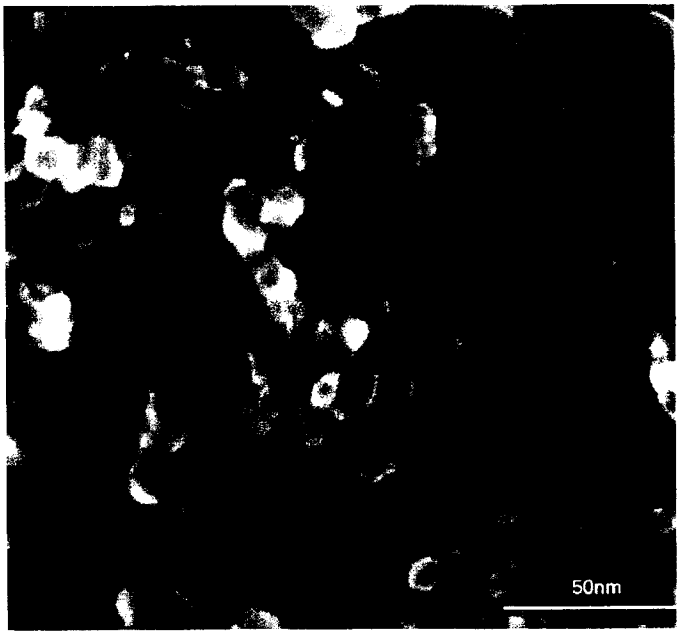

Figure 1.10. SEM image of TiO_2 nanocrystalline film, showing an interconnected network of particles and pores with ~ 20nm particles and ~ 50% porosity. [Ref 11,12]

This mesoscopic TiO_2 structure provides enough surface area for monolayer dye chemisorption, allowing for enough dye adsorption on the surface at a given area so as to absorb as much of the incident light as possible. It has been shown that the grain size of the TiO_2 nanocrystalline film can range from ~ 10nm up to ~ 80nm depending on the processing technique, and that the structures of the anatase TiO_2 nanocrystals[47] are

square-bipyramidal, pseudocubic, and stab-like. In addition, the TiO_2 nanocrystals are faceted with the (101) face mostly exposed, followed by the (100) face and the (001) face, respectively.

1.3.2 Synthesis of TiO_2 nanocrystalline film

There are two general synthesis techniques to form nanocrystalline film that provide a pathway for electrical conduction between particles. One approach[12,48] applies a suspension of particles to a conducting substrate and then requires sintering to form sufficient contact between particles for charge transport to the underlying substrate. Another approach[49,50,51] utilizes direct film formation onto a substrate by way of electrochemical or chemical deposition of nanocrystalline particles. The first approach is the most common synthesis process to obtain TiO_2 film with high porosity and high surface-to-volume ratio. The preparation of crack-free mesoporous TiO_2 thick film for use as suitable electron-transporting electrodes involves the preparation of TiO_2 paste by way of sol-gel processing of commercially-available TiO_2 colloidal precursors containing an amount of organic additives. This conventional method requires the deposition of the prepared paste by either doctor-blading, spin-coating, or screen-printing on a transparent conducting substrate. High temperature sintering is utilized to remove the organic species and to connect the colloidal particles for electrical contact between particles. The pores between colloidal particles are also interconnected and can be filled with electrolyte. Typical thickness[23] of mesoporous TiO_2 film using this method ranges from 2μm to 20μm, depending on the colloidal particle size and the processing conditions, and the

maximum porosity obtained by this technique has reported to be ~ 50% with an average particle size ~ 20nm in diameter.

It has been shown that the film thickness is an important factor in the synthesis of nanocrystalline film that is highly efficient. Studies[52] have shown that an increased probability of recombination with increasing film thickness occurs since electrons have to be transported across an increasing number of particles and grain boundaries. In addition, a thicker film results in a resistance loss that can lead to a decrease in photovoltage and fill factor. Therefore, an optimal film thickness is necessary to obtain a maximum photocurrent. As a result, many other techniques have recently been investigated to synthesize TiO_2 electrodes with improved structure and film thickness for more efficient electron transport and good stability. Chemical vapor deposition (CVD)[53] of Ti_3O_5 has been utilized to deposit layered crystalline anatase TiO_2 thin films that are optically responsive and stable. Gas-phase hydrothermal crystallization[54,55,56] of $TiCl_4$ in aqueous mixed paste has been done to obtain crack-free porous nanocrystalline TiO_2 thick film through low-temperature processing. Compression techniques[57] of TiO_2 powder have also been used to form porous and stable films. More recently, electrospinning[58] and electrodeposition[59] techniques have been used to deposit TiO_2 film on flexible substrates.

1.3.3 Mechanism of light conversion in dye-sensitized solar cells

Studies[52,60] on the charge transport of photoinjected electrons showed that electrons migrating through all the particles and grain boundaries in nanocrystalline TiO_2 films can be efficient enough for generating photocurrent. The common operation of nanocrystalline TiO_2 electrodes consist of the filling of trap states and the separation of

charges controlled by kinetics[61,62,63] at the semiconductor-electrolyte interface[64,65,66]. The energy levels of a dye-sensitized nanocrystalline TiO_2 film in contact with an electrolyte, and the process of light conversion is shown in Figure 1.11.

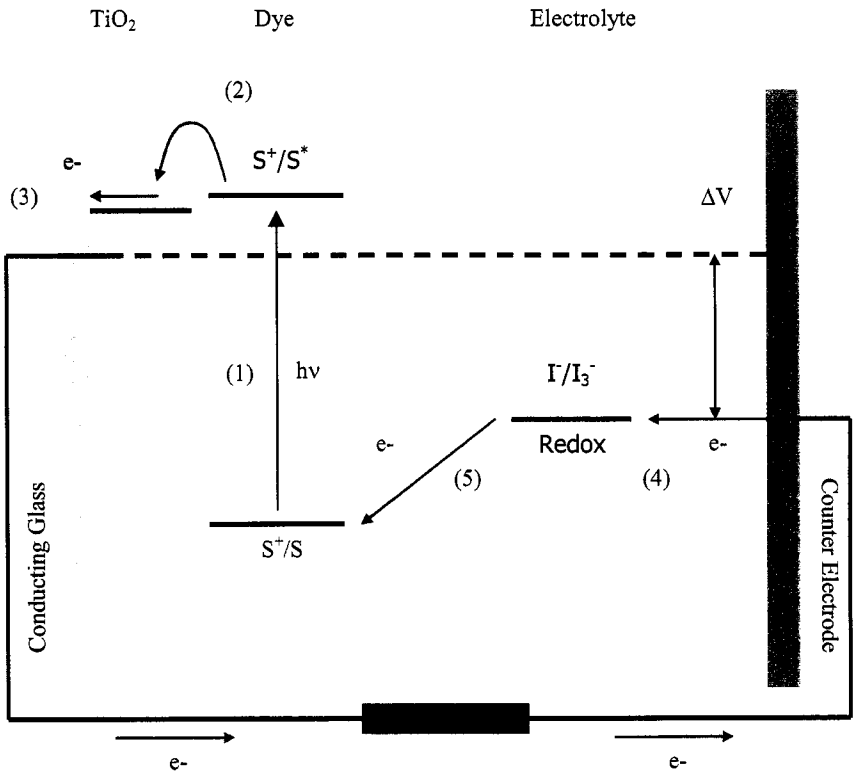

Figure 1.11. Schematic of the light conversion process in dye-sensitized solar cells showing (1) light absorption by the dye sensitizer, (2) electron injection from the dye into the conduction band of TiO_2, (3) electron transport through the TiO_2 film to the conducting substrate, (4) electron capture and reduction of the electrolyte, and (5) dye regeneration from reduction of the oxidized dye. [Ref 52]

It can be seen that the light conversion process of dye-sensitized solar cells consists of TiO_2 as the semiconducting oxide material and an iodine-based redox system as the liquid electrolyte. In this process, the dye adsorbed to TiO_2 is exposed to a light source, absorbs photons upon exposure, and injects electrons into the conduction band of the TiO_2 electrode. Regeneration of the dye is initiated by subsequent hole transfer to the electrolyte and electron capture after the completion of the I^-/I_3^- redox couple at the solid

electrode-liquid electrolyte interface. The photovoltage is also shown, which is the difference between the Fermi level of TiO_2 under illumination and the redox potential of the redox liquid electrolyte.

The typical dye sensitizer[67,68,69] adsorbed to the surface of TiO_2 consist of a ruthenium (Ru) complex, where the carboxylate groups serve to attach the Ru complex to the surface of TiO_2 and establish good electronic coupling. Figure 1.12 shows the desired pathway for a photoexcited electron, showing metal-to-ligand charge transfer (MLCT). At the point of light absorption of the dye sensitizer, charge transfer occurs from the metal to the ligand. The excitation energy is channeled into the ligand where electron injection into the conduction band takes place.

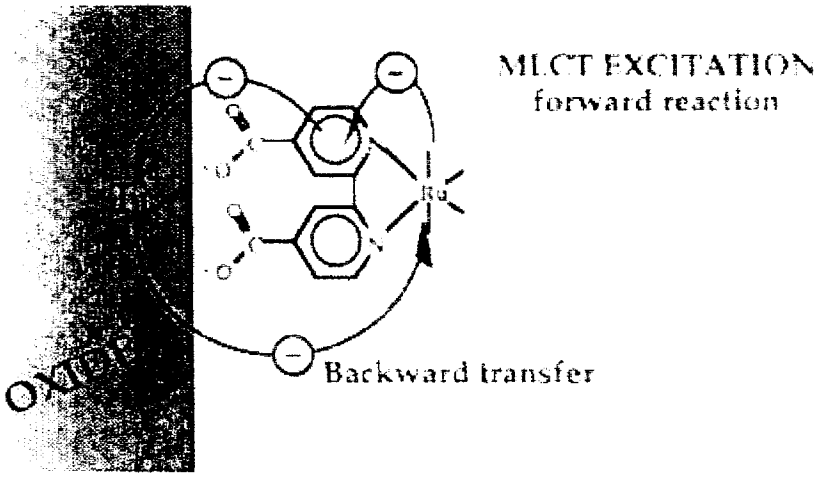

Figure 1.12. Schematic of the metal-to-ligand charge transfer in a ruthenium-based dye sensitizer anchored to the TiO_2 surface. [Ref 52]

The TiO_2 material not only functions as the sensitizer support but also functions as the electron acceptor and electronic conductor. The electrons injected into the conduction band of TiO_2 migrate through the nanocrystalline film to the underlying conducting substrate, which acts as the current collector. The circuit is complete with the

regeneration of the dye by electron transfer from the redox species in solution, which is then reduced at the counter electrode. During this process, it is possible that electron-hole recombination may occur at the interface where injected electrons can recombine with oxidized dye molecules or with oxidized species in the electrolyte. However, the chance of recombination[52] is negligible if the rate of electron injection at the sensitizer-semiconductor interface is much higher than the rate of recombination at the semiconductor-electrolyte interface. Figure 1.13 depicts the rate constants of the various steps associated with the light conversion process. Electron injection from the point of light absorption by the dye sensitizer into the conduction band has been measured to be in the picosecond range, whereas, the back reaction or recombination of electrons and holes has been measured in the microsecond range.

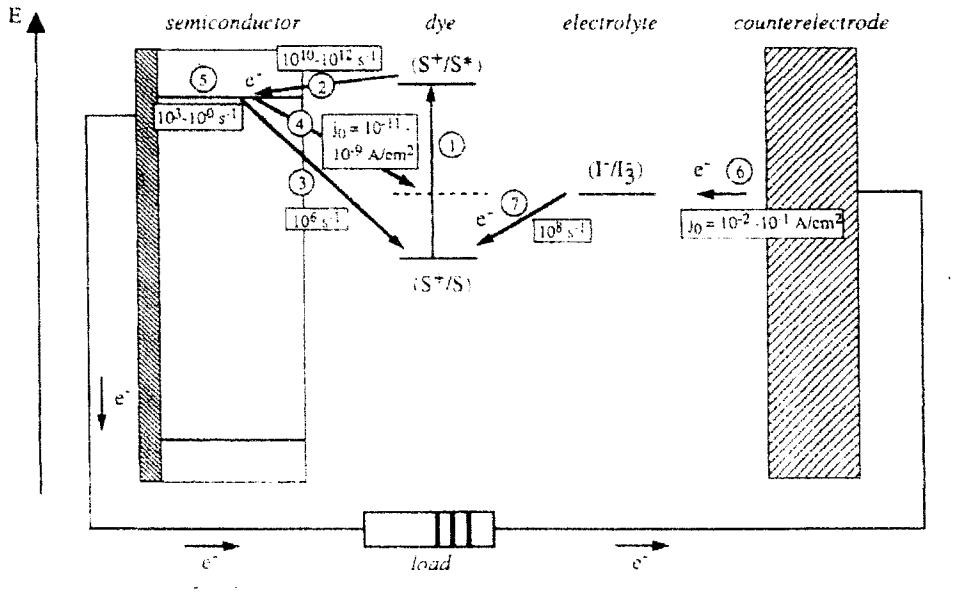

Figure 1.13. Schematic of the rate constants associated with each step of the light conversion process, showing the rate of (1) electron excitation, (2) electron injection, (3) electron and hole recombination, (4) reduction of the electrolyte by conduction band electrons, (5) electron migration, (6) reduction of the electrolyte at the counter electrode, and (7) reduction of the oxidized dye. [Ref 52]

In nanocrystalline film[70,71], it has been shown that conduction band electrons preferentially become trapped at grain boundaries, and that charge carriers can be trapped in localized energy levels in the band gap region, which can be the limiting factors in obtaining higher efficiencies. Electron trapping[72,73] in the bulk of the TiO_2 particles leads to a slow time response of the photocurrent but not to recombination losses, which can reduce the photovoltage. Electrons trapped at the surface of TiO_2 may lead to a recombination pathway, which can reduce the photocurrent and some decrease in photovoltage. Traps[64,74] are likely to include Ti^{3+} states that result from nonstoichiometry, oxygen deficiency and ion intercalation, surface adsorbed species, or other surface or interface states. It has been shown that the filling of trap sites[62,75] increases the ratio of mobile electrons to trapped electrons which can lead to increased sensitivity of current to voltage. The photocurrent generation[52] process can be shown in Figure 1.14.

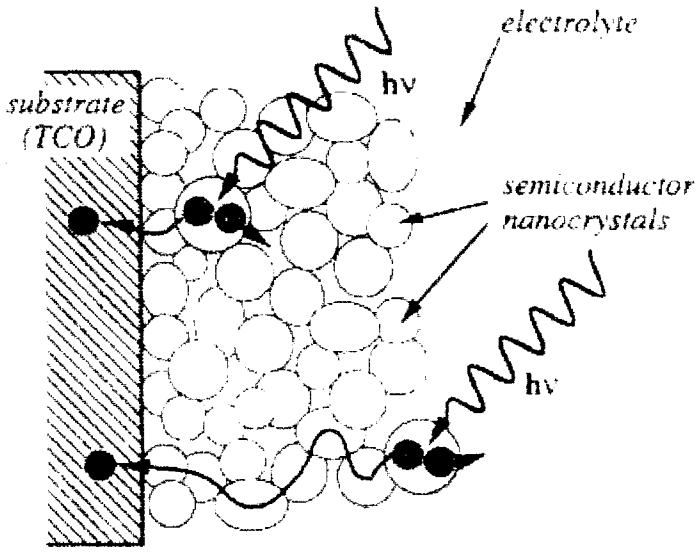

Figure 1.14. Schematic of the interconnected nanoparticle network showing photocurrent generation and electron migration through electron percolation pathways. [Ref 52]

It can be seen that the particle network allows for the electrolyte to penetrate the entire colloidal film all the way through to the surface of the conducting substrate, forming a semiconductor-electrolyte junction at each nanoparticle. Each nanoparticle with a sensitizer layer will then generate an electron-hole pair after light absorption. It is assumed that the charge transfer of holes to the electrolyte is much faster than the recombination process, resulting in the electrons creating a gradient in the electrochemical potential between the particles and the conducting substrate. This gradient thus allows for the transport of electrons through the interconnected network of particles to the conducting substrate, which produces current.

On the basis of a few studies[76,77,78], a schematic of the energy level diagrams of a system consisting of a mesoporous TiO_2 film on a conducting substrate (TCO) in an electrolyte can be assumed. Figure 1.15 shows the energy level diagram of the TCO-TiO_2-electrolyte system in various conditions. In the first case, the system is under equilibrium in the dark. The penetration of the electrolyte through the entire film to the underlying conducting substrate results in a fixed band edge position through the entire TiO_2 film. In the second case, the system is under illumination with short-circuit conditions. A bent quasi-Fermi level of electrons is shown, where a gradient in the electron concentration from the outer layer to the conducting substrate is present and a current is drawn through the system. In the third case, the open-circuit condition results in a buildup of photovoltage. However, more exploration[66,79] in the energetics and chemical nature of the energy levels in the band gap region and trapping states are required. The exact mechanism of charge transport through the colloidal particle network is also unknown. Some studies[71,80] suggested a hopping mechanism of transport with trapping

and untrapping events and other studies[63,65] have suggested a tunneling mechanism through a potential barrier between particles.

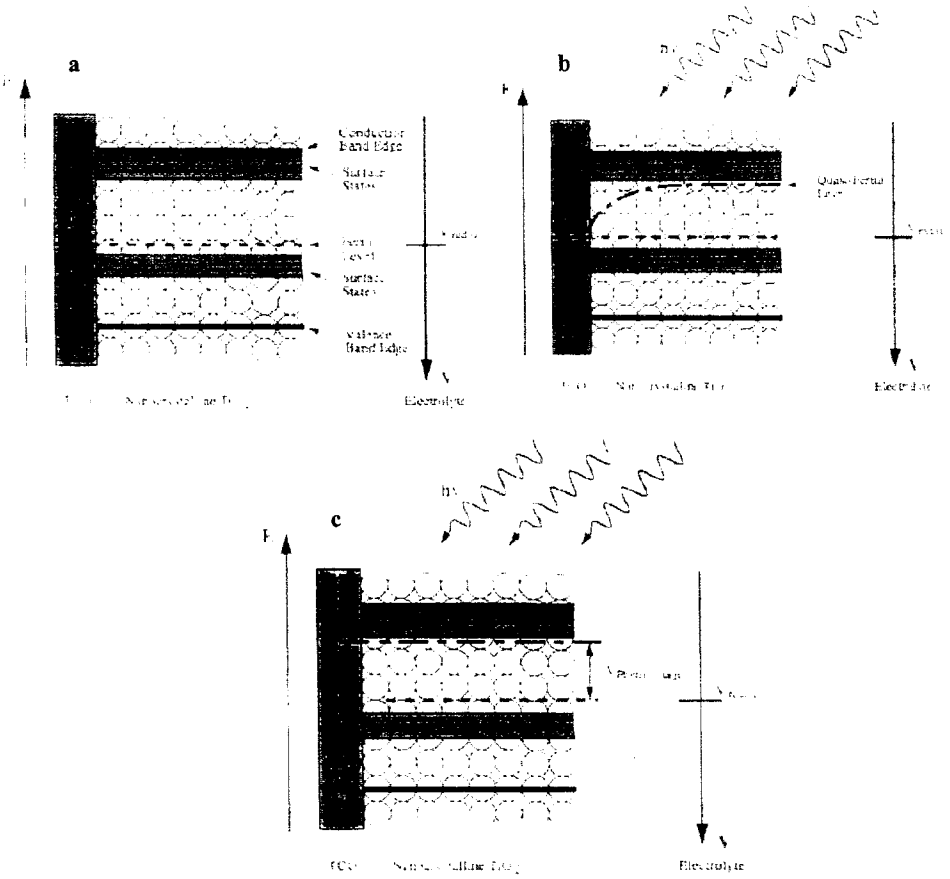

Figure 1.15. Schematic of the band edge positions associated with the energy levels a) under equilibrium in the dark, b) under illumination at short-circuit, and c) under illumination at open-circuit. [Ref 52]

1.3.4 Alternative materials for dye-sensitized solar cells

Although various techniques have been utilized and explored to synthesize a more efficient structure of TiO_2 nanocrystalline film to enhance the electrical and photovoltaic properties of dye-sensitized solar cell devices, the capability of these devices to surpass the 11% light conversion efficiency has been hindered. Efforts to find other dye-sensitized solar cell devices with various broad-band semiconducting oxide materials,

including ZnO[81,82] and SnO_2[83,84,85] films, have been made for possible improvement of the current state of TiO_2-based devices. Composite structures[86,87,88,89] consisting of a combination of TiO_2 and SnO_2, ZnO, or Nb_2O_5 materials, or a combination of other oxides, have also been examined in an attempt to enhance the overall light conversion efficiency. In addition, hybrid structures[40,42] comprised of a blend of semiconducting oxide film and polymeric layers for solid-state dye-sensitized solar cell devices have been explored in an effort to eliminate the liquid electrolyte completely for increased electron transfer and electron regeneration in hopes of increasing the overall efficiency. So far, these devices have achieved an overall light conversion efficiency of up to 5% for ZnO devices, up to 1% for SnO_2 devices, up to 6% for composite devices, and up to 2% for hybrid devices, all of which are still less efficient than solar cell devices based on dye-sensitized TiO_2 nanocrystalline film. Other methods incorporating insulating[90,91,92] or conducting[86,93] oxides to reduce electron-electron hole recombination and enhance electron conduction have also been explored to improve the efficiency.

1.3.4.1 ZnO-based dye-sensitized solar cells

An alternative material for use in dye-sensitized solar cells that has recently been explored more extensively is zinc oxide (ZnO). Since ZnO has a similar band gap to that for TiO_2 at 3.2eV, but has a much higher electron mobility[94,95] of ~ 115-155cm^2/Vs than that for anatase TiO_2 at ~ $10^{-5}cm^2$/Vs, it has the greatest potential as an alternative material for improving the solar cell performance in dye-sensitized solar cells. Figure 1.16 shows the band gap of various semiconducting materials used in various solar cell devices. It can be seen that ZnO has the same band gap as TiO_2, which indicates it has the

same stability to photocorrosion as TiO_2. The highest overall efficiency obtained for ZnO nanoparticle film[81] has been ~ 5% with an open-circuit voltage of ~ 560mV, a short-circuit current density of ~ 1.3mA/cm^2, and a fill factor of ~ 68% under 100mW/cm^2 illumination. The solar cell performance of ZnO is still not as high as that of TiO_2, but since the use of ZnO is still new, as compared to TiO_2, it is still in the process of being optimized for further enhancement of photoresponse properties.

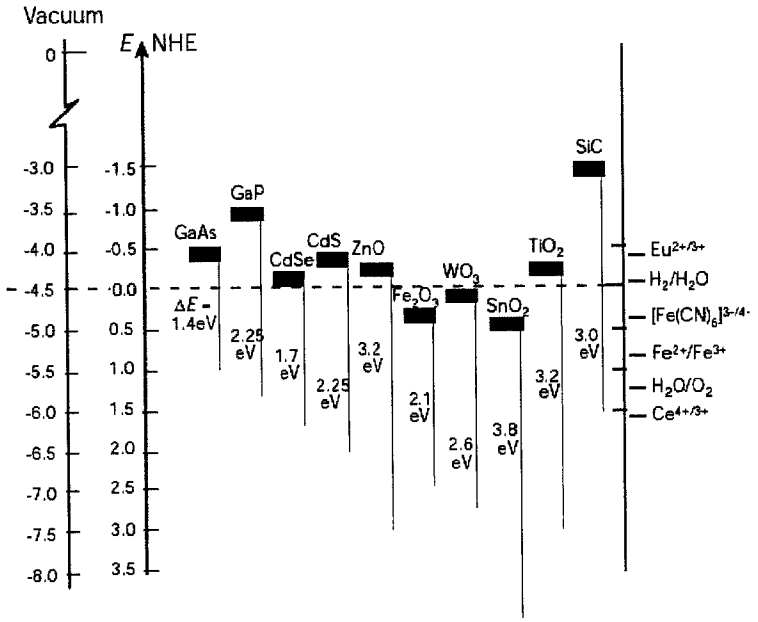

Figure 1.16. The band gap of various semiconducting materials used in various solid-state and dye-sensitized solar cell devices. It can be seen that ZnO and TiO_2 have the same band gap. [Ref 11]

Another factor for using ZnO is the simple processing of ZnO through solution methods[96,97] to tailor the nanostructure. The simple process for tailoring the nanostructure is essential with the emergence of nanoscale materials, or nanowires, to enhance the solar cell performance by utilizing an ordered arrangement of nanowire arrays with simpler electron percolation pathways. These aligned nanowires are thought to provide a more

ordered structure for dye adsorption and electron transport, as well as, provide a higher surface area for more light absorption, depending on the dimensions of the nanowires. Law et al[97] used aqueous chemistry and a seeded growth process to synthesize a dense array of oriented, crystalline ZnO nanowires and obtained an efficiency of ~ 1.5% with nanowires ~ 16-17μm in length and 130-200nm in diameter. The growth of single-crystalline ZnO nanowires is also essential to eliminate any barriers to electron transport typically found in polycrystalline material.

1.3.5 Current state of dye-sensitized solar cells

Initially, the highest overall efficiency obtained was ~ 10%[98] with an open-circuit voltage of ~ 720mV and a short-circuit current density of ~ 17.0mA/cm^2 under 100mW/cm^2 illumination. This efficiency was obtained by sensitizing the TiO_2 nanoparticle film with the standard N3 "red" dye. Later, it was found that the highest overall efficiency that could be obtained was ~ 10.4%[12] with an open-circuit voltage of ~ 720mV and a short-circuit current density of ~ 20.5mA/cm^2.

By sensitizing the TiO_2 nanoparticle film with N3 "black" dye, which has a slightly larger absorption range than the standard N3 "red" dye, the efficiency was improved by increasing the short-circuit current density through extending the wavelength of absorption of the sensitizer. Figure 1.17 compares the absorption behavior of the "black" dye and the N3 "red" dye. It can be seen that the absorption range of the "black" dye extends to ~ 900nm wavelength, whereas the N3 "red" dye extends to ~ 700nm wavelength. The modified "black" dye has a broader absorbance region, giving rise to a greater sensitization to visible light. Therefore, the use of the "black" dye would

allow for more of the visible light to be absorbed by the sensitized TiO_2 nanoparticle film, increasing the amount of electrons generated.

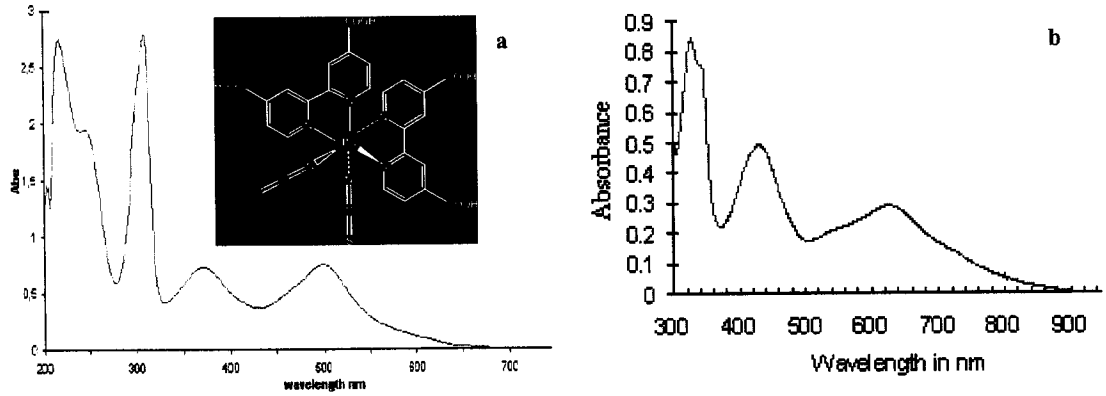

Figure 1.17. Absorbance spectra of a) standard N3 "red" dye, and b) N749 "black" dye, showing the wavelength range of absorption. [Ref 99,100]

However, it was later reported[47] that the highest overall efficiency increased to a little over ~ 11% using the N3 "red" dye with an open-circuit voltage of ~ 860mV and a short-circuit current density of ~ 16.5mA/cm^2. In this case, the increase in the open-circuit voltage occurred from adding guanidinium thiocyanate into the electrolyte. This additive was used as a self-assembly facilitating agent, where the guanidinium cations are adsorbed along with the N3 anions at the interface to facilitate the self-assembly of a compact dye monolayer. This compact assembly initiated more of the dye to adsorb on the surface of the TiO_2 nanoparticle film, increasing the photovoltage.

Many methods to modify the current TiO_2 nanoparticle structure have been explored to surpass the highest efficiency obtained so far. One type of structure explored consist of TiO_2 nanowires[101,102,103], ZnO nanowires[96,97], or TiO_2 nanotubes[104]. Another type of structure studied consist of ZnO-TiO_2 core-shells[105,106], where the TiO_2 nanoparticles are coated with a thin ZnO layer. In addition, other core-shell

structures[107,108] consist of titanium or indium cores with a thin layer of TiO_2 coating in order to utilize the high electron effective mass[109] of TiO_2 and the high electron mobility of the inner core. Other oxide materials[110,111] have also been studied to coat TiO_2 nanoparticles to form core-shell structures to improve charge separation and suppress recombination. With these structures, the overall efficiency has not surpassed 11%, but show great promise for enhancing the overall efficiency with further optimization.

Furthermore, more emphasis has been placed on modifying the ruthenium dye structure[112,113,114] to allow for further increases in light harvesting in the 700-900nm wavelength range. Specifically, ruthenium complexes of quaterpyridyl derivatives have shown the most potential. It is estimated[23,115] that if dye-sensitized solar cells can have optical features similar to gallium-arsenide (GaAs), where a rise in photocurrent occurs close to ~ 920nm absorption, the short-circuit current density would increase to $28mA/cm^2$, raising the overall efficiency to ~ 15%.

1.4 Rationale and motivation for this work

The exploration into alternative fuels and renewable energy has emerged due to current issues involving reduced energy resources and high energy production costs. The availability of the sun's energy has directed research in the area of solar-generated electrical energy. With the emergence of nanotechnology and the study of nanomaterials, in addition to the process of light conversion being on the nanoscale, the exploration of nanostructured materials and their charge transport properties is essential for progress in dye-sensitized solar cells.

The light conversion efficiency of solar cells depends on a number of material and system properties. There are a number of issues that influence the light conversion efficiency: 1) the light absorption and charge generation of the sensitizer, 2) the charge collection and transport properties of the semiconductor material, and 3) the surface area of the semiconducting material.

The surface of the semiconductor material plays a critical role. The more photons the surface absorbs, the more electron and electron-hole pairs can be generated. Many studies have resulted in the discovery of many new materials with better properties. The larger band-gap semiconductors can achieve a larger cell potential with greater stability. However, larger band-gap semiconductors are not able to absorb low energy photons. In order to harvest the most photons with varying energy, measures to modify the sensitizing material, as well as, methods to alter the nanostructure have been studied.

The surface of the semiconductor material is only one important aspect for determining the light conversion efficiency. Another critical issue that is equally important is the charge collection and charge transport properties of the semiconductor material. The energy levels of the semiconductor will determine the efficiency of charge collection, as well as the final achievable open-circuit potential in a solar cell. The transport properties will also have direct impact on the energy conversion efficiency. If electrical resistance in the semiconducting material is large, much of the energy will be consumed internally.

The surface area available for photon absorption at the surface of the semiconductor material is another important factor. The larger the surface area, the greater the amount of photons will be absorbed. Since photons typically have a

penetration depth of ~ 50 nm[116] in most materials, the absorption of photons at any given surface would be far from complete; therefore, multiple surfaces are commonly introduced to achieve a higher fraction of photons. This consideration has led to the usage of highly porous oxide materials, such as mesoporous TiO_2, to introduce the desired surface area large enough for efficient light absorption.

Dye-sensitized solar cells typically consist of TiO_2 nanocrystalline film, where nanocrystals with a size distribution of ~ 15-20nm form an interconnected network for electron conduction. The high surface area of such nanocrystalline film, in conjunction with a dye sensitizer adsorbed to the surface, allows for absorption of much of the photons in the visible region to create electron-hole pairs for current generation.

Although the current mesoporous TiO_2 film offers a significantly enhanced surface area and thus high energy conversion efficiency, there are several challenges to achieve efficiencies comparable to solid-state p-n junction solar cells. In particular, the irregular porous structure[11] may prevent complete coverage of organic dyes within the internal surface of porous TiO_2 films. Such incomplete surface coverage of dyes would not only reduce the efficiency of photon absorption and electron–hole pair generation, but also leave "short circuits" for surface charge recombination at the interface. In addition, the irregular porous structure consists of an irregular solid network that consists of many "bottleneck" connections between individual nanometer-sized particles. These "bottleneck" contact points between adjacent nanoparticles would have lower electrical conductance, not only due to its small cross-sectional area, but also due to an increase in surface scattering which can contribute to electrical resistivity.

This dissertation explores a few areas of interest related to dye-sensitized solar cells in order to examine some of the above issues. Solar cells consisting of TiO_2 nanoparticle film with varying particle sizes were studied and compared to determine whether the electron transport properties and the overall light conversion efficiency are influenced by the differences in surface area or the amount of dye adsorption. Dye-sensitized solar cells widely studied typically consist of TiO_2 nanoparticles ~ 20nm in diameter, where the particle size effect has not been examined extensively. Therefore, a systematic study to determine the particle size effect of TiO_2 on the solar cell performance was explored.

In addition, TiO_2 nanoparticle film with the incorporation of ITO was fabricated to compare the solar cell performance in order to examine the effect of electron mobility and electron conduction. Specifically, films consisting of TiO_2 nanoparticle film with ITO nanoparticles, TiO_2 nanoparticle film with ITO nanorods, and ITO nanorod arrays with TiO_2 coating were fabricated and analyzed. Nanocomposite structures have been studied for better charge separation and suppression of recombination, but ITO has not been studied as one of the composite materials for the utilization of better charge transport properties.

Additionally, ZnO nanoparticle film and ZnO nanowire arrays were explored since ZnO has the greatest potential as an alternative material for dye-sensitized solar cells. Although ZnO has a higher electron mobility than that for TiO_2 with the same band gap, it has so far shown to have a lower light conversion efficiency than TiO_2. However, extensive research in ZnO has recently emerged and needs further exploration to optimize the nanostructure to obtain higher efficiencies.

1.5 Scope

Chapter 1 focuses on the various types of solar cell devices and materials currently explored to convert sunlight to electrical energy. A brief introduction and background based on reported literature is discussed here, and the rationale and motivation of this work is presented.

Chapter 2 presents and discusses the experimental results for the fabrication of dye-sensitized solar cells with TiO_2 nanoparticle films with varying particle size. Films consisting of TiO_2 nanoparticles with particle sizes ranging from ~ 6nm to ~ 18nm are fabricated by hydrothermal treatment of TiO_2 at various temperatures and times. The current-voltage behavior of the TiO_2 nanoparticle film with varying particle sizes are compared to determine whether the electron transport properties and the overall light conversion efficiency are influenced by the differences in particle size.

Chapter 3 examines the solar cell performance of TiO_2 nanoparticle film with the inclusion of ITO nanoparticles or nanorods. The incorporation of ITO to the TiO_2 nanoparticle structure is used as a means to enhance the photocurrent by including a more conductive oxide with higher electron mobility. Three nanocomposite films are explored: 1) TiO_2 nanoparticle film with the addition of ITO nanoparticles, 2) TiO_2 nanoparticle film with the addition of ITO nanorods, and 3) ITO nanorod arrays with a thin layer of TiO_2 coating. The current-voltage behavior of these films are analyzed and compared in an effort to determine whether the incorporation of ITO to the TiO_2 system can improve the current output and overall efficiency by reducing the internal resistance.

Chapter 4 explores the use of ZnO as an alternative material for dye-sensitized solar cells. Both ZnO nanoparticle film, with primary nanoparticles and secondary

colloidal spheres, and ZnO nanowire array film, with 100-300nm diameters, are fabricated. The solar cell performance of the above films is compared. The dye loading of ZnO nanoparticle films is also studied in order to optimize the solar cell performance.

Chapter 5 outlines the possible directions of future work to be pursued further. These areas involve the continuing examination of: 1) the fabrication of TiO_2 film by hydrothermal treatment and electrophoretic deposition, 2) the incorporation of ITO to TiO_2 or ZnO nanostructures, 3) the fabrication of various TiO_2-ITO and ZnO-TiO_2 nanocomposite structures, 4) the use of FTO as an alternative conducting material, and 5) the growth of single-crystal TiO_2 or ZnO nanowires for use in solar cells.

Notes to Chapter 1

[1] M. Grätzel, "Perspectives for Dye-sensitized Nanocrystalline Solar Cells," *Progress in Photovoltaics: Research and Applications* **8**, 171 (2000).

[2] M.A. Green, "Third Generation Photovoltaics: Ultra-high Conversion Efficiency at Low Cost," *Progress in Photovoltaics: Research and Applications* **9**, 123 (2001).

[3] M.D. Archer and R. Hill. *Series on Photoconversion of Solar Energy: Clean Electricity from Photovoltaics*. Vol. 1. London: Imperial College Press, 2001.

[4] M.A. Green, K. Emery, D.L. King, Y. Hishikawa, and W. Warta, "Solar Cell Efficiency Tables (Version 28)," Progress in Photovoltaics: Research and Applications **14**, 455 (2006).

[5] National Aeronautics and Space Administration, *International Space Station*, <http://search.nasa.gov/home/index.html>

[6] National Aeronautics and Space Administration, *Mariner 5 Satellite*, <http://search.nasa.gov/home/index.html>

[7] National Aeronautics and Space Administration, *Sojourner Vehicles*, <http://search.nasa.gov/home/index.html>

[8] U.S. Department of Energy, *Energy Efficiency and Renewable Energy*, <http://eere.energy.gov/>

[9] Evergreen Solar, *Applications*, <http://www.evergreensolar.com/>

[10] Green Car Congress, *Solar-Power-Augmented Prius Takes the Grid Out of "Plug-in"*, 15 August 2005, <http://www.greencarcongress.com/>

[11] M. Grätzel, "Photoelectrochemical Cells," *Nature* **414**, 338 (2001).

[12] A. Hagfeldt and M. Grätzel, "Molecular Photovoltaics," *Accounts of Chemical Research* **33**, 269 (2000).

[13] G. Hodes, I.D.J. Howell, and L.M. Peter, "Nanocrystalline Photoelectrochemical Cells: A New Concept in Photovoltaic Cells," *Journal of the Electrochemical Society* **139**, 3136 (1992).

[14] M. Grätzel, "The artificial leaf, bio-mimetic photocatalysis," *Catalyst Technology* **3**, 4 (1999).

[15] M. Nishida, "A theoretical treatment of charge transfer via surface states at a semiconductor-electrolyte interface: Analysis of the water photoelectrolysis process," *Journal of Applied Physics* **51**, 1669 (1980).

[16] D.E. Aspnes and A. Heller, "Photoelectrochemical Hydrogen Evolution and Water-Photolyzing Semiconductor Suspensions: Properties of Platinum Group Metal Catalyst-Semiconductor Contacts in Air and In Hydrogen," *Journal of Physical Chemistry* **87**, 4919 (1983).

[17] O. Khaselev and J.A. Turner, "A Monolithic Photovoltaic-Photoelectrochemical Device for Hydrogen Production via Water Splitting," *Science* **280**, 425 (1998).

[18] S. Licht, "Solar Water Splitting To Generate Hydrogen Fuel: Photothermal Electrochemical Analysis," *Journal of Physical Chemistry B* **107**, 4254 (2003).

[19] C.J. Barbé, F. Arendse, P. Comte, M. Jirousek, F. Lenzmann, V. Shklover, and M. Grätzel, "Nanocrystalline Titanium Oxide Electrodes for Photovoltaic Applications," *Journal of the American Ceramic Society* **80**, 3157 (1997).

[20] A. Mills and S.L. Hunte, "An overview of semiconductor photocatalysis," *Journal of Photochemistry and Photobiology A: Chemistry* **108**, 1 (1997).

[21] S. Licht, "Multiple Band gap Semiconductor/Electrolyte Solar Energy Conversion," *Journal of Physical Chemistry B* **105**, 6281 (2001).

[22] D. Wöhrle and D. Meissner, "Organic Solar Cells," *Advanced Materials* **3**, 129 (1991).

[23] M. Grätzel, "Dye-sensitized solar cells," Journal of Photochemistry and Photobiology C: Photochemistry Reviews **4**, 145 (2003).

[24] Silicon Solar Inc, *Commercial Solar Cells*, < http://www.siliconsolar.com/index.php>

[25] Live Science Technology, *Personal Power: Bendable Organic Solar Cells*, 24 December 2004, <http://www.livescience.com>

[26] Solaronix SA, *Products*, <http://www.solaronix.com>

[27] B.A. Gregg, "Excitonic Solar Cells," *Journal of Physical Chemistry B* **107**, 4688 (2003).

[28] R.H. Bube. Photoelectronic Properties of Semiconductors. Cambridge: Cambridge University Press, 1992.

[29] J. Zhao, A. Wang, P. Altermatt, and M.A. Green, "Twenty-four percent efficient silicon solar cells with double layer antireflection coatings and reduced resistance loss," *Applied Physics Letters* **66**, 3636 (1995).

[30] M.A. Contreras, B. Egaas, K. Ramanathan, J. Hiltner, A. Swartzlander, F. Hasoon, and R. Noufi, "Towards 20% efficiency in Cu(In,Ga)Se_2 polycrystalline solar cells," *Progress in Photovoltaic Research Applications* **7**, 311 (1999).

[31] R. Tena-Zaera, A. Katty, S. Bastide, C. Lévy-Clément, B. O'Regan, and V. Muñoz-Sanjosé, "ZnO/CdTe/CuSCN, a promising heterostructure to act as inorganic eta-solar cell," *Thin Solid Films* **483**, 372 (2005).

[32] S.R. Kurtz, P. Faine, and J.M. Olson, "Modeling of two-junction, series-connected tandem solar cells using top-cell thickness as an adjustable parameter," *Journal of Applied Physics* **68**, 1890 (1990).

[33] T. Takamoto, E. Ikeda, H. Kurita, and M. Ohmori, "Over 30% efficient InGaP/GaAs tandem solar cells," *Applied Physics Letters* **70**, 381 (1997a).

[34] G. Yu, J. Gao, J.C. Hummelen, F. Wudl, and A.J. Heeger, "Polymer photovoltaic cells: enhanced efficiencies via a network of internal donor acceptor heterojunctions," *Science* **270**, 1789 (1995).

[35] J.J.M. Halls, K. Pickler, R.H. Friend, S.C. Morati, and A.B. Holmes, "Efficient photodiodes from interpenetrating polymer networks," *Nature* **376**, 498 (1995).

[36] C.J. Brabec and N.S. Sariciftci, "Polymeric photovoltaic devices," *Materials Today*, 3 (2000).

[37] P. Peumans, A. Yakimov, and S.R. Forrest, "Small molecular weight organic thin-film photodetectors and solar cells," *Journal of Applied Physics* **93**, 3693 (2003).

[38] B. Kannan, K. Castelino, and A. Majumdar, "Design of Nanostructured Heterojunction Polymer Photovoltaic Devices," *Nanoletters* **3**, 1729 (2003).

[39] H. Hoppe and N.S. Sariciftci, "Organic solar cells: An overview," *Journal of Materials Research* **19**, 1924 (2004).

[40] W.U. Huynh, J.J. Dittmer, and A.P. Alivisatos, "Hybrid Nanorod-Polymer Solar Cells," *Science* **295**, 2425 (2002).

[41] D. Gebeyehu, C.J. Brabec, and N.S. Sariciftci, "Solid-state organic/inorganic hybrid solar cells based on conjugated polymers and dye-sensitized TiO_2 electrodes," *Thin Solid Films* **403-404**, 271 (2002).

[42] W.U. Huynh, X. Peng, and A.P. Alivisatos, "CdSe Nanocrystal Rods/Poly(3-hexylthiophene) Composite Photovoltaic Devices," *Advanced Materials* **11**, 923 (1999).

[43] K. Triyana, T. Yasuda, K. Fujita, and T. Tsutsui, "Tandem-type organic solar cells by stacking different heterojunction materials," *Thin Solid Films* **477**, 198 (2005).

[44] J.L. Segura, N. Martin, and D.M. Guldi, "Materials for organic solar cells: the C60/p-conjugated oligomer approach," *Chemical Society Reviews* **34**, 31 (2005).

[45] J. Bisquert, D. Cahen, G. Hodes, S. Rühle, and A. Zaban, "Physical Chemical Principles of Photovoltaic Conversion with Nanoparticulate, Mesoporous Dye-Sensitized Solar Cells," *Journal of Physical Chemistry B* **108**, 8106 (2004).

[46] U. Bach, D. Lupo, P. Comte, J.E. Moser, F. Weissörtel, J. Salbeck, H. Spreitzer, and M. Grätzel, "Solid-state dye-sensitized mesoporous TiO_2 solar cells with high photon-to-electron conversion efficiencies," *Nature* **395**, 583 (1998).

[47] M. Grätzel, "Conversion of sunlight to electric power by nanocrystalline dye-sensitized solar cells," *Journal of Photochemistry and Photobiology A: Chemistry* **164**, 3 (2004).

[48] J. Jiu, F. Wang, M. Sakamoto, J. Takao, and M. Adachi, "Performance of dye-sensitized solar cell based on nanocrystals of TiO_2 film prepared with mixed template method," *Solar Energy Materials & Solar Cells* **87**, 77 (2005).

[49] C. Natarajan and G. Nogami, "Electrodeposition of Nanocrystalline Titanium Dioxide Thin Films," Journal of the *Electrochemical Society* **143**, 1547 (1996).

[50] S. Karuppuchamy, K. Nonomura, T. Yoshida, T. Sugiura, and H. Minoura, "Cathodic Electrodeposition of oxide semiconductor thin films and their application to dye-sensitized solar cells," *Solid State Ionics* **151**, 19 (2002).

[51] T. Miyasaka and Y. Kijitori, "Low-Temperature Fabrication of Dye-Sensitized Plastic Electrodes by Electrophoretic Preparation of Mesoporous TiO_2 Layers," *Journal of the Electrochemical Society* **151**, A1767 (2004).

[52] A. Hagfeldt and M. Grätzel, "Light-Induced Redox Reactions in Nanocrystalline Systems," *Chemical Reviews* **95**, 49 (1995).

[53] M. Thelakkat, C. Schmitz, and H.W. Schmidt, "Fully Vapor-Deposited Thin-Layer Titanium Dioxide Solar Cells," *Advanced Materials* **14**, 577 (2002).

[54] F. Pichot, J.R. Pitts, and B.A. Gregg, "Low-Temperature Sintering of TiO_2 Colloids: Application to Flexible Dye-Sensitized Solar Cells," *Langmuir* **16**, 5626 (2000).

[55] D. Zhang, T. Yoshida, and H. Minoura, "Low Temperature Synthesis of Porous Nanocrystalline TiO_2 Thick Film for Dye-Sensitized Solar Cells by Hydrothermal Crystallization," *Chemistry Letters*, 874 (2002).

[56] K.J. Jiang, T. Kitamura, H. Yin, S. Ito, and S. Yanagida, "Dye-sensitized Solar Cells Using Brookite Nanoparticle TiO_2 Films as Electrodes," *Chemistry Letters*, 872 (2002).

[57] G. Boschloo, H. Lindström, E. Magnusson, A. Holmberg, and A. Hagfeldt, "Optimization of dye-sensitized solar cells prepared by compression method," *Journal of Photochemistry and Photobiology A: Chemistry* **148**, 11 (2002).

[58] M.Y. Song, D.K. Kim, K.J. Ihn, S.M. Jo, and D.Y. Kim, "Electrospun TiO_2 electrodes for dye-sensitized solar cells," *Nanotechnology* **15**, 1861 (2004).

[59] J.H. Yum, S.S. Kim, D.Y. Kim, and Y.E. Sung, "Electrophoretically deposited TiO_2 photo-electrodes for use in flexible dye-sensitized solar cells," *Journal of Photochemistry and Photobiology A: Chemistry* **173**, 1 (2005).

[60] K. Schwarzburg and F. Willig, "Origin of Photovoltage and Photocurrent in the Nanoporous Dye-Sensitized Electrochemical Solar Cell," *Journal of Physical Chemistry B* **103**, 5743 (1999).

[61] J. Krüger, R. Plass, M. Grätzel, P.J. Cameron, and L.M. Peter, "Charge Transport and Back Reaction in Solid-State Dye-Sensitized Solar Cells: A Study Intensity-Modulated Photovoltage and Photocurrent Spectroscopy," *Journal of Physical Chemistry B* **107**, 7536 (2003).

[62] J.R. Durrant, S.A. Haque, and E. Palomares, "Towards optimization of electron transfer processes in dye sensitized solar cells," *Coordination Chemistry Review* **248**, 1247 (2004).

[63] A.N.M. Green, E. Palomares, S.A. Haque, J.M. Kroon, and J.R. Durrant, "Charge Transport versus Recombination in Dye-Sensitized Solar Cells Employing Nanocrystalline TiO_2 and SnO_2 Films," *Journal of Physical Chemistry B* **109**, 12525 (2005).

[64] B.A. Gregg, "Interfacial processes in the dye-sensitized solar cell," *Coordination Chemistry Reviews* **248**, 1215 (2004).

[65] S. Rühle and D. Cahen, "Electron Tunneling at the TiO2/Substrate Interface Can Determine Dye-Sensitized Solar Cell Performance," *Journal of Physical Chemistry B* **108**, 17946 (2004).

[66] K. Fredin, J. Nissfolk, and A. Hagfeldt, "Brownian dynamics simulations of electrons and ions in mesoporous films," *Solar Energy Materials & Solar Cells* **86**, 283 (2005).

[67] K. Srikanth, V.R. Marathe, and M.K. Mishra, "Role of Electronic Structure of Ruthenium Polypyridyl Dyes in the Photoconversion Efficiency of Dye-Sensitized Solar Cells: Semiempirical Investigation," *International Journal of Quantum Chemistry* **89**, 535 (2002).

[68] Y. Tachibana, M.K. Nazeeruddin, M. Grätzel, D.R. Klug, and J.R. Durrant, "Electron injection kinetics for the nanocrystalline TiO_2 films sensitized with the dye $(Bu_4N)_2Ru(dcbpyH)_2(NCS)_2$," *Chemical Physics* **285**, 127 (2002).

[69] T. Renouard, R.A. Fallahpour, Md.K. Nazeeruddin, R. Humphry-Baker, S.I. Gorelsky, A.B.P. Lever, and M. Grätzel, "Novel Ruthenium Sensitizers Containing Functionalized Hybrid Tetradentate Ligands: Synthesis, Characterization, and INDO/S Analysis," *Inorganic Chemistry* **41**, 367 (2002).

[70] D. Cahen and G. Hodes, "Nature of Photovoltaic Action in Dye-Sensitized Solar Cells," *Journal of Physical Chemistry B* **104**, 2053 (2000).

[71] A.M. Eppler, I.M. Ballard, and J. Nelson, "Charge transport in porous nanocrystalline titanium oxide," *Physica E* **14**, 197 (2002).

[72] J. Nelson, "Continuous-time random-walk model of electron transport in nanocrystalline TiO_2 electrodes," *Physical Review B* **59**, 153 74 (1999).

[73] J. Nelson, S.A. Haque, D.R. Klug, and J.R. Durrant, "Trap-limited recombination in dye-sensitized nanocrystalline metal oxide electrodes," *Physical Review B* **63**, 205321-1 (2001).

[74] J. Bisquert, A. Zaban, and P. Salvador, "Analysis of the Mechanisms of Electron Recombination in Nanoporous TiO_2 Dye-Sensitized Solar Cells. Nonequilibrium Steady-State Statistics and Interfacial Electron Transfer via Surface States," *Journal of Physical Chemistry B* **106**, 8774 (2002).

[75] Y. Tachibana, K. Hara, S. Takano, K. Sayama, and H. Arakawa, "Investigation on anodic photocurrent loss processes in dye sensitized solar cells: comparison between nanocrystalline SnO_2 and TiO_2 films," *Chemical Physics Letters* **364**, 297 (2002).

[76] S. Nakade, M. Matsuda, S. Kambe, Y. Saito, T. Kitamura, T. Sakata, Y. Wada, H. Mori, and S. Yanagida, "Dependence of TiO_2 Nanoparticle Preparation Methods and Annealing Temperature on the Efficiency of Dye-Sensitized Solar Cells," *Journal of Physical Chemistry B* **106**, 10004 (2002).

[77] C. Guillard, B. Beaugiraud, C. Dutriez, J.M. Herrmann, H. Jaffrezic, N. Jaffrezic-Renault, and M. Lacroix, "Physicochemical properties and photocatalytic activities of TiO_2-films prepared by sol-gel methods," *Applied Catalysis B: Environmental* **39**, 331 (2002).

[78] S. Nakada, Y. Saito, W. Kubo, T. Kitamura, Y. Wada, and S. Yanagida, "Influence of TiO_2 Nanoparticle Size on Electron Diffusion and Recombination in Dye-Sensitized TiO_2 Solar Cells," *Journal of Physical Chemistry B* **107**, 8607 (2003).

[79] P.J. Cameron and L.M. Peter, "How Does Back-Reaction at the Conducting Glass Substrate Influence the Dynamic Photovoltage Response of Nanocrystalline Dye-Sensitized Solar Cells?," *Journal of Physical Chemistry B* **109**, 7392 (2005).

[80] F. Pichot and B.A. Gregg, "The Photovoltage-Determining Mechanism in Dye-Sensitized Solar Cells," *Journal of Physical Chemistry B* **104**, 6 (2000).

[81] K. Keis, C. Bauer, G. Boschloo, A. Hagfeldt, K. Westermark, H. Rensmo, and H. Siegbahn, "Nanostructured ZnO electrodes for dye-sensitized solar cell applications," *Journal of Photochemistry and Photobiology A: Chemistry* **148**, 57 (2002).

[82] A.B. Kashyout, M. Soliman, M. El Gamal, and M. Fathy, "Preparation and characterization of nanoparticles ZnO films for dye-sensitized solar cells," *Materials Chemistry and Physics* **90**, 230 (2005).

[83] S. Chappel, S.G. Chen, and A. Zaban, "TiO_2-coated Nanoporous SnO_2 Electrodes for Dye-Sensitized Solar Cells," *Langmuir* **18**, 3336 (2002).

[84] S. Chappel and A. Zaban, "Nanoporous SnO_2 electrodes for dye-sensitized solar cells: improved cell performance by the synthesis of 18 nm SnO_2 colloids," *Solar Energy Materials & Solar Cells* **71**, 141 (2002).

[85] S.C. Lee, J.H. Lee, T.S. Oh, and Y.H. Kim, "Fabrication of tin oxide film by sol-gel method for photovoltaic solar cell system," *Solar Energy Materials & Solar Cells* **75**, 481 (2003).

[86] K. Tennakone, P.K.M. Bandaranayake, P.V.V. Jayaweera, A. Konno, and G.R.R.A. Kumara, "Dye-sensitized composite semiconductor nanostructures," *Physica E* **14**, 190 (2002).

[87] K.M.P Bandaranayake, M.K. Indika Senevirathna, P.M.G.M. Prasad Weligamuwa, and K. Tennakone, "Dye-sensitized solar cells made from nanocrystalline TiO_2 films coated with outer layers of different oxide materials," *Coordination Chemistry Reviews* **248**, 1277 (2004).

[88] T. Stergiopoulos, I.M. Arabatzis, M. Kalbac, I. Lukes, and P. Falaras, "Incorporation of innovative compounds in nanostructured photoelectrochemical cells," *Journal of Materials Processing Technology* **161**, 107 (2005).

[89] S.G. Chen, S. Chappel, Y. Diamant, and A. Zaban, "Preparation of Nb_2O_5 Coated TiO_2 Nanoporous Electrodes and Their Application to Dye-Sensitized Solar Cells," *Chemistry of Materials* **13**, 4629 (2001).

[90] T.S. Kang, S.H. Moon, and K.J. Kim, "Enhanced Photocurrent-Voltage Characteristics of Ru(II)-Dye Sensitized TiO_2 Solar Cells with TiO_2-WO_3 Buffer Layers Prepared by a Sol-Gel Method," *Journal of the Electrochemical Society* **149**, E155 (2002).

[91] E. Palomares, J.N. Clifford, S.A. Haque, T. Lutz, and J.R. Durrant, "Control of Charge Recombination Dynamics in Dye Sensitized Solar Cells by the Use of Conformally Deposited Metal Oxide Blocking Layers," *Journal of the American Chemical Society* **125**, 475 (2003).

[92] P.K.M. Bandaranayake, P.V.V. Jayaweera, and K. Tennakone, "Dye-sensitization of magnesium-oxide-coated cadmium sulfide," *Solar Energy Materials & Solar Cells* **76**, 57 (2003).

[93] J. Bandara, U.W. Pradeep, and R.G.S.J. Bandara, "The role of n-p junction electrodes in minimizing the charge recombination and enhancement of photocurrent and photovoltage in dye sensitized solar cells," *Journal of Photochemistry and Photobiology A: Chemistry* **170**, 273 (2005).

[94] E.M. Kaidashev, M. Lorenz, H. von Wenckstern, A. Rahm, H.C. Semmelhack, K.H. Han, G. Benndorf, C. Bundesmann, H. Hochmuth, and M. Grundmann, "High electron mobility of epitaxial ZnO thin films on c-plane sapphire grown by multistep pulsed-laser deposition," *Applied Physics Letters* **82**, 3901 (2003).

[95] Th. Dittrich, E.A. Lebedev, and J. Weidmann, "Electron Drift Mobility in Porous TiO_2 (Anatase)," *Rapid Research Notes* **165**, R5 (1998).

[96] J.B. Baxter and E.S. Aydil, "Nanowire-based dye-sensitized solar cells," *Applied Physics Letters* **86**, 053114 (2005).

[97] M. Law, L.E. Greene, J.C. Johnson, R. Saykally, and P. Yang, "Nanowire dye-sensitized solar cells," *Nature Materials* **4**, 455 (2005).

[98] M.K. Nazeeruddin, A. Kay, I. Rodicio, R. Humphry-Baker, E. Mueller, P. Liska, N. Vlachopoulos, and M. Graetzel, "Conversion of light to electricity by cis-X_2bis(2,2'-bipyridyl-4,4'-dicarboxylate)ruthenium(II) charge-transfer sensitizers (X = Cl-, Br-, I-, CN-, and SCN-) on nanocrystalline titanium dioxide electrodes," *Journal of the American Chemical Society* **115**, 6382 (1993).

[99] Solterra Fotovoltaica SA, *Photosensitive Dyes: N3"red" dye*, <http://www.solterra.ch>

[100] Solaronix SA, *Ruthenium 620 – 1H3TBA (Black-dye)*, <http://www.solaronix.com>

[101] M.Y. Song, D.K. Kim, K.J. Ihn, S.M. Jo, and D.Y. Kim, "Electrospun TiO_2 electrodes for dye-sensitized solar cells," *Nanotechnology* **15**, 1861 (2004).

[102] M. Adachi, Y. Murata, J. Takao, J. Jiu, M. Sakamoto, and F. Wang, "Highly Efficient Dye-Sensitized Solar Cells with a Titania Thin-Film Electrode Composed of a Network Structure of Single-Crystal-like TiO_2 Nanowires Made by the "Oriented Attachment" Mechanism," *Journal of the American Chemical Society* **126**, 14943 (2004).

[103] M.Y. Song, Y.R. Ahn, S.M. Jo, D.Y. Kim, and J.P. Ahn, "TiO_2 single-crystalline nanorod electrode for quasi-solid-state dye-sensitized solar cells," *Applied Physics Letters* **87**, 113113 (2005).

[104] S. Ngamsinlapasathian, S. Sakulkhaemaruethai, S. Pavasupree, A. Kitiyanan, T. Sreethawong, Y. Suzuki, and S. Yoshikawa, "Highly efficient dye-sensitized solar cell using nanocrystalline titania containing nanotube structure," *Journal of Photochemistry and Photobiology A: Chemistry* **164**, 145 (2004).

[105] N.G. Park, M.G. Kang, K.M. Kim, K.S. Ryu, S.H. Chang, D.K. Kim, J. van de Lagemaat, K.D. Benkstein, and A.J. Frank, "Morphological and Photoelectrochemical Characterization of Core-Shell Nanoparticle Films for Dye-Sensitized Solar Cells: Zn-O Type Shell on SnO_2 and TiO_2 Cores," *Langmuir* **20**, 4246 (2004).

[106] D. Menzies, Q. Dai, Y.B. Cheng, G.P. Simon, and L. Spiccia, "Improvement of the Zirconia shell in nanostructured titania core-shell working electrodes for dye-sensitized solar cells," *Materials Letters* **59**, 1893 (2005).

[107] D.B. Menzies, L. Bourgeois, Y.B. Cheng, G.P. Simon, N. Brack, and L. Spiccia, "Characterization of nanostructured core-shell working electrodes for application in dye-sensitized solar cells," *Surface & Coatings Technology* **198**, 118 (2005).

[108] S. Chappel, L. Grinis, A. Ofir, and A. Zaban, "Extending the Current Collector into the Nanoporous Matrix of Dye Sensitized Electrodes," *Journal of Physical Chemistry B Letters* **109**, 1643 (2005).

[109] J. Bandara, U.W. Pradeep, and R.G.S.J. Bandara, "The role of n-p junction electrodes in minimizing the charge recombination and enhancement of photocurrent and photovoltage in dye sensitized solar cells," *Journal of Photochemistry and Photobiology A: Chemistry* **170**, 273 (2005).

[110] Y. Diamant, S. Chappel, S.G. Chen, O. Melamed, and A. Zaban, "Core-shell nanoporous electrode for dye sensitized solar cells: the effect of shell characteristics on the electronic properties of the electrode," *Coordination Chemistry Reviews* **248**, 1271 (2004).

[111] K.M.P. Bandaranayake, M.K. Indika Senevirathna, P.M.G.M. Prasad Weligamuwa, and K. Tennakone, "Dye-sensitized solar cells made from nanocrystalline TiO_2 films coated with outer layers of different oxide materials," *Coordination Chemistry Reviews* **248**, 1277 (2004).

[112] Y.V. Zubavichus, Y.L. Slovokhotov, M.K. Nazeeruddin, S.M. Zakeeruddin, M. Grätzel, and V. Shklover, "Structural Characterization of Solar Cell Prototypes Based on Nanocrystalline TiO_2 Anatase Sensitized with Ru Complexes. X-ray Diffraction, XPS, and XAFS Spectroscopy Study," *Chemistry of Materials* **14**, 3556 (2002).

[113] P. Wang, S.M. Zakeeruddin, R. Humphry-Baker, J.E. Moser, and M. Grätzel, "Molecular-Scale Interface Engineering of TiO_2 Nanocrystals Improving the Efficiency and Stability of Dye-Sensitized Solar Cells," *Advanced Materials* **15**, 2101 (2003).

[114] Y.C. Hsu, H. Zheng, J.T. Lin, and K.C. Ho, "On the structural variations of Ru(II) complexes for dye-sensitized solar cells," *Solar Energy Materials & Solar Cells* **87**, 357 (2005).

[115] M. Grätzel, "Mesoscopic Solar Cells for Electricity and Hydrogen Production from Sunlight," *Chemistry Letters* **34**, 8 (2005).

[116] G.Z. Cao. Nanostructures & Nanomaterials: Synthesis, Properties, & Applications. London: Imperial College Press, 2004.

2 Dependence of solar cell performance on TiO_2 particle size in dye-sensitized solar cells

2.1 Introduction

With the emergence of nanotechnology and the fabrication of various oxide materials in the nanoscale, opportunities for developing new-age solar cells have surfaced. The exploration of light absorption and photocurrent generation in the conversion of solar energy to electrical power is in the nanoscale. Thus, it is reasonable that the exploration in the development and control of inorganic semiconductors at the nanometer scale for use in solar cell devices has emerged.

To this point, the most efficient electrodes in dye-sensitized solar cells have been 8-12μm thick mesoporous TiO_2 film consisting of an interconnected network[11,12] of nanometer-sized crystals ~ 20nm in size. It has been shown that this type of structure imparts a large enough surface area for suitable dye adsorption, efficient light absorption, and charge formation. These films depend upon suitable sintering processes to bind the colloidal particles together for good electrical connections necessary for electron injection and transport in the film, and electron capture by the underlying substrate. Typically, the colloidal particles are connected by small necking points, or bottlenecks. A decrease in the necking area between adjacent colloidal particles caused by a reduced amount of material and poor sintering processes can diminish the contact area between neighboring colloids. These factors can lead to an increase in surface recombination of electrons and holes at the electrode-electrolyte interface and a loss of current, leading to a reduced overall light conversion efficiency.

In this chapter, solar cells consisting of TiO_2 nanoparticle film with varying particle sizes were studied and compared to determine whether the electron transport properties and the overall light conversion efficiency are influenced by the difference in particle size. There are a few advantages associated with using larger particles, which could enhance the solar cell performance. Figure 2.1 depicts the advantages associated with using larger TiO_2 particles for dye-sensitized solar cells. These advantages include: 1) larger contact points between sintered colloidal particles, 2) larger contact points at the interface between the TiO_2 nanoparticles and the underlying substrate, and 3) better dye assembly associated with larger contact points, where easier access of the dye is present.

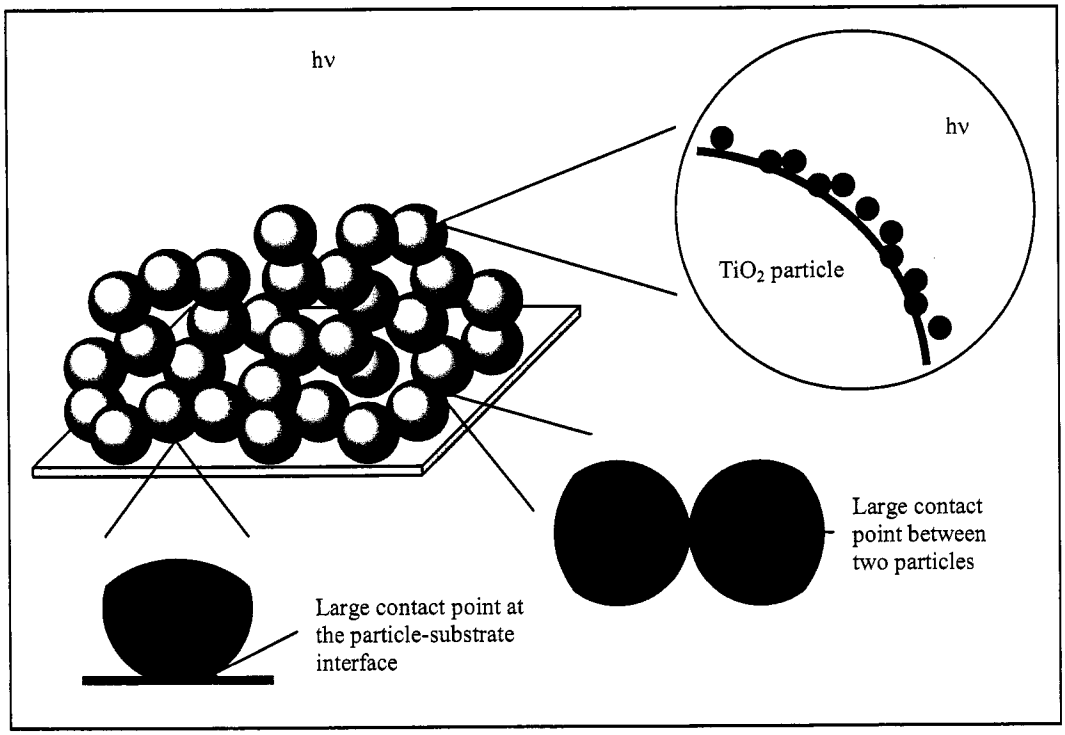

Figure 2.1. Schematic of the advantages associated with using larger particles in TiO_2 nanoparticle film used in dye-sensitized solar cells.

Of course, smaller particles have its advantages that could also enhance the solar cell performance. Figure 2.2 depicts the advantages associated with using smaller TiO_2

particles for dye-sensitized solar cells. These advantages include: 1) a larger surface area for a greater amount of dye adsorption on the TiO_2 surface, 2) a greater number of contact points between sintered colloidal particles, and 3) a greater number of contact points at the interface between the TiO_2 nanoparticles and the underlying substrate. However, films with an interconnected network of very small particles exhibit a larger number of grain boundaries where electrons need to pass through, which results in a higher probability of electron trapping[117,118].

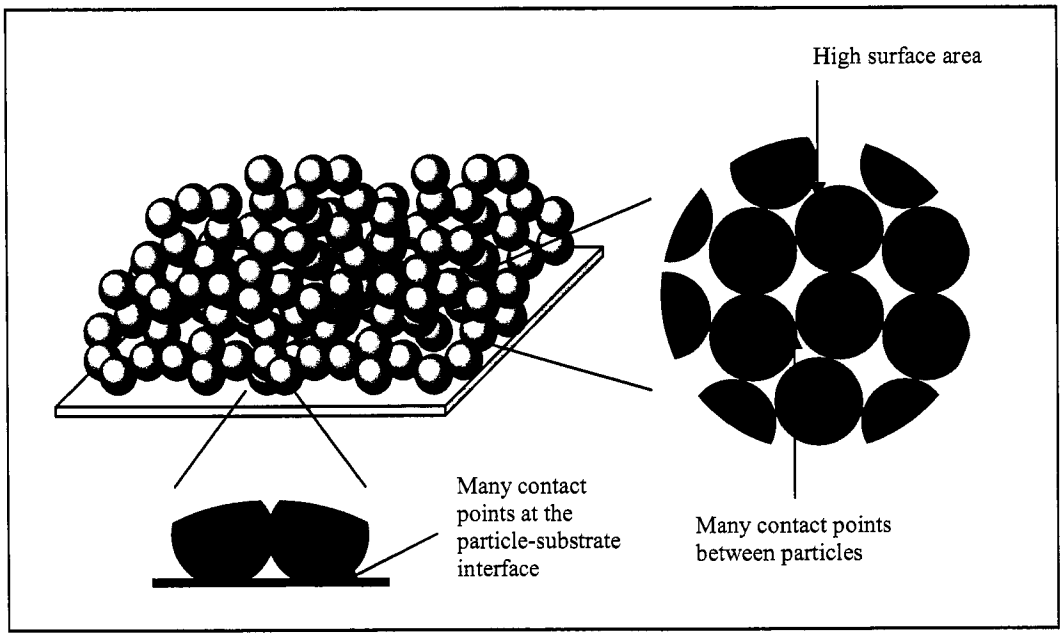

Figure 2.2. Schematic of the advantages associated with using smaller particles in TiO_2 nanoparticle film used in dye-sensitized solar cells.

Films consisting of TiO_2 nanoparticles with varying particle sizes were prepared by way of hydrothermal treatment at 1) varying temperatures, and 2) varying times. Hydrothermal crystallization[119,120] of TiO_2 was performed at 1) 100°C, 150°C, 200°C, 250°C, or 300°C for 60 minutes, and 2) 250°C for 20, 40, 60, or 120 minutes to vary the particle size of TiO_2. Films were fabricated from all hydrothermally-treated TiO_2 particle

powders and tested under illumination, and the I-V behavior of all TiO_2 nanoparticle films from solar cell analysis was compared.

2.2 Experimental procedure

The following sections describe 1) TiO_2 sol preparation, 2) hydrothermal crystallization of TiO_2, 3) fabrication of TiO_2 nanoparticle film, 4) solar cell assembly, 5) general analysis techniques, and 6) solar cell analysis.

2.2.1 TiO_2 sol preparation

Titania (TiO_2) sol[121] was prepared from precursor materials by way of sol-gel processing. The chemicals used in making TiO_2 sol were titanium (IV) isopropoxide (97%, Alfa Aesar, Ward Hill, MA), glacial acetic acid (Fisher Scientific, Fair Lawn, NJ), and deionized water. The sol was prepared by dissolving titanium (IV) isopropoxide [$Ti(OCH(CH_3)_2)_4$] in glacial acetic acid [CH_3CO_2H] and adding deionized water (DI-H_2O) to give a nominal molar ratio of $1.02Ti[OCH(CH_3)_2]_4$:$10.5CH_3CO_2H$:16.6DI-H_2O. Figure 2.3 represents a flow chart for processing TiO_2 sol.

The solution was stirred for approximately 30 minutes at room temperature after the instantaneous formation of a white precipitate disappeared and the solution became clear. The resultant sol had a pH value of ~ 2, resulting in positively-charged TiO_2 sol particles (IEP ~ 6.2). The sol was clear and stable at room temperature for up to seven days, but was stored at -20°C when not in use to minimize reactions. Sonication for roughly 10 minutes was done to bring the sol back to room temperature and to disperse the sol particles before use.

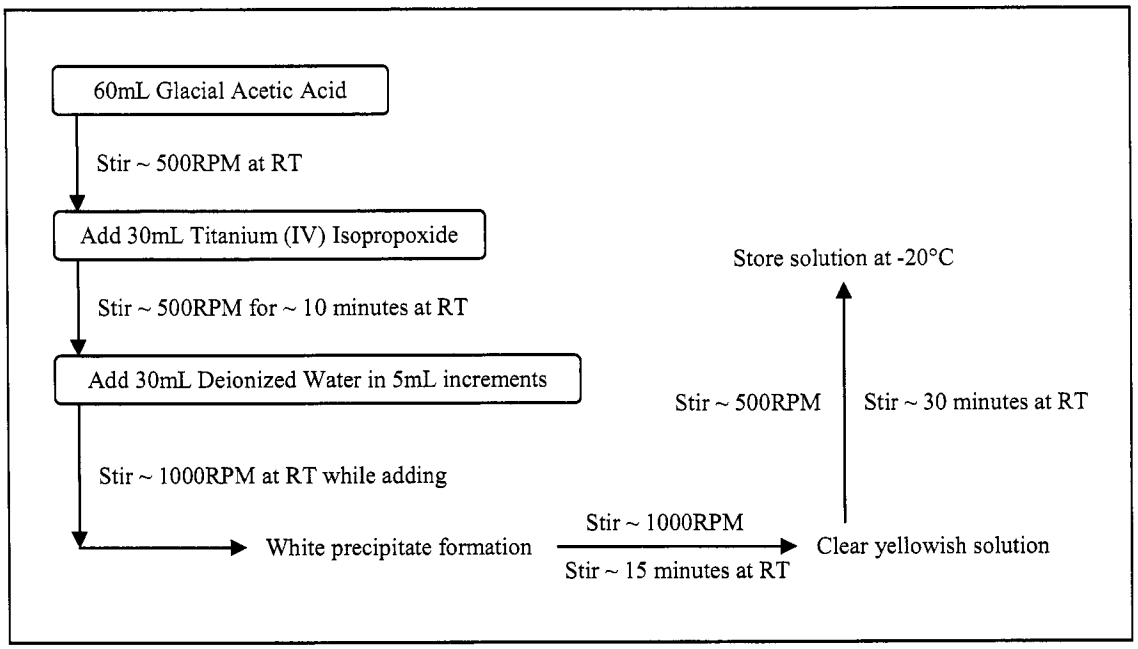

Figure 2.3. Schematic of the steps and procedures involved in sol-gel processing of precursors to obtain TiO_2 sol.

2.2.2 Hydrothermal crystallization of TiO_2

The TiO_2 powders were obtained by hydrothermally treating TiO_2 sol using an acid digestion bomb (Parr Instrument Co, Moline, Il). Using this type of sealed reaction chamber allowed for low temperature heating and relied on a higher pressure in an aqueous environment for crystallization of TiO_2. For each hydrothermal treatment, approximately 10mL of TiO_2 sol was placed in a polytetrafluoroethylene cup (PTFE, Parr Instrument Co, Moline, Il) and sealed in an acid digestion bomb (Parr Instrument Co, Moline, Il). Figure 2.4 is an example of the hydrothermal chamber used to hydrothermally-treat TiO_2 sol.

The entire chamber was then heated to as high as 300°C (the maximum temperature allowable for this type of chamber) for 60 minutes and as low as 100°C for 60 minutes. Additional experiments were also performed at 250°C for various amounts of

time. After heating to a specific temperature and time, the sol became a paste-like substance in all cases. This was then allowed to dry at 100°C for 24 hours and the resultant crystals were ground into a powder using a mortar and pestle.

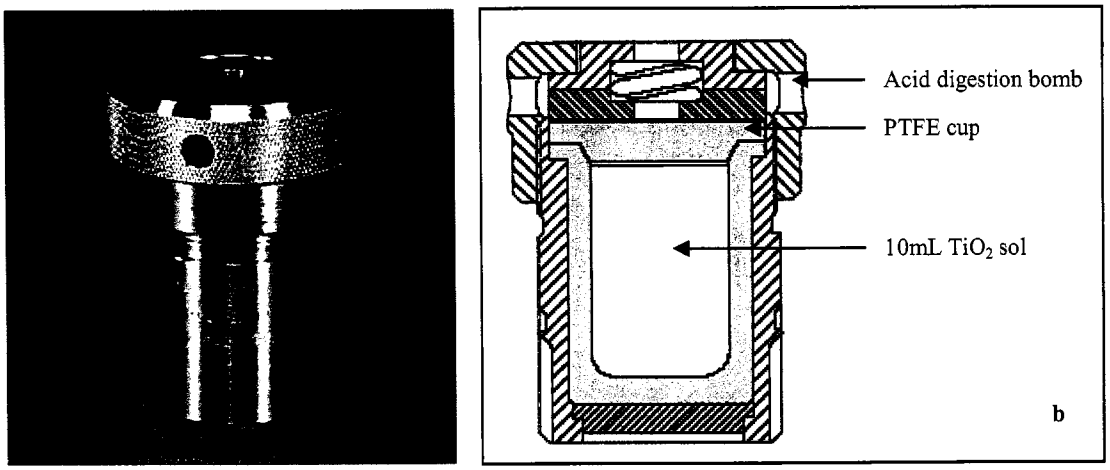

Figure 2.4. Image of the equipment used for hydrothermal crystallization, depicting a) the actual acid digestion bomb, and b) a diagram of the interior of the hydrothermal chamber, showing the PTFE cup containing sol. [Ref 122]

Various hydrothermally-treated TiO_2 powders were obtained by heating 10mL of TiO_2 sol in an acid digestion bomb for 60 minutes either at 100°C, 150°C, 200°C, 250°C, or 300°C to study the variation in particle size by varying the hydrothermal treatment temperature. Additional experiments were also done at 250°C to obtain the variation in TiO_2 particle size based on the amount of time TiO_2 sol was hydrothermally-treated. The various hydrothermally-treated TiO_2 powders were obtained by heating 10mL of TiO_2 sol in an acid digestion bomb at 250°C for either 20, 40, 60, or 120 minutes. In each case, the resultant paste was then dried at 100°C for 24 hours and ground to a fine powder. XRD analysis was performed on each powder sample to obtain the phase and particle size.

2.2.3 Fabrication of TiO_2 nanoparticle film

For solar cell testing, TiO_2 nanoparticle film with ~ 10μm thickness was prepared from the various hydrothermally-treated TiO_2 powders. Samples of 10μm-thick TiO_2 nanoparticle film were directly deposited onto conductive fluorine-tin-oxide (FTO) glass substrates by doctor-blading a dispersion of 20-30 wt% TiO_2 powder in ethanol solution. Figure 2.5 shows the doctor-blading process for forming the TiO_2 film on a substrate. Before preparing the film, the surface of the FTO substrates were hydrolyzed by heating to 90-100°C in DI H_2O for 30-60 minutes. After the substrates were air-dried, two parallel edges of each substrate were covered with ~ 10-μm-thick scotch tape to control the thickness of the film.

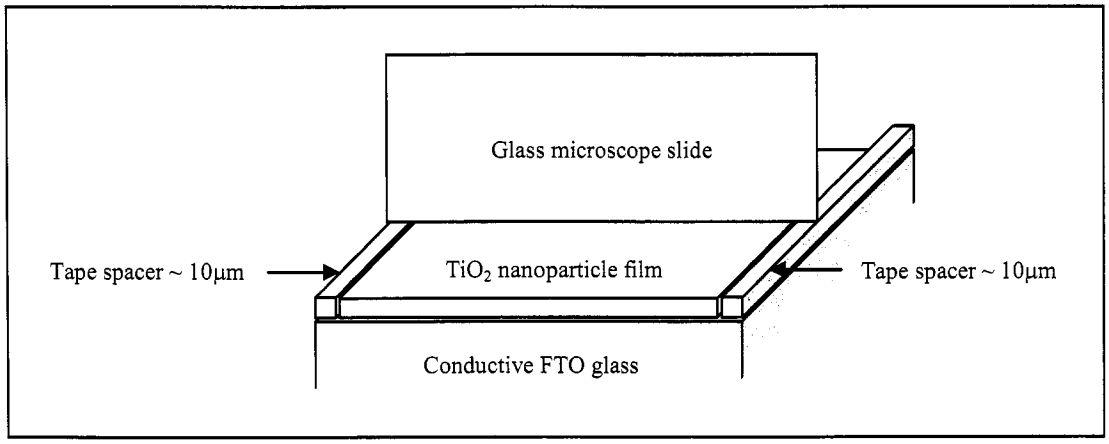

Figure 2.5. A schematic of the doctor-blading process for forming 10μm-thick TiO_2 film on a conductive substrate. The flat edge of a microscope slide was used to spread the film.

To form the film, three drops of the TiO_2 powder dispersion were placed at the center of each substrate and the edge of a glass microscope slide was used to spread the solution to form an even 10μm layer after sliding over the tape-covered edges. The film was then dried in air at 100°C for 1 hour, and sintered at 500°C for 1 hour at a heating

rate of 2°C/min. All the TiO_2 nanoparticle films were prepared on transparent, conductive FTO-coated glass substrates (TCO10-10, R_s ~ 10ohm/sq, Solaronix SA, Switzerland) for film characterization and solar cell analysis.

2.2.4 Solar cell assembly

Each TiO_2 electrode sample was heated to 70°C and subsequently immersed in standard ruthenium-based red dye (N3), cis-bis(isothiocyanato)bis(2,2'-bipyridyl-4,4'-di-carboxylato)ruthenium(II) (Solterra Fotovoltaico SA, Switzerland), with a concentration close to $5x10^{-4}$M in ethanol for ~ 12 hours. The samples were then rinsed with ethanol to remove excess dye on the surface and air-dried at room temperature. Colloidal liquid silver (Ted Pella Inc., Redding, CA) was placed at the electrical contacts to improve the contact points and allowed to cure for 30 minutes at room temperature. Sheets of weigh paper ~ 30-40μm thick were cut into small pieces ~ 1mm x 4mm in dimension and used as spacers. A spacer was placed at each edge of the TiO_2 working electrode and the counter electrode consisting of a Pt-coated silicon (Si) substrate with a Pt layer thickness of ~ 180nm was placed on top, with the Pt-coated side of each Si substrate facing the TiO_2 working electrode. Figure 2.6 illustrates the assembly of each solar cell device. The two electrodes were sandwiched together with two heavy duty clips.

An iodide-based solution was used as the liquid electrolyte, consisting of 0.6M tetra-butylammonium idodide (Sigma-Aldrich, St Louis, MO), 0.1M lithium iodide (LiI, Sigma-Aldrich, St Louis, MO), 0.1M iodine (I_2, Sigma-Aldrich, St Louis, MO), and 0.5M 4-tert-butyl pyridine (Sigma-Aldrich, St Louis, MO) in acetonitrile (Mallinckrodt Baker, Phillipsburg, NJ). Right before analysis, drops of the liquid electrolyte were introduced to

one edge of the sandwich, where capillary force was used to spread the liquid electrolyte in between the two electrodes. The light source was placed next to each solar cell device, allowing light to penetrate through the FTO back-contact to the dye adsorbed onto the TiO_2 nanoparticle film electrode.

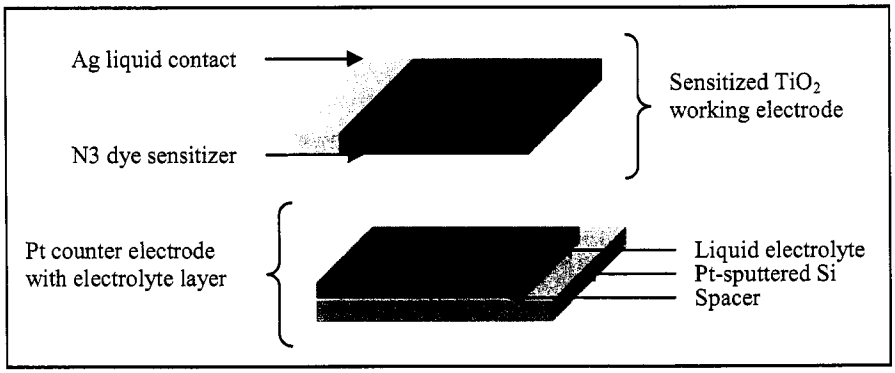

Figure 2.6. Schematic showing the assembly and configuration of the two electrodes used in each solar cell for analysis.

2.2.5 General analysis techniques

A few general techniques were used to characterize TiO_2 nanoparticles and films. Fabricated electrodes made from TiO_2 with various particles sizes were also analyzed by way of current and voltage measurements, which are detailed in the following sections.

2.2.5.1 X-Ray Diffraction (XRD)

X-Ray Diffraction (Philips PW1830 Diffractometer) was used to verify the phase and crystal structure of the TiO_2 nanoparticles and films. The diffractometer was set at 40kV working voltage and 20mA working ampere. Powder samples were placed in a polymer holder and placed into the diffractometer for analysis, and film samples were attached to a glass slide and inserted into the diffractometer for analysis. All samples

were scanned from 20°-80° 2θ at a rate of 0.02scans/second using X'Pert Industry Philips XRD software. The particle sizes of the various prepared TiO_2 powders and films were also analyzed using JADE software (MDI JADE 7 Materials Data XRD Pattern Processing, Identification, and Quantification).

2.2.5.2 Scanning Electron Microscopy (SEM)

Scanning Electron Microscopy (JEOL JSM-5200, JEOL 840A, JSM-7000) was used to study the morphology of the TiO_2 nanoparticles and films. The powders and films were placed on an aluminum SEM stub, using either conductive carbon tape or a layer of silver paste for attachment. All samples were sputter-coated with a thin layer of Au/Pd or Pt prior to SEM observation. The images were obtained at 15kV from 5000X up to 150,000X magnification, depending on the sample.

2.2.5.3 UV/VIS/IR Spectrometry

Optical absorption (Perkin Elmer Lambda 900 UV/VIS/IR Spectrometer) was used to analyze the absorption peaks of the TiO_2 nanoparticle films with and without sensitizer adsorption. The films prepared on ITO or FTO substrates were placed in the analysis chamber and scanned from 900nm to 300nm wavelengths using UV L900 WinLab software. Either ITO or FTO substrates were used as the background sample.

2.2.6 Solar cell analysis

Electrical characteristics and photovoltaic properties of each solar cell were measured using simulated AM1.5 sunlight illumination with 100mW/cm^2 light output.

Figure 2.7 shows the equipment used and the testing setup. An Ultraviolet Solar Simulator (Model 16S, Solar Light Co., Philadelphia, PA) with a 200W Xenon Lamp Power Supply (Model XPS 200, Solar Light Co., Philadelphia, PA) was used as the light source, and a Semiconductor Parameter Analyzer (4155A, Hewlett-Packard, Japan) was used to measure the current and voltage. The intensity of the light source provided by the Xenon lamp was measured with a Photometer/Radiometer (PMA2200, Solar Light Co., Philadelphia, PA) connected with a full spectrum Pyranometer (PMA2141, Solar Light Co., Philadelphia, PA). The resulting current-voltage curves of the cells in the dark and as a function of incident light intensity were used to derive the open-circuit voltage (V_{oc}) and the short-circuit current density (J_{sc}). A spot size of ~ $1cm^2$ was used in all measurements and was taken as the active area of each solar cell sample. The following sections describe the measurements and calculations associated with the I-V curve obtained from solar cell analysis.

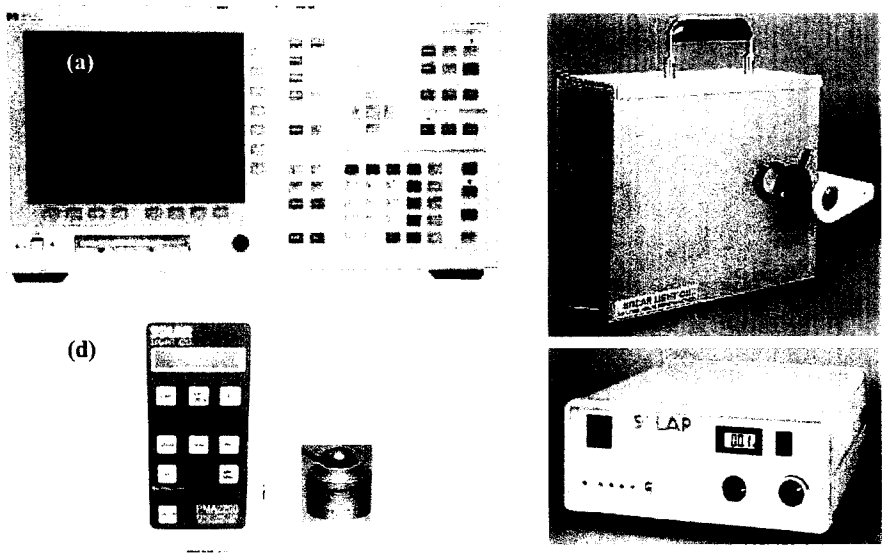

Figure 2.7. Schematic of the equipment used for solar cell analysis, consisting of (a) a Semiconductor Parameter Analyzer attached to (b) an Ultraviolet Solar Simulator that is controlled by (c) a Xenon Lamp Power Supply Unit. The light intensity was tested using (d) a Photometer/Radiometer with a full spectrum Pyranometer attachment. [Ref 123]

The light source used to simulate AM1.5 sunlight illumination follows the ASTM standard for photovoltaic testing, referenced in ASTM[124] G173-03. Figure 2.8 shows the solar irradiance spectrum[125] of sunlight at sea level and the angle of the sun at an air mass of 1.5, which correlates with the spectrum at sea level. The terrestrial solar spectrum[123] that occurs when the sun's position vector has rotated ~ 48.3 degrees away from its perpendicular position is used to alter the simulator output. This is based on the air mass value of 1.5, which occurs with direct solar irradiance at sea level.

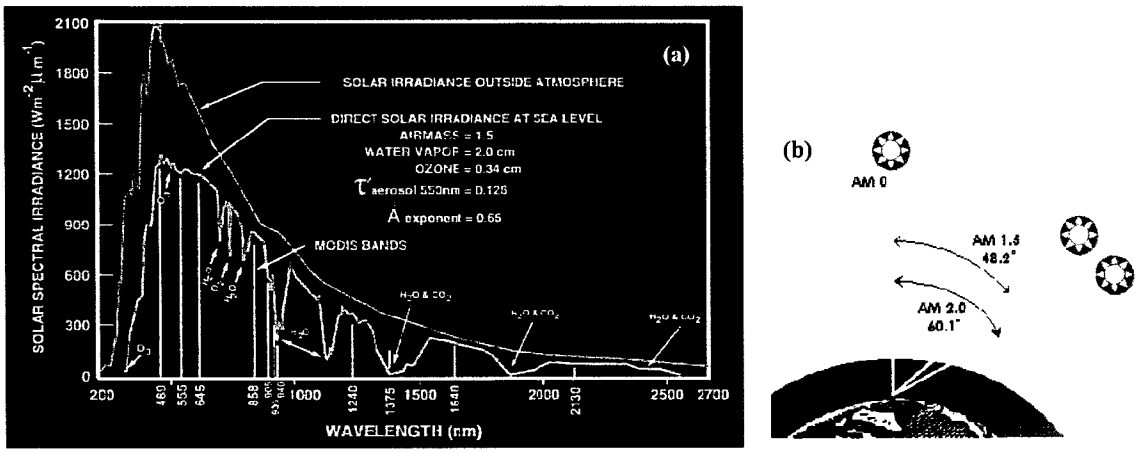

Figure 2.8. Schematic of (a) the solar irradiance spectrum at sea level (yellow line), and (b) the correlating solar angle associated with 1.5 air mass. [Ref 123,124,125]

Figure 2.9 compares the solar irradiance spectrum of the light source to that of sunlight at sea level. It can be seen that the irradiance of the light source is similar to the irradiance of sunlight. The power output of the light source is modified to emit ~ 100mW/cm^2 of power by using various filters to control the intensity. In addition, it is uncertain how the light source degrades; therefore, the distance between the solar cell and the light source is also modified to maintain a constant light intensity of ~ 100mW/cm^2. This intensity value is measured and kept constant using the photometer/pyranometer.

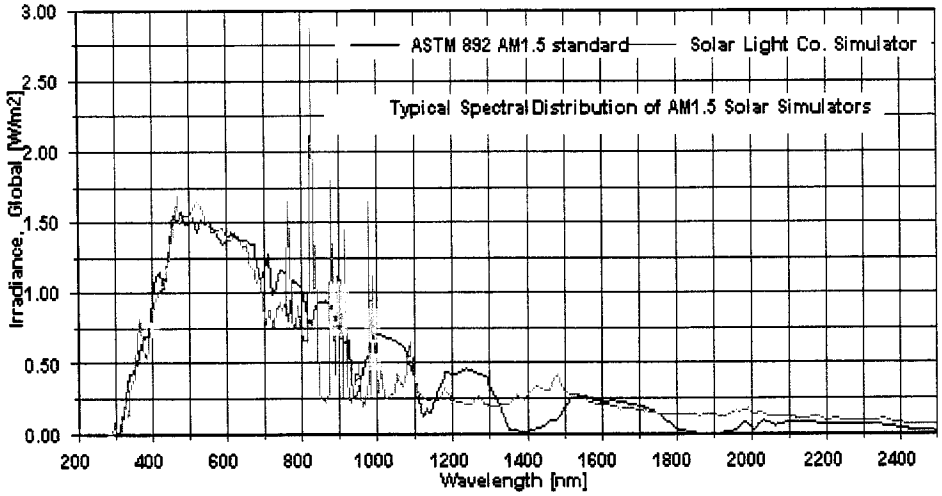

Figure 2.9. Comparison of the solar irradiance spectrum of sunlight (red line) and the solar irradiance spectrum of the light source (green line) at sea level. [Ref 123]

2.2.6.1 Current-Voltage (I-V) measurements

Each solar cell was connected to the current and voltage analyzer with alligator clips, where the negative connection was placed at the TiO_2 electrode and the positive connection was placed at the Pt electrode. All the I-V curves of the solar cells were obtained in the dark and under illumination, where a voltage range from -0.3V to 2V was used during each measurement. The I-V characteristics as a function of incident light intensity was used to obtain the open-circuit voltage (V_{oc}), short-circuit current density (J_{sc}), the maximum voltage point (V_{max}), and the maximum current density point (J_{max}). The ideal I-V behavior of a solar cell to give the highest overall light conversion efficiency is represented by Figure 2.10, where minimal current loss occurs with an increase in the voltage. This ideal curve represents a fill factor of 100%. Although 100% fill factor is not likely to occur in the electrode films, this curve represents the optimal goal in the performance of dye-sensitized solar cells.

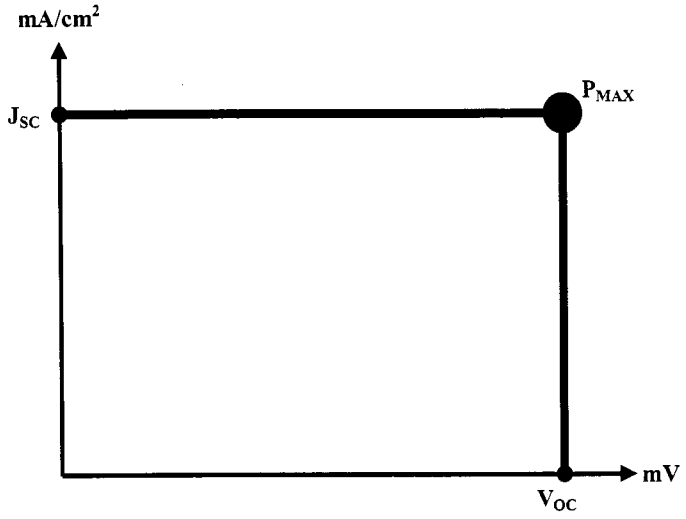

Figure 2.10. Representation of the ideal I-V curve for a highly efficient solar cell, showing minimal current loss with the increase in voltage. The points on the I-V curve show the short-circuit current density (J_{sc}), open-circuit voltage (V_{oc}), and the maximum power output (P_{max}). [Ref 126]

As seen in the figure, the V_{oc} is obtained where the current density is equal to zero (point crossing the x-axis), and the J_{sc} is obtained where the voltage is equal to zero (point crossing the y-axis). The maximum output (P_{max}) is obtained at the point on the curve where the highest value of current is obtained with the highest value of voltage to give the overall light conversion efficiency.

2.2.6.2 Characterization of I-V behavior

The values found from the I-V curve were used to derive values for the fill factor (FF), the maximum power output density (P_{max}), and the overall power conversion efficiency (η) for each solar cell. A $1cm^2$ spot size area used in all the measurements was taken into account for the derivation of the short-circuit current density (J_{sc}) and the maximum current density (J_{max}). The short-circuit current density (J_{sc}) and the maximum current density (J_{max}) was calculated by the equation:

$$J\ (mA/cm^2) = I\ (mA) \div A\ (cm^2), \quad [1]$$

where J is the equivalent to J_{sc} or J_{max}; I is the equivalent to I_{sc} or I_{max}, the short-circuit current or the current at the maximum point, respectively; and A is the active area of the solar cell equal to $1cm^2$. The fill factor (FF) was calculated by the equation[115]:

$$FF\ (\%) = [V_{max}\ (V) \bullet J_{max}\ (mA/cm^2)] \div [V_{oc}\ (V) \bullet J_{sc}\ (mA/cm^2)] \bullet 100\%, \quad [2]$$

where V_{max} is the voltage at the maximum point, J_{max} is the maximum current density value taken from equation [1], V_{oc} is the open-circuit voltage, and J_{sc} is the short-circuit current density also taken from equation [1]. The maximum power output density (P_{max}) was calculated by the equation:

$$P_{max}\ (mW/cm^2) = V_{max}\ (V) \bullet J_{max}\ (mA/cm^2), \quad [3]$$

where V_{max} and J_{max} are the maximum voltage and current density values found at the maximum power point on the I-V curve, respectively. The sunlight to electrical energy, or overall light conversion efficiency (η) was calculated by the equation[115]:

$$\eta\ (\%) = P_{max}\ (mW/cm^2) \div P_{source}\ (mW/cm^2) \bullet 100\%, \quad [4]$$

where P_{max} is the maximum power output density taken from equation [3] and P_{source} is the power input density of the incident light with a value of approximately $100mW/cm^2$. The overall light conversion efficiency (η) can also be calculated using the equation:

$$\eta\ (\%) = FF \bullet V_{oc} \bullet J_{sc} \div P_{source} \bullet 100\%$$

2.3 Results and discussion

The following sections describe results from 1) the hydrothermal treatment of TiO_2, 2) the solar cell performance of TiO_2 nanoparticle film by way of hydrothermal treatment at various temperatures, 3) the solar cell performance of TiO_2 nanoparticle film

by way of hydrothermal treatment at various times, 4) the characterization of the various TiO_2 nanoparticle films, and 5) the dye loading of TiO_2 nanoparticle film.

2.3.1 Hydrothermal treatment of TiO_2

Powders of TiO_2 with varying particle sizes were obtained by hydrothermally-treating TiO_2 sol for 60 minutes at temperatures of 100°C, 150°C, 200°C, 250°C, and 300°C. Powders of TiO_2 were also obtained at 250°C at various hydrothermal treatment times of 20, 40, 60, and 120 minutes to compare the particle sizes. XRD analysis was performed for each powder sample and the results are discussed in the following sections.

2.3.1.1 TiO_2 particle size dependence on varying temperature

XRD analysis was done on TiO_2 powders obtained by hydrothermal treatment for 60 minutes at temperatures of 100°C, 150°C, 200°C, 250°C, and 300°C. Figure 2.11 shows the XRD patterns of the five TiO_2 powder samples obtained by hydrothermal treatment at various temperatures. It can be seen that the crystallinity improves as the hydrothermal treatment temperature increases, all showing the anatase phase of TiO_2.

By analyzing the XRD peaks, the particle sizes of each TiO_2 powder sample were calculated. The (101), (004), (200), (105), (211), (204), (116), (220), and (215) peaks were used to estimate the particle size of each TiO_2 powder sample by averaging the particle sizes at each peak for each TiO_2 powder sample. The particle sizes were estimated at each peak using the Scherer equation[127]:

$$t = (0.9\lambda) \div (B\cos\theta_B),$$

where t is the particle size in angstroms, λ is equal to 1.54056Å, the wavelength for Cu-$K\alpha_1$ radiation, B is the width of the peak at an intensity equal to half the maximum intensity in radians, and θ_B is the diffracted angle at maximum intensity. Table 2.1 summarizes the actual particle sizes at various temperatures treated for 60 minutes. Figure 2.12 is a plot of the particle size versus the temperature used to hydrothermally treat TiO_2, all treated for 60 minutes.

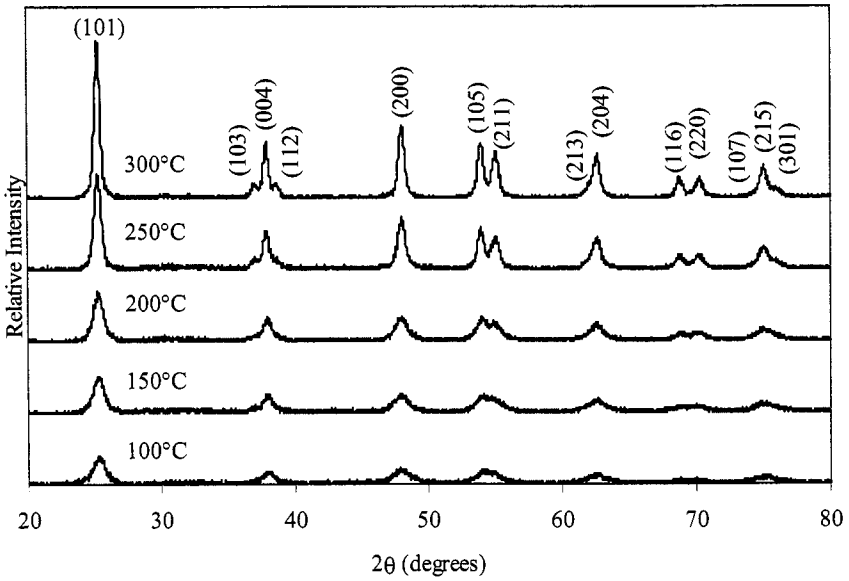

Figure 2.11. XRD peaks showing the crystallinity of hydrothermally-treated TiO_2 at 100°C, 150°C, 200°C, 250°C, and 300°C for 60 minutes. The peaks show the anatase phase of TiO_2.

Table 2.1. Summary of TiO_2 particle sizes obtained by hydrothermal treatment at 100°C, 150°C, 200°C, 250°C, and 300°C for 60 minutes. All the particle sizes were obtained from powders.

Temperature (°C)	Particle Size (nm)	Standard Deviation (nm)	Standard Error (nm)
100	6.72	1.04	0.423
150	7.06	2.03	0.766
200	9.66	1.28	0.453
250	13.6	2.37	0.789
300	17.7	2.16	0.624

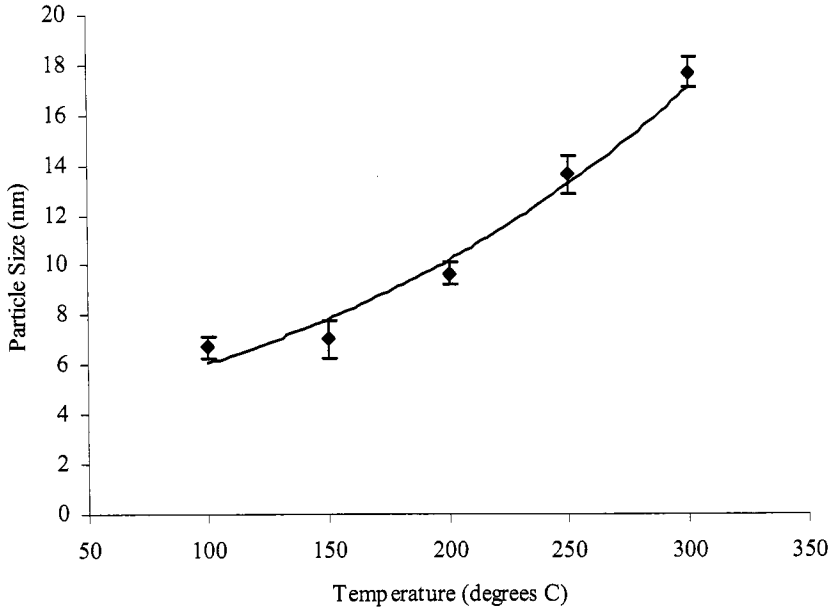

Figure 2.12. Plot of particle size as a function of temperature for hydrothermally-treated TiO_2 obtained at 100°C, 150°C, 200°C, 250°C, and 300°C for 60 minutes.

The particle size correlates with the temperature used, where the size increases with increasing temperature. It has been estimated that sol particles prepared through sol-gel processing are ~ 4nm in size. With additional hydrothermal treatment, the particle size increased to ~ 6.7nm at 100°C, ~ 7.1nm at 150°C, ~ 9.7nm at 200°C, ~ 13.6nm at 250°C, and ~ 17.7nm at 300°C. With every 50°C increase in hydrothermal treatment temperature, the particle size increased by approximately 0.3nm, 2.6nm, 4.0nm, and 4.1nm between 100°C to 150°C, 150°C to 200°C, 200°C to 250°C, and 250°C to 300°C, respectively. It can be seen that larger particle size differences occurred at higher hydrothermal treatment temperatures. Smaller particle size differences were observed at temperatures under 200°C. Since the hydrothermal chamber was limited to a temperature of 300°C without rupture, higher temperatures were not used.

2.3.1.2 TiO_2 particle size dependence on varying time

XRD analysis was done on TiO_2 powders obtained by hydrothermal treatment at 250°C for 20, 40, 60, and 120 minutes. Figure 2.13 shows the XRD patterns of the four TiO_2 powder samples obtained by hydrothermal treatment at various times. It can be seen that the crystallinity also improves as the amount of time increases at a hydrothermal treatment temperature of 250°C. The XRD pattern also shows that the anatase phase is present in all cases for TiO_2.

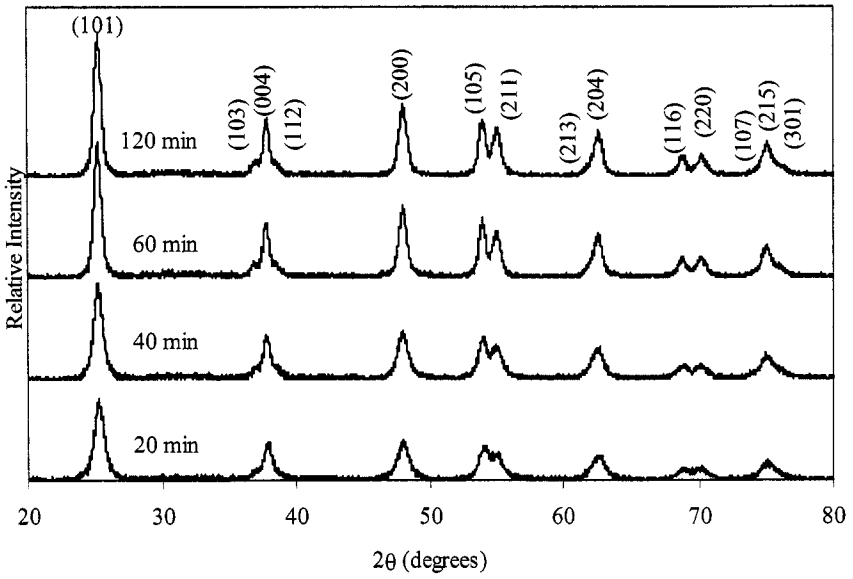

Figure 2.13. XRD peaks showing the crystallinity of hydrothermally-treated TiO_2 at 250°C for 20, 40, 60, and 120 minutes. The peaks show the anatase phase of TiO_2.

In addition, from the XRD patterns, the particle sizes of each TiO_2 powder sample were also calculated. The (101), (004), (200), (105), (211), (204), (116), (220), and (215) peaks were used to estimate the particle size of each TiO_2 powder sample by averaging the particle sizes at each peak for each TiO_2 powder sample obtained from the Scherer equation, as previously detailed. Table 2.2 summarizes the actual particle sizes at 250°C

for various times. Figure 2.14 is a plot of the particle size versus the amount of time used to hydrothermally treat TiO_2 at 250°C.

Table 2.2. Summary of TiO_2 particle sizes obtained by hydrothermal treatment at 250°C for 20, 40, 60, and 120 minutes. All the particle sizes were obtained from powders.

Time (minutes)	Particle Size (nm)	Standard Deviation (nm)	Standard Error (nm)
20	8.93	0.65	0.245
40	10.6	2.16	0.721
60	13.6	2.37	0.789
120	14.0	2.21	0.783

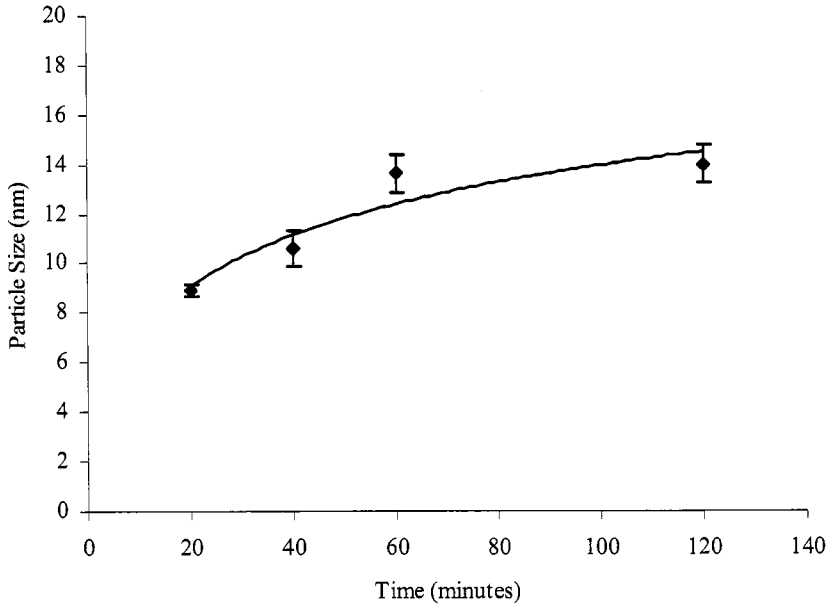

Figure 2.14. Plot of particle size as a function of time for hydrothermally-treated TiO_2 obtained at 250°C for 20, 40, 60, and 120 minutes.

The particle size correlates with the amount of time used for hydrothermal treatment, where the size gradually increases with increasing time, eventually leveling off at much longer times. It can be seen that the particle size increased to ~ 8.9nm and ~ 10.6nm at 20 and 40 minute hydrothermal treatment times, respectively. At 60 minutes, the particle size increased to ~ 13.6nm and slightly increased in size to ~ 14nm after 120

minutes of hydrothermal treatment at 250°C. With every 20 minute increase in hydrothermal treatment time, the particle size increased by approximately 1.7nm, 3.0nm, and 0.4nm, between 20 to 40 minutes, 40 to 60 minutes, and 60 to 120 minutes, respectively, as depicted in Figure 2.14.

Furthermore, it can be seen that larger particle size differences occurred within the first hour of hydrothermal treatment. Hydrothermal treatment for longer times improved the crystallinity of TiO_2, but did not result in a large increase in particle size. Between 60 and 120 minutes, the particle size remained relatively the same.

2.3.2 Solar cell performance of TiO_2 nanoparticle film obtained by hydrothermal treatment at various temperatures

To compare the photoresponse of TiO_2 films consisting of nanoparticles with varying sizes, solar cell analysis was performed. Solar cells with TiO_2 nanoparticle film prepared from TiO_2 nanoparticle powder obtained by hydrothermal treatment at either 100°C, 150°C, 200°C, 250°C, or 300°C for 60 minutes were assembled and tested under illumination with 100mW/cm^2 intensity. Table 2.3 summarizes the measured and calculated values obtained from the I-V curves of each solar cell consisting of TiO_2 nanoparticle film with varying particle size. Figure 2.15 compares the I-V characteristics of each solar cell. It can be seen that the overall I-V curve of TiO_2 nanoparticle film is very similar at lower temperatures between 100°C and 150°C, which can be due to the slight increase in particle size at those temperatures.

As the hydrothermal treatment temperature increases, a more noticeable difference in the short-circuit current density and overall light conversion efficiency is

observed. The most notable trend is the increase in short-circuit density and overall light conversion efficiency with the increase in hydrothermal treatment temperature, which can be associated with the larger increase in particle size. A closer look at the trends comparing open-circuit voltage, short-circuit current density, fill factor, and overall light conversion efficiency is detailed in the following sections.

Table 2.3. The measured and calculated values obtained from the I-V curves for each solar cell with TiO_2 nanoparticle films consisting of particles ranging from ~ 6nm to ~ 18nm in size.

Temperature (°C)	V_{oc} (mV)	J_{sc} (mA/cm^2)	V_{max} (mV)	J_{max} (mA/cm^2)	FF (%)	P_{max} (mW/cm^2)	P_{in} (mW/cm^2)	η (%)
100	730	3.59	510	2.75	53.5	1.40	100	1.40
150	710	3.75	500	2.98	56.0	1.49	100	1.49
200	710	6.39	500	5.17	57.0	2.59	100	2.59
250	720	10.6	470	9.04	55.7	4.25	100	4.25
300	730	12.2	490	10.6	58.3	5.19	100	5.19

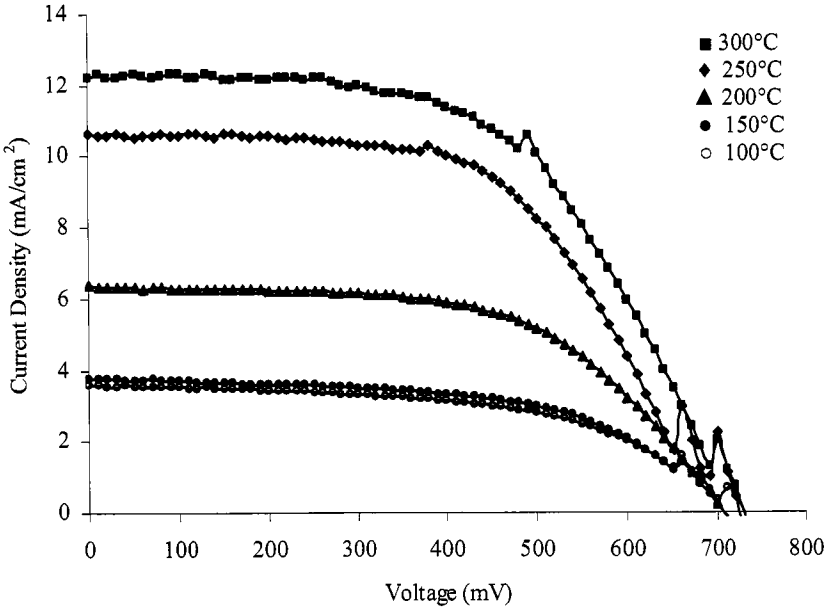

Figure 2.15. Plot and comparison of the I-V characteristics for each solar cell with TiO_2 nanoparticle films consisting of particles ranging from ~ 6nm to ~ 18nm in size.

2.3.2.1 Open-circuit voltage

Since the open-circuit voltage is associated with the potential difference between the TiO_2 working electrode and the Pt counter electrode in a solar cell, it is expected that films with similar surface chemistry have similar open-circuit voltages. Figure 2.16 is a plot of open-circuit voltage as a function of a) hydrothermal treatment temperature and b) particle size for each TiO_2 nanoparticle film in a solar cell. Table 2.4 summarizes the actual open-circuit voltage values.

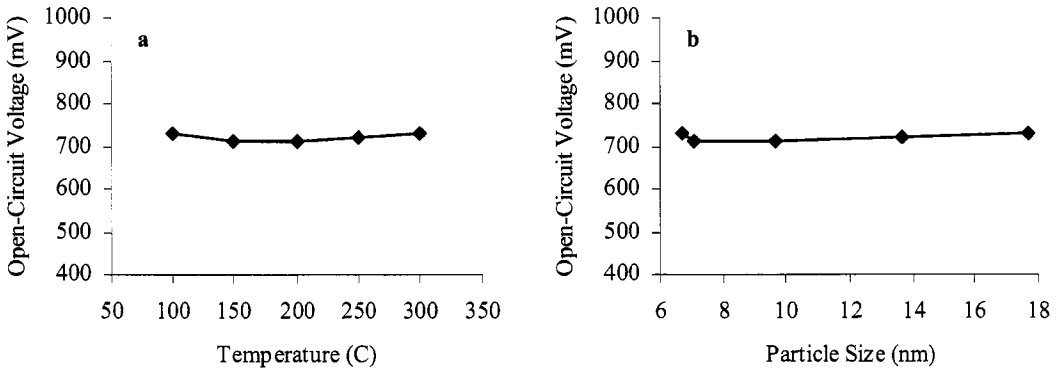

Figure 2.16. Plot of the open-circuit voltage as a function of a) hydrothermal treatment temperature, and b) particle size for various TiO_2 nanoparticle films.

Table 2.4. The open-circuit voltage values obtained from the I-V curves relative to the hydrothermal treatment temperature and the TiO_2 particle size.

Temperature (°C)	Particle Size (nm)	V_{oc} (mV)
100	6.72	730
150	7.06	710
200	9.66	710
250	13.6	720
300	17.7	730

It can be seen that the open-circuit voltage remains fairly constant with varying temperature. The open-circuit voltage stayed steady in the range of ~ 720mV with a small

deviation of ~ 10mV. This trend is expected since the TiO_2 nanoparticle films were all prepared from the same TiO_2 sol, therefore, resulting in the same surface chemistry.

2.3.2.2 Short-circuit current density

Many factors can influence the short-circuit current density, including 1) the surface area of the TiO_2 film, which can influence the amount of dye adsorbed on the TiO_2 surface, and 2) the contact points between sintered colloidal particles. From comparing the solar cell performance of TiO_2 nanoparticle films with varying particle size, it is shown that the particle size can also influence the short-circuit current density. Figure 2.17 is a plot of short-circuit current density as a function of a) hydrothermal treatment temperature, and b) particle size for each TiO_2 nanoparticle film in a solar cell. Table 2.5 summarizes the actual short-circuit current density values and the differences in short-circuit current density between films, and relative to the film obtained at 100°C, with reference to the difference in particle size. It can be seen that the short-circuit current density increases with increasing hydrothermal treatment temperature, or in other words, an increase in particle size.

In addition, a larger increase in short-circuit current density was shown to occur between 150°C and 250°C, and smaller increases in short-circuit current density occurred at lower temperatures and at higher temperatures. The short-circuit current density increased slightly from ~ 3.6 mA/cm^2 to ~ 3.8mA/cm^2 with a slight particle size increase from ~ 6.7nm to ~ 7.1nm. With an even larger increase in particle size to ~ 9.7nm and ~ 13.6nm, the short-circuit current density increased further to ~ 6.4mA/cm^2 and ~ 10.6mA/cm^2, respectively. This increasing trend in short-circuit current density relative

to the particle size could be due to the larger particles having 1) better crystallinity, 2) better connectivity, and 3) more dye adsorption.

The better crystallinity is evidenced by the sharper peaks in the XRD plot in Figure 2.11 of the particles obtained at 300°C hydrothermal treatment temperature. With better crystallinity, the number of defects would be reduced, which would decrease the probability of electron trapping. With better connectivity between larger particles, larger contact points and a minimal number of contact points is present, which would reduce the number of barriers to electron transport. More dye adsorption would also occur with larger contact points. Dye adsorption is less likely to occur at small "bottlenecks" so larger contact points allows for easier access of the dye, which would increase the generation of electron-hole pairs. Larger contact points between sintered colloidal particles would also provide a more efficient pathway for electron transport.

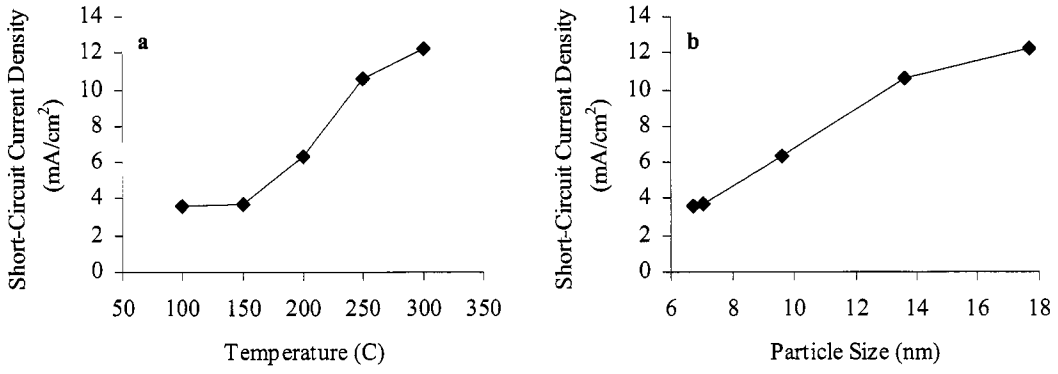

Figure 2.17. Plot of the short-circuit current density as a function of a) hydrothermal treatment temperature, and b) particle size for various TiO_2 nanoparticle films.

In addition, between 250°C and 300°C, a similar particle size increase from ~ 13.6nm to ~ 17.7nm was observed as compared to the particle size increase between 200°C and 250°C, but a smaller increase in short-circuit current density from

10.6mA/cm^2 to ~ 12.2mA/cm^2 was observed. Figure 2.18 is a plot of the difference in particle size and the difference in short-circuit current density as a function of every 50°C increase in hydrothermal treatment temperature. It can be seen that a small change in particle size < 0.5nm resulted in a small change in short-circuit current density < 0.2mA/cm^2, and a larger change in particle size ~ 3-4nm resulted in a much more noticeable change in short-circuit current density ~ 3-4mA/cm^2.

Table 2.5. The short-circuit current density values obtained from the I-V curves relative to the hydrothermal treatment temperature and the TiO_2 particle size. The difference within each temperature range and the total difference in the particle size and the short-circuit current density relative to the values at 100°C are also shown.

Temperature (°C)	Particle Size (nm)	J_{sc} (mA/cm^2)	Δ Particle Size (nm)	Δ J_{sc} (mA/cm^2)	Total Δ Particle Size (nm)	Total Δ J_{sc} (mA/cm^2)
100	6.72	3.59				
150	7.06	3.75	0.34	0.16	0.34	0.16
200	9.66	6.39	2.60	2.64	2.94	2.80
250	13.6	10.6	3.96	4.21	6.90	7.01
300	17.7	12.2	4.08	1.60	11.0	8.61

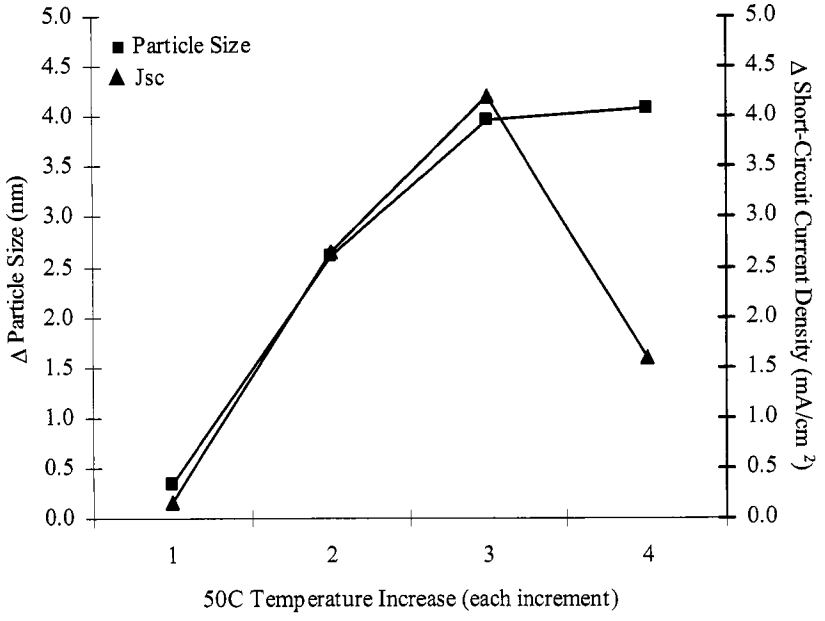

Figure 2.18. Plot of the difference in particle size and the difference in short-circuit current density within each range of temperature change.

Furthermore, the change in short-circuit current density dropped to ~ 2mA/cm^2 between 250°C and 300°C even with a similar change in particle size ~ 4nm as shown between 200°C and 250°C. This change in short-circuit current density could be due to the limitations in the change in short-circuit density relative to the increase in particle size. With the increase in particle size, the short-circuit current density also increased but at a slower rate, indicating that the further reduction in surface area with the presence of ~ 18nm particles may have been a factor in the short-circuit current density than the presence of larger contact points between larger particles.

Moreover, by looking at the total change in particle size and in the short-circuit current density relative to the initial particle size at 100°C, a similar rate of change was observed. Figure 2.19 shows the total difference in particle size and in short-circuit current density as a function of the total change in temperature. With a 50°C increase in hydrothermal treatment temperature, the particle size increased by ~ 0.3nm and the short-circuit current density increased by ~ 0.2mA/cm^2. A 100°C increase in hydrothermal treatment temperature resulted in the particle size increasing by ~ 3nm and the short-circuit current density increasing by ~ 2.8mA/cm^2. Furthermore, with a 150°C and 200°C increase in hydrothermal treatment temperature, the particle size increased by ~ 7nm and ~ 11nm, and the short-circuit current density increased by ~ 7mA/cm^2 and ~ 8.6mA/cm^2, respectively. The rate of change for both particle size and short-circuit current density were fairly similar, where an increase in hydrothermal treatment temperature resulted in an increase in particle size, increasing the short-circuit current density. This indicates that larger contact points may have been influential in the increase in the short-circuit current density, where more dye adsorption may have occurred, generating more electrons.

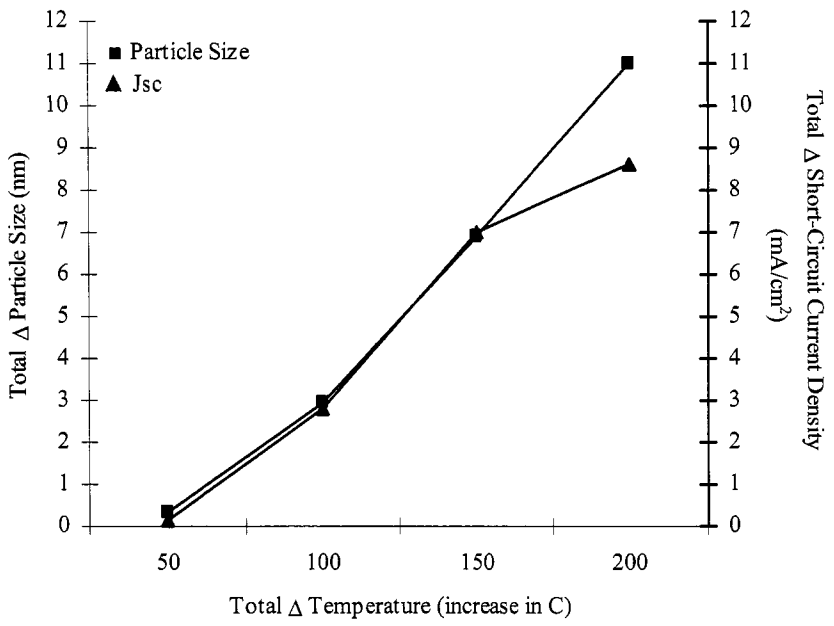

Figure 2.19. Plot of the total difference in particle size and the total difference in short-circuit current density as a function of the total change in temperature, relative to values obtained at 100°C.

2.3.2.3 Fill factor

The fill factor represents the "squareness" of the I-V curve and depends on the resistance of the TiO_2 nanoparticle film. A film with higher internal resistance will result in a more linear I-V curve, resulting in a reduced fill factor. Figure 2.20 shows the plot of fill factor as a function of a) hydrothermal treatment temperature and b) particle size for each TiO_2 nanoparticle film in a solar cell. Table 2.6 summarizes the fill factor values. It can be seen that the fill factor remains fairly constant with varying temperature and particle size. The fill factor stayed steady in the range of ~ 56.1% with a small deviation of ~ 1.8%. This trend is expected since the TiO_2 nanoparticle films were all prepared in the same manner, where 500°C sintering for 60 minutes was used to enhance the

connectivity at the contact points between colloidal particles and at the interface between the FTO substrate and the TiO_2 nanoparticle film.

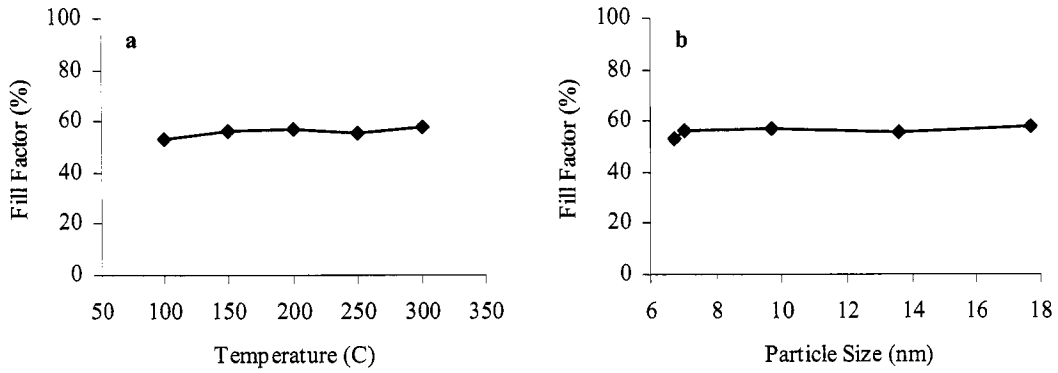

Figure 2.20. Plot of the fill factor as a function of a) hydrothermal treatment temperature, and b) particle size for various TiO_2 nanoparticle films.

Table 2.6. The fill factor values obtained from the I-V curves relative to the hydrothermal treatment temperature and the TiO_2 particle size.

Temperature (°C)	Particle Size (nm)	FF (%)
100	6.72	53.5
150	7.06	56.0
200	9.66	57.0
250	13.6	55.7
300	17.7	58.0

2.3.2.4 Overall light conversion efficiency

As shown previously with the short-circuit current density, the overall light conversion efficiency is also influenced by the particle size in the same manner. The overall efficiency also increases with increasing hydrothermal treatment temperature, or particle size. Figure 2.21 is a plot of overall efficiency as a function of a) hydrothermal treatment temperature, and b) particle size for each TiO_2 nanoparticle film in a solar cell.

Table 2.7 summarizes the actual overall efficiency values and the differences in overall efficiency between films.

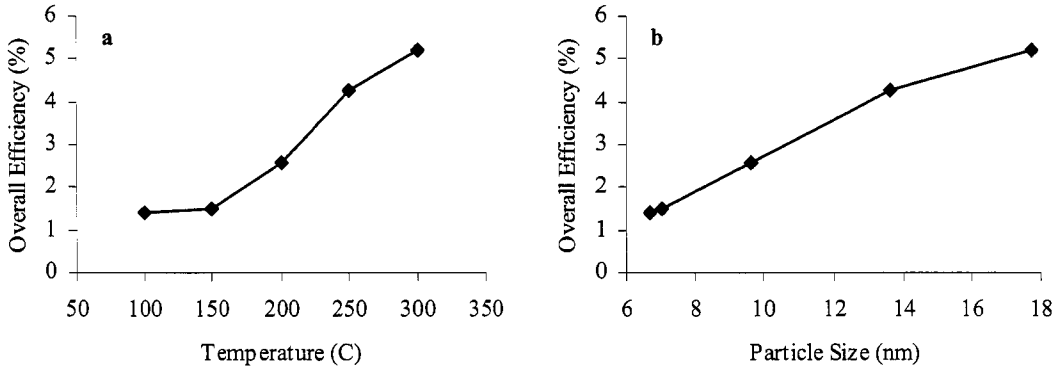

Figure 2.21. Plot of the overall efficiency as a function of a) hydrothermal treatment temperature, and b) particle size for various TiO_2 nanoparticle films.

Table 2.7. The overall efficiency values obtained from the I-V curves relative to the hydrothermal treatment temperature and the TiO_2 particle size. The difference within each temperature range and the total difference in the particle size and the overall efficiency relative to the values at 100°C are also shown.

Temperature (°C)	Particle Size (nm)	η (%)	Δ Particle Size (nm)	Δ η (%)	Total Δ Particle Size (nm)	Total Δ η (%)
100	6.72	1.40				
150	7.06	1.49	0.34	0.09	0.34	0.09
200	9.66	2.59	2.60	1.10	2.94	1.19
250	13.6	4.25	3.96	1.66	6.90	2.85
300	17.7	5.19	4.08	0.94	11.0	3.79

It is shown that a steady increase in overall efficiency was shown to occur between 150°C and 300°C, and small increases in overall efficiency occurred at lower temperatures. The overall efficiency increased slightly from ~ 1.4% to ~ 1.5% with a slight particle size increase from ~ 6.7nm to ~ 7.1nm. With a larger increase in particle size to ~ 9.7nm, ~ 13.6nm, and ~ 17.7nm, the overall efficiency increased to ~ 2.6%, ~ 4.3%, and 5.2%, respectively. This increase in overall efficiency relative to the increase in particle size also correlates with the increase in short-circuit current density.

Figure 2.22 is a plot of the difference in particle size and in overall efficiency as a function of every 50°C increase in hydrothermal treatment temperature. It can be seen that a small change in particle size < 0.5nm resulted in a small change in overall efficiency ~ 0.1%, and a change in particle size between 2-4nm resulted in a steady increase in overall efficiency by ~ 1-2% for every increase in particle size.

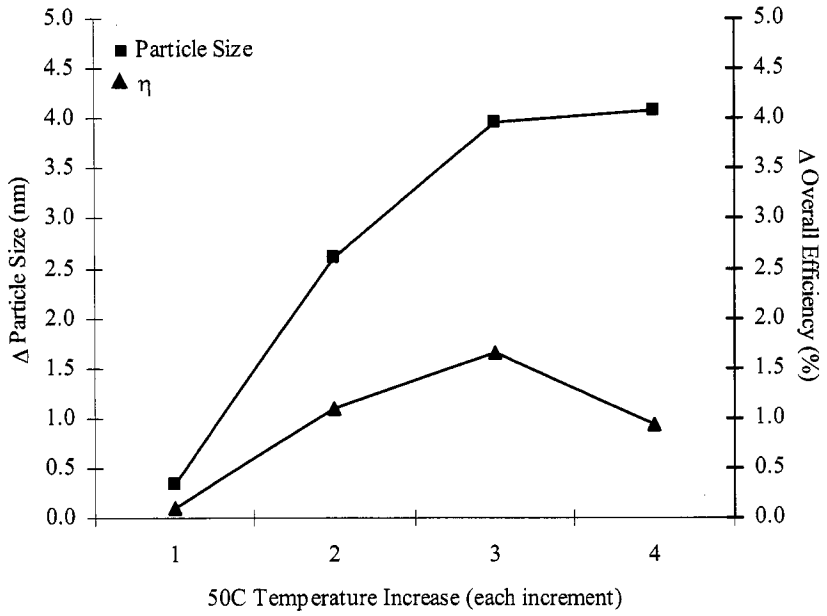

Figure 2.22. Plot of the difference in particle size and the difference in overall efficiency within each range of temperature change.

However, it is also shown that the change in overall efficiency dropped slightly between 250°C and 300°C even with a similar change in particle size as shown between 200°C and 250°C. This slight drop in overall efficiency could be due to the smaller change in short-circuit current density in this region, as previously mentioned. The larger reduction in surface area with the presence of ~ 18nm particles seemed to slightly affect

the overall efficiency, but did not have as much of an influence on the change in value when compared to the short-circuit current density.

By looking at the total change in particle size and in the overall efficiency relative to the initial particle size at 100°C, an increasing trend was observed. Figure 2.23 shows the total difference in particle size and in overall efficiency as a function of the total change in temperature. With a 50°C increase in hydrothermal treatment temperature, the particle size increased by ~ 0.3nm and the overall efficiency increased by ~ 0.1%. A 100°C increase in hydrothermal treatment temperature resulted in the particle size increasing by ~ 3nm and the overall efficiency increasing by ~ 1.2%.

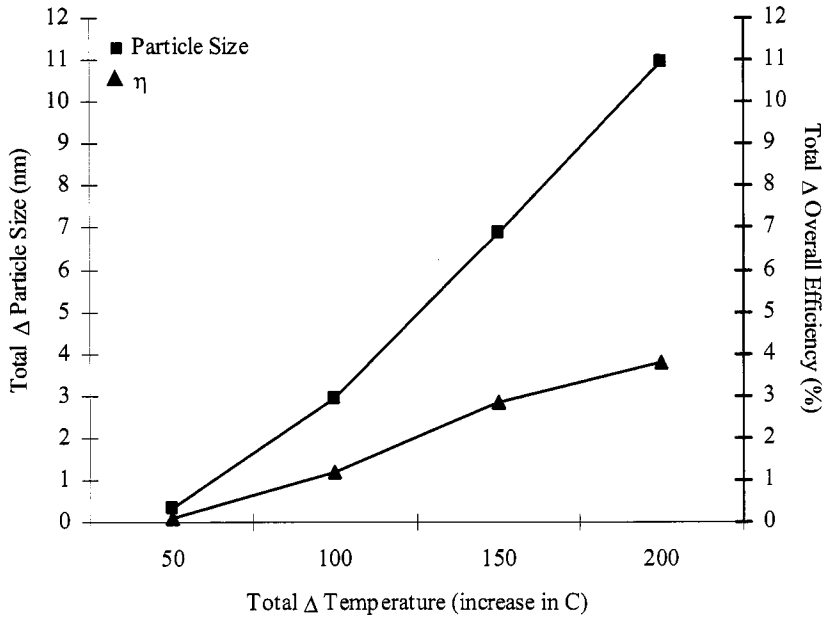

Figure 2.23. Plot of the total difference in particle size and the total difference in overall efficiency as a function of the total change in temperature, relative to the values obtained at 100°C.

Furthermore, with a 150°C and 200°C increase in hydrothermal treatment temperature, the particle size increased by ~ 7nm and ~ 11nm, and the overall efficiency

increased by ~ 2.9% and ~ 3.8%, respectively. Although both the particle size and the overall efficiency increased, the rate of change for the particle size was much greater than that for the overall efficiency, where the slope for the total change in particle size was much steeper than the slope for the total change in overall efficiency, as shown in Figure 2.23. This also shows that the particle size had a greater influence on the short-circuit current density than that on the overall efficiency. A higher rate of change was associated with the short-circuit current density, as compared to the overall efficiency.

2.3.3 Solar cell performance of TiO_2 nanoparticle film obtained by hydrothermal treatment at various times

Additional comparisons were made by observing the photoresponse of solar cells with TiO_2 nanoparticle films prepared from TiO_2 nanoparticle powders obtained by hydrothermal treatment at 250°C for either 20, 40, 60, or 120 minutes. All the solar cells were assembled and tested under illumination with 100mW/cm^2 intensity. Table 2.8 summarizes the measured and calculated values obtained from the I-V curves of each solar cell consisting of TiO_2 nanoparticle film with varying particle size. Figure 2.24 compares the I-V characteristics of each solar cell. It can be seen that all the overall I-V curves representing each TiO_2 nanoparticle film are very similar in behavior, and that the short-circuit current density fluctuates in the same general region, even at short or long hydrothermal treatment times.

The values for open-circuit voltage, short-circuit current density, fill factor, and overall efficiency remained fairly constant with the increase in hydrothermal treatment time, or a slight increase in particle size. A closer look at the trends comparing open-

circuit voltage, short-circuit current density, fill factor, and overall light conversion efficiency is detailed in the following sections.

Table 2.8. The measured and calculated values obtained from the I-V curves for each solar cell with TiO_2 nanoparticle films consisting of particles ranging from ~ 6nm to ~ 18nm in size.

Time (minutes)	V_{oc} (mV)	J_{sc} (mA/cm^2)	V_{max} (mV)	J_{max} (mA/cm^2)	FF (%)	P_{max} (mW/cm^2)	P_{in} (mW/cm^2)	η (%)
20	720	12.8	450	10.4	50.8	4.68	100	4.68
40	720	11.6	430	10.2	52.5	4.39	100	4.39
60	720	10.6	470	9.0	55.7	4.25	100	4.25
120	710	11.7	450	10.4	56.3	4.68	100	4.68

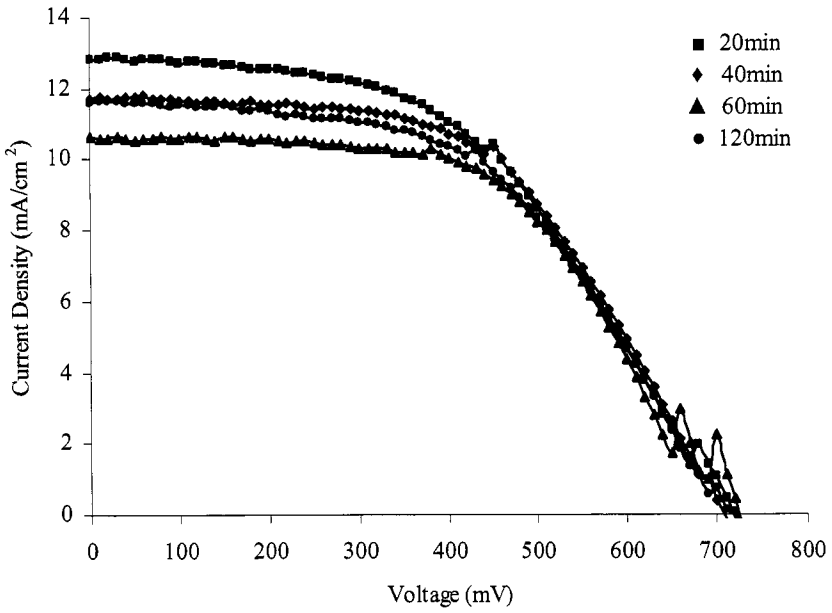

Figure 2.24. Plot and comparison of the I-V characteristics for each solar cell with TiO_2 nanoparticle films consisting of particles ranging from ~ 8nm to ~ 14nm in size.

2.3.3.1 Open-circuit voltage

As previously mentioned, the open-circuit voltage is dependent on the potential difference between the TiO_2 working electrode and the Pt counter electrode in a solar cell. Figure 2.25 is a plot of open-circuit voltage as a function of a) hydrothermal

treatment time and b) particle size for each TiO_2 nanoparticle film in a solar cell. Table 2.9 summarizes the actual open-circuit voltage values.

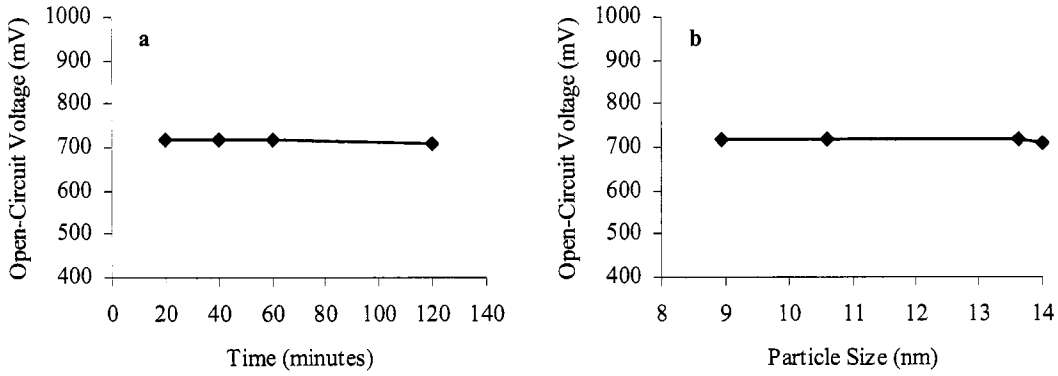

Figure 2.25. Plot of the open-circuit voltage as a function of a) hydrothermal treatment time, and b) particle size for various TiO_2 nanoparticle films.

Table 2.9. The open-circuit voltage values obtained from the I-V curves relative to the hydrothermal treatment time and the TiO_2 particle size.

Time (min)	Particle Size (nm)	V_{oc} (mV)
20	8.93	720
40	10.6	720
60	13.6	720
120	14.0	710

It can be seen that the open-circuit voltage remains fairly constant with varying hydrothermal treatment time and slight differences in particle size. The open-circuit voltage stayed steady in the range of ~ 718mV with a small deviation of ~ 5mV. Since the TiO_2 nanoparticle films were all prepared from the same TiO_2 sol, and assumed to have the same surface chemistry, no noticeable difference in the open-circuit voltage is expected, which is shown in Figure 2.25.

2.3.3.2 Short-circuit current density

Although the particle size increased slightly with increasing hydrothermal treatment time at 250°C, the relative short-circuit current density remained fairly constant in the current density range of ~ 11.7mA/cm^2 with a small deviation of ~ 0.9%. In this case, from comparing the short-circuit current density of the TiO_2 nanoparticle films, the particle size did not have as much of an influence on the solar cell performance as previously shown. Figure 2.26 is a plot of short-circuit current density as a function of a) hydrothermal treatment time, and b) particle size for each TiO_2 nanoparticle film. Table 2.10 summarizes the actual short-circuit current density values and the differences in short-circuit current density between films.

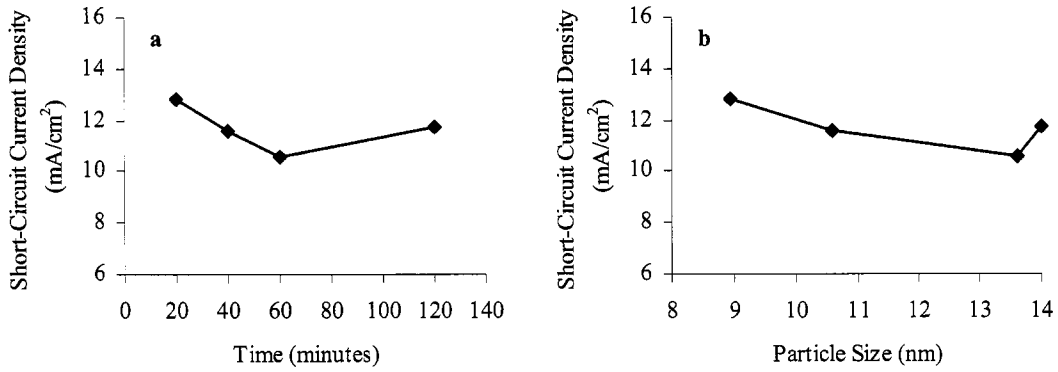

Figure 2.26. Plot of the short-circuit current density as a function of a) hydrothermal treatment time, and b) particle size for various TiO_2 nanoparticle films.

It can be seen that the short-circuit current density did not have much of an increase and remained fairly constant with slight increases in particle size, showing that the short-circuit current density was not affected by the slight increase in particle size. The short-circuit current density slightly decreased from ~ 12.8 mA/cm^2 to ~ 11.6mA/cm^2 to ~ 10.6mA/cm^2 with a particle size increase from ~ 8.9nm to ~ 10.6nm to

~ 13.6nm, respectively. With a slight increase in particle size even further to ~ 14nm, the short-circuit current density jumped back up to ~ 11.7mA/cm^2.

Table 2.10. The short-circuit current density values obtained from the I-V curves relative to the hydrothermal treatment time and the TiO_2 particle size. The difference within each time period and the total difference in the particle size and the short-circuit current density relative to the values at 20 minutes are also shown.

Time (min)	Particle Size (nm)	J_{sc} (mA/cm^2)	Δ Particle Size (nm)	Δ J_{sc} (mA/cm^2)	Total Δ Particle Size (nm)	Total Δ J_{sc} (mA/cm^2)
20	8.93	12.8				
40	10.6	11.6	1.67	(1.2)	1.67	(1.20)
60	13.6	10.6	3.02	(1.0)	4.69	(2.20)
120	14.0	11.7	0.38	1.1	5.07	(1.10)

Figure 2.27 is a plot of the difference in particle size and the difference in short-circuit current density as a function of every 20-minute increase in hydrothermal treatment time. It can be seen that the change in short-circuit current density stayed steady in the range of ~ 1mA/cm^2, either decreasing or increasing in number, within a 1-3nm particle size change. This shows that changing the hydrothermal treatment time to change the particle size did not have as much of an influence on the short-circuit current density as changing the hydrothermal treatment temperature to change the particle size.

By looking at the total change in particle size and in the short-circuit current density relative to the initial particle size at 20 minutes, slight decreases in short-circuit current density is observed with increasing particle size. Figure 2.28 shows the total difference in particle size and in short-circuit current density as a function of the total change in time. With a 20-minute, 40-minute, and 100-minute increase in hydrothermal treatment time, the particle size increased by ~ 1.7nm, ~ 4.7nm, and ~ 5.1nm but the short-circuit current density consistently decreased by ~ 1.2mA/cm^2, ~ 2.2mA/cm^2, and

1.1mA/cm^2, respectively. The rate of change for the short-circuit current density remained fairly constant even with increasing particle size.

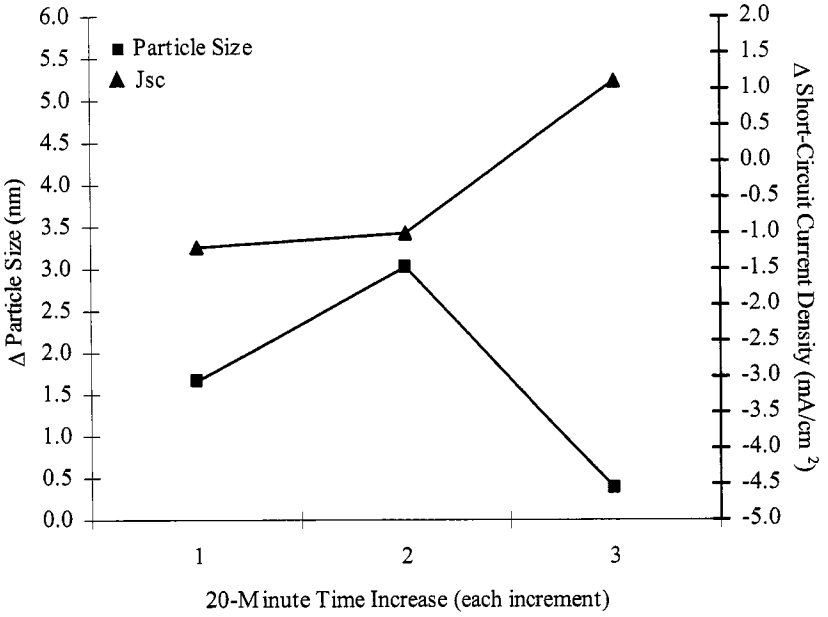

Figure 2.27. Plot of the difference in particle size and the difference in short-circuit current density within each change of period of time.

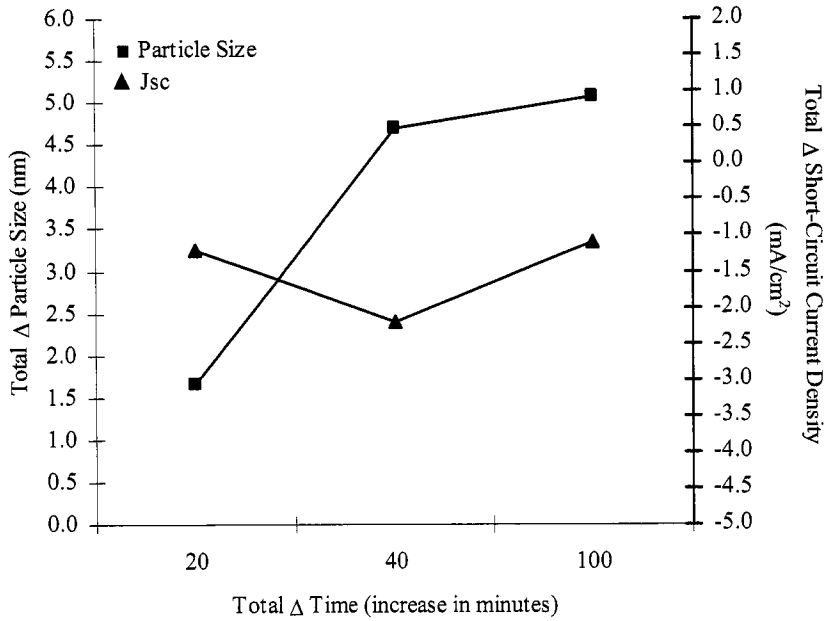

Figure 2.28. Plot of the total difference in particle size and the total difference in short-circuit current density as a function of the total change in time, relative to values obtained at 20 minutes.

2.3.3.3 Fill factor

Showing the same trend as the open-circuit voltage, the fill factor also remained fairly constant, which is expected since all the films were prepared in the same manner. Figure 2.29 shows the plot of fill factor as a function of a) hydrothermal treatment time and b) particle size for each TiO_2 nanoparticle film in a solar cell. Table 2.11 summarizes the fill factor values.

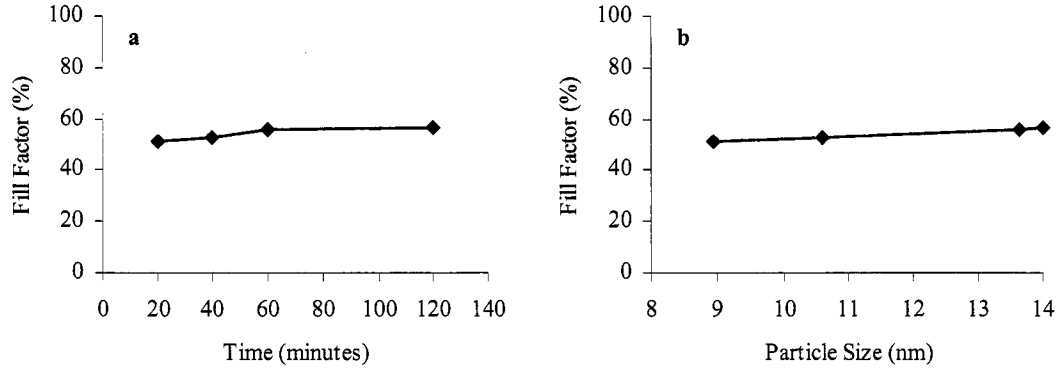

Figure 2.29. Plot of the fill factor as a function of a) hydrothermal treatment time, and b) particle size for various TiO_2 nanoparticle films.

Table 2.11. The fill factor values obtained from the I-V curves relative to the hydrothermal treatment time and the TiO_2 particle size.

Time (min)	Particle Size (nm)	FF (%)
20	8.93	50.8
40	10.6	52.5
60	13.6	55.7
120	14.0	56.3

It can be seen that the fill factor remains fairly constant with varying time and particle size. The fill factor stayed steady in the range of ~ 53.8% with a small deviation of ~ 2.6%. This trend is expected since all the TiO_2 nanoparticle films were sintered at

500°C for 60 minutes to enhance the connectivity at the contact points between colloidal particles and at the interface between the FTO substrate and the TiO_2 nanoparticle film.

2.3.3.4 Overall light conversion efficiency

With a similar trend to the short-circuit current density, the overall light conversion efficiency remained fairly constant with increasing hydrothermal treatment time, or increasing particle size. Figure 2.30 is a plot of overall efficiency as a function of a) hydrothermal treatment time, and b) particle size for each TiO_2 nanoparticle film. Table 2.12 summarizes the actual overall efficiency values and the differences in overall efficiency between films. Although the particle size slightly increased with increasing hydrothermal treatment time at 250°C, the relative overall efficiency remained fairly constant in the range of ~ 4.5% with a small deviation of ~ 0.2%.

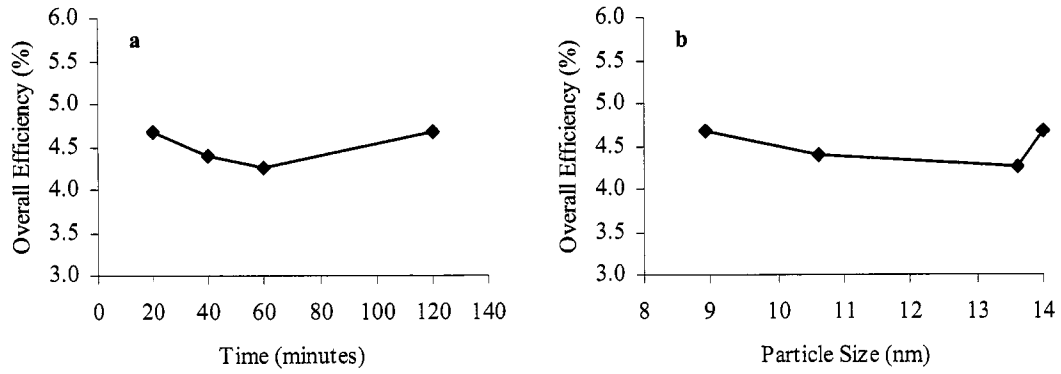

Figure 2.30. Plot of the overall efficiency as a function of a) hydrothermal treatment time, and b) particle size for various TiO_2 nanoparticle films.

In this case, from comparing the overall efficiency of the TiO_2 nanoparticle films, the particle size did not have as much of an influence on the solar cell performance as previously shown. Figure 2.31 is a plot of the difference in particle size and in overall

efficiency as a function of every 20-minute increase in hydrothermal treatment time. It can be seen that the change in overall efficiency stayed steady in the range of < 0.5%, either decreasing or increasing in number, within a 1-3nm particle size change.

Table 2.12. The overall efficiency values obtained from the I-V curves relative to the hydrothermal treatment time and the TiO_2 particle size. The difference within each time period and the total difference in the particle size and the overall efficiency relative to the values at 20 minutes are also shown.

Time (min)	Particle Size (nm)	η (%)	Δ Particle Size (nm)	Δ η (%)	Total Δ Particle Size (nm)	Total Δ η (%)
20	8.93	4.68				
40	10.6	4.39	1.67	(0.29)	1.67	(0.29)
60	13.6	4.25	3.02	(0.14)	4.69	(0.43)
120	14.0	4.68	0.38	0.43	5.07	0.00

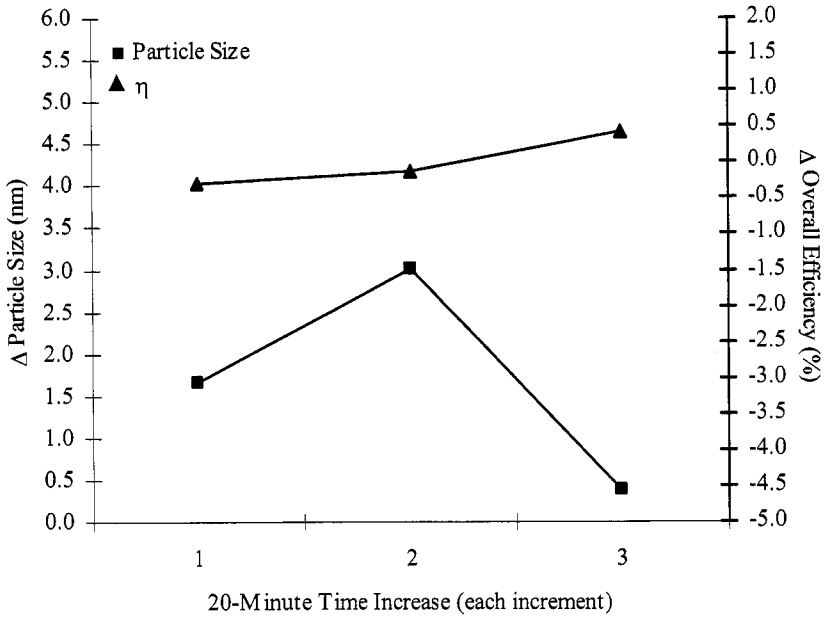

Figure 2.31. Plot of the difference in particle size and the difference in overall efficiency within each change of period of time.

By looking at the total change in particle size and in the overall efficiency relative to the initial particle size at 20 minutes, a fairly constant change in the overall efficiency with increasing particle size was observed. Figure 2.32 shows the total difference in

particle size and in overall efficiency as a function of the total change in time. With a 20-minute and 40-minute increase in hydrothermal treatment time, the particle size increased by ~ 1.7nm and ~ 4.7nm, but the overall efficiency decreased by ~ 0.3% and ~ 0.4%, respectively. In addition, a 100-minute increase in hydrothermal treatment time resulted in the particle size increasing by ~ 5.1nm but the overall efficiency did not change and remained the same. Although the rate of change for the particle size increased, the rate of change for the overall efficiency was very small or negligible. This shows that changing the hydrothermal treatment time to change the particle size did not have as much of an influence on the overall efficiency as changing the hydrothermal treatment temperature to change the particle size, and that the hydrothermal treatment temperature may be more of a factor in the solar cell performance than the amount of time for hydrothermal treatment.

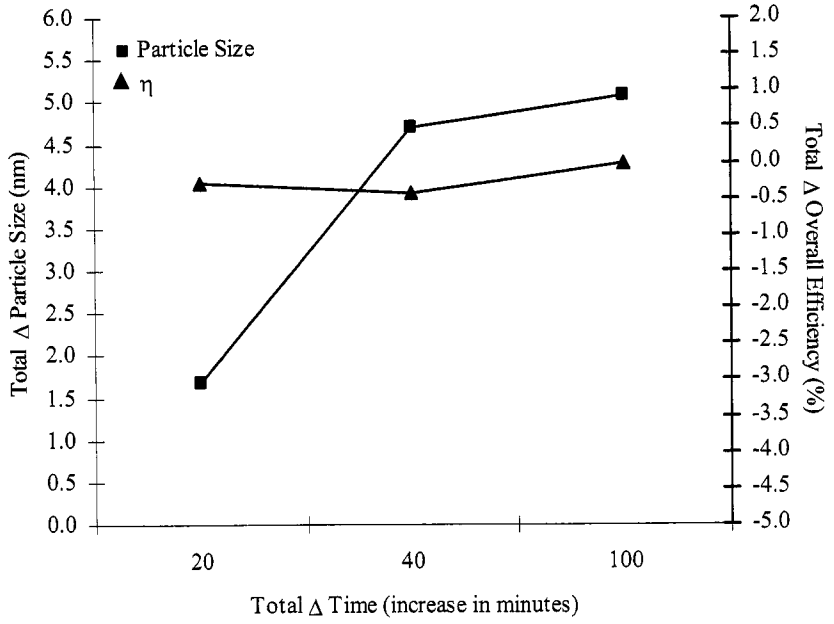

Figure 2.32. Plot of the total difference in particle size and the total difference in overall efficiency as a function of the total change in time, relative to values obtained at 20 minutes.

2.3.4 Characterization of TiO_2 nanoparticle films

To increase the TiO_2 nanoparticle size, hydrothermal treatment at 1) varying temperatures, and 2) varying times were performed. Since a much more noticeable change in the short-circuit current density and the overall efficiency was shown for an increase in particle size by way of increasing the hydrothermal treatment temperature than by way of increasing the hydrothermal treatment time, SEM analysis was used to compare the structure of each prepared TiO_2 nanoparticle film. The following sections detail the structure for films prepared from TiO_2 nanoparticles obtained by way of 1) hydrothermal treatment at 100°C, 150°C, 200°C, 250°C, and 300°C for 60 minutes, and 2) hydrothermal treatment at 250°C for 20, 40, 60, and 120 minutes. All the films were sintered at 500°C for 60 minutes for better particle connectivity.

2.3.4.1 TiO_2 film obtained by hydrothermal treatment at various temperatures

Based on the solar cell performance of TiO_2 nanoparticle films prepared from TiO_2 nanoparticle powder with varying particle size by varying the hydrothermal treatment temperature, it was shown that larger particles resulted in higher short-circuit current density and overall light conversion efficiency. As previously mentioned, the TiO_2 nanoparticle films prepared from nanoparticles hydrothermally-treated at 250°C and 300°C for 60 minutes resulted in higher short-circuit current density values of ~ 10.6mA/cm^2 and ~ 12.2mA/cm^2, respectively. In addition, the TiO_2 nanoparticle films prepared from nanoparticles hydrothermally-treated at 250°C and 300°C for 60 minutes resulted in higher overall efficiency values of ~ 4.3% and ~ 5.2%, respectively. The

smaller nanoparticles obtained at lower hydrothermal treatment temperatures resulted in lower short-circuit current density and overall efficiency values.

Figure 2.33 shows the SEM image of TiO_2 nanoparticle film obtained by hydrothermal treatment at 100°C, 200°C, 250°C, and 300°C for 60 minutes. The TiO_2 nanoparticle film obtained by hydrothermal treatment at 150°C was omitted since the particle size and solar cell performance was very similar to that for the TiO_2 nanoparticle film obtained by hydrothermal treatment at 100°C.

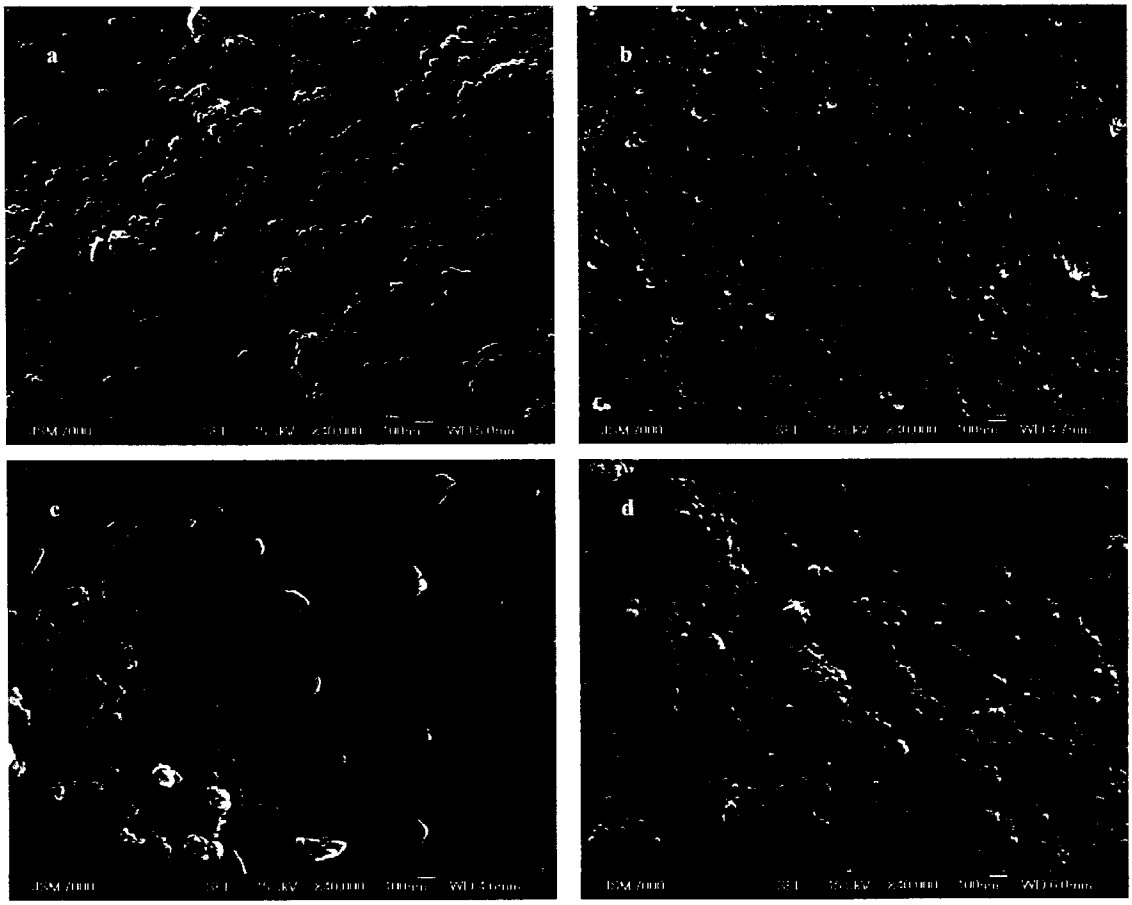

Figure 2.33. SEM images of TiO_2 nanoparticle film obtained from hydrothermal treatment at a) 100°C, b) 200°C, c) 250°C, and d) 300°C temperature for 60 minutes. All the images were taken at 40,000X magnification.

In all cases, it can be seen that the nanoparticles are agglomerated. It seems that the smaller nanoparticles are shown to be fused together to form larger non-uniform clusters. Since the size of the nanoparticles obtained by hydrothermal treatment at 100°C, 150°C, and 200°C were estimated to be ~ 6.7nm, ~ 7.1nm, and ~ 9.7nm, respectively, by way of XRD analysis, it is assumed that the nanoparticles are too small to estimate the size using the SEM. At 250°C and 300°C, XRD analysis estimated the particle size to be ~ 13.6nm and ~ 17.7nm. Although the particle sizes are larger, it is difficult to view the individual particles by way of SEM analysis. Further XRD analysis is required to find out the exact particle size of each film since 500°C sintering for 1 hour was performed on each film before solar cell analysis to improve the connectivity of the particles. This additional sintering step may have increased the particle size from its original particle size, previously determined directly after hydrothermal treatment.

By comparison, it is observed that the roughness of the films slightly varied, but it is difficult to see any noticeable differences. Both agglomeration and clustering occurred in all of the films even with smaller or larger particles. All the films show smaller nanoparticles fused together to form an almost complete film. The films at 100°C and 200°C are expected to have higher porosity and may have had small pores throughout the film, but it was difficult to see from SEM analysis. At 250°C and 300°C, larger clusters seem to be present but the pores of the film are not visible. As the hydrothermal treatment temperature increased, the size of the clusters of individual particles seemed to increase, but it is not for certain that this is the case using SEM analysis.

2.3.4.2 TiO_2 film obtained by hydrothermal treatment at various times

Based on the solar cell performance of TiO_2 nanoparticle films prepared from TiO_2 nanoparticle powder with varying particle size by way of varying the hydrothermal treatment time, it was shown that the particle size slightly increased from increasing the hydrothermal treatment time. However, the short-circuit current density and the overall light conversion efficiency did not dramatically change. As previously mentioned, the TiO_2 nanoparticle films prepared from nanoparticles hydrothermally-treated at 250°C for 20, 40, 60, and 120 minutes resulted in an average short-circuit current density value of ~ 11.7mA/cm^2 with a deviation of ~ 0.9mA/cm^2. In addition, the TiO_2 nanoparticle films prepared from nanoparticles hydrothermally-treated at 250°C for 20, 40, 60, and 120 minutes resulted in an average overall efficiency value of ~ 4.5% with a deviation of ~ 0.2%, respectively. With smaller or larger nanoparticles obtained at shorter and longer hydrothermal treatment times, respectively, the short-circuit current density and overall efficiency values stayed relatively in the same range.

Figure 2.34 shows the SEM images of TiO_2 nanoparticle film obtained by hydrothermal treatment at 250°C for 20, 40, 60, and 120 minutes. The TiO_2 nanoparticle film obtained by hydrothermal treatment at 250°C for 60 minutes is the same image taken from the previous section. It can be seen that in all cases, the nanoparticles are agglomerated and formed clusters. The smaller nanoparticles are shown to be fused together to form larger non-uniform clusters. Although the size of the nanoparticles obtained by hydrothermal treatment at 250°C for 20, 40, 60, and 120 minutes were estimated to be ~ 8.9nm, ~ 10.6nm, ~ 13.6nm, and ~ 14.0nm, respectively, by way of XRD analysis, the nanoparticles are shown to be similar in size using the SEM. However,

it is observed that a deviation in the nanoparticle diameter is difficult to distinguish using SEM analysis with such a small difference in size. It is observed that the roughness of the films is slightly different, although some of the films were not taken on a flat surface.

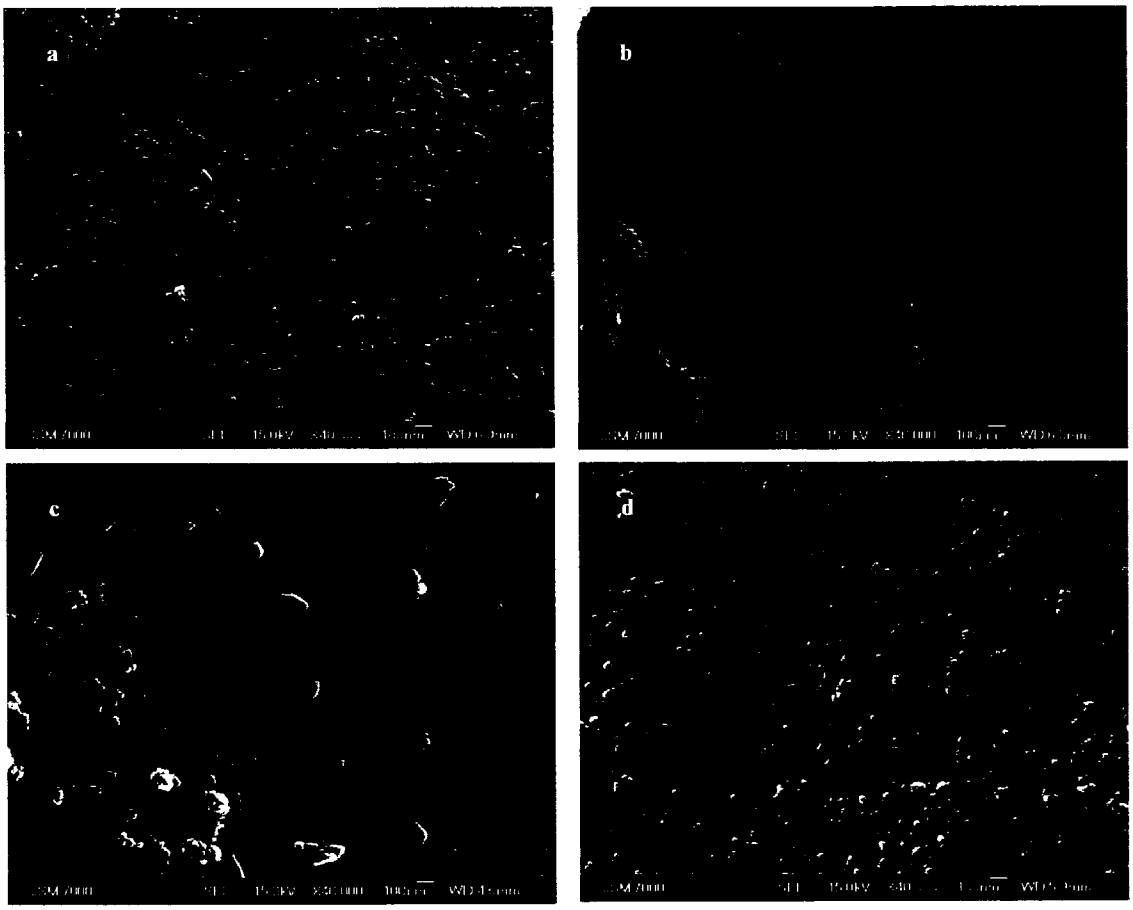

Figure 2.34. SEM images of TiO_2 nanoparticle film obtained from hydrothermal treatment at 250°C for a) 20 minutes, b) 40 minutes, c) 60 minutes, and d) 120 minutes. All the images were taken at 40,000X magnification.

By comparison, it is observed that the roughness of the films slightly varied and the quality of the films were not similar. Both agglomeration and clustering occurred in all of the films even with smaller or larger particles. However, the quality of the film obtained at 250°C for 40 minutes was not as good as the rest of the films. In addition, the

films obtained at 250°C for 20 and 120 minutes had a bit more roughness and were not as flat as the film obtained at 250°C for 60 minutes.

The slightly lower short-circuit current density and overall efficiency with the film obtained at 250°C for 60 minutes, when compared to the films obtained at 250°C for 20 and 120 minutes, may have been due to the flatness of the film. The slightly lower short-circuit current density and overall efficiency with the film obtained at 250°C for 40 minutes, as compared to the films obtained at 250°C for 20 and 120 minutes may have been due to the unevenness of the film. From the SEM images, it could be assumed that the slight differences in the short-circuit current density and overall efficiency were influenced by the quality of the films and not necessarily the particle size. On the other hand, the initial particle size would also have an influence on the quality and packing of the films. This could explain the fluctuation and no definite trend in the short-circuit current density and overall efficiency for the films obtained by hydrothermal treatment at 250°C for various times, where a definite trend is observed for the films obtained by hydrothermal treatment at various temperatures for 60 minutes.

2.3.5 Dye loading in TiO_2 nanoparticle film

The solar cell performance of TiO_2 nanoparticle film with a variation in dye loading was also analyzed and compared. Films consisting of TiO_2 nanoparticles prepared on FTO substrates were sensitized in N3 dye with concentrations of 100%, 50%, 20%, 10%, and 5%. For each N3 dye concentration, the films were immersed for 30, 60, 180, and 300 minutes to compare the overall efficiency. Each TiO_2 film was assembled in a solar cell and tested under illumination to compare the I-V behavior.

Table 2.13 summarizes the measured and calculated values obtained from the I-V characteristics of each TiO_2 film sensitized in various concentrations for various times.

Table 2.13. The measured and calculated values obtained from the I-V curves for each solar cell with TiO_2 nanoparticle films sensitized in various concentrations for various times.

Concentration (%)	Time (minutes)	V_{oc} (mV)	I_{sc} (mA/cm^2)	V_{max} (mV)	I_{max} (mA/cm^2)	FF (%)	P_{max} (mW/cm^2)	P_{in} (mW/cm^2)	η (%)
100	30	690	16.0	350	8.93	28.3	3.13	100	3.13
	60	680	14.8	350	8.00	27.8	2.80	100	2.80
	180	660	15.8	340	8.43	27.5	2.87	100	2.87
	300	680	15.4	350	8.15	27.2	2.85	100	2.85
50	30	700	13.9	360	7.70	28.5	2.77	100	2.77
	60	690	16.9	380	10.3	33.6	3.91	100	3.91
	180	690	15.1	360	8.00	27.6	2.88	100	2.88
	300	690	12.4	370	7.05	30.5	2.61	100	2.61
20	30	660	10.7	340	6.34	30.5	2.16	100	2.16
	60	690	14.7	350	8.69	30.0	3.04	100	3.04
	180	690	16.9	340	10.2	29.7	3.47	100	3.47
	300	670	17.2	370	8.89	28.5	3.29	100	3.29
10	30	580	5.83	340	4.03	40.5	1.37	100	1.37
	60	630	9.27	350	5.93	35.5	2.08	100	2.08
	180	680	13.4	340	7.36	27.5	2.50	100	2.50
	300	680	12.3	380	8.49	38.6	3.23	100	3.23
5	30	610	7.47	340	5.07	37.8	1.72	100	1.72
	60	650	10.9	340	6.87	33.0	2.34	100	2.34
	180	650	14.0	340	10.30	38.5	3.50	100	3.50
	300	680	16.3	370	10.2	34.0	3.77	100	3.77

By comparing the overall efficiency within a group of samples sensitized in the same N3 dye concentration, a trend is observed. Figure 2.35 is a plot of overall efficiency as a function of immersion time for a) 100%, b) 50%, c) 20%, and d) 10% N3 dye concentrations. It is shown that the highest point, or highest overall efficiency, in each plot occurs at 30, 60, 180, and 300 minutes for 100%, 50%, 20%, and 10% N3 dye concentrations. Figure 2.36 is a plot of the highest overall efficiency obtained within each concentration as a function of time immersed in the various concentrations.

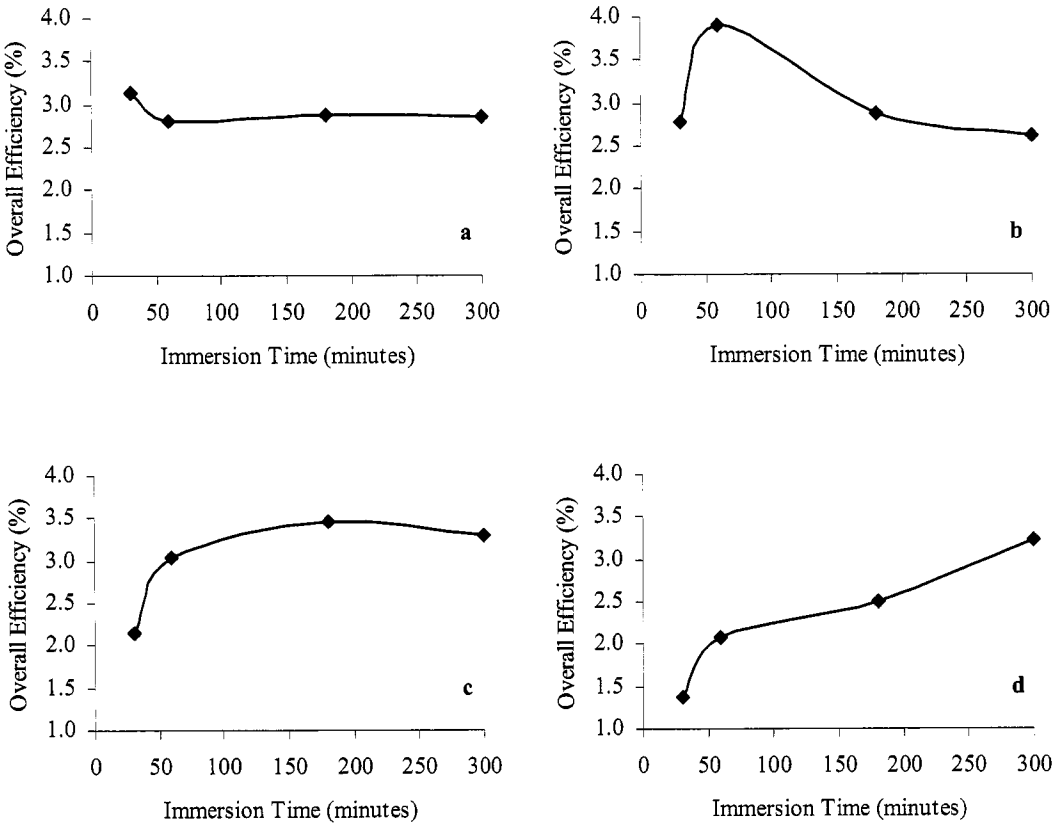

Figure 2.35. Plot of overall efficiency as a function of dye immersion time in a) 100%, b) 50%, c) 20%, and d) 10% concentrations. The TiO_2 nanoparticle films were immersed for 30, 60, 180, and 300 minutes in each N3 dye concentration before testing.

It can be seen that a higher N3 dye concentration required a shorter amount of immersion time for sufficient dye adsorption to obtain a higher overall efficiency. A lower N3 dye concentration required a longer amount of immersion time for sufficient dye sensitization, resulting in a higher overall efficiency. The TiO_2 nanoparticle film had the highest overall efficiency at ~ 3.13% when sensitized in N3 dye with 100% concentration for 30 minutes. With a 50% N3 dye concentration, the TiO_2 nanoparticle film immersed for 60 minutes had the highest overall efficiency of ~ 3.91%. At 20% N3 dye concentration, the highest overall efficiency of ~ 3.47% was obtained from the TiO_2

nanoparticle film immersed for 180 minutes. Additionally, the TiO_2 nanoparticle films sensitized in N3 dye with 10% and 5% concentrations for 300 minutes resulted in a higher overall efficiency of ~ 3.23% and 3.77%, respectively.

At higher concentrations, shorter immersion times in N3 dye was needed for sufficient dye adsorption. At lower concentrations, a longer immersion time in N3 dye was needed for sufficient dye adsorption. The TiO_2 nanoparticle film sensitized in 100%, 50%, 20%, and 10% N3 dye concentration was observed to require 30, 60, 180, and 300 minutes of immersion, respectively, to obtain a higher overall efficiency. At 5% N3 dye concentration, the same immersion time as required at 10% N3 dye concentration was observed to obtain a higher overall efficiency.

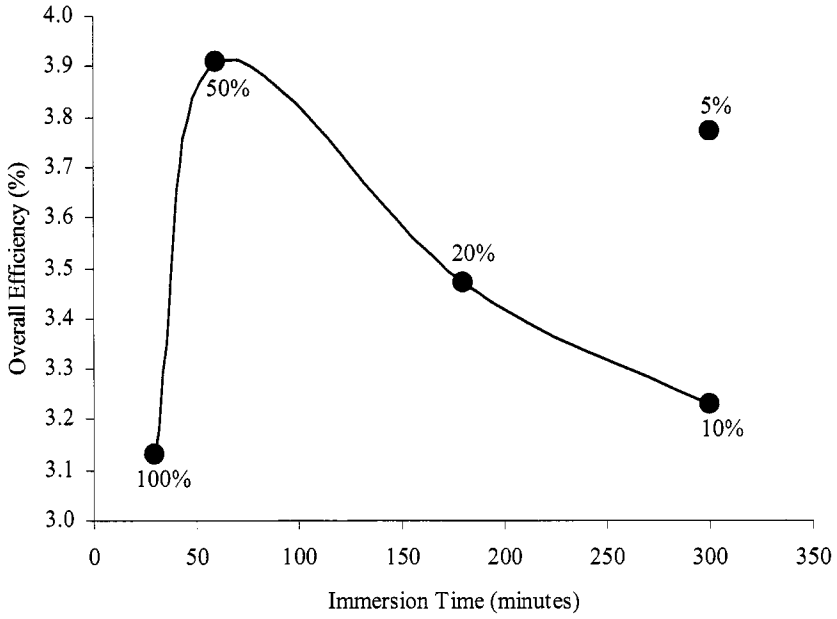

Figure 2.36. Plot of the highest overall efficiency obtained from TiO_2 nanoparticle film immersed in 100%, 50%, 20%, 10%, and 5% N3 dye concentrations. For each N3 dye concentration, films were immersed for 30, 60, 180, and 300 minutes. The highest overall efficiency in each group is plotted.

2.3.6 Comparison of data obtained from prepared TiO_2 nanoparticle film with values found in literature

In the case of the TiO_2 nanoparticle films prepared in this chapter, the standard N3 "red" dye was used. Since this dye has been widely used, is readily available, and is well understood, it was used to analyze the dependence of solar cell performance on the TiO_2 particle size. Using the N3 "red" dye without additional additives, the highest overall efficiency obtained so far is a little less than ~ 10%, as previously mentioned, with an open-circuit voltage of ~ 720mV and a short-circuit current density of ~ 17.0mA/cm^2 under 100mW/cm^2 illumination. The highest efficiency obtained in analyzing the prepared film obtained from hydrothermal treatment at 300°C for 60 minutes was ~ 5% with an open-circuit voltage of ~ 730mV, a short-circuit current density of ~ 12.2mA/cm^2, and a fill factor of ~ 58% under 100mW/cm^2 illumination. This lower overall efficiency may have been due to the quality of the film, as well as the particle size. The quality and assembly of the TiO_2 film studied by Grätzel et al[11,23] have been optimized for the past decade; whereas, the films in this study were recently explored, where the fill factor value > 70% that have been reported, have not been attained. This difference in quality can be seen by comparing the SEM images of the prepared TiO_2 nanoparticle film to that of Grätzel's TiO_2 nanoparticle film in Figure 1.10. In addition, the short-circuit current density has not reached greater than 15.0mA/cm^2, which may have also been influenced by the film quality. The reason for poor film quality may have been due to the fabrication of the TiO_2 nanoparticles, where the variation in particle size, the agglomeration and clustering of particles, and the non-uniformity of the particles may have been a factor.

2.4 Conclusions

In summary, TiO_2 nanoparticle films were prepared to compare the solar cell performance of films with varying particle size. The variations in particle size were obtained from 1) hydrothermally-treated TiO_2 at 100°C, 150°C, 200°C, 250°C, and 300°C temperatures for 60 minutes, and 2) hydrothermally-treated TiO_2 at 250°C for 20, 40, 60, and 120 minutes. The dye loading effect of TiO_2 was also examined.

In conclusion, it was found that larger particles resulted in higher short-circuit current density and overall light conversion efficiency. Films consisting of TiO_2 nanoparticles with ~ 7nm diameter resulted in a short-circuit current density of ~ 3.6mA/cm^2 and an overall light conversion efficiency of ~ 1.4%. With an increase in the particle size to ~ 18nm diameter, the TiO_2 nanoparticle film resulted in a higher short-circuit current density of ~ 12.2mA/cm^2 and a higher overall light conversion efficiency of ~ 5.2%. This increase in short-circuit current density and overall light conversion efficiency may have been due to a few possible factors: 1) better crystallinity, or a reduction in the number of defects; 2) better connectivity, or larger contact points; and 3) more dye adsorption through easier access of dyes at larger contact points, resulting in more generation of electrons and holes.

Additionally, it was found that a higher concentration of N3 dye requires a shorter amount of immersion time and a lower concentration of N3 dye requires a longer amount of immersion time for better dye adsorption.

[117] F. Gracia, J.P. Holgado, and A.R. González-Elipe, "Photoefficiency and Optical, Microstructural, and Structural Properties of TiO_2 Thin Films Used as Photoanodes," *Langmuir* **20**, 1688 (2004).

[118] A. Hagfeldt, G. Boschloo, H. Lindstrom, E. Figgemeier, A. Holmberg, V. Aranyos, E. Magnusson, and L. Malmqvist, "A system approach to molecular solar cells," *Coordination Chemistry Reviews* **248**, 1501 (2004).

[119] I. Kartini, D. Menzies, D. Blake, J.C.D. da Costa, P. Meredith, J.D. Riches, and G.Q. Lu, "Hydrothermal seeded synthesis of mesoporous titania for application in dye-sensitised solar cells (DSSCs)," *Journal of Materials Chemistry* **14**, 2917 (2004).

[120] D. Zhang, T. Yoshida, K. Furuta, and H. Minoura, "Hydrothermal preparation of porous nano-crystalline TiO_2 electrodes for flexible solar cells," *Journal of Photochemistry and Photobiology A: Chemistry* **163**, 159 (2004).

[121] S.J. Limmer, T.P. Chou, and G.Z. Cao, "A study on the growth of TiO_2 nanorods using sol electrophoresis," *Journal of Materials Science* **39**, 895 (2004).

[122] Parr Instrument Company 2006, *General Purpose Acid Digestion Bombs*, <http://www.parrinst.com/>

[123] Solar Light Company 2006, *Products*, < http://www.solar.com/>

[124] ASTM International Standards, <http://www.astm.org>

[125] Wikipedia: The Free Encyclopedia, *Solar Radiation*, <http://en.wikipedia.org>

[126] G.P. Smestad, "*Nanocrystalline Solar Cell Kit: Recreating Photosynthesis*," eds. A. Huseth and K. Shanks, ICE Publication, 1998.

[127] B.D. Cullity. *Elements of X-Ray Diffraction.* 2nd ed. Reading, Mass: Addison-Wesley Publishing Co, 1956.

3 TiO_2-ITO nanocomposite films for dye-sensitized solar cells

3.1 Introduction

Transparent conducting oxides, specifically indium-tin-oxide (ITO), have been widely used in a number of photonic applications, including organic light-emitting diodes[128], electrochromic displays[129], and photovoltaics[130]. The advantage of ITO is its combined property of high electrical conductivity and optical transparency.

There have been studies on dye-sensitized TiO_2 solar cells with the addition of Al_2O_3, MgO, NiO, SnO_2, ZnO, or Nb_2O_5 in combination to form hybrid or nanocomposite films for better charge separation and suppression of recombination, as mentioned in Chapter 1. In addition, hybrid structures comprised of oxide materials and polymeric layers have been examined. However, to this point, there have been no studies on the fabrication of TiO_2-ITO nanocomposites for the application of solar cells. By utilizing ITO nanostructures in the TiO_2 nanoparticle film, it is assumed that the charge transport properties would improve, resulting in higher short-circuit current density and overall light conversion efficiency. This assumption is based on ITO having much higher electron mobility[131] ~ 40-70cm^2/Vs, as compared to the electron mobility[95] of anatase TiO_2 with a value ~ $10^{-5}$$cm^2$/Vs.

In this chapter, solar cells with films combining the properties of TiO_2 and ITO were analyzed and compared. Films consisting of 1) TiO_2 nanoparticles with the addition of ITO nanoparticles, 2) TiO_2 nanoparticles with the addition of ITO nanorods, and 3) ITO nanorod arrays with a layer of TiO_2 coating were fabricated and compared to TiO_2 nanoparticle film. Figure 3.1 depicts the ideal TiO_2-ITO nanocomposite structures. These

nanocomposite films were studied in an attempt to utilize the high conductivity of ITO to reduce the resistance and improve the ability for electron transport.

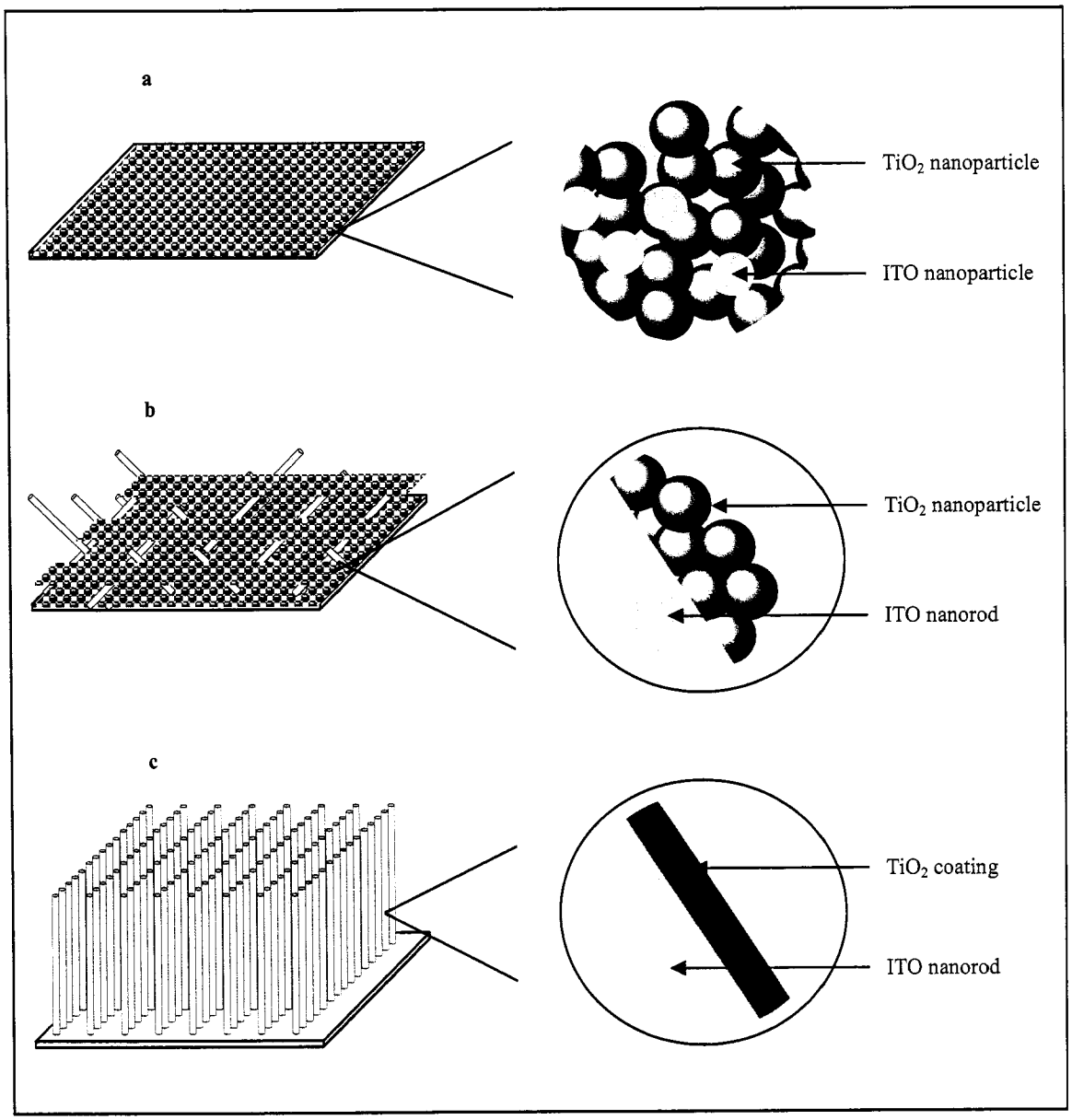

Figure 3.1. Schematic of the ideal TiO_2-ITO nanocomposite films depicting film with a) TiO_2 nanoparticles with ITO nanoparticles, b) TiO_2 nanoparticles with ITO nanorods, and c) ITO nanorod arrays with TiO_2 coating on the surface.

The dye-sensitized TiO_2 material acts as the point of photon absorption, electron injection, and electron capture, and the ITO material acts as the point of electron transport

to increase the rate of electron conduction. In this manner, the nanocomposite films combine the advantages of both materials: 1) TiO_2 has high electron effective mass to prevent leakage of trapped electrons to the electrolyte or adsorbed dye, and has been widely studied as a sufficient electron capturing and transporting material with good stability; and 2) ITO has a higher electron mobility to provide better electron transport properties. Each nanocomposite film was assembled in a solar cell and tested under illumination to compare the I-V behavior of each type of TiO_2-ITO nanocomposite film to that of TiO_2 nanoparticle film.

3.2 Experimental procedure

The following sections describe 1) the formation of ITO nanostructures, most notably ITO nanoparticles and ITO nanowires; 2) the fabrication of TiO_2-ITO nanocomposite films, specifically TiO_2 nanoparticles with ITO nanoparticles, TiO_2 nanoparticles with ITO nanorods, and ITO nanorod arrays with TiO_2 coating; and 3) the analysis techniques used to compare the nanocomposite films.

3.2.1 Formation of ITO nanostructures

Indium-Tin-Oxide (ITO) sol[132] was used to prepare 1) ITO nanoparticles, and 2) ITO nanorods. Nanoparticle powders were prepared by way of sol-gel processing and sintering at an elevated temperature. Nanorod powders and arrays were prepared by way of sol-gel processing, template-assisted electrophoretic deposition at room temperature, and sintering at an elevated temperature. The following sections describe the process for preparing ITO sol, ITO nanoparticles, and ITO nanorods.

3.2.1.1 ITO sol preparation

The sol was prepared from precursor materials by way of sol-gel processing. The chemicals used in making ITO sol were tin (IV) chloride (98%, anhydrous, Alfa Aesar, Ward Hill, MA), indium (III) chloride (99.99%, anhydrous, Alfa Aesar, Ward Hill, MA), citric acid (monohydrate, JT Baker, Phillipsburg, NJ), ethylene glycol (JT Baker, Phillipsburg, NJ), ethanol (200 proof, AAPER, Shelbyville, KY), and deionized water (DI-H_2O). Figure 3.2 is a flow chart of the process involved in preparing ITO sol.

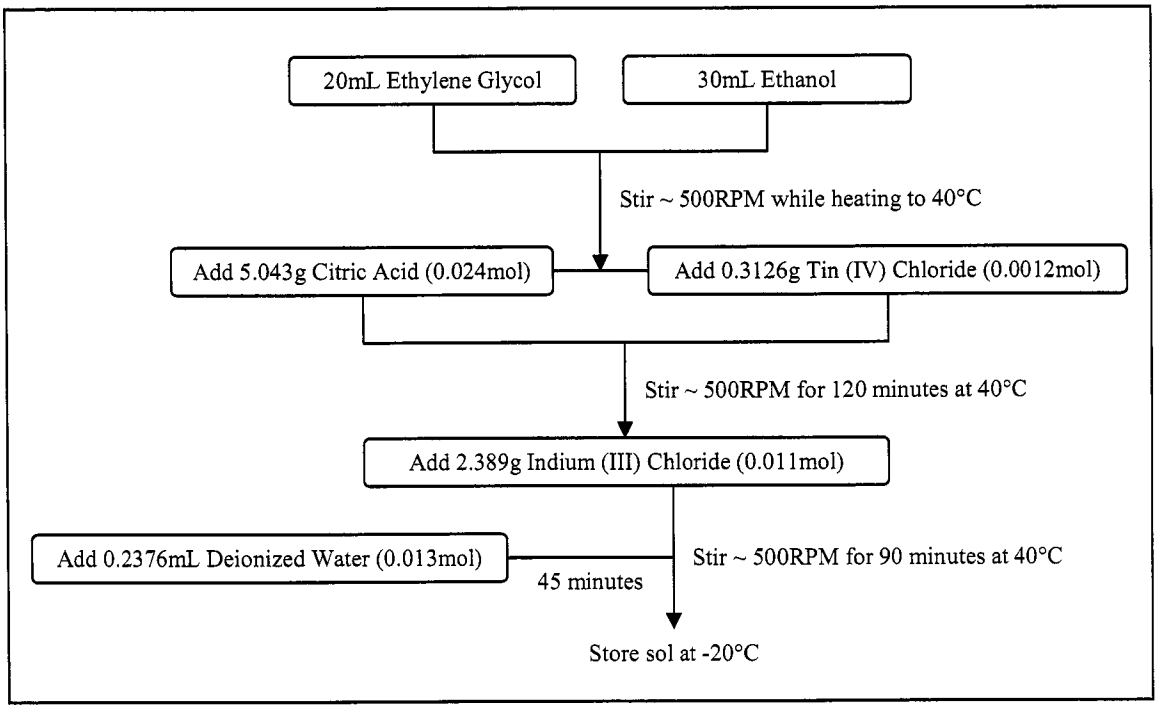

Figure 3.2. Schematic of the steps and procedures involved in sol-gel processing of precursors to obtain ITO sol.

The sol was prepared by combining ethylene glycol [$HOCH_2CH_2OH$], ethanol [C_2H_5OH], citric acid [$HOC(CO_2H)(CH_2CO_2H)_2$], tin (IV) chloride [$SnCl_4$], indium (III) chloride [$InCl_3$], and DI-H_2O with a nominal molar ratio of $1.00:1.42:6.67x10^{-2}:3.34x10^{-3}:3.06x10^{-2}:3.61x10^{-2}$, respectively. Citric acid and $SnCl_4$ were added to a mixture of

ethylene glycol and ethanol, and stirred at a rate of 500RPM at 40°C for 60 minutes. An amount of $InCl_3$ was then added and stirred for another 90 minutes at 40°C; DI-H_2O was added 45 minutes into the stirring. The resultant sol had a pH value ~ 1, resulting in positively-charged ITO sol particles. The sol was clear and stable at room temperature, but was stored at -20°C when not in use to minimize hydrolysis and condensation reactions. Sonication was also used to disperse the sol particles before use.

3.2.1.2 ITO nanoparticles

Nanoparticle powder formed from ITO sol was obtained by first drying 20mL of ITO sol in a crucible at 100°C for 24 hours in air and then sintering at 700°C for 1 hour at a heating rate of 2°C/min. The resultant ITO powder obtained was then ground down to smaller particles using a mortar and pestle.

3.2.1.3 ITO nanorods

Nanorods grown from ITO sol were formed from a technique combining sol-gel processing and template-assisted electrophoretic deposition (EPD). Track-etched hydrophilic polycarbonate membranes (PCM, Millipore, Bedford, MA) with a thickness of approximately 10μm were used as the templates. The pore density of the PCM templates was roughly estimated to be ~ 10^9pores/cm^2 with a pore diameter ranging from 100nm to 200 nm. During the EPD process, an aluminum cathode was in contact with one side of the template and the sol was in contact with the other side of the template. A platinum anode was also immersed into the sol, which was used as the counter electrode. Figure 3.3 shows a schematic of the EPD process using PCM as the template. The sol

was initially drawn into the pores of the template by capillary action, and the applied potential directed the sol particles to deposit within the pore channels of the template, filling the pores completely after a certain amount of time.

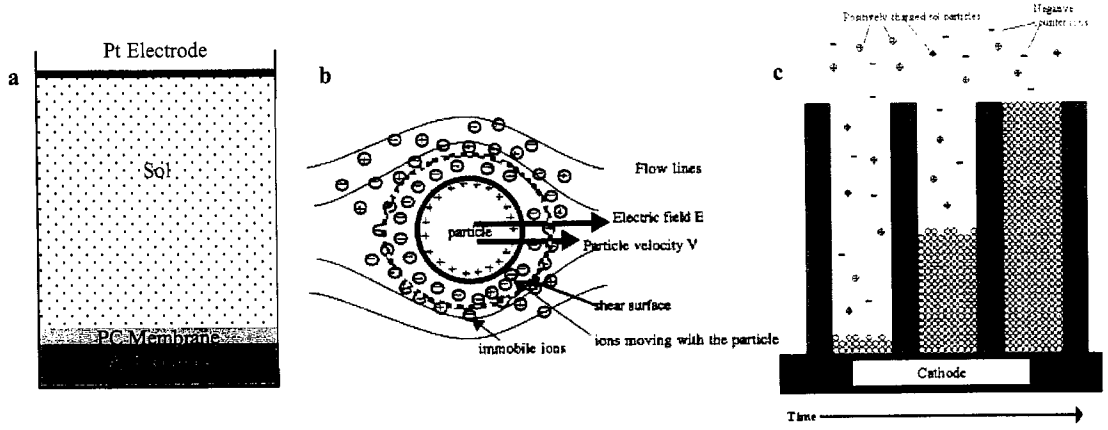

Figure 3.3. Depiction of the EPD process showing a) the setup for nanorod growth, b) the driving force for nanoparticle migration, and c) the deposition of nanoparticles in the membrane pore channels. [Ref 133]

For the growth of ITO nanorods, an applied potential of ~ 1.67V/cm was performed for ~ 50 minutes. After EPD, each filled template was dried in air at 100°C for 24 hours. To obtain nanorod powders, high temperature sintering at 700°C at a heating rate of 2°C/min was then used to pyrolyze the PCM and to densify the nanorods after drying. A small amount of powder consisting of ITO nanorods was obtained. To obtain nanorod arrays, the side of the template that was in contact with the aluminum cathode during EPD was attached to a conductive ITO-coated glass substrate using a drop of ITO sol on the substrate surface. This technique was anticipated to initiate the attachment of one end of the nanorods to the substrate surface by a conductive layer so as to obtain an array of free-standing nanorods perpendicular to the substrate surface. After attachment, each sample was dried in air for 24 hours at 100°C and then sintered at 500°C for 1 hour

at a heating rate of 2°C/min. High-temperature sintering was performed to burn off the PCM, to densify the nanorods, and to crystallize the material.

It is also important to note that the growth of ITO nanorods were also possible using a template-assisted centrifugation process[134]. Each PCM template was securely placed flat at the bottom of a 13mm diameter syringe tube and 3mL of sol was added. The tube was sealed with Parafilm® and placed in a centrifuge tube. Centrifugation was performed at a rate of approximately 1400 revolutions per minute (RPM) for 60 minutes. Upon contact of the sol to the PCM template, the sol was initially drawn into the membrane pores by capillary action and the process of rotation initiated the migration of particles from the sol into the template pores by centrifugation force, resulting in the enrichment of solid within the pores. All the templates with filled pores were rinsed with DI water after centrifugation and dried in air at approximately 100°C for 24 hours.

3.2.2 Fabrication of TiO_2-ITO nanocomposite films

Nanocomposite films consisting of 1) TiO_2 nanoparticles and ITO nanoparticles, 2) TiO_2 nanoparticles and ITO nanorods, and 3) ITO nanorod arrays with a layer of TiO_2 coating were fabricated to compare the solar cell response to that of TiO_2 nanoparticle film. The nanocomposite films consisted of a 20 wt% ITO composition relative to the amount of TiO_2 nanoparticles. Films consisting of TiO_2 nanoparticles and a mixture of TiO_2 and ITO nanoparticles were fabricated on both transparent, conductive indium-tin-oxide (ITO, R_s ~ 8-12 ohms, Delta Technologies Ltd, Stillwater, MN) and fluorine-tin-oxide (FTO, TCO10-10, R_s ~ 10ohm/sq, Solaronix SA, Switzerland) coated glass substrates. Films consisting of a mixture of TiO_2 nanoparticles and ITO nanorods were

fabricated on FTO substrates, and films consisting of ITO nanorod arrays with a layer of TiO_2 coating were fabricated on ITO substrates. The following sections describe the fabrication process of the films.

3.2.2.1 TiO_2 nanoparticle film with ITO nanoparticles

For the preparation of TiO_2-ITO nanoparticle film, a mixture of TiO_2 nanoparticle powder and ITO nanoparticle powder was used. As previously mentioned, the TiO_2 nanoparticle powder was obtained by hydrothermally-treating 10mL of TiO_2 sol at 250°C for 20 minutes and the ITO nanoparticle powder was obtained by first drying 20mL of ITO sol at 100°C and subsequent sintering to 700°C for 1 hour at a heating rate of 2°C/min. The powder composition used to prepare the films consisted of 20 wt% ITO powder relative to the TiO_2 powder. The dispersion used to deposit the film on an ITO substrate consisted of 20-30 wt% TiO_2-ITO powder in ethanol solution.

Before preparing the film, the surface of the FTO and ITO substrates were hydrolyzed by heating to 90-100°C in DI H_2O for 30-60 minutes. After the substrates were air-dried, two parallel edges of each substrate were covered with ~ 10-μm-thick scotch tape to control the thickness of the film. To form the film, three drops of the TiO_2-ITO powder dispersion were placed at the center of each substrate and the edge of a glass microscope slide was used to spread the solution to form an even 10μm layer after sliding over the tape-covered edges. The film was then dried in air at room temperature for ~ 15 minutes before tape removal, further dried at 100°C for 1 hour, and sintered at 500°C for 1 hour at a heating rate of 2°C/min.

3.2.2.2 TiO_2 nanoparticle film with ITO nanorods

Films consisting of TiO_2 nanoparticles with the addition of ITO nanorods were obtained by adding an amount of TiO_2 nanoparticle powder to the nanorod powder, so as to obtain a powder composition with 20 wt% ITO relative to the amount of TiO_2 powder. The nanorod powder was obtained from 20 PCM templates completely filled with ITO sol by way of the EPD process, as previously detailed. A dispersion consisting of 20-30 wt% TiO_2-ITO powder in ethanol solution was prepared for forming the film.

Before preparing the film, the surface of the FTO and ITO substrates were hydrolyzed by heating to 90-100°C in DI H_2O for 30-60 minutes. After the substrates were air-dried, two parallel edges of each substrate were covered with ~ 10-μm-thick scotch tape to control the area of film coverage. To form the film, drops of the dispersion were placed on the substrate and allowed to dry. This process continued until all of the dispersion was used. The film was then dried in air at 100°C for 1 hour and sintered at 500°C for 1 hour at a heating rate of 2°C/min.

3.2.2.3 ITO nanorod arrays with TiO_2 coating

To add an additional coating of TiO_2 to the ITO nanorod array film, an aqueous solution of hydrothermally-treated TiO_2 paste was prepared. The preparation of hydrothermal-treated TiO_2 was previously described in Chapter 2. In summary, the TiO_2 paste was prepared by placing 10mL of TiO_2 sol in a PTFE cup, sealing the cup with TiO_2 sol in an acid digestion bomb, and heating to 250°C for 20 minutes. The resultant white paste was diluted with DI-H_2O with a weight ratio of 10:1 DI-H_2O:TiO_2 and stirred for ~ 10 minutes at room temperature to obtain a milky-white solution.

To coat the ITO nanorod arrays, further dilution of the aqueous TiO_2 solution was required. An additional 10mL of ethanol was added to 10mL of the above aqueous TiO_2 solution to give a 1:1 volume ratio of ethanol to TiO_2:DI-H_2O. The resultant white solution had a similar consistency to water. Before coating, the ITO nanorod arrays were hydrolyzed in DI-H_2O at ~ 90°C-100°C for ~ 5-10 minutes to aid in the bonding and attachment of the TiO_2 coating. A total of 15 drops were added five at a time to the top of the nanorod arrays to allow for slow capillary force to drive the solution in between each nanorod to coat the surface. Each set of drops were added after the previous set was dried. The film was then dried in air at 100°C for 1 hour and sintered at 500°C for 1 hour at a heating rate of 2°C/min.

3.2.3 Analysis techniques

X-Ray Diffraction (XRD) was used to verify the crystal structure of ITO nanoparticles and nanorods. The preparation of samples for XRD was previously described in Chapter 2. Scanning Electron Microscopy (SEM) was used to study the morphology of the ITO nanoparticles and nanorods, as well as the structure of the nanocomposite films. The sample preparation for SEM was previously described in Chapter 2. Solar cells were assembled and tested in the same manner as previously described in Chapter 2.

3.3 Results and discussion

The following sections describe the results from 1) the characterization of ITO nanostructures, 2) the solar cell performance of TiO_2-ITO nanocomposite films on FTO

substrates, 3) the solar cell performance of TiO_2-ITO nanocomposite films on ITO substrates, 4) the comparison of FTO and ITO substrates, and 5) the characterization of TiO_2-ITO nanocomposite films.

3.3.1 Characterization of ITO nanostructures

To identify the crystallinity and particle size of the ITO nanoparticles, XRD analysis was performed. For the nanorod structure, both XRD and SEM analysis were used to identify the crystallinity and the morphology of the ITO nanorods. Additional SEM analysis was performed on the ITO nanoparticles. The following sections detail the XRD and SEM results for both ITO nanoparticles and ITO nanorods.

3.3.1.1 ITO nanoparticles

Utilizing both sol-gel processing and high temperature sintering, ITO nanoparticles were obtained. Figure 3.4 shows the SEM images of the ITO nanoparticles at two magnifications. It can be seen that the diameters of the ITO nanoparticles were difficult to estimate at such a small size, and that the majority of the ITO nanoparticles shown in the SEM image are agglomerated and formed clusters after drying. However, XRD analysis was used to estimate the particle size, as well as to verify the crystallinity.

Figure 3.5 shows the XRD peaks obtained from ITO nanoparticle powder. The peaks show that the ITO nanoparticles consisted of a cubic structure, similar to indium oxide. Since the doping level of tin is very small, only peaks associated with indium oxide are seen. Using the Scherer equation, as previously mentioned in Chapter 2, the XRD peaks at (222), (400), (411), (440), (611), (622), and (631) were used to estimate

the particle size at each peak. The average particle size obtained for ITO was ~ 7.8nm with a deviation of ~ 1.4nm.

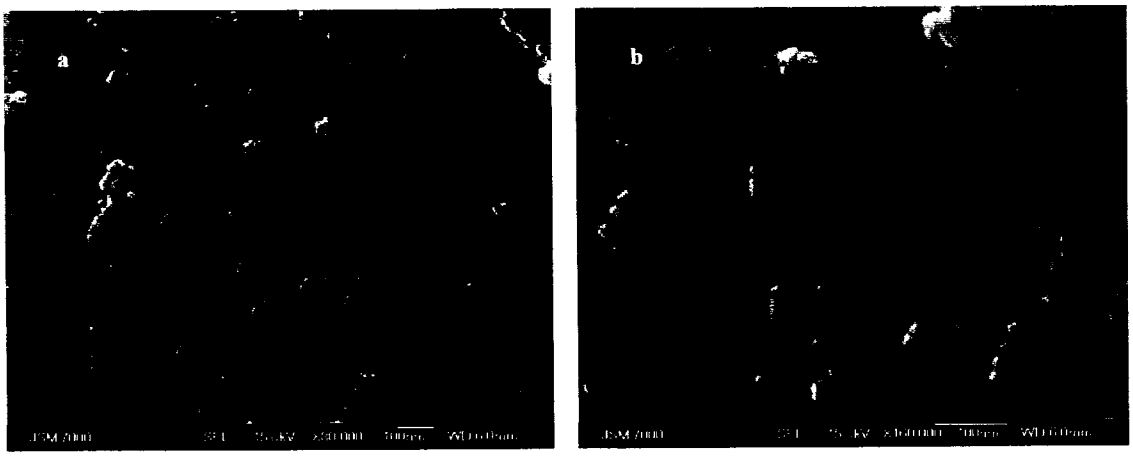

Figure 3.4. SEM images of ITO nanoparticles at a) 80,000X magnification and b) 160,000X magnification obtained by way of sol-gel processing and high temperature sintering.

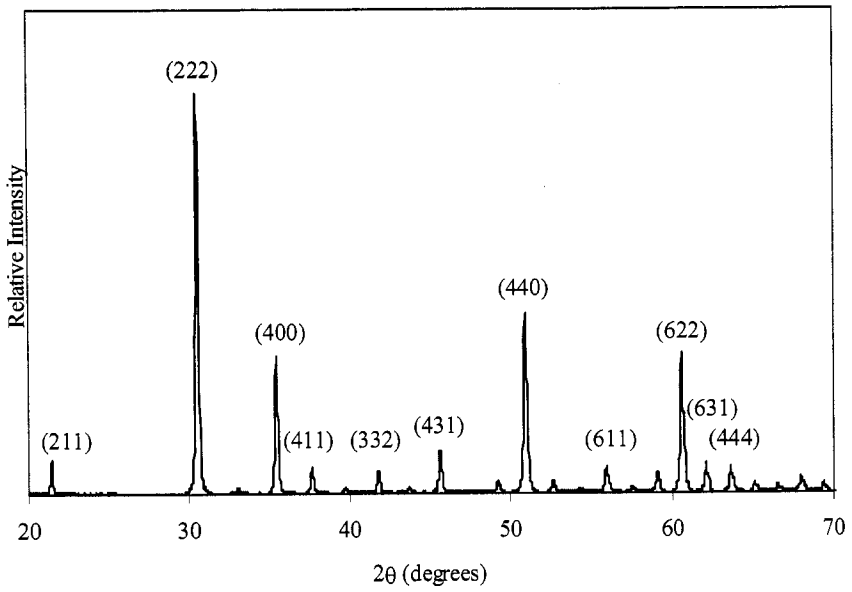

Figure 3.5. XRD plot obtained from ITO nanoparticles, showing the cubic structure of indium oxide. It should be noted that the amount of tin is too small to detect with XRD.

In order to obtain ITO nanoparticles with the lowest resistivity, an elevated temperature ~ 700°C was used. This temperature was based on an examination of the

conductivity of ITO films sintered at various temperatures, as previously reported[132] in literature. Figure 3.6 is a plot of resistivity as a function of sintering temperature for ITO films prepared from the same ITO sol. The sheet resistance of the films was measured with a Veeco four-point probe, and converted to a bulk resistivity value by multiplying by the film thickness (~ 550nm) obtained by cross-sectional observation with an SEM. It can be seen that the film with the best properties was sintered at 700°C for 1 hour, resulting in a resistivity value of ~ 1.44 x 10^{-2} Ω-cm, as compared to the films sintered at 400°C, 500°C, and 600°C temperatures.

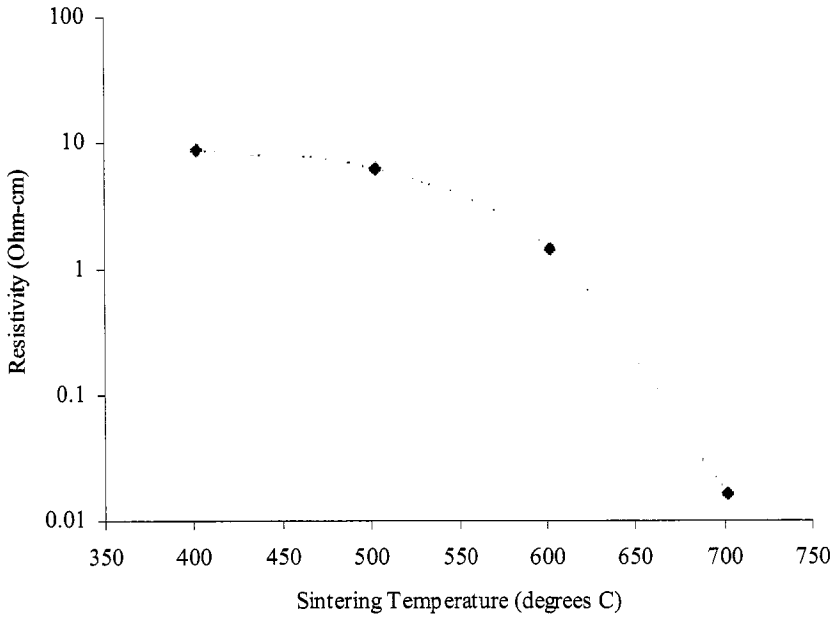

Figure 3.6. Plot of resistivity as a function of sintering temperature for ITO films prepared on glass substrates. The lowest resistivity of ~ 1.44x10^{-2}ohm-cm was obtained at 700°C sintering temperature.

Since the lowest resistivity, or in other words, the highest conductivity of the ITO film was obtained by sintering to 700°C, the ITO nanoparticles, as well as, the ITO nanorods were sintered to 700°C as well. It was difficult to measure the resistivity of the

individual nanoparticles and nanorods; therefore, the resistivity of ITO film was used as a measure of the conductivity properties of ITO nanoparticles and nanorods.

3.3.1.2 ITO nanorods

By way of template-based sol electrophoresis, ITO nanorods can easily be grown in PC membranes. An array of ITO nanorods can also be obtained by using ITO sol to attach the nanorods to the substrate surface. Figure 3.7 shows SEM images of ITO nanorods grown in PC membranes by way of electrophoresis, and attached to an ITO substrate using ITO sol. Figure 3.8 shows SEM images of ITO nanorods grown in PC membranes by way of centrifugation, and attached to an ITO substrate using ITO sol.

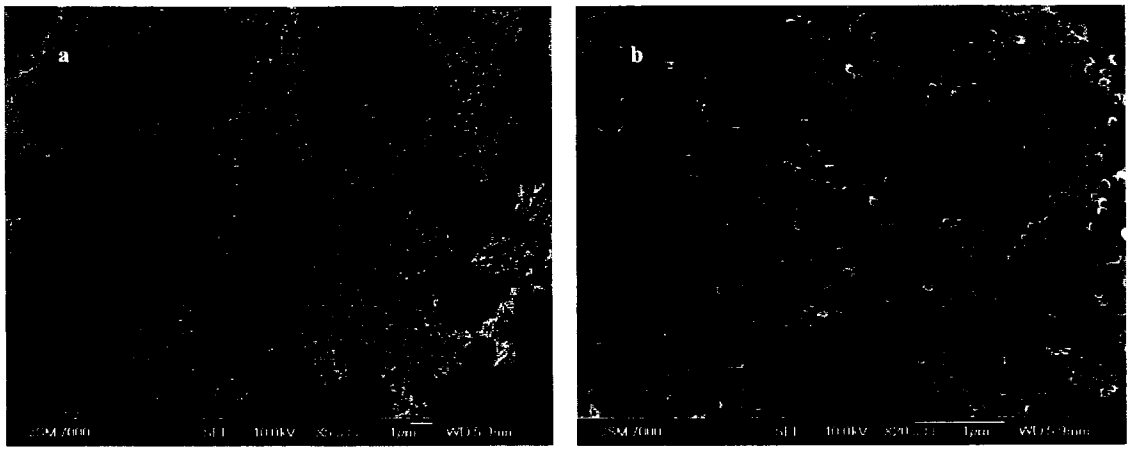

Figure 3.7. SEM images of ITO nanorod arrays attached to an ITO substrate at a) 5,000X magnification and b) 20,000X magnification. The ITO nanorods were grown by way of template-assisted electrophoretic deposition in polycarbonate membranes.

It can be seen that solid, dense rods with good uniformity were obtained with ~ 70nm diameters and ~ 10μm lengths, similar to the thickness of PCM using both template-assisted sol electrophoresis and template-assisted centrifugation. In each case, the nanorods were all measured to have roughly the same diameter and length. Based on

the measured diameters of the nanorods as compared to the 100nm pore size of the templates, ~ 30% lateral shrinkage was observed, most likely caused by organic burnout and densification during high temperature sintering.

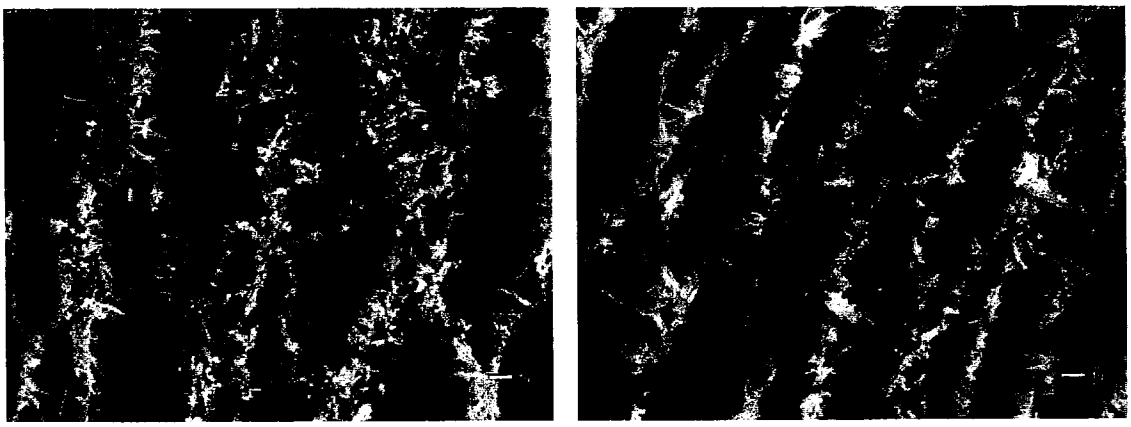

Figure 3.8. SEM images of ITO nanorod arrays attached to an ITO substrate at 10,000X magnification. The ITO nanorods were grown by way of centrifugation.

Figure 3.9 shows the XRD peaks obtained from the ITO nanorods. By comparing the XRD peaks for the ITO nanorods with that for the ITO nanoparticles, it was confirmed that the nanorods consisted of ITO. Since the amount of nanorods is much smaller than that of nanoparticles, the intensity of some of the peaks were small, but by comparison, similar peaks were observed for ITO nanorods and ITO nanoparticles.

Additional characterization of the ITO nanorods using Energy-Dispersive Spectroscopy (EDS, Princeton Gamma Tech IMIX) was also performed on the ITO nanorods. As reported[132] previously, the recorded EDS data from a single nanorod shows both the indium (In) and tin (Sn) Kα lines. Figure 3.10 shows the EDS data. The In and Sn Kα lines were present at 24.14keV and 25.20keV, respectively. The intensity ratio suggested ~ 8 at% of Sn in In_2O_3, showing that the desired doped phase of the ITO nanorods was obtained successfully.

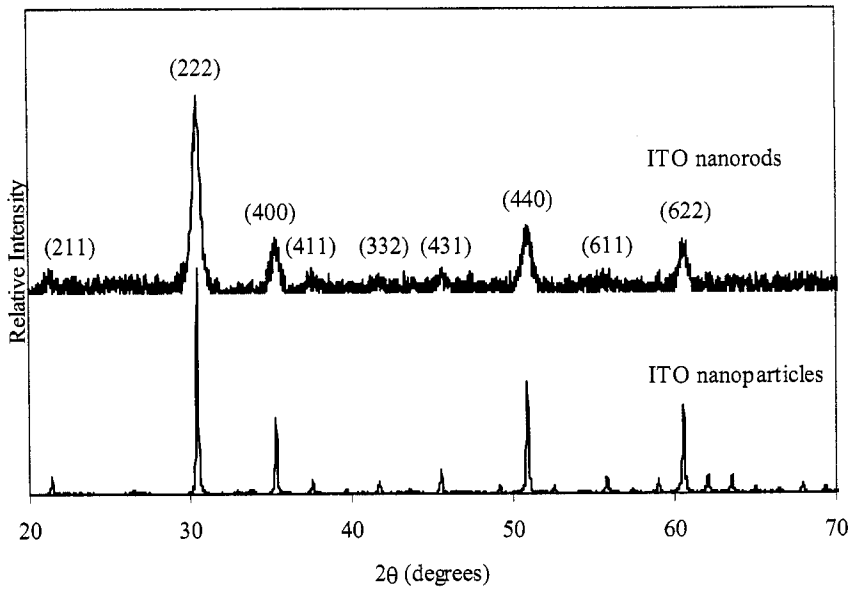

Figure 3.9. XRD plot comparing the peaks obtained from ITO nanorods to the peaks obtained from ITO nanoparticles. The peaks show a cubic structure, similar to indium oxide.

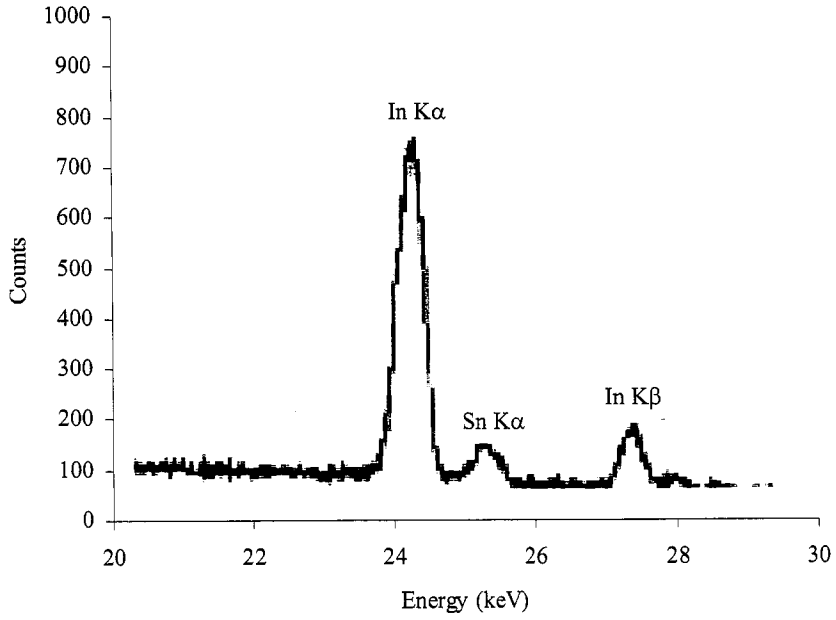

Figure 3.10. EDS plot of a single ITO nanorod showing the In Kα line at ~ 24keV, the Sn Kα line at ~ 25keV, and the In Kβ line at ~ 27.5keV. This shows that the desired composition was obtained.

3.3.2 Solar cell performance of TiO_2-ITO nanocomposite films on conductive FTO substrates

The photoresponse of TiO_2 films with the addition of ITO were compared in order to show whether the addition of ITO could enhance the solar cell performance of TiO_2. Two types of nanocomposite films were prepared on FTO: 1) TiO_2 nanoparticles with ITO nanoparticles, and 2) TiO_2 nanoparticles with ITO nanorods. Solar cells with these films were assembled and tested under illumination with $100mW/cm^2$ intensity, and compared to films with only TiO_2 nanoparticles. Table 3.1 summarizes the measured and calculated values obtained from the I-V curves of 1) TiO_2 nanoparticle film, 2) TiO_2-ITO nanoparticle film, and 3) TiO_2 nanoparticle-ITO nanorod film. Figure 3.11 compares the I-V characteristics of each solar cell.

Table 3.1. The measured and calculated values obtained from the I-V curves for each solar cell consisting of TiO_2 nanoparticle, TiO_2-ITO nanoparticle, and TiO_2 nanoparticle-ITO nanorod films.

Film on FTO	V_{oc} (mV)	J_{sc} (mA/cm^2)	V_{max} (mV)	J_{max} (mA/cm^2)	FF (%)	P_{max} (mW/cm^2)	P_{in} (mW/cm^2)	η (%)
TiO_2 nanoparticles	720	12.8	450	10.4	50.8	4.68	100	4.68
TiO_2 nanoparticles ITO nanoparticles	710	15.3	450	12.5	51.6	5.60	100	5.60
TiO_2 nanoparticles ITO nanorods	680	11.0	450	9.14	55.0	4.11	100	4.11

It can be seen that the short-circuit current density increased with the addition of ITO nanoparticles, but decreased with the addition of ITO nanorods. The most notable difference is in the short-circuit current density and in the overall light conversion efficiency. A closer look at the trends comparing open-circuit voltage, short-circuit current density, fill factor, and overall efficiency is detailed in the following sections.

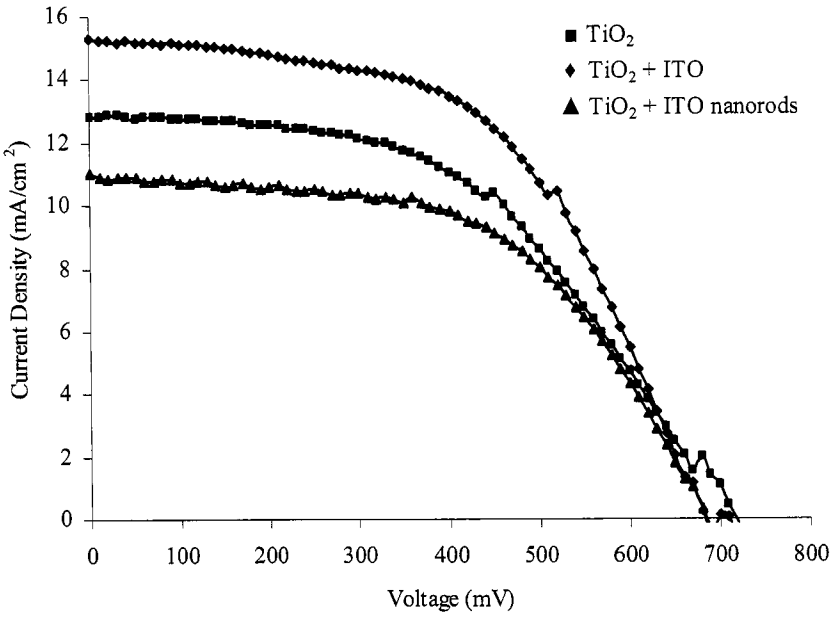

Figure 3.11. Plot and comparison of the I-V characteristics for each solar cell consisting of TiO_2 nanoparticle, TiO_2-ITO nanoparticle, and TiO_2 nanoparticle-ITO nanorod films.

3.3.2.1 Open-circuit voltage

Since the open-circuit voltage is dependent on the potential difference between the working electrode and the counter electrode in a solar cell, films with similar surface chemistry should have similar open-circuit voltage values. Figure 3.12 is a comparison of open-circuit voltage values between TiO_2 nanoparticle film, TiO_2-ITO nanoparticle film, and TiO_2 nanoparticle-ITO nanorod film. Table 3.2 summarizes the actual open-circuit voltage values.

From Figure 3.12, it can be seen that the open-circuit voltage remains fairly constant even with the addition of ITO. The open-circuit voltage stayed steady in the range of ~ 703mV with a deviation of ~ 21mV, which shows that the amount of ITO was not enough to dramatically change the surface chemistry of the films. However, a slight

decrease in the open-circuit voltage with the addition of ITO nanorods may have been due to the process of fabricating the ITO nanorods, which requires polycarbonate membranes. Incomplete burnout of the membranes could have resulted in an excess amount of carbon on the surface of the ITO nanorods to alter the surface chemistry. Not enough carbon was present to cause a dramatic decrease in open-circuit voltage, but the slight decrease does show that some amount of carbon may have been left.

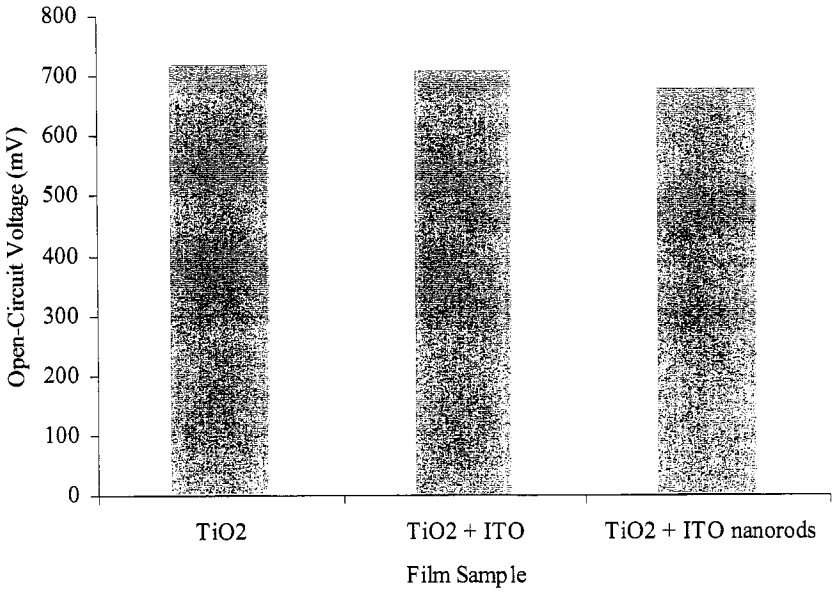

Figure 3.12. Comparison of the open-circuit voltage for films with TiO_2 nanoparticles, TiO_2 nanoparticles and ITO nanoparticles, and TiO_2 nanoparticles and ITO nanorods.

Table 3.2. The open-circuit voltage values obtained for films with TiO_2 nanoparticles, TiO_2 nanoparticles and ITO nanoparticles, and TiO_2 nanoparticles and ITO nanorods.

Film Sample	**V_{oc} (mV)**
TiO_2 nanoparticles	720
TiO_2 + ITO nanoparticles	710
TiO_2 nanoparticles + ITO nanorods	680

3.3.2.2 Short-circuit current density

With the addition of ITO, a change in the short-circuit current density was observed. A higher short-circuit current density was observed with the addition of ITO nanoparticles to TiO_2 nanoparticles. However, the addition of ITO nanorods to TiO_2 nanoparticles resulted in a slight decrease in short-circuit current density. Figure 3.13 is a comparison of the short-circuit current density between TiO_2 nanoparticle film, TiO_2-ITO nanoparticle film, and TiO_2 nanoparticle-ITO nanorod film. Table 3.3 summarizes the actual short-circuit current density values.

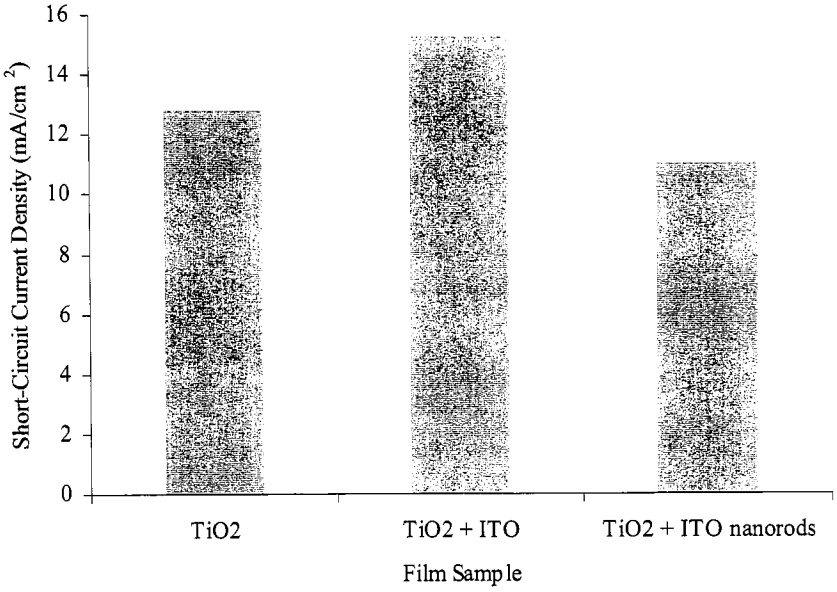

Figure 3.13. Comparison of the short-circuit current density for films with TiO_2 nanoparticles, TiO_2 nanoparticles and ITO nanoparticles, and TiO_2 nanoparticles and ITO nanorods.

Table 3.3. The short-circuit current density values obtained for films with TiO_2 nanoparticles, TiO_2 nanoparticles and ITO nanoparticles, and TiO_2 nanoparticles and ITO nanorods. The differences in the short-circuit current density compared to the TiO_2 nanoparticle film are also shown.

Film Sample	**J_{sc} (mA/cm^2)**	**ΔJ_{sc} (mA/cm^2)**
TiO_2 nanoparticles	12.8	
TiO_2 + ITO nanoparticles	15.3	2.5
TiO_2 nanoparticles + ITO nanorods	11.0	(1.8)

It can be seen that the short-circuit current density increased from ~ 12.8mA/cm^2 to ~ 15.3mA/cm^2 with the addition of ITO nanoparticles. The short-circuit current density increased by ~ 2.5mA/cm^2 when ITO nanoparticles were mixed in with TiO_2 nanoparticles. This could be due to ITO having higher electron mobility and better conductivity than TiO_2, which could be beneficial for more efficient electron transport through the film to the back-contact.

On the other hand, the short-circuit current density slightly decreased from ~ 12.8mA/cm^2 to ~ 11mA/cm^2 with the addition of ITO nanorods. The decrease in short-circuit current density by ~ 1.8mA/cm^2 with ITO nanorods mixed in with TiO_2 nanoparticles may have been due to the difference in structure. The particle packing and contact points may have been slightly affected, where there may have been a slight reduction in particle packing with the addition of rods and smaller contact points between the rods and particles. The differences in short-circuit current density shows that the addition of ITO nanoparticles had more of a positive effect than that of ITO nanorods.

3.3.2.3 Fill factor

Showing the same trend as the open-circuit voltage, the fill factor also remained fairly constant. Figure 3.14 is a comparison of the fill factor values between TiO_2 nanoparticle film, TiO_2-ITO nanoparticle film, and TiO_2 nanoparticle-ITO nanorod film. Table 3.4 summarizes the actual fill factor values. It can be seen that the fill factor remained fairly constant with or without the addition of ITO. The fill factor stayed steady in the range of ~ 52.4% with a deviation of ~ 2.2%. This steady trend is expected since all the films were sintered at 500°C for 60 minutes in an attempt to improve the connectivity

at the contact points between colloidal particles, at the contact points between particles and rods, and at the interface between the substrate and the film. The "squareness" of the I-V curves in Figure 3.11 is also an indication of the fill factor, or how much resistance is in the films. The slight increase in the fill factor with the addition of ITO could be due to ITO having lower resistance and higher conductivity than TiO_2.

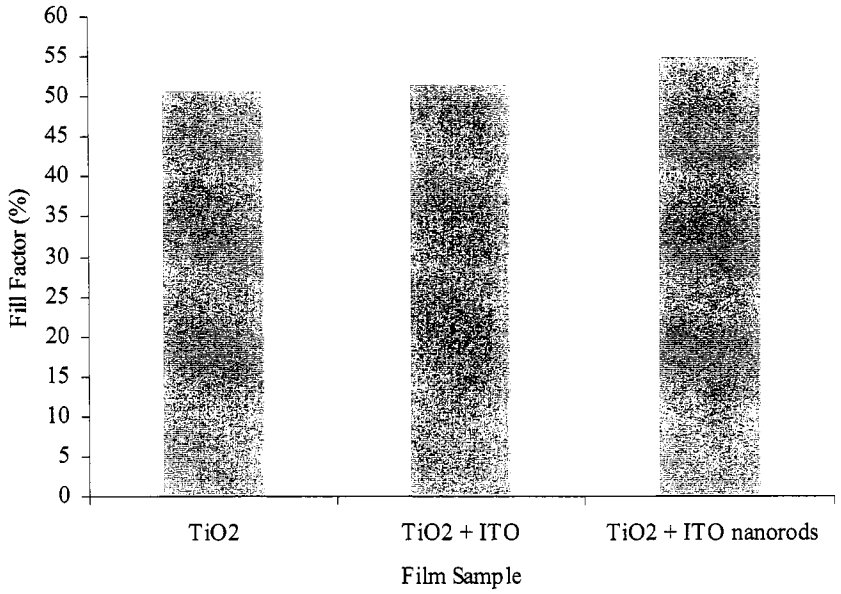

Figure 3.14. Comparison of the fill factor for films with TiO_2 nanoparticles, TiO_2 nanoparticles and ITO nanoparticles, and TiO_2 nanoparticles and ITO nanorods.

Table 3.4. The fill factor values obtained for films with TiO_2 nanoparticles, TiO_2 nanoparticles and ITO nanoparticles, and TiO_2 nanoparticles and ITO nanorods.

Film Sample	**FF (%)**
TiO_2 nanoparticles	50.8
TiO_2 + ITO nanoparticles	51.6
TiO_2 nanoparticles + ITO nanorods	55.0

3.3.2.4 Overall light conversion efficiency

Having a similar trend as the short-circuit current density, a change in the overall efficiency was also observed. A higher overall efficiency was observed with the addition of ITO nanoparticles to TiO_2 nanoparticles. However, the addition of ITO nanorods to TiO_2 nanoparticles resulted in a slight decrease in overall efficiency. Figure 3.15 is a comparison of the overall efficiency between TiO_2 nanoparticle film, TiO_2-ITO nanoparticle film, and TiO_2 nanoparticle-ITO nanorod film. Table 3.5 summarizes the actual overall efficiency values. It can be seen that the overall efficiency increased from ~ 4.7% to ~ 5.6% with the addition of ITO nanoparticles. The overall efficiency increased by ~ 1% when ITO nanoparticles were mixed in with TiO_2 nanoparticles.

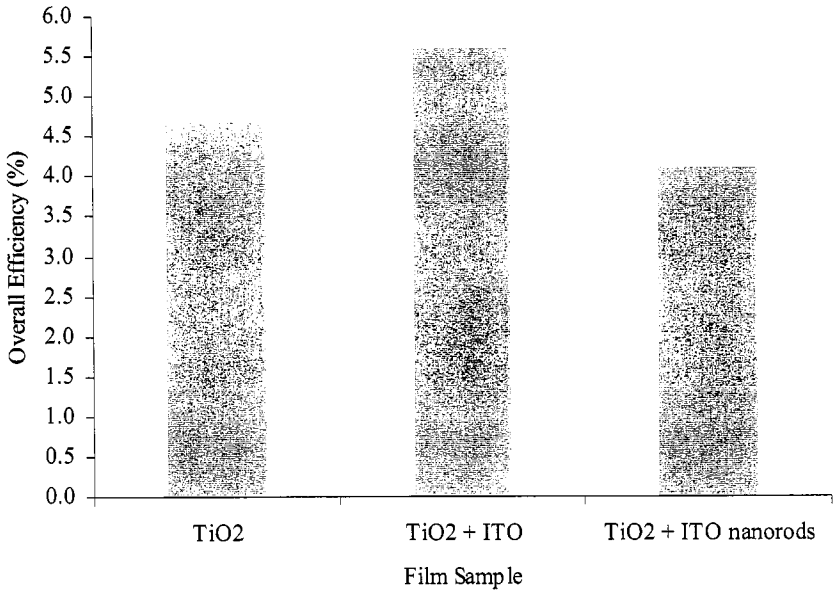

Figure 3.15. Comparison of the overall efficiency for films with TiO_2 nanoparticles, TiO_2 nanoparticles and ITO nanoparticles, and TiO_2 nanoparticles and ITO nanorods.

On the other hand, the overall efficiency slightly decreased from ~ 4.7% to ~ 4.1% with the addition of ITO nanorods, resulting in the overall efficiency decreasing by

~ 0.6%. Since the short-circuit current density increased with the addition of ITO nanoparticles, as previously shown, the overall efficiency also increased. A slight decrease in the short-circuit current density with the addition of ITO nanorods, as shown previously, also resulted in a slight decrease in the overall efficiency. The differences in overall efficiency, similar to that of the short-circuit current density, show that the addition of ITO nanoparticles had more of a positive effect on the short-circuit current density than that of ITO nanorods.

Table 3.5. The overall efficiency values obtained for films with TiO_2 nanoparticles, TiO_2 nanoparticles and ITO nanoparticles, and TiO_2 nanoparticles and ITO nanorods. The differences in the overall efficiency compared to the TiO_2 nanoparticle film are also shown.

Film Sample	**η (%)**	**$\Delta\eta$ (%)**
TiO_2 nanoparticles	4.68	
TiO_2 + ITO nanoparticles	5.60	0.9
TiO_2 nanoparticles + ITO nanorods	4.11	(0.6)

3.3.3 Solar cell performance of TiO_2-ITO nanocomposite films on conductive ITO substrates

Additional comparisons were made by observing the photoresponse of TiO_2 films on ITO. Since ITO sol was used for the attachment of ITO nanorod arrays to the substrate, ITO substrates were used to aid in the attachment of these nanorod arrays. The use of ITO substrates would help improve the bonding of the nanorods to the substrate surface since the sol, nanorods, and substrate all had similar ITO compositions.

Two types of nanocomposite films were prepared on ITO: 1) TiO_2 nanoparticles with ITO nanoparticles, and 2) ITO nanorod arrays with a layer of TiO_2 coating. Solar cells with these films were assembled and tested under illumination with 100mW/cm^2 intensity, and compared to films with only TiO_2 nanoparticles. Table 3.6 summarizes the

measured and calculated values obtained from the I-V curves of each solar cell consisting of 1) TiO_2 nanoparticle film, 2) TiO_2-ITO nanoparticle film, and 3) TiO_2-coated ITO nanorod array film. Figure 3.16 compares the I-V characteristics of each solar cell.

Table 3.6. The measured and calculated values obtained from the I-V curves for each solar cell consisting TiO_2 nanoparticle, TiO_2-ITO nanoparticle, and TiO_2-coated ITO nanorod array films.

Film on ITO	**V_{oc} (mV)**	**J_{sc} (mA/cm^2)**	**V_{max} (mV)**	**J_{max} (mA/cm^2)**	**FF (%)**	**P_{max} (mW/cm^2)**	**P_{in} (mW/cm^2)**	**η (%)**
TiO_2 nanoparticles	660	15.9	350	10.3	34.4	3.61	100	3.61
TiO_2 nanoparticles ITO nanoparticles	660	19.7	410	10.3	32.5	4.22	100	4.22
ITO nanorod arrays TiO_2 coating	530	4.20	310	2.69	37.5	0.83	100	0.83

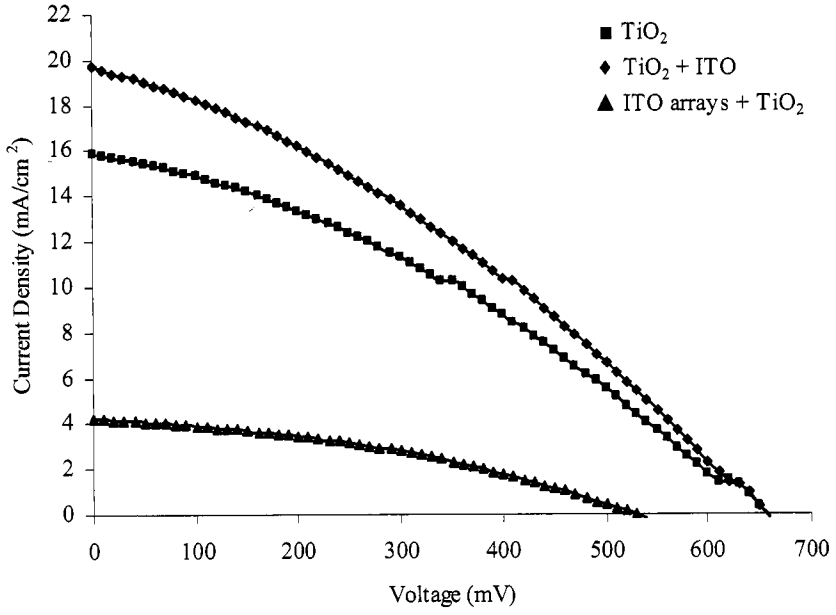

Figure 3.16. Plot and comparison of the I-V characteristics for each solar cell consisting of TiO_2 nanoparticle, TiO_2-ITO nanoparticle, and TiO_2-coated ITO nanorod array films.

It can be seen that the short-circuit current density increased with the addition of ITO nanoparticles, but dramatically decreased with the presence of ITO nanorods. The most notable difference is in the short-circuit current density and in the overall light conversion efficiency. In addition, the I-V curves are shown to be more linear than expected, showing higher resistance in the films. A closer look at the trends comparing open-circuit voltage, short-circuit current density, fill factor, and overall efficiency is detailed in the following sections.

3.3.3.1 Open-circuit voltage

The open-circuit voltage stayed the same between TiO_2 nanoparticle film and TiO_2-ITO nanoparticle film. However, the open-circuit voltage decreased with ITO nanorod arrays. Figure 3.17 is a comparison of open-circuit voltage values between TiO_2 nanoparticle film, TiO_2-ITO nanoparticle film, and TiO_2-coated ITO nanorod array film. Table 3.7 summarizes the actual open-circuit voltage values. It can be seen that the open-circuit voltage remained the same with and without ITO nanoparticles with the value of ~ 660mV. With the ITO nanorod arrays, the open-circuit voltage decreased to ~ 530mV. This shows that the amount of TiO_2 may have been insufficient since the lower open-circuit voltage indicated a difference in the surface chemistry.

In addition, the decrease in the open-circuit voltage could have been due to incomplete burnout of the polycarbonate membrane used to fabricate the ITO nanorod arrays. Excess amounts of carbon on the surface of the ITO nanorods may have altered the surface chemistry, resulting in a lowered open-circuit voltage. Furthermore, in general, the open-circuit voltage of the TiO_2 nanoparticle and TiO_2-ITO nanoparticle

films on ITO substrates was shown to be slightly lower in value than that on FTO substrates. This trend will be discussed in later sections.

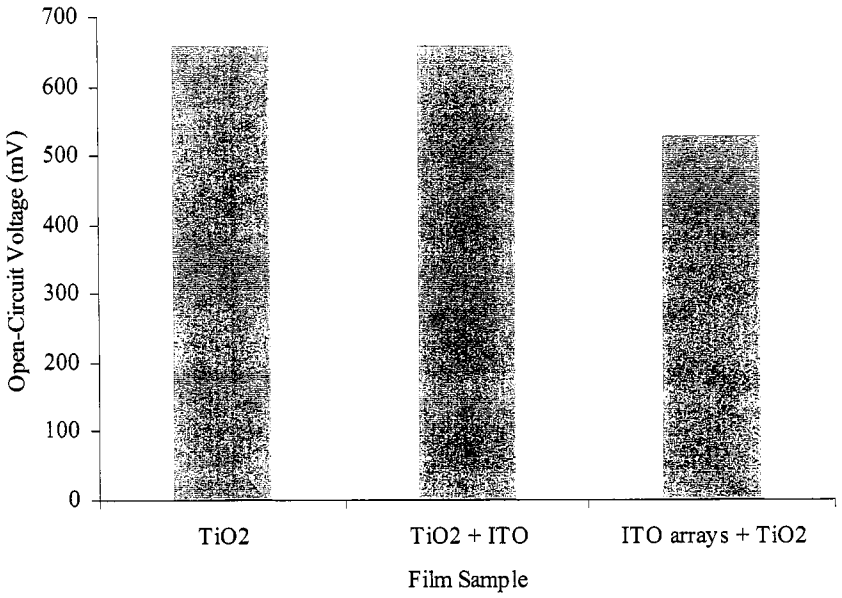

Figure 3.17. Comparison of the open-circuit voltage for films with TiO_2 nanoparticles, TiO_2-ITO nanoparticles, and TiO_2-coated ITO nanorod arrays.

Table 3.7. The open-circuit voltage values obtained for films with TiO_2 nanoparticles, TiO_2-ITO nanoparticles, and TiO_2-coated ITO nanorod arrays.

Film Sample	**V_{oc} (mV)**
TiO_2 nanoparticles	660
TiO_2 + ITO nanoparticles	660
ITO nanorods + TiO_2 coating	530

3.3.3.2 Short-circuit current density

A change in the short-circuit current density was also observed for films prepared on ITO substrates. A higher short-circuit current density was observed with the addition of ITO nanoparticles to TiO_2 nanoparticles. However, the use of ITO nanorod arrays resulted in a dramatic decrease in short-circuit current density. Figure 3.18 is a

comparison of the short-circuit current density between TiO_2 nanoparticle film, TiO_2-ITO nanoparticle film, and TiO_2-coated ITO nanorod arrays. Table 3.8 summarizes the actual short-circuit current density values. It can be seen that the short-circuit current density increased from ~ 15.9mA/cm^2 to ~ 19.7mA/cm^2 with the addition of ITO nanoparticles. The short-circuit current density increased by ~ 3.8mA/cm^2 when ITO nanoparticles were mixed in with TiO_2 nanoparticles.

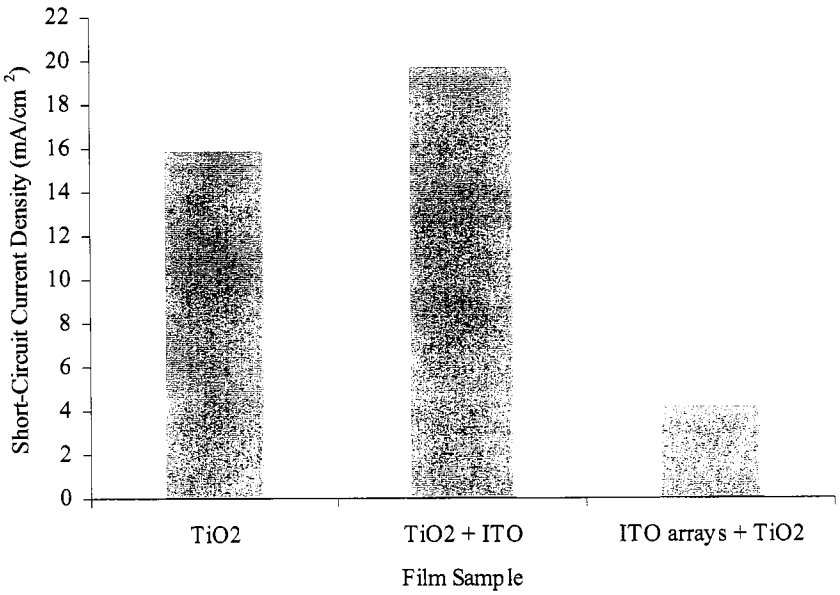

Figure 3.18. Comparison of the short-circuit current density for films with TiO_2 nanoparticles, TiO_2-ITO nanoparticles, and TiO_2-coated ITO nanorod arrays.

Table 3.8. The short-circuit current density values obtained for films with TiO_2 nanoparticles, TiO_2-ITO nanoparticles, and TiO_2-coated ITO nanorod arrays. The differences in the short-circuit current density compared to the TiO_2 nanoparticle film are also shown.

Film Sample	**J_{sc} (mA/cm^2)**	**ΔJ_{sc} (mA/cm^2)**
TiO_2 nanoparticles	15.9	
TiO_2 + ITO nanoparticles	19.7	3.8
ITO nanorods + TiO_2 coating	4.20	(11.7)

As previously mentioned, ITO having higher electron mobility and better conductivity than TiO_2 could have improved the short-circuit current density. On the other hand, the short-circuit current density dramatically decreased from ~ 15.9mA/cm^2 to ~ 4.2mA/cm^2 with the use of ITO nanorod arrays. The large decrease in short-circuit current density by ~ 11.7mA/cm^2 may have been due to the insufficient amount of TiO_2 on the surface of the nanorods. In addition, the structure of the nanorod arrays, as shown in the Figure 3.7, may have prevented the incorporation of a uniform coating of TiO_2, resulting in a decrease in the short-circuit current density. In general, the short-circuit current density of the TiO_2 nanoparticle and TiO_2-ITO nanoparticle films on ITO substrates was shown to be higher in value than that on FTO substrates. This trend will be discussed in later sections.

3.3.3.3 Fill factor

The fill factor remained fairly constant between the three different types of film. Figure 3.19 is a comparison of the fill factor values between TiO_2 nanoparticle film, TiO_2-ITO nanoparticle film, and TiO_2-coated ITO nanorod array film. Table 3.9 summarizes the actual fill factor values. It can be seen that the fill factor remained fairly constant with or without the addition of ITO. The fill factor stayed steady in the range of ~ 34.8% with a deviation of ~ 2.5%. The low value of fill factor can be seen in the I-V curves in Figure 3.16. The linearity of the I-V curves indicates a low fill factor, which can be caused by the high resistance in the film or in the substrate. The fill factor of the TiO_2 nanoparticle and TiO_2-ITO nanoparticle films on ITO substrates was shown to be lower in value than that on FTO substrates. This trend will be discussed in later sections.

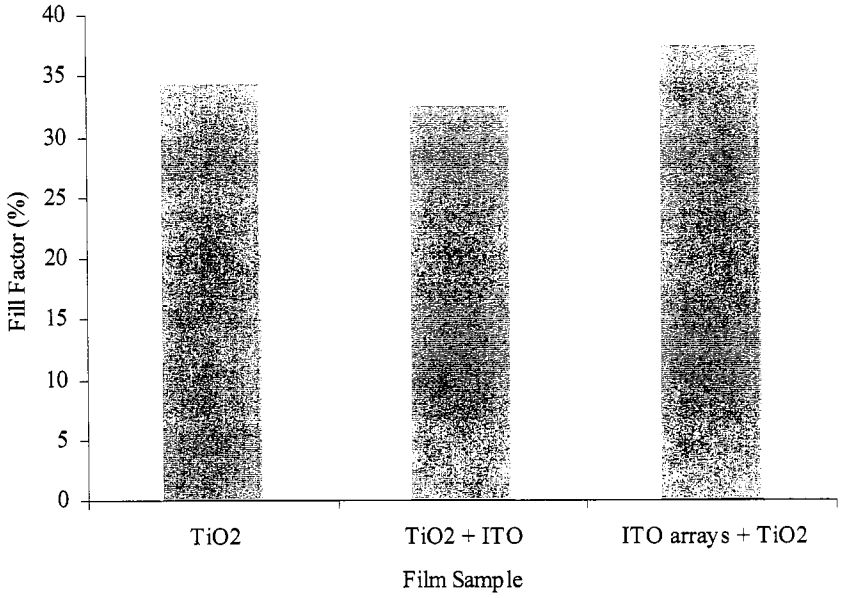

Figure 3.19. Comparison of the fill factor for films with TiO_2 nanoparticles, TiO_2-ITO nanoparticles, and TiO_2-coated ITO nanorod arrays.

Table 3.9. The fill factor values obtained for films with TiO_2 nanoparticles, TiO_2-ITO nanoparticles, and TiO_2-coated ITO nanorod arrays.

Film Sample	**FF (%)**
TiO_2 nanoparticles	34.4
TiO_2 + ITO nanoparticles	32.5
ITO nanorods + TiO_2 coating	37.5

3.3.3.4 Overall light conversion efficiency

Correlating with the short-circuit current density, a change in the overall efficiency was also observed. A higher overall efficiency was observed with the addition of ITO nanoparticles to TiO_2 nanoparticles. However, the use of ITO nanorod arrays resulted in a large decrease in overall efficiency. Figure 3.20 is a comparison of the overall efficiency between TiO_2 nanoparticle film, TiO_2-ITO nanoparticle film, and TiO_2-coated ITO nanorod array film. Table 3.10 summarizes the actual overall efficiency

values. It can be seen that the overall efficiency increased from ~ 3.6% to ~ 4.2% with the addition of ITO nanoparticles. The overall efficiency increased by ~ 0.6% when ITO nanoparticles were mixed in with TiO_2 nanoparticles.

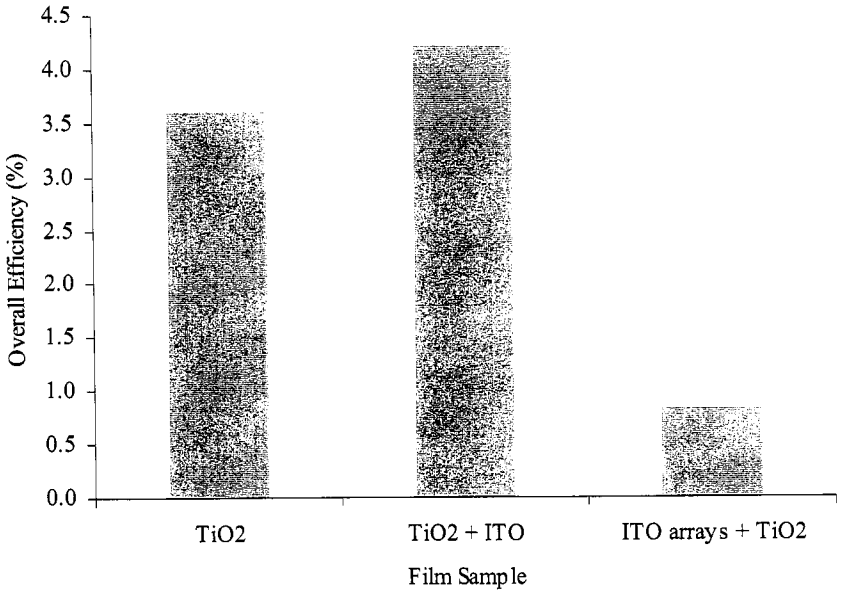

Figure 3.20. Comparison of the overall efficiency for films with TiO_2 nanoparticles, TiO_2-ITO nanoparticles, and TiO_2-coated ITO nanorod arrays.

Table 3.10. The overall efficiency values obtained for films with TiO_2 nanoparticles, TiO_2-ITO nanoparticles, and TiO_2-coated ITO nanorod arrays. The differences in the overall efficiency compared to the TiO_2 nanoparticle film are also shown.

Film Sample	**η (%)**	**$\Delta\eta$ (%)**
TiO_2 nanoparticles	3.61	
TiO_2 + ITO nanoparticles	4.22	0.6
ITO nanorods + TiO_2 coating	0.83	(2.8)

On the other hand, the overall efficiency slightly decreased from ~ 3.6% to ~ 0.8% using the TiO_2-coated ITO nanorod arrays, resulting in the overall efficiency decreasing by ~ 2.8%. Since the short-circuit current density increased with the addition of ITO nanoparticles, as previously shown, the overall efficiency also increased. A large

decrease in the short-circuit current density using the TiO_2-coated ITO nanorod arrays, as shown previously, also resulted in a large decrease in the overall efficiency. The differences in overall efficiency, similar to that of the short-circuit current density, show that the addition of ITO nanoparticles had more of a positive effect on the short-circuit current density than that of ITO nanorod arrays. In addition, the overall efficiency of the TiO_2 nanoparticle and TiO_2-ITO nanoparticle films on ITO substrates was shown to be lower in value than that on FTO substrates. This trend will be discussed in later sections.

3.3.4 Comparison of I-V characteristics using FTO and ITO substrates

From the previous sections, it was shown that the open-circuit voltage, short-circuit current density, fill factor, and overall light conversion efficiency values were different for the TiO_2 nanoparticle and TiO_2-ITO nanoparticle films on FTO substrates, as compared to those films on ITO substrates. It was shown that the open-circuit voltage, fill factor, and overall efficiency values were higher using FTO substrates. However, using ITO substrates resulted in higher short-circuit current density values. The following sections detail the differences in values.

3.3.4.1 Open-circuit voltage

It was shown that the open-circuit voltage of films on FTO substrates was slightly higher than that of films on ITO substrates. Figure 3.21 shows the plot comparing the open-circuit voltage for TiO_2 nanoparticle and TiO_2-ITO nanoparticle films prepared on FTO substrates and ITO substrates. It can be seen that the open-circuit voltage is higher for both films when prepared on FTO substrates. This difference in open-circuit voltage

could be due to the difference in the quality of the film. However, the change in the open-circuit voltage is small enough that the values can be considered very similar.

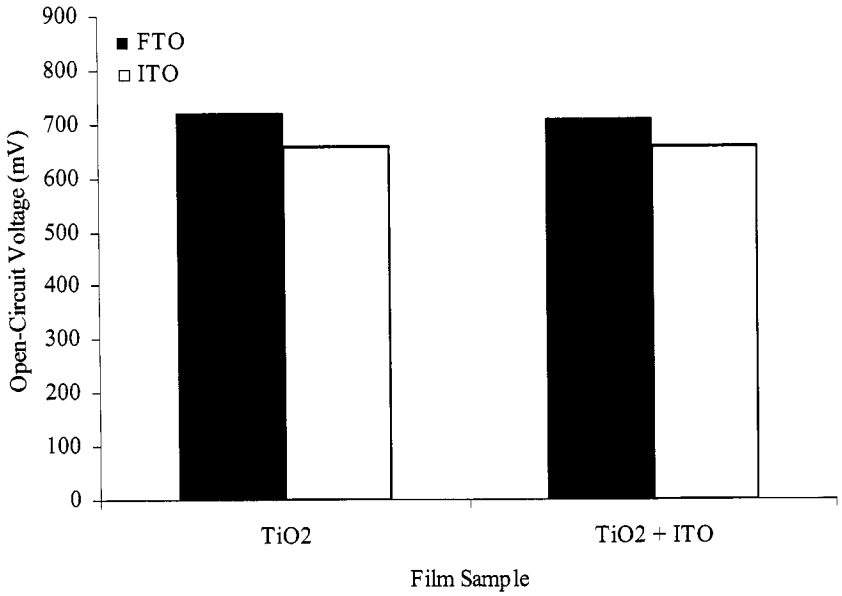

Figure 3.21. Comparison of the open-circuit voltage for films with TiO_2 nanoparticles and TiO_2-ITO nanoparticles on FTO and ITO substrates.

3.3.4.2 Short-circuit current density

For the short-circuit current density, it was shown that the films on FTO substrates had lower short-circuit current density than that on ITO substrates. Figure 3.22 is a plot comparing the short-circuit current density for TiO_2 nanoparticle and TiO_2-ITO nanoparticle films on FTO and ITO substrates. It can be seen that the short-circuit current density is higher for both films when prepared on ITO substrates. This could be due to better bonding at the film and substrate interface. When preparing the films, it was more difficult to form the films on FTO substrates than it was to form the films on ITO substrates even though both types of substrates were hydrolyzed in boiling DI-H_2O. Therefore, the adhesion of the film to the FTO substrates may not have been as good,

reducing the amount of material. In addition, the reduction of material may cause a reduction in the surface area and the amount of dye adsorption, which would affect the number of electrons generated.

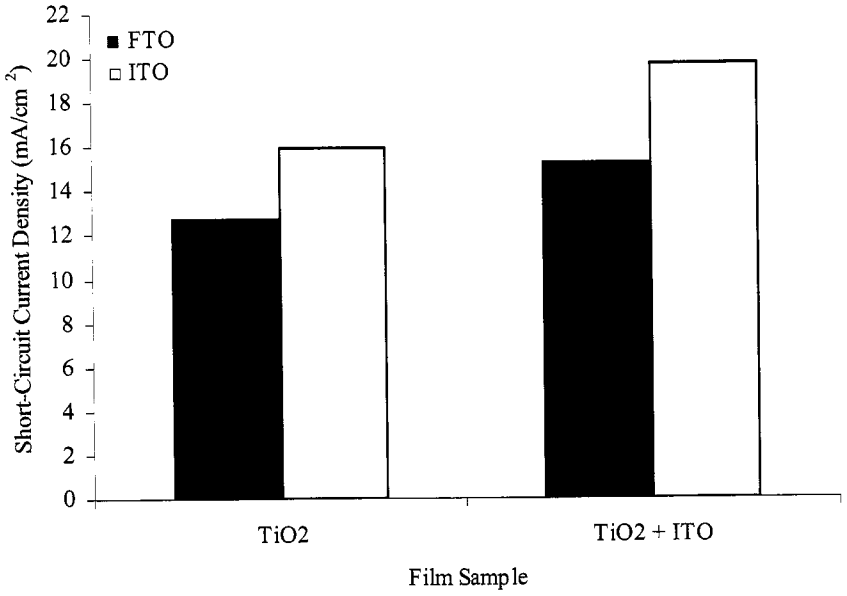

Figure 3.22. Comparison of the short-circuit current density for films with TiO_2 nanoparticles and TiO_2-ITO nanoparticles on FTO and ITO substrates.

3.3.4.3 Fill factor

As for the fill factor, it was shown that the films on FTO substrates had higher fill factor values than that on ITO substrates. Figure 3.23 is a plot comparing the fill factor for TiO_2 nanoparticle and TiO_2-ITO nanoparticle films on FTO and ITO substrates. It can be seen that the fill factor is higher for both films when prepared on FTO substrates.

As previously mentioned, the fill factor represents the "squareness" of the I-V curves, or in other words, describes the resistance of the film and substrate. With ITO substrates, it has been shown that the resistance increases from ~ 25 ohm/cm to over 100

ohm/cm after sintering to 500°C. However, this behavior is negligible with FTO substrates, where the resistance stays at ~ 25 ohm/cm before and after sintering to 500°C. Therefore, the increase in resistance associated with the ITO substrates had a large influence on the linearity of the I-V curves. When comparing Figure 3.11 and Figure 3.16, the I-V curves for the films on FTO substrates are more "square" than that for films on ITO substrates. The greater linearity in the I-V curves indicate higher resistance and thus result in lower fill factor values.

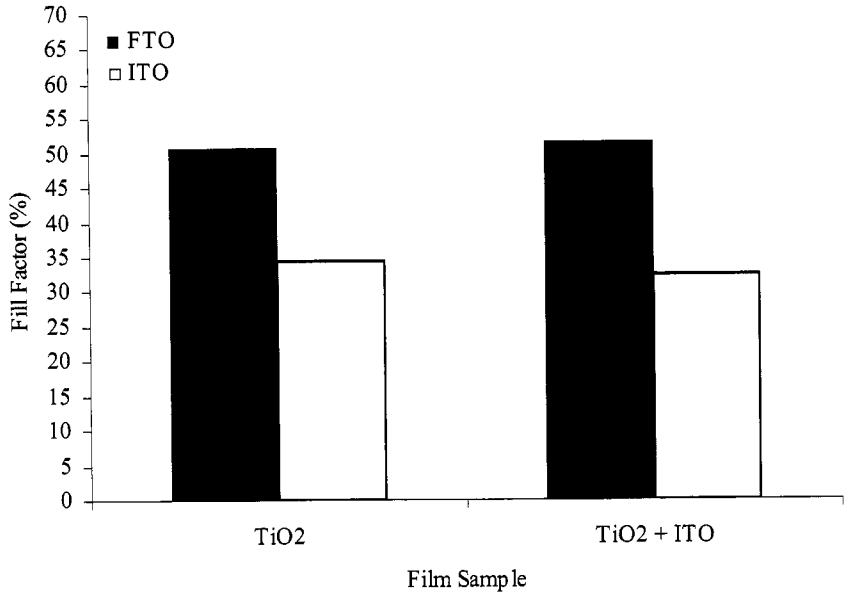

Figure 3.23. Comparison of the fill factor for films with TiO_2 nanoparticles and TiO_2-ITO nanoparticles on FTO and ITO substrates.

3.3.4.4 Overall light conversion efficiency

With the overall efficiency, it was shown that the films on FTO substrates had higher values than that on ITO substrates. Figure 3.24 is a plot comparing the overall efficiency for TiO_2 nanoparticle and TiO_2-ITO nanoparticle films on FTO and ITO

substrates. It can be seen that the overall efficiency is higher for both films when prepared on FTO substrates. Although the short-circuit current density was higher for both types of films on ITO substrates, the overall efficiency was lower since the overall efficiency is dependent on the open-circuit voltage and fill factor, in addition to the short-circuit current density. It was shown that the open-circuit voltage and fill factor was higher for both types of films on FTO substrates, which most likely factored into the higher overall efficiency. In addition, the higher electron mobility[131] of ITO ~ 40-70cm^2/Vs, as compared to the electron mobility[135] of FTO ~ 9.3-11.8cm^2/Vs, may have played a role in the higher short-circuit current density using ITO substrates. However, the better thermal stability of FTO may have factored into the higher fill factor using FTO substrates.

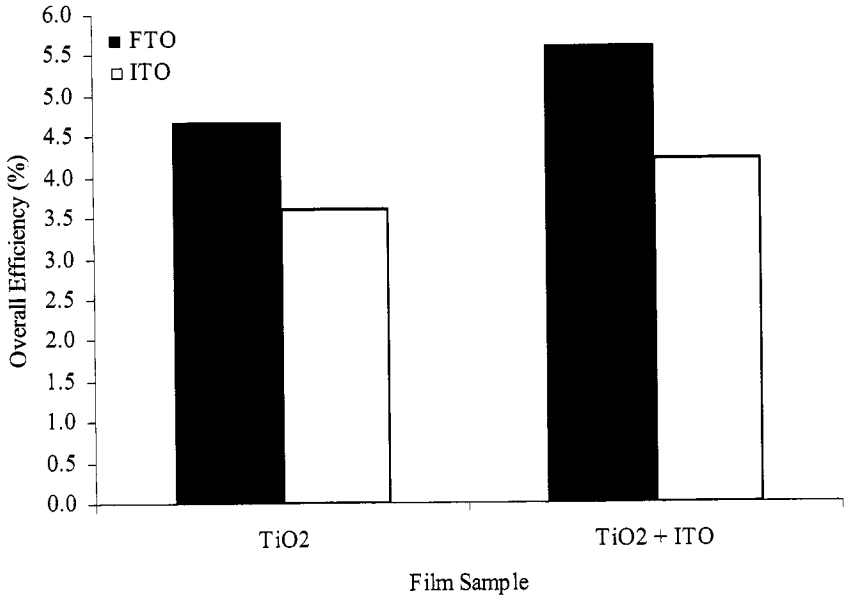

Figure 3.24. Comparison of the overall efficiency for films with TiO_2 nanoparticles and TiO_2-ITO nanoparticles on FTO and ITO substrates.

3.3.5 Characterization of TiO_2-ITO nanocomposite films

Since the short-circuit current density and the overall efficiency values differed between the TiO_2 nanoparticle film with ITO nanoparticles, the TiO_2 nanoparticle film with ITO nanorods, and the ITO nanorod arrays with TiO_2 coating, SEM analysis was performed in an attempt to compare the top morphology of each prepared TiO_2-ITO nanocomposite film. The following sections detail the structure for films with 1) TiO_2-ITO nanoparticles, 2) TiO_2 nanoparticles-ITO nanorods, and 3) TiO_2-coated ITO nanorod arrays to explain the differences in solar cell performance.

3.3.5.1 TiO_2 nanoparticle film with ITO nanoparticles

As previously mentioned, it was shown that the TiO_2 nanoparticle film with the addition of ITO nanoparticles had a higher short-circuit current density and overall efficiency when compared to the TiO_2 nanoparticle film. Figure 3.25 shows the SEM images of the TiO_2-ITO nanoparticle film. It can be seen that the film is highly porous, but it was difficult to distinguish TiO_2 and ITO nanoparticles since the amount of ITO nanoparticles is much smaller. It is expected that the TiO_2 nanoparticles are more prevalent than the ITO nanoparticles.

Figure 3.26 shows the TiO_2-ITO film at a higher magnification. With closer imaging, it can be seen that the nanoparticles are fused together to form a network of particles. In addition, smaller particles are seen to form clusters. It was difficult to compare the structure with the TiO_2 nanoparticle film, as previously shown, because of the small particle size, but the TiO_2-ITO nanoparticle film looks very similar in structure. Agglomeration and clustering of particles occurred for both films after sintering. The

addition of ITO may have been the reason for the higher short-circuit current density and overall efficiency due to ITO having a higher electron mobility.

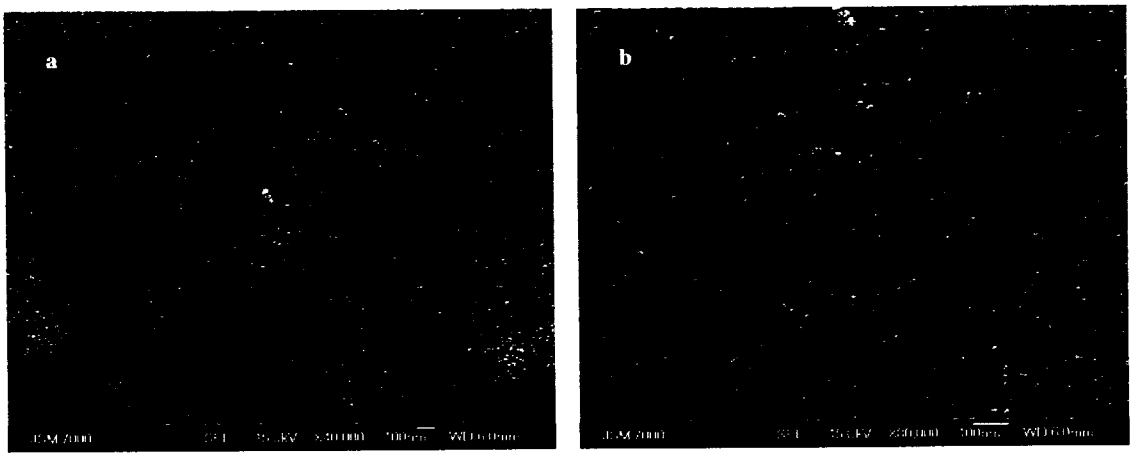

Figure 3.25. SEM images of TiO_2 nanoparticle film with the addition of ITO nanoparticles at a) 40,000X and b) 80,000X magnification.

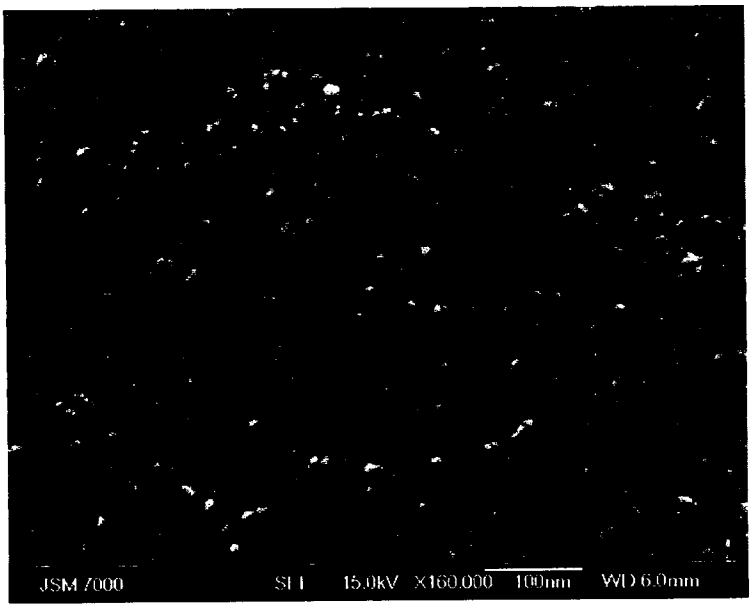

Figure 3.26. SEM image of TiO_2 nanoparticle film with the addition of ITO nanoparticles at 160,000X magnification.

3.3.5.2 TiO_2 nanoparticle film with ITO nanorods

It was also shown that the TiO_2 nanoparticle film with the addition of ITO nanorods, when compared with the TiO_2 nanoparticle film, had a lower short-circuit current density and overall efficiency. Figure 3.27 shows the SEM image of the TiO_2 nanoparticle film with the addition of ITO nanorods. It can be seen that the film is not as porous, where the majority of the particles are fused together to form an almost complete film, when compared to the TiO_2 nanoparticle film, as previously shown.

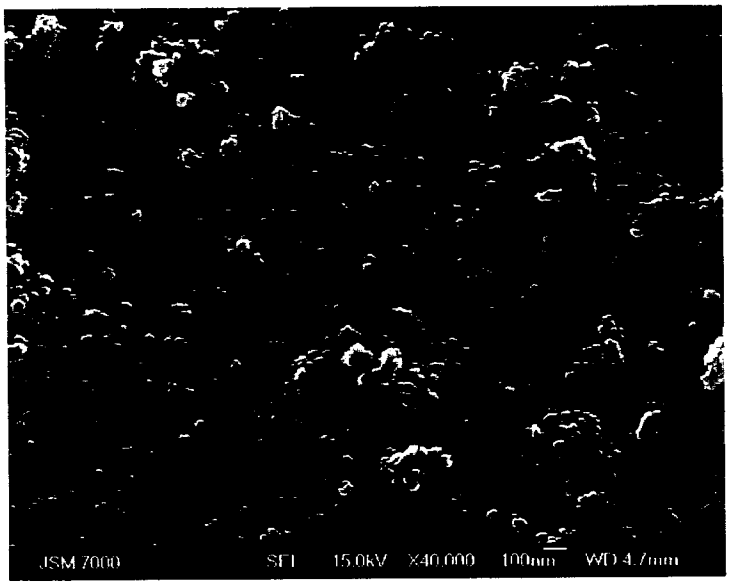

Figure 3.27. SEM image of TiO_2 nanoparticle film with the addition of ITO nanorods at 40,000X magnification. It can be seen that the ITO nanorods are not visible.

It is also observed that the ITO nanorods are not visible. This could be due to the nanorods being imbedded within the TiO_2 nanoparticle film after sintering, or possibly underneath the TiO_2 nanoparticle film. The lower short-circuit current density and the lower overall efficiency with the addition of ITO nanorods may have been due to the reduction in porosity or the presence of broken nanorods. In addition, if the nanorods are

underneath the TiO_2 nanoparticle film, it may have increased the resistance between the TiO_2 nanoparticle film and the underlying substrate, reducing the short-circuit current density. In addition, the lack of intermixing of nanoparticles and nanorods may have also played a role in the lowered short-circuit current density.

3.3.5.3 ITO nanorod arrays with a layer of TiO_2 coating

The film with TiO_2-coated ITO nanorod arrays had much lower short-circuit current density and overall efficiency, when compared to the TiO_2 nanoparticle film, the TiO_2-ITO nanoparticle film, and the TiO_2 nanoparticle film with ITO nanorods. This may have been due to an insufficient amount of TiO_2 coating on the surface of the nanorods. Figure 3.28 shows the SEM images of the ITO nanorods with an additional TiO_2 coating.

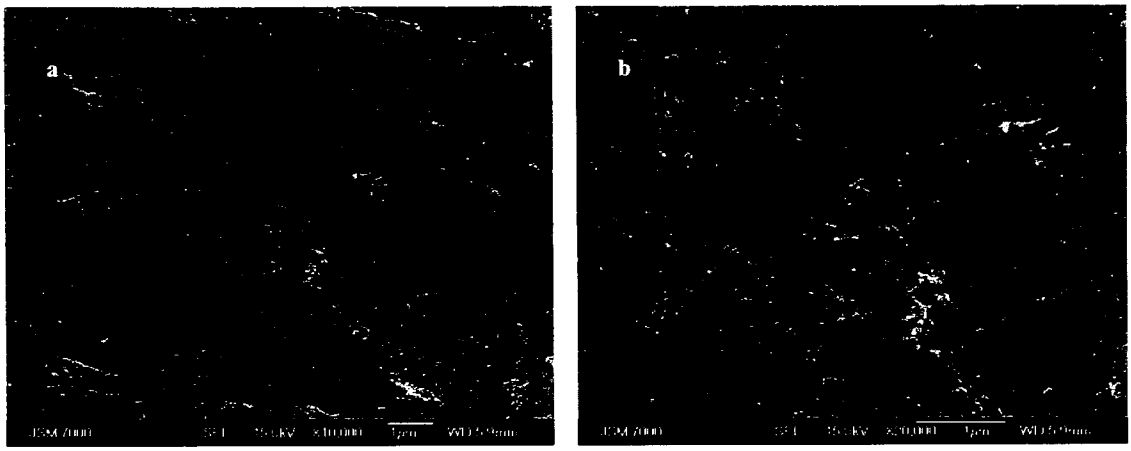

Figure 3.28. SEM images of ITO nanorod arrays with the addition of TiO_2 coating at a) 10,000X and b) 20,000X magnification.

It can be seen that the nanorods collapsed and were not perpendicular to the substrate, as in the ideal case. The nanorods were randomly scattered throughout the substrate and did not have an ordered arrangement. In addition, it can be seen that the

ITO nanorods were not completely coated. Small islands of TiO_2 were present. This incomplete coverage of TiO_2 and the randomness of the ITO nanorods may have caused the reduction in the short-circuit current density and overall efficiency. The photoresponse of the TiO_2-coated ITO nanorod arrays did indicate that TiO_2 was present since ITO does not have the same photovoltage effect under illumination, but the lower short-circuit current density indicated that an insufficient amount was present.

In order to confirm that the islands on the surface of the ITO nanorods were indeed TiO_2, EDS analysis was performed. Figure 3.29 shows the SEM image of the ITO nanorods at a higher magnification and the correlating EDS spectra.

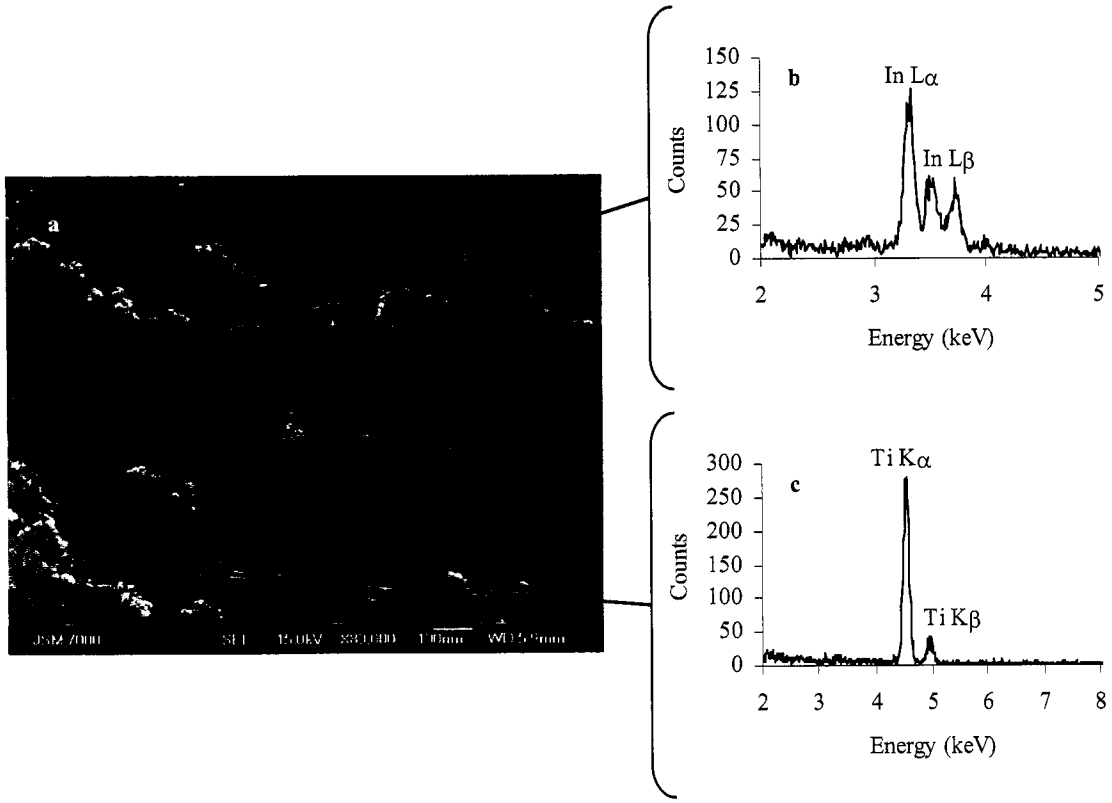

Figure 3.29. SEM image a) of the TiO_2-coated ITO nanorod arrays at 80,000X. The correlating EDS spectrum of b) an island of TiO_2 coating, and c) a section of the ITO nanorod are also shown.

It can be seen that the islands are TiO_2, as shown by the presence of Ti Kα and Ti Kβ at ~ 4.5keV and ~ 5.0keV, respectively, in the EDS spectrum. In addition, the EDS spectrum of the ITO nanorods shows the presence of In Lα and In Lβ at ~ 3.3keV and ~ 3.5-3.7keV, respectively. It was also observed that the surface of the ITO nanorods also had the presence of Pt from the sputter coat ~ 18nm in size to improve the SEM imaging by improving the conductivity. This was evident from EDS analysis, but is not included in either EDS spectra in Figure 3.29.

3.3.6 Comparison of data to examine improvement in solar cell performance

By incorporating ITO nanoparticles into the TiO_2 nanoparticle film, it was observed that the short-circuit current density increased from ~ 12.8mA/cm^2 to ~ 15.3mA/cm^2. In addition, the incorporation of the ITO nanoparticles into the TiO_2 nanoparticle film increased the overall efficiency from ~ 4.7% to ~ 5.6%. The addition of 20 wt% ITO increased the efficiency by almost 1%, which could be due to the higher electron mobility of ITO. This 19% improvement in the overall efficiency is a considerable improvement considering the increase in the overall efficiency of dye-sensitized solar cells has been slow, typically < 1% with every improvement in the solar cell. As previously mentioned, changing the sensitizer dye from the standard N3 "red" dye to a "black" dye that absorbs ~ 100nm more of the light improved the efficiency from ~ 10% to ~ 10.4%. By adding additives to the electrolyte to improve the assembly of standard N3 dye, the efficiency improved from ~ 10% to ~ 11%. Therefore, the improvement of the efficiency of the TiO_2 nanoparticle film with the addition of ITO nanoparticles does show great potential for further increasing the overall efficiency.

3.4 Conclusions

In summary, TiO_2-ITO nanocomposite films were prepared to compare the solar cell performance of films with the addition of various ITO nanostructures. Solar cells consisting of 1) TiO_2 nanoparticle film with ITO nanoparticles, 2) TiO_2 nanoparticle film with ITO nanorods, and 3) ITO nanorod arrays with a layer of TiO_2 coating were fabricated and tested under illumination. Sol-gel processing was used to successfully fabricate ITO nanoparticles and template-assisted electrophoretic deposition was used to successfully grow ITO nanorods.

In conclusion, it was found that the addition of ITO nanoparticles to the TiO_2 nanoparticle film increased the short-circuit current density and overall light conversion efficiency. The TiO_2 nanoparticle film was shown to have a short-circuit current density of ~ 12.8mA/cm^2 and an overall efficiency of ~ 4.7%. The TiO_2-ITO nanocomposite film was shown to have a higher short-circuit current density of ~ 15.3mA/cm^2 and a higher overall efficiency of ~ 5.6%. With the addition of ITO nanoparticles, the short-circuit current density increased by ~ 2.5mA/cm^2 and the overall efficiency increased by ~ 1%, showing a 19% improvement in the efficiency. This increase may have been due to the higher electron mobility associated with ITO, enhancing the charge transport properties.

However, the addition of ITO nanorods reduced the short-circuit current density and the overall light conversion efficiency. This reduction may have been due to 1) the insufficient intermixing of the nanoparticles and nanorods, 2) the higher internal resistance associated with the nanorod structure, and 3) the incomplete surface coverage of TiO_2 on the nanorod array surface.

Notes to Chapter 3

[128] Y.H. Tak, K.B. Kim, H.G. Park, K.H. Lee, and J.R. Lee, "Criteria for ITO (indium-tin-oxide) thin film as the bottom electrode of an organic light emitting diode," *Thin Solid Films* **411**, 12 (2002).

[129] N. Ozer, F. Tepehan, and N. Bozkurt, "An 'all-gel' electrochromic device," *Thin Solid Films* **219**, 193 (1992).

[130] B. Kannan, K. Castelino, and A. Majumdar, "Design of Nanostructured Heterojunction Polymer Photovoltaic Devices," *Nanoletters* **3**, 1729 (2003).

[131] D. Mergel, M. Schenkel, M. Ghebre, and M. Sulkowski, "Structural and electrical properties of In_2O_3:Sn films prepared by radio-frequency sputtering," *Thin Solid Films* **392**, 91 (2001).

[132] S.J. Limmer, S.V. Cruz, and G.Z. Cao, "Films and nanorods of transparent conducting oxide ITO by a citric acid sol route," *Applied Physics A* **79**, 421 (2004).

[133] S.J. Limmer, S. Seraji, M.J. Forbess, Y. Wu, T.P. Chou, C. Nguyen, and G.Z. Cao, "Template-Based Growth of Various Oxide Nanorods by Sol-Gel Electrophoresis," *Advanced Functional Materials* **12**, 59-64 (2002).

[134] T.L. Wen, J. Zhang, T.P. Chou, S.J. Limmer, and G.Z. Cao, "Template-Based Growth of Oxide Nanorod Arrays by Centrifugation," *Journal of Sol-Gel Science and Technology* **33**, 193 (2005).

[135] A.E. Rakhshani, Y. Makdisi, and H.A. Ramazaniyan, "Electronic and optical properties of fluorine-doped tin oxide films," *Journal of Applied Physics* **83**, 1049 (1998).

4 Dye-sensitized solar cells with ZnO nanoparticles and nanowires

4.1 Introduction

Zinc oxide (ZnO) has recently been explored as an alternative material in dye-sensitized solar cells. The reasons behind this increase in research include 1) ZnO having a band gap similar to that for TiO_2 at 3.2eV, and 2) ZnO having a much higher electron mobility ~ 115-155cm^2/Vs than that for anatase TiO_2, which is ~ $10^{-5}cm^2$/Vs, as previously mentioned. Using ZnO as the semiconductor electrode has the greatest potential as an alternative material for improving the solar cell performance in dye-sensitized solar cells due to a few advantages. These include: 1) higher electron mobility than that for TiO_2, 2) simpler tailoring of the nanostructure as compared to TiO_2, and 3) easier growth of single-crystalline ZnO nanowires to eliminate any barriers to electron transport typically found in polycrystalline material. The greater potential for increasing the surface area of ZnO through surface structure modification, in conjunction with a higher electron mobility associated with the ZnO material, could provide a promising means for improving the solar cell performance of dye-sensitized solar cells.

It has been shown that the surface structure, the particle size and shape, and the porosity are all important factors for optimizing the solar cell performance of dye-sensitized solar cells. With ZnO, these factors can easily be tailored through the modification of solution growth and wet-chemical methods, which is not feasible for the fabrication of TiO_2 films. There have been studies on dye-sensitized ZnO solar cells with ZnO nanoparticles, where the surface structure and crystallinity can be easily modified through the use of aqueous solution methods to increase the surface area. In addition,

dye-sensitized solar cells consisting of a dense array of oriented, crystalline ZnO nanowires have been fabricated through aqueous chemistry methods to simplify the electron percolation pathway for efficient transport and collection of electrons. So far the highest efficiency obtained for ZnO nanoparticle film is ~ 5% and the highest efficiency obtained for ZnO nanowire arrays is ~ 1.5%, as described in Chapter 1.

In this chapter, solar cells with films consisting of ZnO nanoparticles and ZnO nanowires were analyzed and compared in an effort to improve the overall efficiency of ZnO-based dye sensitized solar cells. Figure 4.1 is a schematic of the various ZnO nanostructures studied. Films consisting of 1) sol-gel-derived ZnO nanoparticle and 2) solution-grown ZnO nanowires were fabricated by way of solution methods, and compared to commercially-obtained ZnO nanoparticle film. The ZnO nanoparticle film consists of secondary colloidal spheres ~ 300nm in diameter and primary nanoparticles ~ 20nm in diameter on the surface of the spheres, as reported in literature[136]. This type of structure with large secondary colloidal spheres and smaller primary nanoparticles on the surface of the colloidal spheres imparts a much higher surface area and increased photon scattering. In addition, the ZnO nanowire arrays are hierarchically-structured to retain a high surface area and promote a simple pathway for electron transport. The nanowire arrays standing perpendicular to the substrate have a more ordered structure to allow for more efficient charge transport from the point of electron injection at the sensitizer-nanowire interface to the nanowire-substrate interface. These unique structures were fabricated and tested in an effort to improve the short-circuit current density and the overall light conversion efficiency.

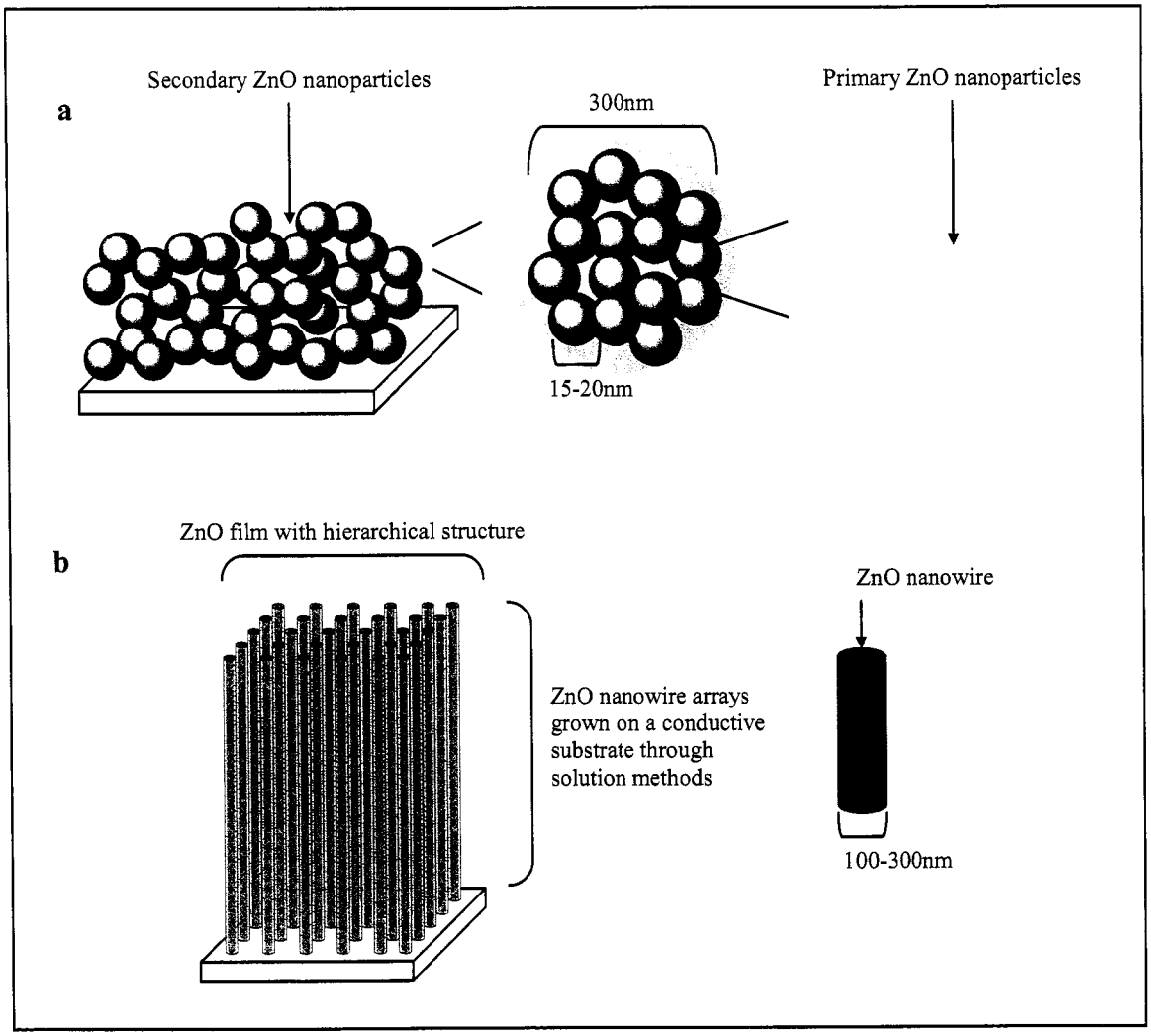

Figure 4.1. Schematic of a) sol-gel-derived ZnO nanoparticle film, and b) solution-grown ZnO nanowire arrays. The ZnO nanoparticle film consists of primary and secondary particles. The ZnO nanowire film consists of hierarchically-structured ZnO nanowires.

Additional ZnO nanoparticle films were prepared on ITO and FTO substrates in order to study the effect of dye loading on the overall performance. Films consisting of ZnO nanoparticles prepared on ITO substrates were 1) sensitized in N3 dye with concentrations of 100%, 50%, 20%, 10%, and 5%, and 2) sensitized in N3 dye with 20% concentration for 20, 40, 60, 120, and 180 minutes to compare the open-circuit voltage, short-circuit current density, fill factor, and overall efficiency. Films consisting of ZnO

nanoparticles prepared on FTO substrates were 1) sensitized in N3 dye with concentrations of 100%, 50%, 20%, 10%, and 5%, and 2) sensitized in N3 dye with 100% concentration for 20, 40, 60, 120, and 180 minutes to compare the open-circuit voltage, short-circuit current density, fill factor, and overall efficiency. Each ZnO film was assembled in a solar cell and tested under illumination to compare the I-V behavior.

4.2 Experimental procedure

The following sections describe 1) the formation of ZnO nanostructures, most notable ZnO nanoparticles and ZnO nanowires, and 2) the analysis techniques used.

4.2.1 Formation of ZnO nanostructures

Zinc oxide (ZnO) sol was prepared from precursor materials by way of sol-gel processing. The chemicals used in making ZnO sol were zinc acetate (98%, Alfa-Aesar, Ward Hill, MA), diethylene glycol (98%, Sigma-Aldrich, St. Louis, MO), and deionized water (DI-H_2O). An aqueous solution prepared from precursor materials was used to grow ZnO nanowires. The chemicals used in making the aqueous solution were zinc nitrate hexahydrate (98%, Sigma-Aldrich, St. Louis, MO), methenamine or hexamethylenetetramine (99%, Sigma-Aldrich, St. Louis, MO), and deionized water (DI-H_2O). Films consisting of commercially-available ZnO nanoparticles (99.99%, Alfa-Aesar, Ward Hill, MA) were also prepared for comparison. The following sections describe the process for fabricating ZnO nanoparticles and ZnO nanowires. Films consisting of ZnO nanoparticles were fabricated on both indium-tin-oxide (ITO, $R_s \sim 8$-12 ohms, Delta Technologies Ltd, Stillwater, MN) and fluorine-tin-oxide (FTO, TCO10-

10, R_s ~ 10ohm/sq, Solaronix SA, Switzerland) coated glass substrates. Films consisting of commercially-obtained ZnO nanoparticles and ZnO nanowires were fabricated on conductive ITO glass substrates.

4.2.1.1 ZnO nanoparticle film

The ZnO sol was prepared by hydrolyzing 0.01mol of zinc acetate [$(CH_3CO_2)_2Zn$] in 100mL diethylene glycol [$(HOCH_2CH_2)_2O$], as described by Jezequel et al[136]. Figure 4.2 shows the process for preparing ZnO sol. The reaction occurred when the mixed solution was heated under reflux to 160°C for ~ 24 hours. The as-synthesized solution was then placed in a centrifuge tube. The solution was centrifuged at a rate of ~ 1400 revolutions per minute (RPM) for ~ 5 hours. After centrifugation, the precipitation of ZnO colloids segregated to the bottom of the tube. Part of the supernatant was removed and the colloids were then redispersed in ethanol by sonication for ~ 10 minutes. The resultant ZnO colloidal spheres were sealed and stored at room temperature. The colloidal spheres produced by this method are typically monodispersed with a diameter size of ~ 300nm, and consist of many primary nanoparticles with a diameter of ~ 20nm.

To fabricate ZnO nanoparticle films, the substrates were first hydrolyzed in boiling DI-H_2O at 90°C-100°C for ~ 30 minutes. Then a few drops of the resultant ZnO colloidal spheres were placed onto ITO or FTO glass substrates. The films were then immediately heat treated at a temperature of 450°C for 1 hour, forming a layer of white film during the quick evaporation of the solvent. The thickness of the films varied from 2μm to 10μm, depending on the concentration of the colloidal spheres and the quantity added to the substrate surface. Before solar cell testing, the ZnO nanoparticle films were

sensitized with standard ruthenium-based red dye (N3), cis-bis(isothiocyanato)bis(2,2'-bipyridyl-4,4'-di-carboxylato)ruthenium(II) (Solterra Fotovoltaico SA, Switzerland), with varying concentration for various immersion times. The original $5x10^{-4}$M N3 dye concentration in ethanol (100%) was modified to obtain 50%, 20%, 10%, and 5% concentrations. In addition, the ZnO nanoparticle films were immersed in N3 dye for various times ranging from 20 minutes to 3 hours.

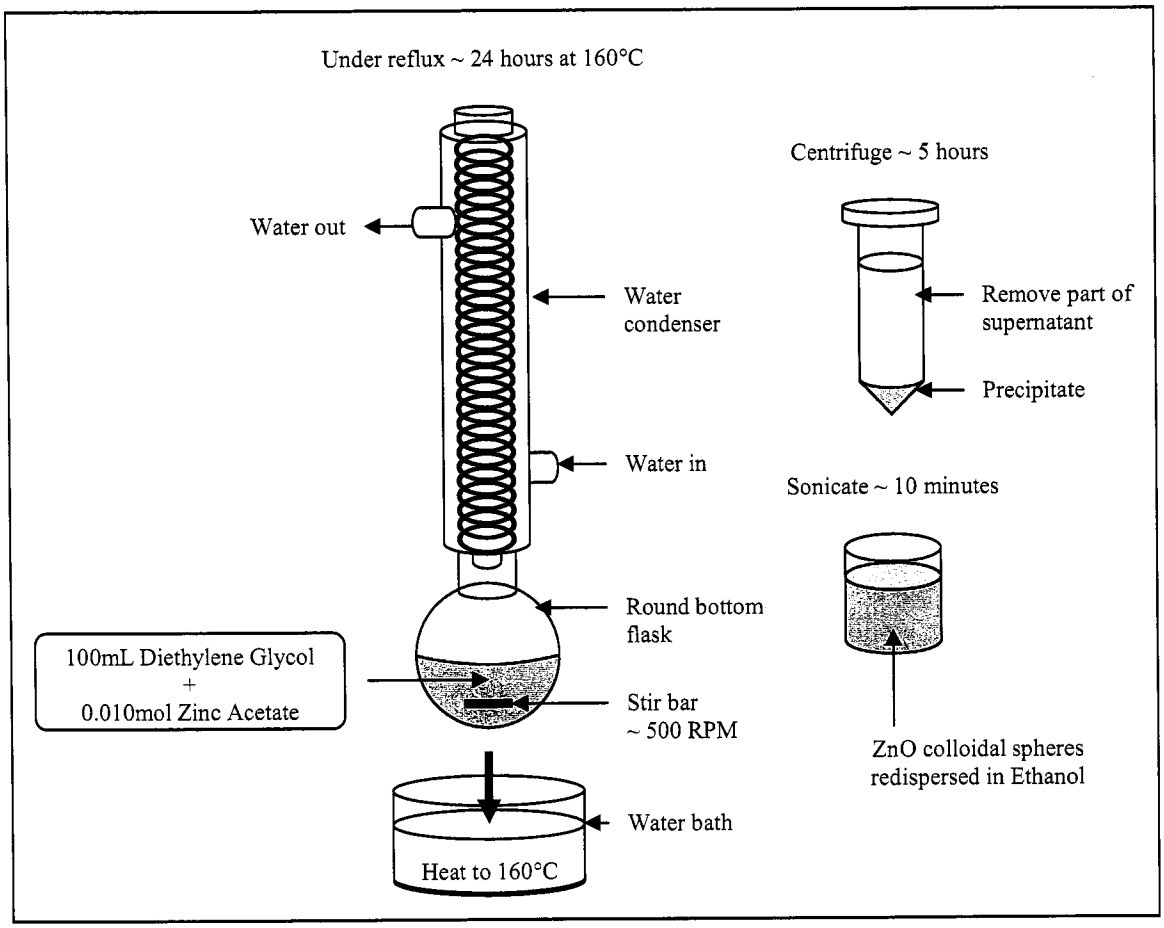

Figure 4.2. Schematic of the process involved in sol-gel processing of precursors for obtaining ZnO sol. Following the preparation of the solution under reflux, centrifugation was used to separate the ZnO particles from the supernatant, and sonication was used to redisperse the particles in ethanol.

4.2.1.2 ZnO nanowire film

The aqueous solution used to prepare ZnO nanowires was prepared by mixing 0.05M zinc nitrate hexahydrate [$Zn(NO_3)_2 \cdot 6H_2O$] and 0.05M methenamine [$C_6H_{12}N_4$]. Figure 4.3 shows the process for growing ZnO nanowires by a solution method. To grow ZnO nanowires, ITO substrates were immersed into the aqueous solution and heated to 90°C for 6 hours to promote nanowire growth. The resulting films were then rinsed with DI-H_2O to remove any residual salts or amine complexes. Before solar cell testing, the films were sensitized in N3 dye with 10% concentration for 1 hour.

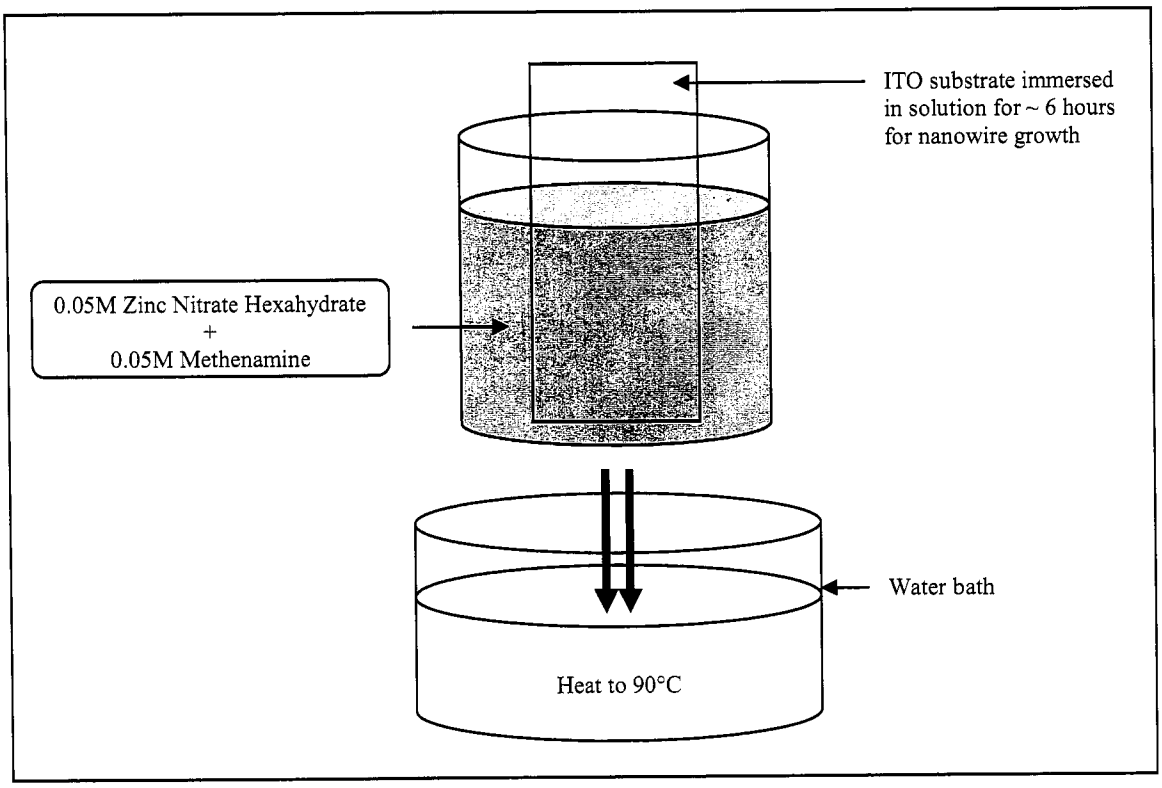

Figure 4.3. Schematic of the steps and procedures involved in preparing the ZnO aqueous solution and growing ZnO nanowires on a conductive substrate.

4.2.2 Analysis techniques

Scanning Electron Microscopy (SEM) was used to study the morphology of the ZnO nanoparticles and nanowires, and UV/VIS/IR Spectroscopy was used to analyze the absorption characteristics of fabricated ZnO colloidal spheres. The sample preparation for SEM, and the method for obtaining optical absorption data was previously described in Chapter 2. Solar cells were assembled and tested in the same manner, as previously described in Chapter 2, with the exception of the variation in the concentration and immersion time of the sensitizer material (N3 dye).

4.3 Results and discussion

The following sections describe the results from 1) the formation of ZnO nanostructures, 2) the solar cell performance of ZnO nanostructures, 3) the solar cell performance of ZnO nanoparticle film sensitized in N3 dye at various concentrations, 4) the solar cell performance of ZnO nanoparticle film sensitized in N3 dye at various times, and 5) the overall dye loading effect of ZnO nanoparticle film.

4.3.1 ZnO nanostructures

For the ZnO nanoparticle films, SEM analysis was used to examine the morphology and estimate the particle size of the primary colloidal spheres and the secondary nanoparticles. In addition, SEM analysis was performed on the ZnO nanowire films to study the morphology and estimate the dimensions of the nanowires. The following sections detail the SEM results for both ZnO nanoparticles and ZnO nanowires.

4.3.1.1 ZnO nanoparticles

By way of sol-gel processing, ZnO particles were produced with secondary colloidal spheres and primary nanoparticles on the surface of the spheres. Figure 4.4 shows SEM images of the ZnO particles before heat treatment. It can be seen that the secondary colloidal spheres have a diameter ~ 300nm and that the surface of each secondary sphere have numerous primary nanoparticles with a diameter ~ 20nm. The secondary spheres and primary nanoparticles were all measured to have roughly the same diameter throughout the film.

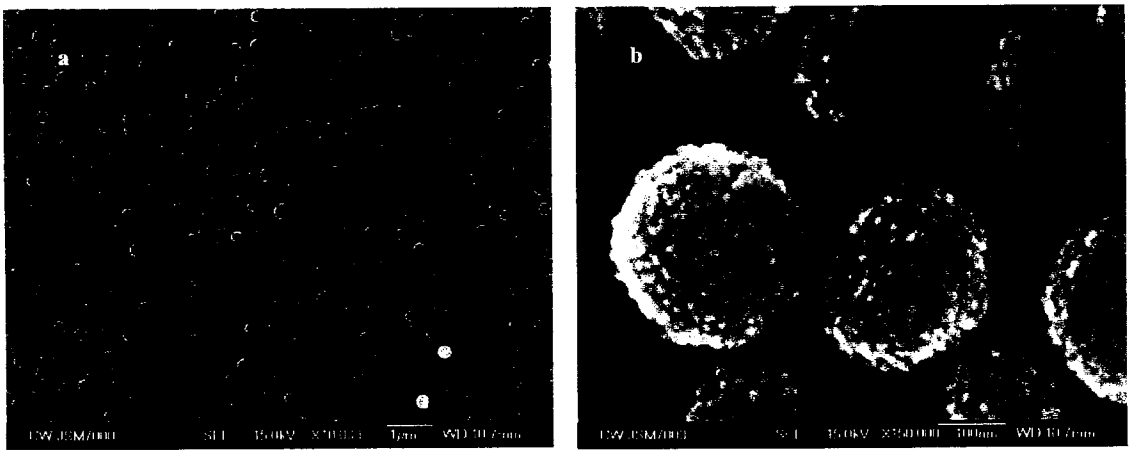

Figure 4.4. SEM images of the sol-gel-derived ZnO nanoparticles before heat treatment at a) 10,000X magnification and b) 150,000X magnification.

With 450°C heat treatment, the connectivity of the ZnO particles improved. Figure 4.5 shows SEM images of the ZnO particles after 450°C sintering. It can be seen that the connectivity between the primary nanoparticles and between the secondary colloidal spheres improved.

Further heat treatment at 550°C did not seem to improve the connectivity even further. Figure 4.6 shows SEM images of ZnO particles after 550°C sintering. Hence, it

was observed that 450°C was a sufficient sintering temperature for treating the ZnO particle films to obtain sufficient connectivity between particles.

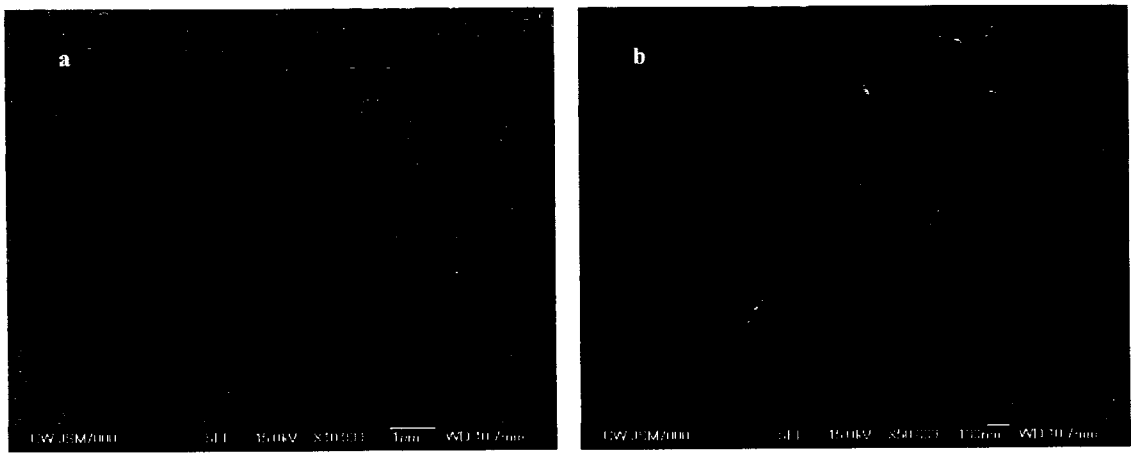

Figure 4.5. SEM images of the sol-gel-derived ZnO nanoparticles after 450°C heat treatment at a) 10,000X magnification and b) 50,000X magnification.

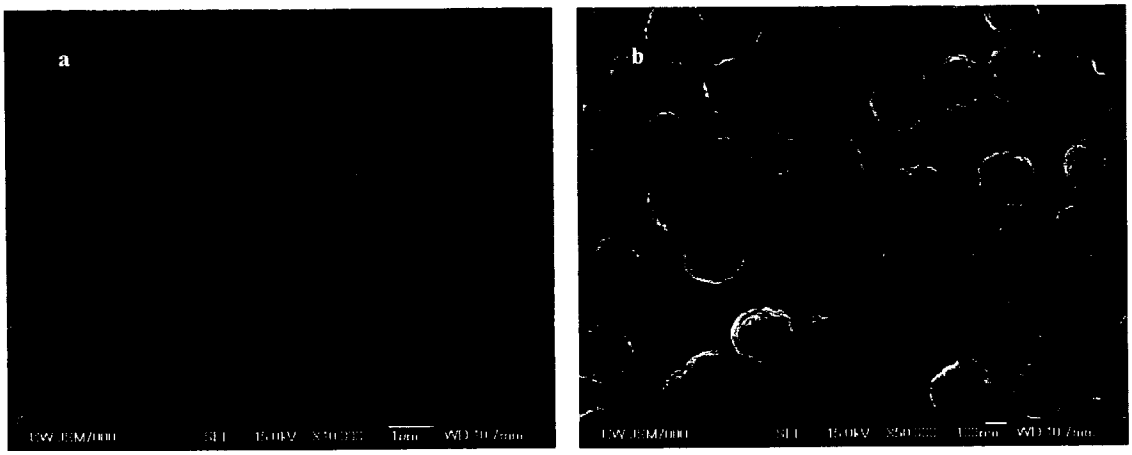

Figure 4.6. SEM images of the sol-gel-derived ZnO nanoparticles after 550°C heat treatment at a) 10,000X magnification and b) 50,000X magnification.

4.3.1.2 ZnO nanowires

To estimate the dimensions of the grown ZnO nanowires, SEM analysis was performed on the nanowire films. An array of ZnO nanowires were obtained by solution methods, as previously described. Figure 4.7 shows SEM images of ZnO nanowires

grown on an ITO substrate. It can be seen that solid, dense nanowires were obtained with diameters ranging from ~ 100nm to ~ 300nm. The lengths of the nanowires were estimated to be ~ 2μm. In each case, the nanowires were all measured to have roughly the same length. On the other hand, the diameter of the nanowires varied by ~ 100-200nm. It can also be seen that all the nanowires are all faceted. Ideally, the grown nanowire arrays are arranged perpendicular to the substrate in an ordered manner. However, from the SEM images, it can be seen that the arrangement of the nanowires are randomly oriented. It is also noted that some of the nanowires are agglomerated, or bonded, to other nanowires. This could lead to a reduced surface area and inefficient charge transport, resulting in lower short-circuit current density and overall efficiency values. Details of the solar cell performance of these nanowires are presented in the next section.

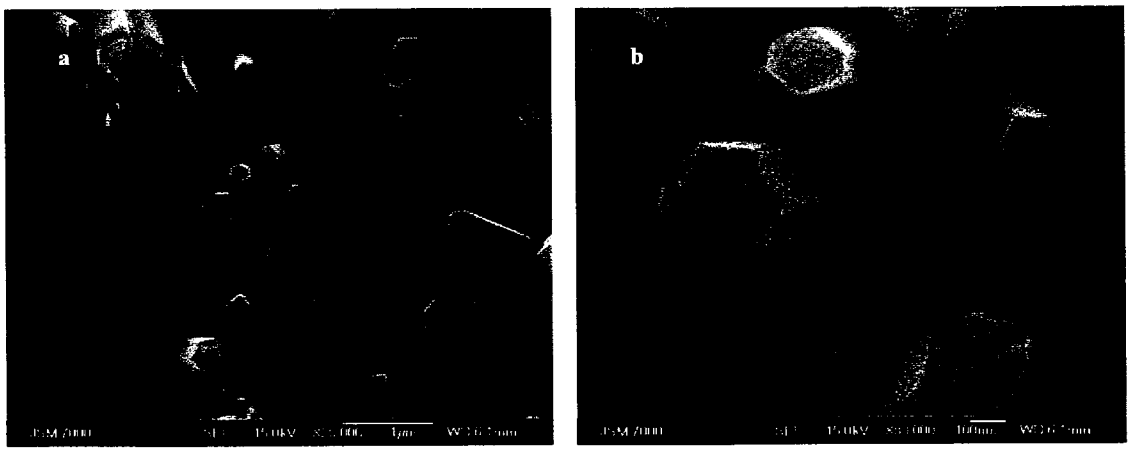

Figure 4.7. SEM images of the solution-grown ZnO nanowires at a) 20,000X magnification and b) 80,000X magnification.

4.3.2 Comparison of solar cell performance of ZnO film with various nanostructures

The photoresponse of the various ZnO films were tested and compared. Solar cells consisting of films with 1) ZnO nanoparticles and 2) ZnO nanowires were

assembled and tested under illumination with 100mW/cm^2 intensity, and compared to films with commercially-available ZnO nanoparticles. Table 4.1 summarizes the measured and calculated values obtained from the I-V curves of each solar cell consisting of 1) commercially-obtained ZnO nanoparticle film, 2) sol-gel-derived ZnO nanoparticle film, and 3) solution-grown ZnO nanowire film.

Table 4.1. The measured and calculated values obtained from the I-V curves for each solar cell consisting of sol-gel-derived ZnO nanoparticle film, commercially-obtained ZnO nanoparticle film, and solution-grown ZnO nanowire film.

Film Sample	V_{oc} (mV)	J_{sc} (mA/cm^2)	V_{max} (mV)	J_{max} (mA/cm^2)	FF (%)	P_{max} (mW/cm^2)	P_{in} (mW/cm^2)	η (%)
ZnO nanoparticles (commercial)	600	6.57	330	3.67	30.7	1.21	100	1.21
ZnO nanoparticles (sol-gel)	700	8.46	390	5.18	34.1	2.02	100	2.02
ZnO nanowires (solution)	530	1.90	270	1.36	36.5	0.37	100	0.37

Figure 4.8 compares the I-V characteristics of each solar cell consisting of 1) commercially-obtained ZnO nanoparticle film, 2) sol-gel-derived ZnO nanoparticle film, and 3) solution-grown ZnO nanowire film. It can be seen that the open-circuit voltage, short-circuit current density, and overall efficiency of the ZnO nanoparticle film prepared by way of sol-gel processing was higher than that of the ZnO nanoparticle film prepared from commercially-available ZnO nanoparticles. This difference could be due to the difference in absorption behavior between the two types of ZnO nanoparticles, which will be described in later sections. However, the open-circuit voltage, short-circuit current density, and overall efficiency of the ZnO nanowire film was lower than that of the ZnO nanoparticle film prepared from commercially-available ZnO nanoparticles. The most notable difference between the three types of ZnO films is in the open-circuit voltage, the

short-circuit current density, and the overall light conversion efficiency. A more detailed look at the trends comparing open-circuit voltage, short-circuit current density, fill factor, and overall efficiency is described in the following sections.

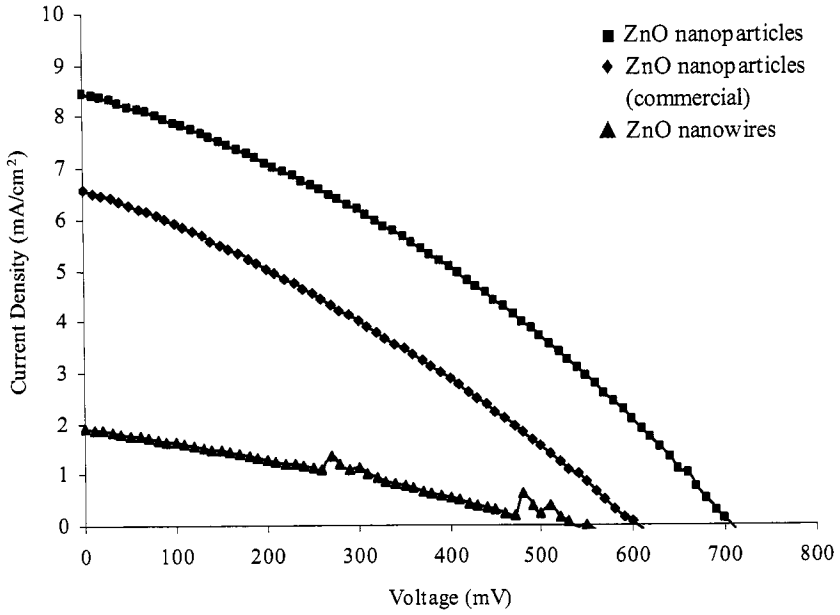

Figure 4.8. Plot and comparison of the I-V characteristics for each solar cell consisting of sol-gel-derived ZnO nanoparticle film, commercially-obtained ZnO nanoparticle film, and solution-grown ZnO nanowires.

4.3.2.1 Open-circuit voltage

By comparing the open-circuit voltage for sol-gel-derived ZnO nanoparticles and ZnO nanowires with that for commercially-available ZnO nanoparticles, the open-circuit voltage values differed. Figure 4.9 is a comparison of open-circuit voltage values between the three films. Table 4.2 summarizes the actual open-circuit voltage values. It can be seen that sol-gel-derived ZnO nanoparticles had a higher open-circuit voltage and solution-grown ZnO nanowires had a lower open-circuit voltage than that for commercially-available ZnO nanoparticles.

The open-circuit voltage for commercially-obtained ZnO nanoparticles, sol-gel-derived ZnO nanoparticles, and solution-grown ZnO nanowires was ~ 700mV, 600mV, and ~ 530mV, respectively. The differences in the open-circuit voltage could have been due to the differences in the processing of the ZnO nanoparticles and nanowires since the open-circuit voltage is dependent on the potential difference between the working electrode and the counter electrode, or in other words, on the surface chemistry of the ZnO material. Since the processing of the ZnO nanostructures are not optimized at this point, some deviation in the open-circuit voltage is expected.

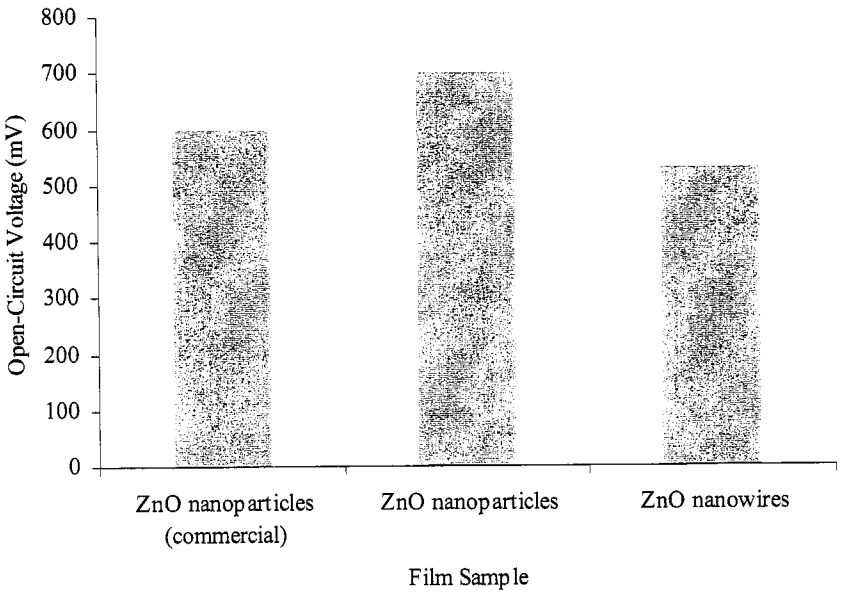

Figure 4.9. Plot of the open-circuit voltage for films consisting of commercially-obtained ZnO nanoparticles, sol-gel-derived ZnO nanoparticles, and solution-grown ZnO nanowires.

Table 4.2. The open-circuit voltage values obtained from the I-V curves for commercially-obtained ZnO nanoparticles, sol-gel-derived ZnO nanoparticles, and solution-grown ZnO nanowires.

Film Sample	**V_{oc} (mV)**
ZnO nanoparticles (commercial)	600
ZnO nanoparticles	700
ZnO nanowires	530

4.3.2.2 Short-circuit current density

It was also evident that the short-circuit current density differed between the three films. A higher short-circuit current density was observed for the sol-gel-derived ZnO nanoparticle film and a lower short-circuit current density was observed for the ZnO nanowire film, as compared to the commercially-obtained ZnO nanoparticle film. Figure 4.10 is a comparison of the short-circuit current density between commercially-obtained ZnO nanoparticle film, sol-gel-derived ZnO nanoparticle film, and solution-grown ZnO nanowire film. Table 4.3 summarizes the actual short-circuit current density values.

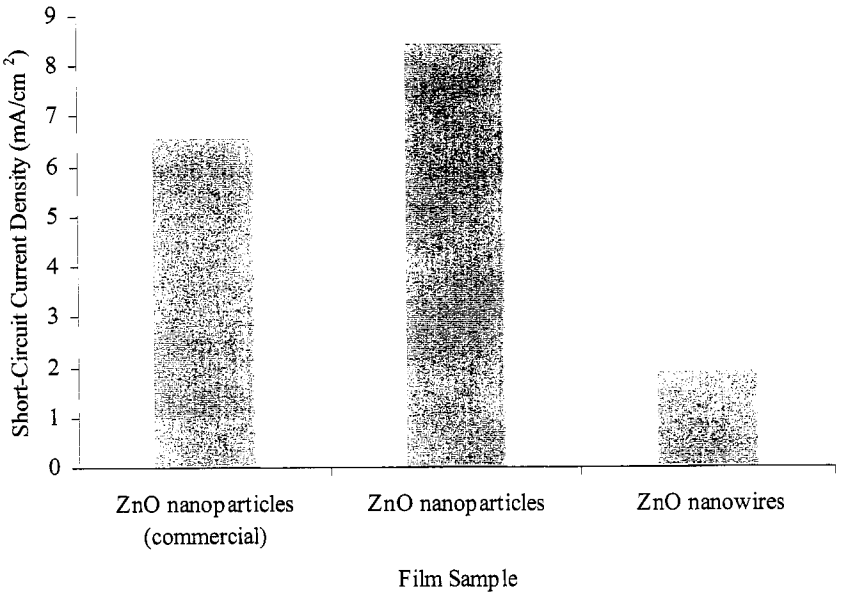

Figure 4.10. Plot of the short-circuit current density for films consisting of commercially-obtained ZnO nanoparticles, sol-gel-derived ZnO nanoparticles, and solution-grown ZnO nanowires.

Table 4.3. The short-circuit current density values obtained from the I-V curves for commercially-obtained ZnO nanoparticles, sol-gel-derived ZnO nanoparticles, and solution-grown ZnO nanowires. The difference in short-circuit current density is relative to the commercial ZnO nanoparticles.

Film Sample	**J_{sc} (mA/cm^2)**	**ΔJ_{sc} (mA/cm^2)**
ZnO nanoparticles (commercial)	6.57	
ZnO nanoparticles	8.46	1.89
ZnO nanowires	1.90	(6.56)

The short-circuit current density for the commercially-obtained ZnO nanoparticle film, sol-gel-derived ZnO nanoparticle film, and solution-grown ZnO nanowire film were ~ 6.6mA/cm^2, ~ 8.5mA/cm^2, and ~ 1.9mA/cm^2, respectively. It can be seen that the short-circuit current density for the sol-gel-derived ZnO nanoparticle film was higher by ~ 1.9mA/cm^2 and the short-circuit current density for the solution-grown ZnO nanowire film was much lower by ~ 6.6mA/cm^2. One reason for the increased short-circuit current density of the sol-gel-derived ZnO nanoparticle film could be the better assembly and packing of the primary spheres and secondary nanoparticles, resulting in a higher surface area and improved contact between colloidal spheres. Another reason for the increased short-circuit current density of the sol-gel-derived ZnO nanoparticle film could be the improved absorption behavior with the presence of primary colloidal spheres and secondary nanoparticles. Figure 4.11 compares the absorption behavior of commercially-obtained ZnO nanoparticle film and sol-gel-derived ZnO nanoparticle film.

It can be seen that an absorption peak at ~ 390nm is present for both films, representing the band gap of ~ 3.2eV, which is equivalent to the wavelength of ~ 387nm. By comparing the absorption spectra of the two ZnO films, it can be seen that an additional absorption peak is shown at ~ 440nm for sol-gel-derived ZnO nanoparticles, which is not seen for the commercially-obtained ZnO nanoparticle film. This additional absorption peak could be due to photon scattering caused by the presence of larger secondary colloidal spheres. The photon scattering ability of larger particles would enhance the ability of the sol-gel-derived ZnO nanoparticle film to absorb more of the photons, resulting in an increase in the short-circuit current density. In addition, the higher short-circuit current density for the sol-gel-derived ZnO nanoparticle film may

also have been due to the increased surface area of the film with the presence of both secondary spheres and primary nanoparticles on the surface, which would allow for more dye adsorption and greater generation of electrons.

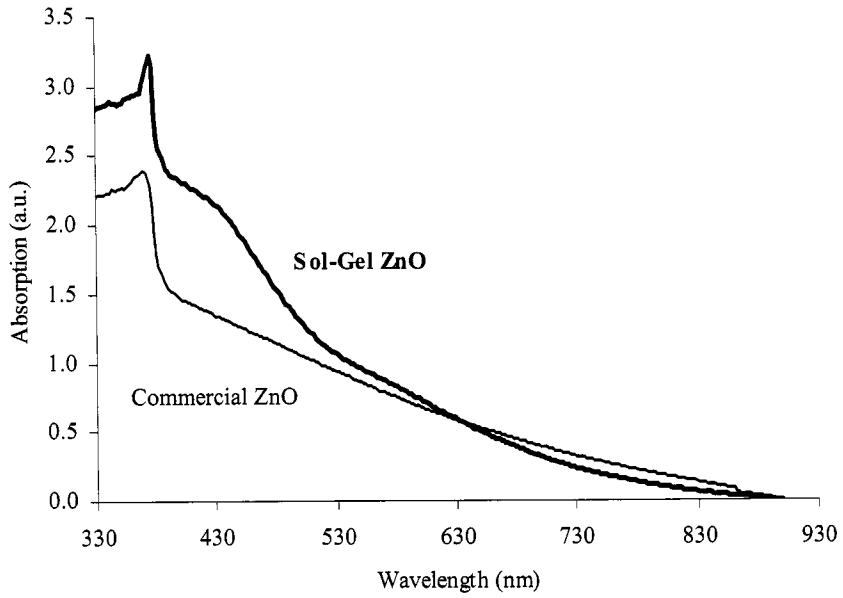

Figure 4.11. Absorption spectra comparing the optical behavior of sol-gel-derived ZnO nanoparticle film to that of commercially-obtained ZnO nanoparticle film.

On the other hand, the lower short-circuit current density for solution-grown ZnO nanowire film may have been due to the large reduction in surface area from the ~ 2μm length of the nanowires. In addition, the non-uniformity and random growth of the nanowires, as well as the agglomeration of some of the ZnO nanowires, as seen in the SEM images in Figure 4.7, may have influenced the electron percolation pathway, causing the presence of barriers to hinder efficient electron transport. Furthermore, the adhesion between the ZnO nanowires and the ITO substrate may have affected the contact points, where the transfer of electrons may have been hindered.

4.3.2.3 Fill factor

Showing a steady trend, the fill factor did not dramatically change and remained fairly constant. Figure 4.12 is a comparison of the fill factor values between commercially-obtained ZnO nanoparticles, sol-gel-derived ZnO nanoparticles, and solution-grown ZnO nanowires. Table 4.4 summarizes the actual fill factor values.

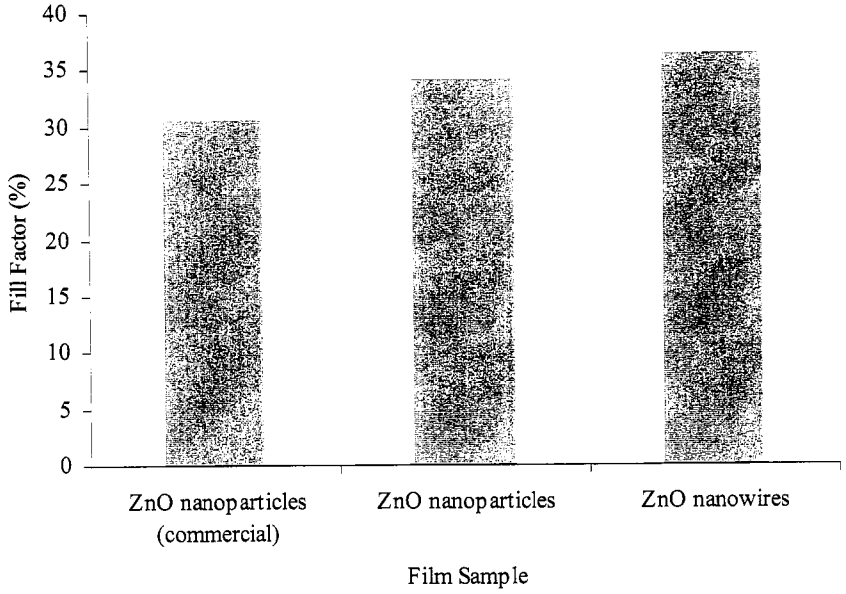

Figure 4.12. Plot of the fill factor for films consisting of commercially-obtained ZnO nanoparticles, sol-gel-derived ZnO nanoparticles, and solution-grown ZnO nanowires.

Table 4.4. The fill factor values obtained from the I-V curves for commercially-obtained ZnO nanoparticles, sol-gel-derived ZnO nanoparticles, and solution-grown ZnO nanowires.

Film Sample	**FF (%)**
ZnO nanoparticles (commercial)	30.7
ZnO nanoparticles	34.1
ZnO nanowires	36.5

It can be seen that the fill factor stayed fairly steady in the range of ~ 33.8% with a deviation of ~ 2.9%. This steady trend is expected since all the films were prepared on ITO substrates and sintered at 450°C for 60 minutes in an attempt to improve the

connectivity of the films. The "squareness" of the I-V curves in Figure 4.8 is also an indication of the fill factor, or how much resistance is in the films. The linearity of the I-V curves indicates that the films all had higher resistance than anticipated, when compared to the ideal case.

4.3.2.4 Overall light conversion efficiency

Having a similar behavior as the short-circuit current density, the overall efficiency of the three films was also observed to be different. A higher overall efficiency was observed for the sol-gel-derived ZnO nanoparticle film and a lower overall efficiency was observed for the solution-grown ZnO nanowire film, when compared to the commercially-obtained ZnO nanoparticle film. Figure 4.13 is a comparison of the overall efficiency between the three types of film structures. Table 4.5 summarizes the actual overall efficiency values.

The overall efficiency for the commercially-obtained ZnO nanoparticle film, the sol-gel-derived ZnO nanoparticle film, and the solution-grown ZnO nanowire film was ~ 1.2%, ~ 2.0%, and ~ 0.4%, respectively. It can be seen that the overall efficiency for the sol-gel-derived ZnO nanoparticle film was higher by ~ 0.8% and the overall efficiency for the solution-grown ZnO nanowire film was lower by ~ 0.8%. The differences in the overall efficiency can be due to the differences in the short-circuit current density, which is dependent upon the absorption behavior of the films, as previously shown. A higher short-circuit current density would result in a higher overall efficiency since the overall efficiency is dependent upon the short-circuit current density.

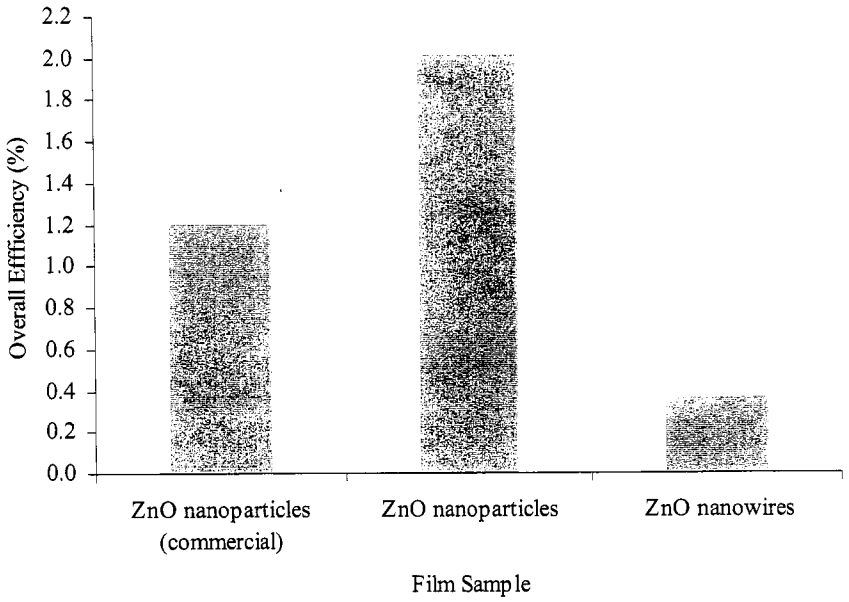

Figure 4.13. Plot of the overall efficiency for films consisting of commercially-obtained ZnO nanoparticles, sol-gel-derived ZnO nanoparticles, and solution-grown ZnO nanowires.

Table 4.5. The overall efficiency values obtained from the I-V curves for commercially-obtained ZnO nanoparticles, sol-gel-derived ZnO nanoparticles, and solution-grown ZnO nanowires. The difference in overall efficiency is relative to the commercial ZnO nanoparticles.

Film Sample	η (%)	$\Delta\eta$ (%)
ZnO nanoparticles (commercial)	1.21	
ZnO nanoparticles	2.02	0.81
ZnO nanowires	0.37	(0.84)

Correlating with the higher short-circuit current density for the sol-gel-derived ZnO nanoparticle film, as previously shown, the overall efficiency was also higher. A lower short-circuit current density for the solution-grown ZnO nanowire film, as shown previously, also resulted in a lower overall efficiency. However, the differences in short-circuit current density between the three types of film structures were much larger than the differences in overall efficiency between the three types of film. Therefore, it was observed that the different nanostructures had a greater influence on the short-circuit

current density than that on the overall efficiency. The overall efficiency is dependent on the short-circuit current density, but is also dependent on the fill factor and the open-circuit voltage. The photon scattering ability and better assembly of the secondary colloidal spheres and the primary nanoparticles in sol-gel-derived ZnO nanoparticle film may have had more of an influence on the short-circuit current density than on the overall light conversion efficiency.

Since the commercially-obtained ZnO film consists of ~ 25nm diameter particles, the increase in the short-circuit current density and the overall light conversion efficiency shown in sol-gel-derived ZnO film may have been due to: 1) the hierarchical structure of sol-gel-derived ZnO particles consisting of ~ 20nm primary nanoparticles and ~ 300nm secondary colloidal spheres, 2) the light scattering effects of secondary colloidal spheres, possibly resulting in more absorption of photons and a greater number electrons and holes generated, and 3) the increase in surface area from the secondary colloidal spheres and primary nanoparticles, resulting in more dye adsorption and more photon absorption.

4.3.3 Solar cell performance of ZnO nanoparticle film sensitized with N3 dye at various concentrations

Since the sol-gel-derived ZnO nanoparticle film had the highest open-circuit voltage, short-circuit current density, and overall efficiency when compared to the commercially-available ZnO nanoparticle film and the solution-grown ZnO nanowire film, modification to the sensitization of the film was examined in order to improve the solar cell performance of the sol-gel-derived ZnO nanoparticle film even further. The initial ZnO nanoparticle film was sensitized in N3 dye with a concentration of ~ 20% for

~ 20 minutes, and it has been shown that the amount of dye adsorption is critical for electron generation, which is essential for higher short-circuit current density and overall efficiency. Therefore, the photoresponse of ZnO nanoparticle films sensitized in N3 dye with concentrations of 100%, 50%, 20%, 10%, and 5% were tested and compared.

Table 4.6 and Table 4.7 summarizes the measured and calculated values obtained from the I-V curves of each solar cell consisting of ZnO nanoparticle film fabricated on ITO and FTO substrates, respectively, sensitized for 20 minutes in N3 dye with various concentrations. Figure 4.14 and Figure 4.15 compares the I-V characteristics of each solar cell consisting of ZnO nanoparticle film fabricated on ITO and FTO substrates, respectively, sensitized for 20 minutes in N3 dye with various concentrations.

Table 4.6. The measured and calculated values obtained from the I-V curves for each solar cell consisting of sol-gel-derived ZnO nanoparticle film prepared on ITO substrates.

Dye Concentration (%)	V_{oc} (mV)	J_{sc} (mA/cm^2)	V_{max} (mV)	J_{max} (mA/cm^2)	FF (%)	P_{max} (mW/cm^2)	P_{in} (mW/cm^2)	η (%)
100	690	6.37	380	3.49	30.2	1.33	100	1.33
50	690	7.17	380	4.08	31.3	1.55	100	1.55
20	700	8.46	390	5.18	34.1	2.02	100	2.02
10	640	5.42	380	3.26	35.7	1.24	100	1.24
5	590	3.29	340	2.23	39.1	0.76	100	0.76

Table 4.7. The measured and calculated values obtained from the I-V curves for each solar cell consisting of sol-gel-derived ZnO nanoparticle film prepared on FTO substrates.

Dye Concentration (%)	V_{oc} (mV)	J_{sc} (mA/cm^2)	V_{max} (mV)	J_{max} (mA/cm^2)	FF (%)	P_{max} (mW/cm^2)	P_{in} (mW/cm^2)	η (%)
100	670	10.9	420	8.35	48.1	3.51	100	3.51
50	660	7.75	400	5.57	43.6	2.23	100	2.23
20	540	1.91	360	1.49	52.0	0.54	100	0.54
10	600	1.89	360	1.41	44.8	0.51	100	0.51
5	510	1.15	350	0.82	48.9	0.29	100	0.29

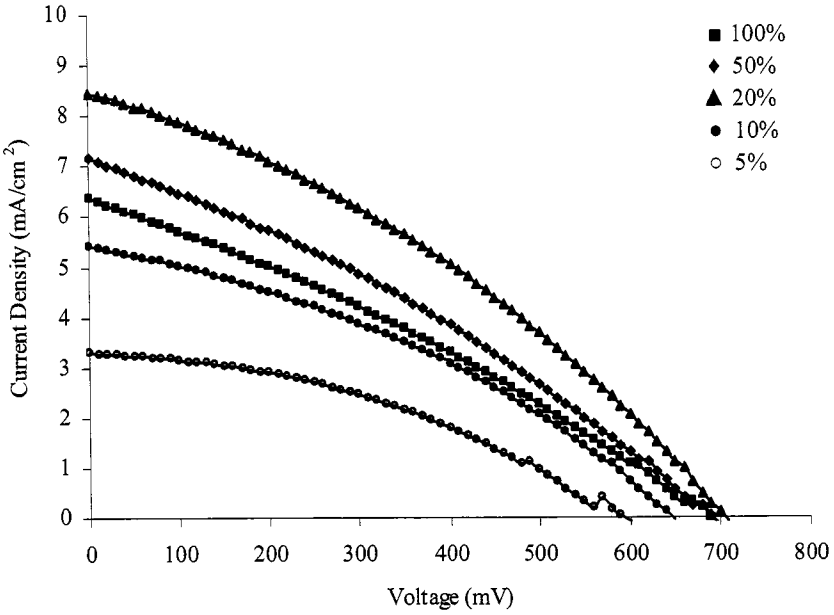

Figure 4.14. Plot and comparison of the I-V characteristics for each solar cell consisting of sol-gel-derived ZnO nanoparticle films prepared on ITO substrates and sensitized in N3 dye at various concentrations for 20 minutes.

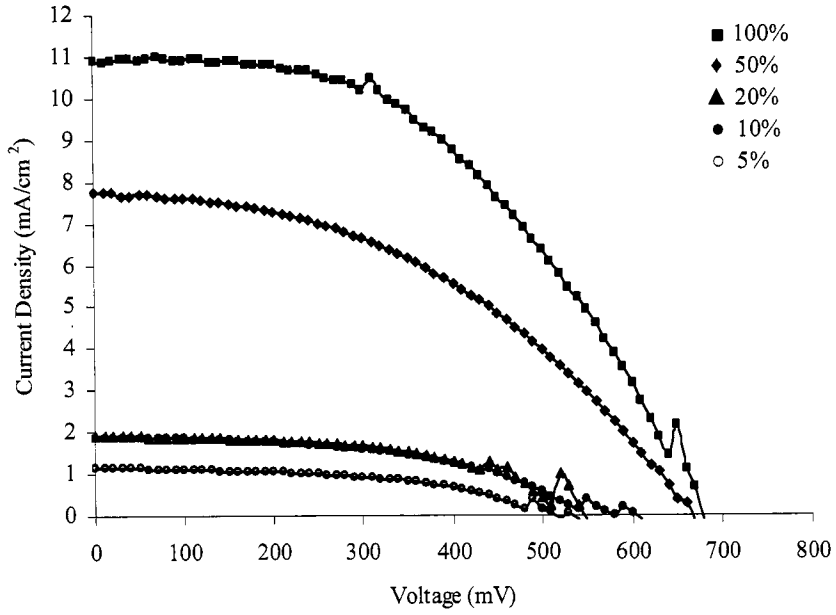

Figure 4.15. Plot and comparison of the I-V characteristics for each solar cell consisting of sol-gel-derived ZnO nanoparticle films prepared on FTO substrates and sensitized in N3 dye at various concentrations for 20 minutes.

It can be seen that the ZnO nanoparticle film prepared on an FTO substrate and sensitized in N3 dye with 100% concentration had the highest short-circuit current density and overall efficiency, when compared to the other ZnO nanoparticle films prepared on FTO substrates. On the other hand, the ZnO nanoparticle film prepared on an ITO substrate and sensitized in N3 dye with 20% concentration had the highest short-circuit current density and overall efficiency, when compared to the other ZnO nanoparticle films prepared on ITO substrates. A closer look at the trends comparing open-circuit voltage, short-circuit current density, fill factor, and overall light conversion efficiency is detailed in the following sections.

4.3.3.1 Open-circuit voltage

The open-circuit voltage decreased with increasing and decreasing dye concentration for the ZnO nanoparticle films prepared on ITO substrates. In addition, the open-circuit voltage decreased with decreasing dye concentration for the ZnO nanoparticle films prepared on FTO substrates. Figure 4.16 is a comparison of the open-circuit voltage values of the ZnO nanoparticle films prepared on a) ITO substrates and b) FTO substrates, and sensitized with N3 dye at various concentrations. Table 4.8 summarizes the actual open-circuit voltage values.

For the case of the ZnO nanoparticle films prepared on ITO substrates, the open-circuit voltage deviated in the range of 590-700mV with an average deviation of ~ 47mV. For the case of the ZnO nanoparticle films prepared on FTO substrates, the open-circuit voltage deviated in the range of 510-670mV with an average deviation of ~ 71mV. The open-circuit voltage decreased with increasing and decreasing dye concentration for the

films prepared on ITO substrates, and the open-circuit voltage decreased with decreasing dye concentration for the films prepared on FTO substrates.

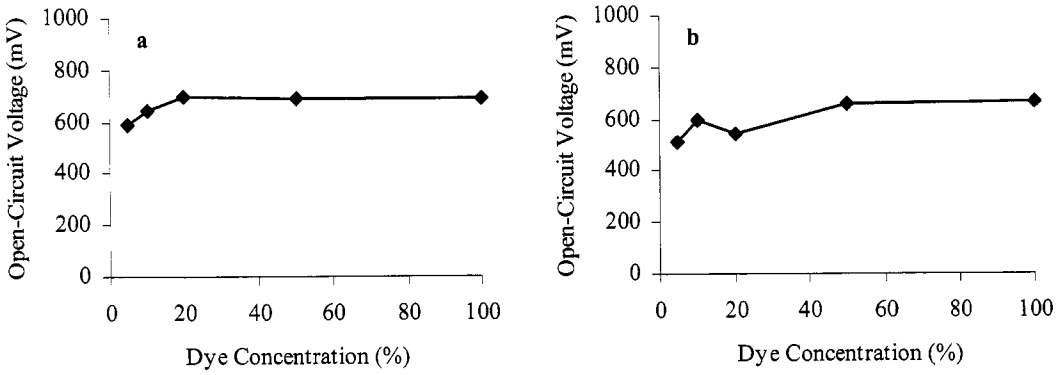

Figure 4.16. Plot of the open-circuit voltage for films consisting of sol-gel-derived ZnO nanoparticles prepared on a) ITO substrates and b) FTO substrates, and sensitized in N3 dye for 20 minutes at various dye concentrations.

Table 4.8. The open-circuit voltage values for each solar cell consisting of sol-gel-derived ZnO nanoparticle film prepared on ITO and FTO substrates, and sensitized in N3 dye for 20 minutes at various dye concentrations.

Dye Concentration (%)	ITO	FTO
	V_{oc} (mV)	V_{oc} (mV)
100	690	670
50	690	660
20	700	540
10	640	600
5	590	510

4.3.3.2 Short-circuit current density

The amount of dye adsorbed to the surface of the ZnO nanoparticles can influence the short-circuit current density, where the generation of electrons is dependent on the number of dye molecules present on the surface. Figure 4.17 is a plot of short-circuit current density as a function of dye concentration for ZnO nanoparticle film prepared on a) ITO substrates and b) FTO substrates. Table 4.9 summarizes the actual short-circuit

current density values, and the total difference in short-circuit current density relative to the film with the highest short-circuit current density at 20% for ITO and 100% for FTO. It can be seen that the short-circuit current density decreased with an increase and decrease in the dye concentration for the films on ITO substrates. On the other hand, the short-circuit current density decreased with a decrease in the dye concentration for the films on FTO substrates.

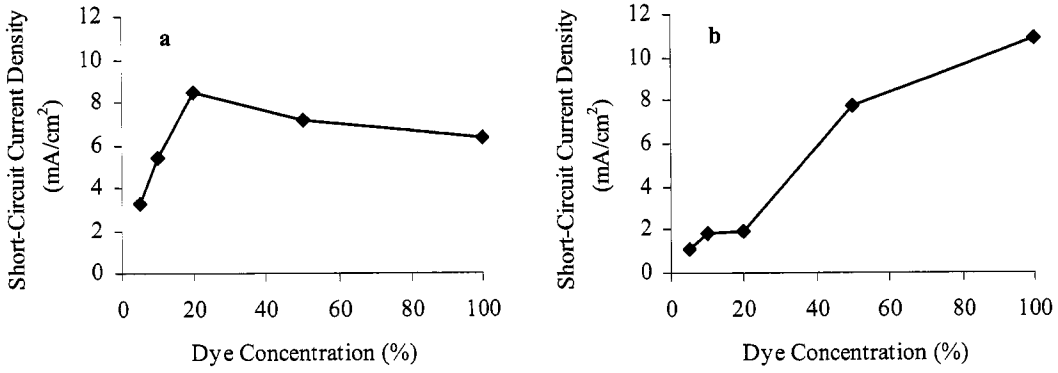

Figure 4.17. Plot of the short-circuit current density for films consisting of sol-gel-derived ZnO nanoparticles prepared on a) ITO substrates and b) FTO substrates, and sensitized in N3 dye for 20 minutes at various dye concentrations.

Table 4.9. The short-circuit current density values for each solar cell consisting of sol-gel-derived ZnO nanoparticle film prepared on ITO and FTO substrates, and sensitized in N3 dye for 20 minutes at various dye concentrations. The difference in short-circuit current density for the ZnO nanoparticle films prepared on ITO and FTO is relative to the values at 20% and 100%, respectively.

Dye Concentration (%)	ITO		FTO	
	J_{sc} (mA/cm^2)	Total Δ J_{sc} (mA/cm^2)	J_{sc} (mA/cm^2)	Total Δ J_{sc} (mA/cm^2)
100	6.37	(2.09)	10.9	
50	7.17	(1.29)	7.75	(3.14)
20	8.46		1.91	(8.98)
10	5.42	(3.04)	1.89	(9.00)
5	3.29	(5.17)	1.15	(9.74)

For the case of the ZnO nanoparticle films on ITO substrates, the short-circuit current density decreased slightly from ~ 8.5mA/cm^2 to ~ 7.2mA/cm^2 and ~ 6.4mA/cm^2

with an increase in dye concentration from 20% to 50% and 100%, respectively. With a decrease in dye concentration from 20% to 10% and 5%, the short-circuit current density decreased from ~ 8.5mA/cm^2 to ~ 5.4mA/cm^2 and ~ 3.3mA/cm^2, respectively. Figure 4.18 is a plot of the total difference in short-circuit current density as a function of the total change in dye concentration relative to the highest short-circuit current density obtained at 20% dye concentration using ITO substrates. It can be seen that with an increase in dye concentration by 30% and 80%, the short-circuit current density decreased by ~ 1.3mA/cm^2 and ~ 2.1mA/cm^2, respectively. In addition, a decrease in dye concentration by 10% and 15% also resulted in the short-circuit current density decreasing by ~ 3.0mA/cm^2 and ~ 5.2mA/cm^2, respectively.

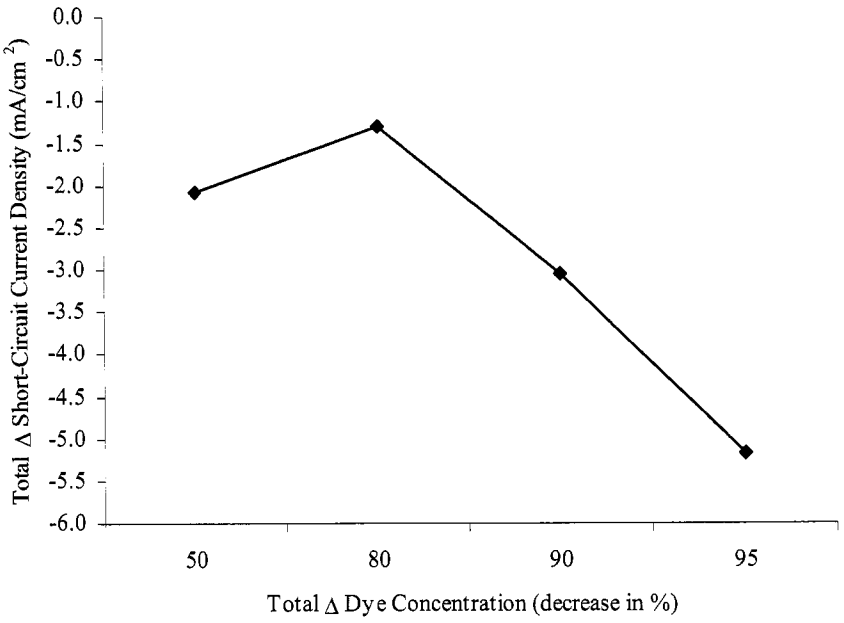

Figure 4.18. Plot of the total difference in short-circuit current density for films consisting of sol-gel-derived ZnO nanoparticles prepared on ITO substrates and sensitized in N3 dye for 20 minutes at various dye concentrations. The difference is relative to values obtained with 20% concentration.

For the case of the ZnO nanoparticle films on FTO substrates, the short-circuit current density decreased from ~ 10.9mA/cm^2 to ~ 7.8mA/cm^2, ~ 1.9mA/cm^2, ~ 1.9mA/cm^2, and ~ 1.2mA/cm^2 with a decrease in dye concentration from 100% to 50%, 20%, 10%, and 5%, respectively. Figure 4.19 is a plot of the total difference in short-circuit current density as a function of the total change in dye concentration relative to the highest short-circuit current density obtained at 100% dye concentration using FTO substrates. It can be seen that with a decrease in dye concentration by 50%, the short-circuit current density decreased by ~ 3.1mA/cm^2. With a decrease in dye concentration by 80%, 90%, and 95%, the short-circuit current density all decreased by ~ 9-10mA/cm^2.

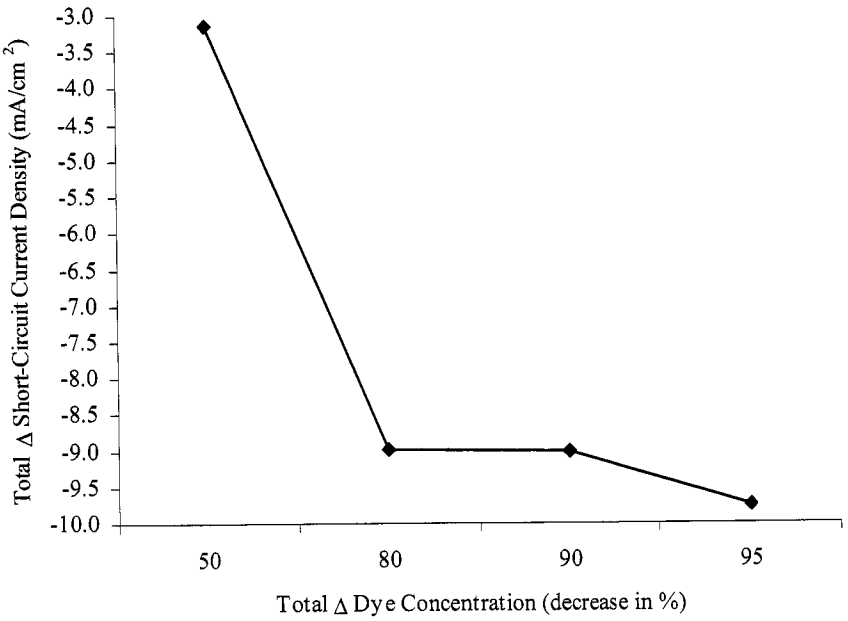

Figure 4.19. Plot of the total difference in short-circuit current density for films consisting of sol-gel-derived ZnO nanoparticles prepared on FTO substrates and sensitized in N3 dye for 20 minutes at various dye concentrations. The difference is relative to values obtained with 100% concentration.

4.3.3.3 Fill factor

Showing a steady trend, the fill factor did not dramatically change and remained fairly constant between the films. Figure 4.20 is a comparison of the fill factor values of the ZnO nanoparticle films sensitized with N3 dye at various concentrations, prepared on a) ITO substrates and b) FTO substrates. Table 4.10 summarizes the actual fill factor values. It can be seen that the fill factor stayed fairly steady in the range of ~ 34.1% and ~ 47.5% with a deviation of ~ 3.6% and ~ 3.4% for the ZnO nanoparticle film prepared on ITO and FTO substrates, respectively. In both cases, the fill factor deviated slightly but did not dramatically change even with differing amount of dye adsorption, as shown in the case for the short-circuit current density, where the change in sensitizer concentration caused a change in the short-circuit current density by the difference in dye adsorption.

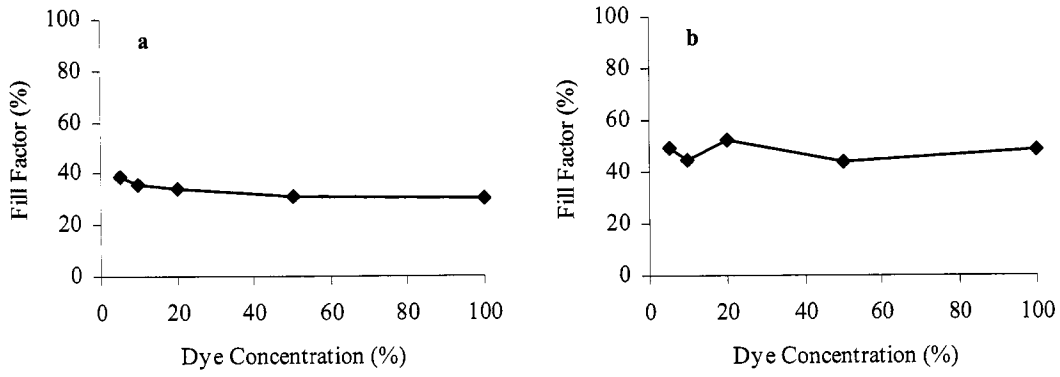

Figure 4.20. Plot of the fill factor for films consisting of sol-gel-derived ZnO nanoparticles prepared on a) ITO substrates and b) FTO substrates, and sensitized in N3 dye for 20 minutes at various dye concentrations.

However, the steady trend is expected since all the films were prepared on ITO and FTO substrates, and sintered at 450°C for 60 minutes in an attempt to improve the connectivity of the films. Furthermore, the fill factor values for the ZnO nanoparticle

films on FTO substrates generally had higher fill factor values than that for the ZnO nanoparticle films on ITO substrates. This difference can be seen by comparing the "squareness" of the I-V curves in Figure 4.14 and in Figure 4.15, which is also an indication of the fill factor. The ZnO nanoparticle films prepared on ITO substrates had higher resistance than the ZnO nanoparticle films prepared on FTO substrates, as shown by the linearity of the I-V curves in Figure 4.14.

Table 4.10. The fill factor values for each solar cell consisting of sol-gel-derived ZnO nanoparticle film prepared on ITO and FTO substrates, and sensitized in N3 dye for 20 minutes at various dye concentrations.

Dye Concentration (%)	ITO	FTO
	FF (%)	FF (%)
100	30.2	48.1
50	31.3	43.6
20	34.1	52.0
10	35.7	44.8
5	39.1	48.9

4.3.3.4 Overall light conversion efficiency

The overall efficiency had a similar trend as the short-circuit current density for ZnO nanoparticle films prepared on both ITO and FTO substrates. Figure 4.21 is a plot of overall efficiency as a function of dye concentration for ZnO nanoparticle film prepared on a) ITO substrates and b) FTO substrates. Table 4.11 summarizes the actual overall efficiency values, and the total difference in overall efficiency relative to the film with the highest overall efficiency at 20% for ITO and 100% for FTO. It can be seen that the overall efficiency decreased with an increase and decrease in the dye concentration for the films on ITO substrates. On the other hand, the overall efficiency decreased with a decrease in the dye concentration for the films on FTO substrates.

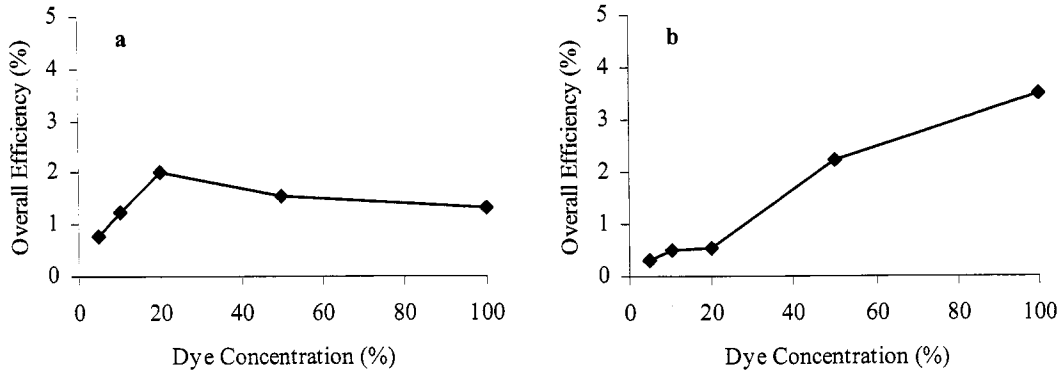

Figure 4.21. Plot of the overall efficiency for films consisting of sol-gel-derived ZnO nanoparticles prepared on a) ITO substrates and b) FTO substrates, and sensitized in N3 dye for 20 minutes at various dye concentrations.

Table 4.11. The overall efficiency values for each solar cell consisting of sol-gel-derived ZnO nanoparticle film prepared on ITO and FTO substrates, and sensitized in N3 dye for 20 minutes at various dye concentrations. The difference in overall efficiency for the ZnO nanoparticle films prepared on ITO and FTO is relative to the values at 20% and 100%, respectively.

Dye Concentration (%)	ITO		FTO	
	η (%)	Total Δ η (%)	η (%)	Total Δ η (%)
100	1.33	(0.69)	3.51	
50	1.55	(0.47)	2.23	(1.28)
20	2.02		0.54	(2.97)
10	1.24	(0.78)	0.51	(3.00)
5	0.76	(1.26)	0.29	(3.22)

For the case of the ZnO nanoparticle films on ITO substrates, the overall efficiency decreased slightly from ~ 2.0% to ~ 1.6% and ~ 1.3% with an increase in dye concentration from 20% to 50% and 100%, respectively. With a decrease in dye concentration from 20% to 10% and 5%, the overall efficiency decreased from ~ 2.0% to 1.2% and ~ 0.8%, respectively. Figure 4.22 is a plot of the total difference in overall efficiency as a function of the total change in dye concentration relative to the highest overall efficiency obtained at 20% dye concentration using ITO substrates. It can be seen that with an increase in dye concentration by 30% and 80%, the overall efficiency

decreased by ~ 0.5% and ~ 0.7%, respectively. In addition, a decrease in dye concentration by 10% and 15% also resulted in the overall efficiency decreasing by ~ 0.8% and ~ 1.3%, respectively.

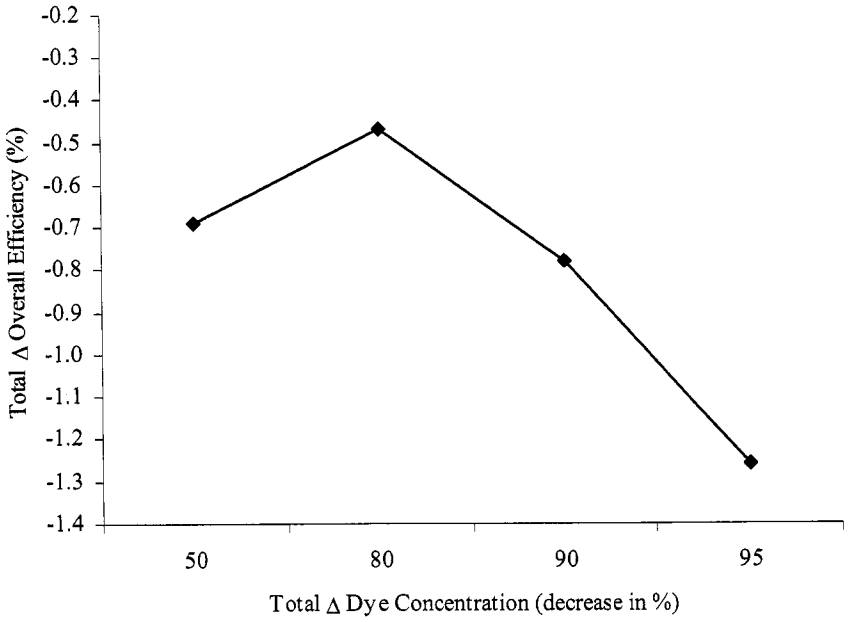

Figure 4.22. Plot of the total difference in overall efficiency for films consisting of sol-gel-derived ZnO nanoparticles prepared on ITO substrates and sensitized in N3 dye for 20 minutes at various dye concentrations. The difference is relative to values obtained with 20% concentration.

For the case of the ZnO nanoparticle films on FTO substrates, the overall efficiency decreased from ~ 3.5% to ~ 2.2%, ~ 0.5%, ~ 0.5%, and ~ 0.3% with a decrease in dye concentration from 100% to 50%, 20%, 10%, and 5%, respectively. Figure 4.23 is a plot of the total difference in overall efficiency as a function of the total change in dye concentration relative to the highest overall efficiency obtained at 100% dye concentration using FTO substrates. It can be seen that with a decrease in dye concentration by 50%, the overall efficiency decreased by ~ 1.3%. With a decrease in dye concentration by 80%, 90%, and 95%, the overall efficiency all decreased by ~ 3.0-3.2%.

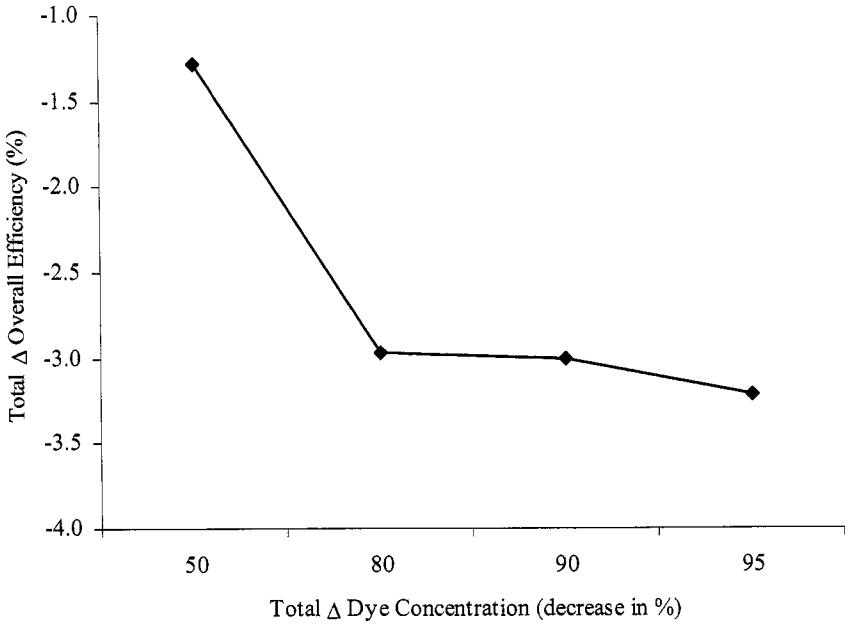

Figure 4.23. Plot of the total difference in overall efficiency for films consisting of sol-gel-derived ZnO nanoparticles prepared on FTO substrates and sensitized in N3 dye for 20 minutes at various dye concentrations. The difference is relative to values obtained with 100% concentration.

4.3.4 Solar cell performance of ZnO nanoparticle film sensitized with N3 dye for various times

Additional ZnO nanoparticle films prepared from sol-gel-derived ZnO nanoparticles and sensitized with N3 dye were made to study whether the amount of time exposed to the sensitizer had an influence on the solar cell performance. Since the concentrations of the N3 dye that resulted in the highest short-circuit current density and overall efficiency for the ZnO nanoparticle film prepared on an ITO substrate and on an FTO substrate were 20% and 100%, respectively, the immersion time was varied starting from 20 minutes using those concentrations. Therefore, the photoresponse of ZnO nanoparticle films sensitized in N3 dye with concentrations of 20% and 100% for 20, 40, 60, 120, and 180 minutes were tested and compared.

Table 4.12 and Table 4.13 summarizes the measured and calculated values obtained from the I-V curves of each solar cell consisting of ZnO nanoparticle film on ITO and FTO substrates sensitized in N3 dye with a concentration of ~ 20% and ~ 100%, respectively, for various immersion times. Figure 4.24 and Figure 4.25 compares the I-V characteristics of each solar cell consisting of ZnO nanoparticle film on ITO and FTO substrates sensitized in N3 dye with a concentration of ~ 20% and ~ 100%, respectively, for various immersion times. Figure 4.24 and Figure 4.25 correlate with the values shown in Table 4.12 and Table 4.13, respectively.

Table 4.12. The measured and calculated values obtained from the I-V curves for each solar cell consisting of sol-gel-derived ZnO nanoparticle film prepared on ITO substrates and sensitized in N3 dye at 20% concentration for various times.

Dye Immersion Time (minutes)	V_{oc} (mV)	J_{sc} (mA/cm^2)	V_{max} (mV)	J_{max} (mA/cm^2)	FF (%)	P_{max} (mW/cm^2)	P_{in} (mW/cm^2)	η (%)
20	700	8.46	390	5.18	34.1	2.02	100	2.02
40	710	5.51	370	2.86	27.0	1.06	100	1.06
60	700	7.89	400	4.43	32.1	1.77	100	1.77
120	690	5.30	370	2.78	28.1	1.03	100	1.03
180	700	5.25	360	2.68	26.3	0.96	100	0.96

Table 4.13. The measured and calculated values obtained from the I-V curves for each solar cell consisting of sol-gel-derived ZnO nanoparticle film prepared on FTO substrates and sensitized in N3 dye at 100% concentration for various times.

Dye Immersion Time (minutes)	V_{oc} (mV)	J_{sc} (mA/cm^2)	V_{max} (mV)	J_{max} (mA/cm^2)	FF (%)	P_{max} (mW/cm^2)	P_{in} (mW/cm^2)	η (%)
20	670	10.9	420	8.35	48.1	3.51	100	3.51
40	670	7.75	360	5.37	37.2	1.93	100	1.93
60	590	8.35	300	4.77	29.0	1.43	100	1.43
120	680	8.58	350	5.51	33.1	1.93	100	1.93
180	660	8.93	340	5.14	29.7	1.75	100	1.75

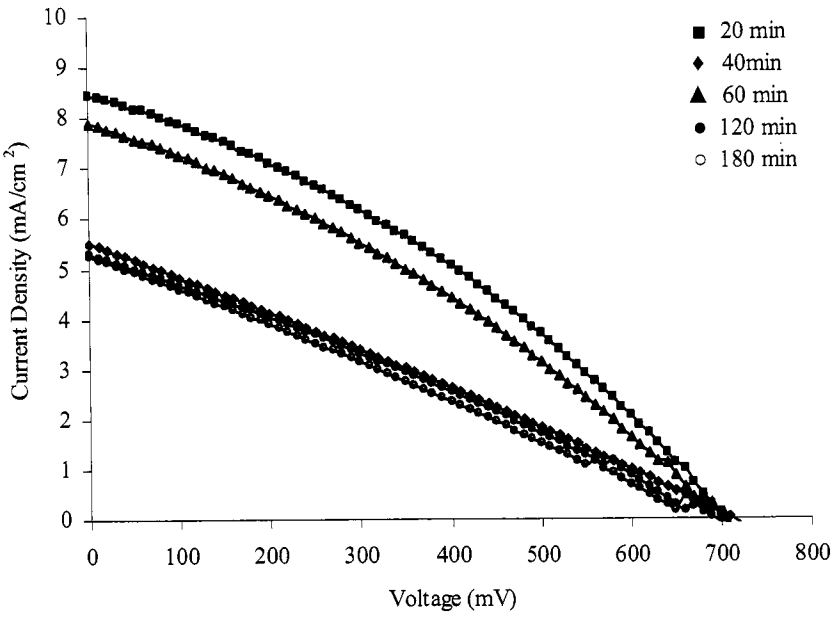

Figure 4.24. Plot and comparison of the I-V characteristics for each solar cell consisting of sol-gel-derived ZnO nanoparticle films prepared on ITO substrates and sensitized in N3 dye at 20% concentration for various times.

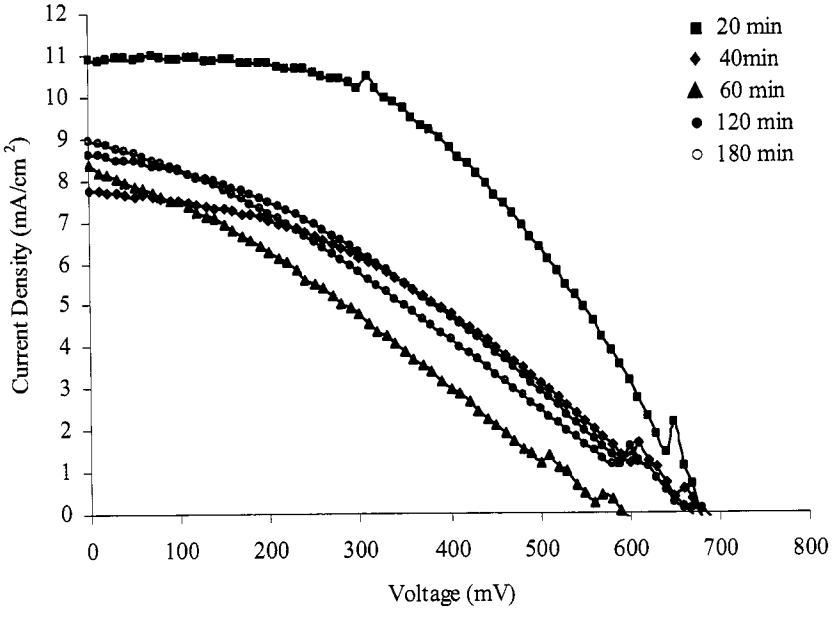

Figure 4.25. Plot and comparison of the I-V characteristics for each solar cell consisting of sol-gel-derived ZnO nanoparticle films prepared on FTO substrates and sensitized in N3 dye at 100% concentration for various times.

It can be seen that the ZnO nanoparticle film prepared on an ITO substrate and sensitized in N3 dye with 20% concentration for 20 minutes had the highest short-circuit current density and overall efficiency, compared to the other ZnO nanoparticle films prepared on ITO substrates. In addition, the ZnO nanoparticle film prepared on an FTO substrate and sensitized in N3 dye with 100% concentration for 20 minutes also had the highest short-circuit current density and overall efficiency, compared to the other ZnO nanoparticle films prepared on FTO substrates. A closer look at the trends comparing open-circuit voltage, short-circuit current density, fill factor, and overall light conversion efficiency is detailed in the following sections.

4.3.4.1 Open-circuit voltage

By varying the dye immersion time, the open-circuit voltage remained fairly constant for the ZnO nanoparticle films prepared on ITO substrates. In addition, the open-circuit voltage remained somewhat constant with a slight deviation for the ZnO nanoparticle films prepared on FTO substrates. Figure 4.26 is a comparison of the open-circuit voltage values of the ZnO nanoparticle films prepared on a) ITO substrates and b) FTO substrates, and sensitized with 20% and 100% N3 dye concentration, respectively, at various times. Table 4.14 summarizes the actual open-circuit voltage values. For the case of the ZnO nanoparticle films prepared on ITO substrates, the open-circuit voltage stayed in the range of ~ 700mV with a deviation of ~ 7mV. For the case of the ZnO nanoparticle films prepared on FTO substrates, the open-circuit voltage deviated in the range of 590-680mV with an average deviation of ~ 36mV.

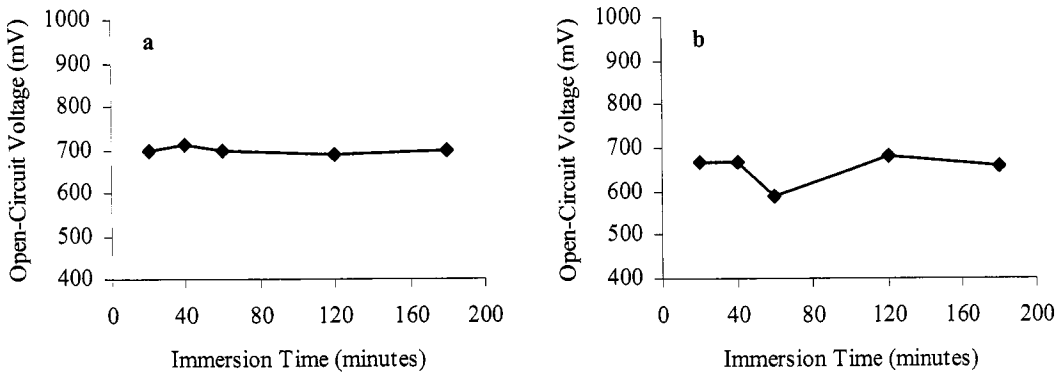

Figure 4.26. Plot of the open-circuit voltage for films consisting of sol-gel-derived ZnO nanoparticles prepared on a) ITO substrates and sensitized in N3 dye at 20% concentration, and b) FTO substrates and sensitized in N3 dye at 100% concentration for various times.

Table 4.14. The open-circuit voltage values for each solar cell consisting of sol-gel-derived ZnO nanoparticle film prepared on ITO and FTO substrates, and sensitized in N3 dye with 20% and 100% concentrations, respectively, for 20 minutes.

Time (minutes)	ITO	FTO
	V_{oc} (mV)	V_{oc} (mV)
20	700	670
40	710	670
60	700	590
120	690	680
180	700	660

4.3.4.2 Short-circuit current density

The amount of time for dye adsorption can slightly influence the short-circuit current density, where the generation of electrons is dependent on the number of dye molecules present on the surface. Figure 4.27 is a plot of short-circuit current density as a function of immersion time in a) 20% dye concentration for ZnO nanoparticle film prepared on ITO substrates and b) 100% dye concentration for ZnO nanoparticle film prepared on FTO substrates. Table 4.15 summarizes the actual short-circuit current density values, and the total difference in short-circuit current density relative to the film

with the highest short-circuit current density at 20% concentration for 20 minutes for ITO and 100% concentration for 20 minutes for FTO. In both cases, the short-circuit current density decreased with increasing immersion time.

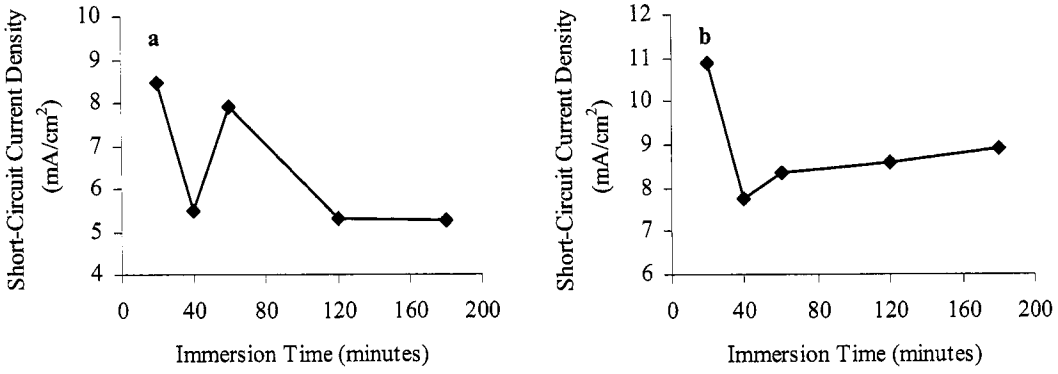

Figure 4.27. Plot of the short-circuit current density for films consisting of sol-gel-derived ZnO nanoparticles prepared on a) ITO substrates and sensitized in N3 dye at 20% concentration, and b) FTO substrates and sensitized in N3 dye at 100% concentration for various times.

Table 4.15. The short-circuit current density values for each solar cell consisting of sol-gel-derived ZnO nanoparticle film prepared on ITO and FTO substrates, and sensitized in N3 dye with 20% and 100% concentrations, respectively, for 20 minutes. The difference in short-circuit current density for the ZnO nanoparticle films prepared on ITO and FTO is relative to the values at 20 minutes.

Time (minutes)	ITO		FTO	
	J_{sc} (mA/cm^2)	Total Δ J_{sc} (mA/cm^2)	J_{sc} (mA/cm^2)	Total Δ J_{sc} (mA/cm^2)
20	8.46		10.9	
40	5.51	(2.95)	7.75	(3.14)
60	7.89	(0.57)	8.35	(2.54)
120	5.30	(3.16)	8.58	(2.31)
180	5.25	(3.21)	8.93	(1.96)

For the case of the ZnO nanoparticle films on ITO substrates, the short-circuit current density decreased slightly from ~ 8.5mA/cm^2 to ~ 5.5mA/cm^2, ~ 7.9mA/cm^2, ~ 5.3mA/cm^2, and ~ 5.3mA/cm^2 with an increase in immersion time from 20 minutes to 40, 60, 120, and 180 minutes, respectively. Figure 4.28 is a plot of the total difference in short-circuit current density as a function of the total change in immersion time in 20%

dye concentration relative to the highest short-circuit current density obtained at 20-minute immersion time using ITO substrates. It can be seen that with an increase in immersion time by 20, 40, 100, and 160 minutes, the short-circuit current density decreased by ~ 3.0mA/cm^2, ~ 0.6mA/cm^2, ~ 3.2mA/cm^2, and ~ 3.2mA/cm^2, respectively.

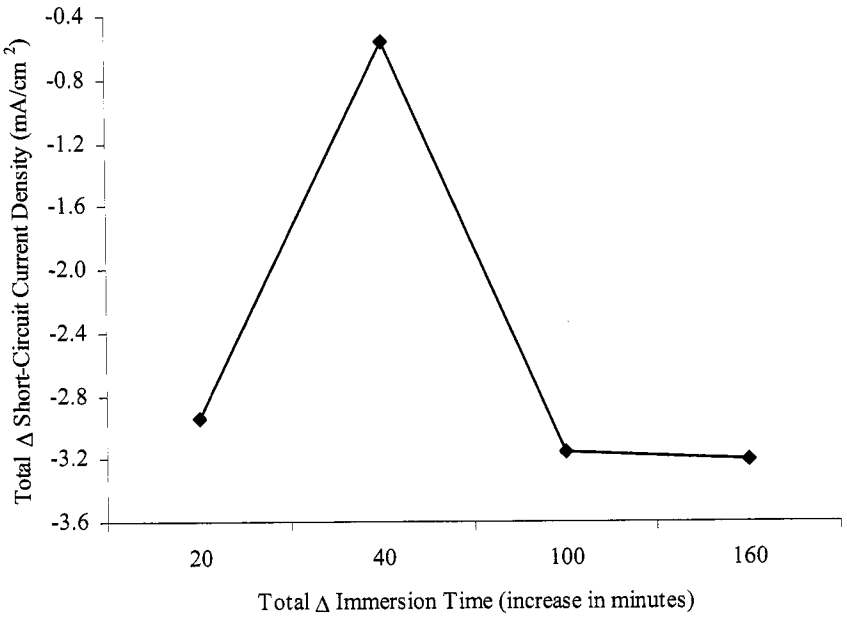

Figure 4.28. Plot of the total difference in short-circuit current density for films consisting of sol-gel-derived ZnO nanoparticles prepared on ITO substrates and sensitized in N3 dye at 20% concentration for various times. The difference is relative to values obtained at 20 minutes.

For the case of the ZnO nanoparticle films on FTO substrates, the short-circuit current density decreased from ~ 10.9mA/cm^2 to ~ 7.8mA/cm^2, ~ 8.4mA/cm^2, ~ 8.6mA/cm^2, and ~ 8.9mA/cm^2 with an increase in immersion time from 20 minutes to 40, 60, 120, and 180 minutes, respectively. Figure 4.29 is a plot of the total difference in short-circuit current density as a function of the total change in immersion time in 100% dye concentration relative to the highest short-circuit current density obtained at 20-minute immersion time using FTO substrates. It can be seen that with an increase in

immersion time by 20, 40, 100, and 160 minutes, the short-circuit current density decreased by ~ 3.1mA/cm^2, ~ 2.5mA/cm^2, ~ 2.3mA/cm^2, and ~ 2.0mA/cm^2, respectively.

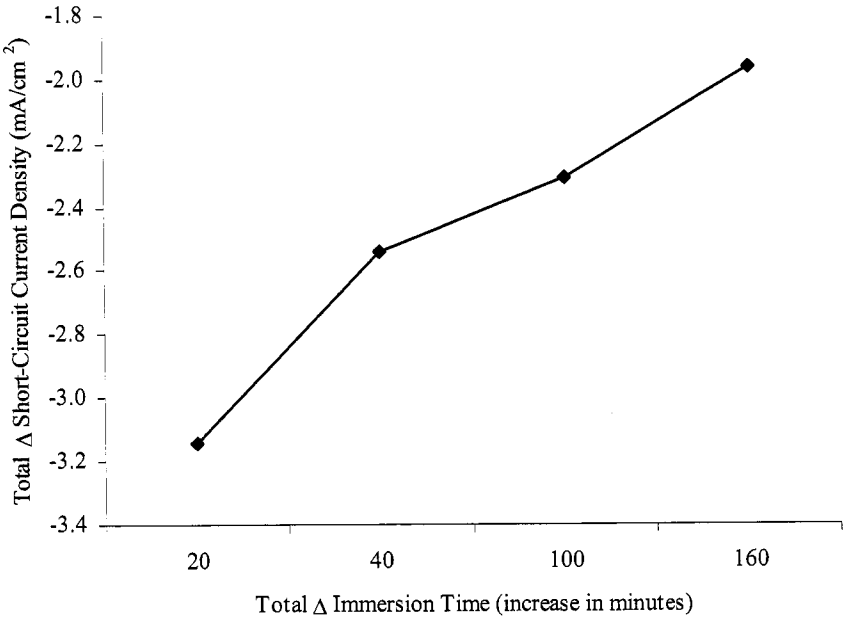

Figure 4.29. Plot of the total difference in short-circuit current density for films consisting of sol-gel-derived ZnO nanoparticles prepared on FTO substrates and sensitized in N3 dye at 100% concentration for various times. The difference is relative to values obtained at 20 minutes.

4.3.4.3 Fill factor

The fill factor varied in value with an increase in immersion time in 20% and 100% dye concentration for the ZnO nanoparticle films prepared on ITO and FTO substrates, respectively. Figure 4.30 is a comparison of the fill factor values of the ZnO nanoparticle films prepared on a) ITO substrates and b) FTO substrates, and sensitized with 20% and 100% N3 dye concentration, respectively, at various times. Table 4.16 summarizes the actual fill factor values.

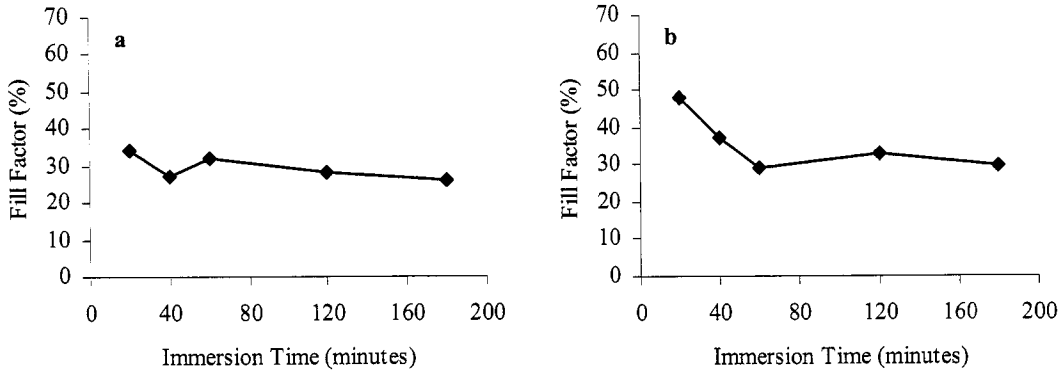

Figure 4.30. Plot of the fill factor for films consisting of sol-gel-derived ZnO nanoparticles prepared on a) ITO substrates and sensitized in N3 dye at 20% concentration, and b) FTO substrates and sensitized in N3 dye at 100% concentration for various times.

Table 4.16. The fill factor values for each solar cell consisting of sol-gel-derived ZnO nanoparticle film prepared on ITO and FTO substrates, and sensitized in N3 dye with 20% and 100% concentrations, respectively, for 20 minutes.

Time (minutes)	ITO	FTO
	FF (%)	FF (%)
20	34.1	48.1
40	27.0	37.2
60	32.1	29.0
120	28.1	33.1
180	26.3	29.7

For the case of the ZnO nanoparticle films prepared on ITO substrates, the fill factor deviated in the range of 26-34% with an average deviation of ~ 3%. For the case of the ZnO nanoparticle films prepared on FTO substrates, the open-circuit voltage deviated in the range of 29-48% with an average deviation of ~ 8%. In general, for both cases, the fill factor values were lower with increasing immersion time in 20% and 100% dye concentration for ZnO nanoparticle film prepared on ITO and FTO substrates, respectively. This could be due to the difference in dye adsorption on the surface since the assembly of the dye affects the open-circuit voltage and the fill factor is also dependent on the open-circuit voltage.

4.3.4.4 Overall light conversion efficiency

Having a similar trend as the short-circuit current density, the overall efficiency also decreased with an increase immersion time in 20% and 100% dye concentration for ZnO nanoparticle film prepared on ITO and FTO substrates, respectively. Figure 4.31 is a plot of overall efficiency as a function of immersion time in a) 20% dye concentration for ZnO nanoparticle film prepared on ITO substrates and b) 100% dye concentration for ZnO nanoparticle film prepared on FTO substrates. Table 4.17 summarizes the actual overall efficiency values, and the total difference in overall efficiency relative to the film with the highest overall efficiency at 20% concentration for 20 minutes for ITO and 100% concentration for 20 minutes for FTO. In both cases, the overall efficiency decreased with an increase in immersion time.

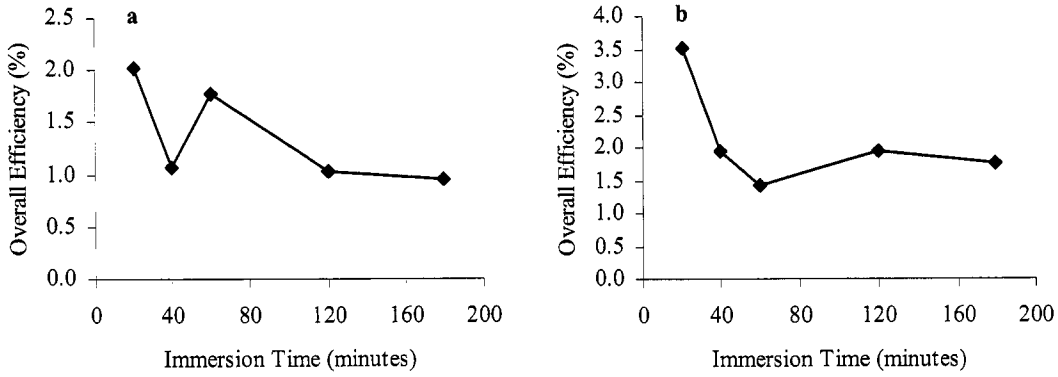

Figure 4.31. Plot of the overall efficiency for films consisting of sol-gel-derived ZnO nanoparticles prepared on a) ITO substrates and sensitized in N3 dye at 20% concentration, and b) FTO substrates and sensitized in N3 dye at 100% concentration for various times.

For the case of the ZnO nanoparticle films on ITO substrates, the overall efficiency decreased from ~ 2.0% to ~ 1.1%, ~ 1.8%, ~ 1.0%, and ~ 1.0% with an increase in immersion time from 20 minutes to 40, 60, 120, and 180 minutes,

respectively. Figure 4.32 is a plot of the total difference in overall efficiency as a function of the total change in immersion time in 20% dye concentration relative to the highest overall efficiency obtained at 20-minute immersion time using ITO substrates. It can be seen that with an increase in immersion time by 20, 40, 100, and 160 minutes, the overall efficiency decreased by ~ 1.0%, ~ 0.3%, ~ 1.0%, and ~ 1.1%, respectively.

Table 4.17. The overall efficiency values for each solar cell consisting of sol-gel-derived ZnO nanoparticle film prepared on ITO and FTO substrates, and sensitized in N3 dye with 20% and 100% concentrations, respectively, for 20 minutes. The difference in overall efficiency for the ZnO nanoparticle films prepared on ITO and FTO is relative to the values at 20 minutes.

Time (minutes)	ITO		FTO	
	η (%)	Total Δ η (%)	η (%)	Total Δ η (%)
20	2.02		3.51	
40	1.06	(0.96)	1.93	(1.58)
60	1.77	(0.25)	1.43	(2.08)
120	1.03	(0.99)	1.93	(1.58)
180	0.96	(1.06)	1.75	(1.76)

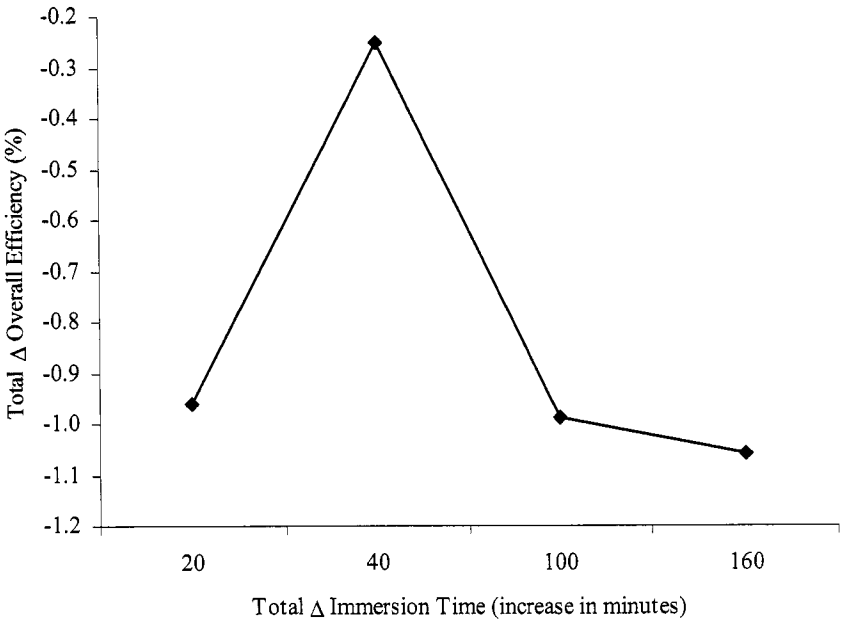

Figure 4.32. Plot of the total difference in overall efficiency for films consisting of sol-gel-derived ZnO nanoparticles prepared on ITO substrates and sensitized in N3 dye at 20% concentration for various times. The difference is relative to values obtained at 20 minutes.

For the case of the ZnO nanoparticle films on FTO substrates, the overall efficiency decreased from ~ 3.5% to ~ 1.9%, ~ 1.4%, ~ 1.9%, and ~ 1.8% with an increase in immersion time from 20 minutes to 40, 60, 120, and 180 minutes, respectively. Figure 4.33 is a plot of the total difference in overall efficiency as a function of the total change in immersion time in 100% dye concentration relative to the highest overall efficiency obtained at 20-minute immersion time using FTO substrates. It can be seen that with an increase in immersion time by 20, 40, 100, and 160 minutes, the overall efficiency decreased by ~ 1.6%, ~ 2.1%, ~ 1.6%, and ~ 1.8%, respectively.

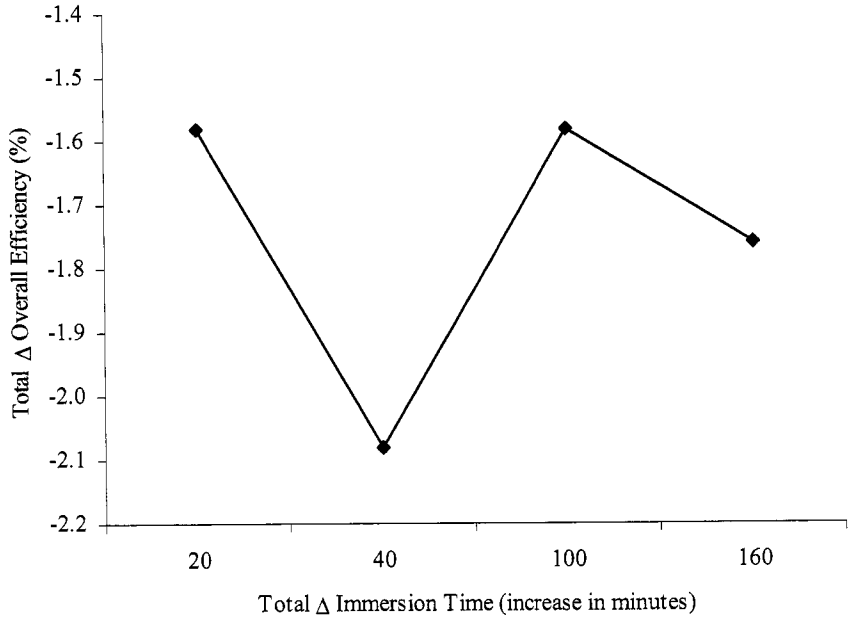

Figure 4.33. Plot of the total difference in overall efficiency for films consisting of sol-gel-derived ZnO nanoparticles prepared on FTO substrates and sensitized in N3 dye at 100% concentration for various times. The difference is relative to values obtained at 20 minutes.

4.3.5 Dye loading of ZnO nanoparticle film

The solar cell performance of ZnO nanoparticle film with a variation in dye loading was also analyzed and compared. Films consisting of ZnO nanoparticles prepared

on FTO substrates were sensitized in N3 dye with concentrations of 100%, 50%, 20%, 10%, and 5%. For each N3 dye concentration, the films were immersed for 20, 40, 60, 120, and 180 minutes to compare the overall efficiency. Each ZnO film was assembled in a solar cell and tested under illumination to compare the I-V behavior. Table 4.18 summarizes the measured and calculated values obtained from the I-V characteristics of each ZnO film sensitized in various concentrations for various times.

Table 4.18. The measured and calculated values obtained from the I-V curves for each solar cell with ZnO nanoparticle films sensitized in various concentrations for various times.

Concentration (%)	Time (minutes)	V_{oc} (mV)	I_{sc} (mA/cm^2)	V_{max} (mV)	I_{max} (mA/cm^2)	FF (%)	P_{max} (mW/cm^2)	P_{in} (mW/cm^2)	η (%)
100	20	670	10.9	420	8.35	48.1	3.51	100	3.51
	40	670	7.75	360	5.37	37.2	1.93	100	1.93
	60	590	8.35	300	4.77	29.0	1.43	100	1.43
	120	680	8.58	350	5.51	33.1	1.93	100	1.93
	180	660	8.93	340	5.14	29.7	1.75	100	1.75
50	20	660	7.75	400	5.57	43.6	2.23	100	2.23
	40	680	7.79	400	5.30	40.0	2.12	100	2.12
	60	680	9.79	390	5.89	34.5	2.30	100	2.30
	120	660	8.12	380	5.55	39.4	2.11	100	2.11
	180	660	7.94	350	5.51	36.8	1.93	100	1.93
20	20	540	1.91	360	1.49	52.0	0.54	100	0.54
	40	600	2.77	400	2.19	52.7	0.88	100	0.88
	60	630	4.49	390	3.48	48.0	1.36	100	1.36
	120	650	7.73	440	6.04	52.9	2.66	100	2.66
	180	670	9.55	400	6.42	40.1	2.57	100	2.57
10	20	600	1.89	360	1.41	44.8	0.51	100	0.51
	40	610	3.21	390	2.47	49.2	0.96	100	0.96
	60	620	4.89	400	3.89	51.3	1.56	100	1.56
	120	650	7.14	410	5.17	45.7	2.12	100	2.12
	180	660	9.16	400	6.76	44.7	2.70	100	2.70
5	20	510	1.15	350	0.82	48.9	0.29	100	0.29
	40	560	2.09	370	1.54	48.7	0.57	100	0.57
	60	600	2.77	390	2.08	48.8	0.81	100	0.81
	120	620	4.62	390	3.44	46.8	1.34	100	1.34
	180	630	6.75	410	5.20	50.1	2.13	100	2.13
	480	700	9.45	440	6.57	43.7	2.89	100	2.89

By comparing the overall efficiency within a group of samples sensitized in the same N3 dye concentration, a trend is observed. Figure 4.34 is a plot of overall efficiency as a function of immersion time for a) 100%, b) 50%, c) 20%, and d) 10% N3 dye concentrations. It is shown that the highest point, or the highest overall efficiency, in each plot occurs at 20, 60, 120, and 180 minutes for 100%, 50%, 20%, and 10% N3 dye concentrations, respectively. Figure 4.35 is a plot of the highest overall efficiency obtained within each concentration as a function of time immersed in the various concentrations. It can be seen that a higher N3 dye concentration required a shorter amount of immersion time for sufficient dye adsorption to obtain a higher overall efficiency. A lower N3 dye concentration required a longer amount of immersion time for sufficient dye sensitization, resulting in a higher overall efficiency.

The ZnO nanoparticle film had the highest overall efficiency of ~ 3.51% when sensitized in N3 dye with 100% concentration for 20 minutes. With a 50% N3 dye concentration, the ZnO nanoparticle film immersed for 60 minutes had the highest overall efficiency with a value of ~ 2.30%. At 20% N3 dye concentration, the highest overall efficiency of ~ 2.66% was obtained from the ZnO nanoparticle film immersed for 120 minutes. Additionally, the ZnO nanoparticle film sensitized in N3 dye with 10% concentration for 180 minutes resulted in a higher overall efficiency of ~ 2.70%. An even longer immersion time was used with the 5% dye concentration. The ZnO nanoparticle film sensitized in N3 dye with 5% concentration for 480 minutes resulted in a higher overall efficiency with a value of ~ 2.89%.

At higher concentrations, shorter immersion times in N3 dye was needed for sufficient dye adsorption. At lower concentrations, a longer immersion time in N3 dye

was needed for sufficient dye adsorption. The ZnO nanoparticle film sensitized in 100%, 50%, 20%, and 10% N3 dye concentration was observed to require 20, 60, 120, 180, and 480 minutes of immersion, respectively, to obtain a higher overall efficiency. At 5% N3 dye concentration, a much longer time was needed to obtain a higher overall efficiency.

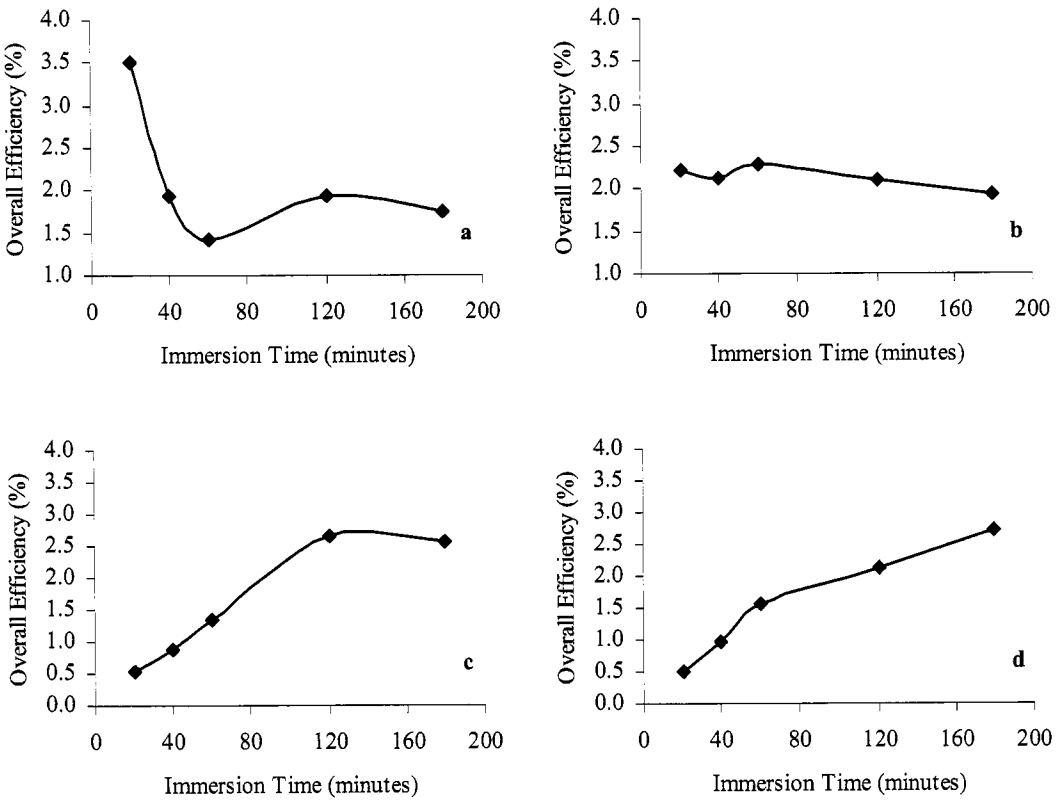

Figure 4.34. Plot of overall efficiency as a function of dye immersion time in a) 100%, b) 50%, c) 20%, and d) 10% concentrations. The ZnO nanoparticle films were immersed for 20, 40, 60, 120, and 180 minutes in each N3 dye concentration before testing.

From the data, it can be observed that the amount of dye loading in ZnO nanoparticle film is highly dependent on the dye concentration and the amount of immersion time. With high dye concentration, a shorter time is needed for sufficient dye adsorption since a larger number of dye molecules are available to attach to the ZnO surface so not much time is needed for complete dye coverage. If longer times are used in

highly concentrated dye, less adsorption would occur due to surface dissolution, where dye molecules are desorbed from the ZnO surface. This is evident by the lower overall efficiency obtained for ZnO nanoparticle film immersed in 100% concentration for over 60 minutes. With low dye concentration, a longer time is needed for sufficient dye adsorption since a smaller number of dye molecules are present. With low concentrations, better assembly of the dye is allowed but the process of assembly for complete coverage is slow, resulting in the need for longer times. This is evident by the higher overall efficiency obtained for ZnO nanoparticle film immersed in 10% and 5% concentrations for over 120 minutes. Therefore, high concentrations require shorter immersion times and low concentrations require longer immersion times, as evident in Figure 4.35.

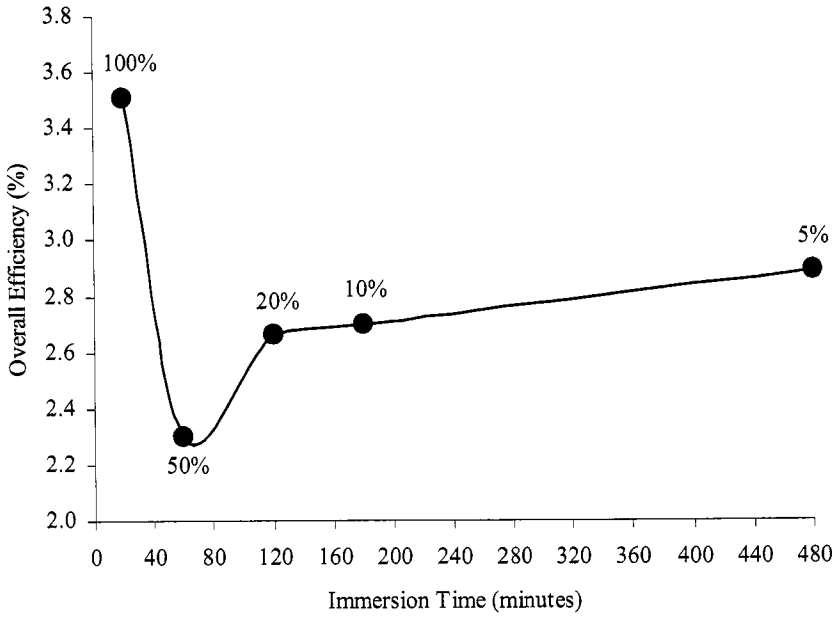

Figure 4.35. Plot of the highest overall efficiency obtained from ZnO nanoparticle film immersed in 100%, 50%, 20%, 10%, and 5% N3 dye concentrations. For each N3 dye concentration, films were immersed for 20, 40, 60, 120, and 180 minutes. The highest overall efficiency in each group is plotted.

4.3.6 Comparison of data obtained from prepared ZnO nanoparticle and nanowire film with values found in literature

Based on the literature data, the highest overall efficiency obtained for ZnO nanoparticle film[81] has been ~ 5% with an open-circuit voltage of ~ 560mV, a short-circuit current density of ~ 1.3mA/cm^2, and a fill factor of ~ 68% under 100mW/cm^2 illumination. For ZnO nanowire film[97], the highest efficiency has been ~ 1.5% with an open-circuit voltage of ~ 700mV, a short-circuit current density of ~ 6.0mA/cm^2, and a fill factor of ~ 37% under 100mW/cm^2 illumination. In this chapter, it was observed that ZnO nanoparticle films with secondary colloidal spheres and primary nanoparticles had an efficiency of ~ 3.5% with an open-circuit voltage of ~ 670mV, a short-circuit current density of ~ 10.9mA/cm^2, and a fill factor of ~ 48% under 100mW/cm^2 illumination. In addition, ZnO nanowire arrays had an efficiency of ~ 0.4% with an open-circuit voltage of ~ 530mV, a short-circuit current density of ~ 1.90mA/cm^2, and a fill factor of ~ 37% under 100mW/cm^2 illumination. The reason for much lower values could be due to the fabrication and quality of the films since the fabrication of ZnO nanostructured films for dye-sensitized solar cells was recently started and still in the experimental stage. In addition, the ZnO films with the highest efficiency ~ 5% were prepared using an additional compression step to pack the ZnO nanoparticle more closely. However, in the tested films, compression was not used, which could have been the reason for the lower efficiency. Other reports[86] of ZnO film without the utilization of the compression method resulted in efficiency ~ 2%. Therefore, the results for sol-gel-derived ZnO nanoparticle films and ZnO nanowire films show great potential for further improving the solar cell performance of ZnO electrodes.

4.4 Conclusions

In summary, ZnO nanoparticles were fabricated by way of sol-gel processing and consist of secondary colloidal spheres and primary nanoparticles on the surface. In addition, ZnO nanowire arrays were fabricated by way of an aqueous solution method. Both types of films were tested in solar cells and compared to the solar cell performance of commercially-available ZnO nanoparticle film.

In conclusion, it was found that the sol-gel-derived ZnO nanoparticle film resulted in a higher short-circuit current density of ~ 10.9mA/cm^2 and a higher overall efficiency of ~ 3.5%. The increase in short-circuit current density by ~ 4.2mA/cm^2 and the increase in overall efficiency by ~ 2.3%, as compared to the values obtained for commercially-obtained ZnO nanoparticle film, may have been due to the presence of larger secondary spheres and smaller primary nanoparticles in the sol-gel-derived ZnO film. The presence of primary nanoparticles on the surface of the secondary spheres is thought to increase the surface area, resulting in more dye adsorption and electrons generated. The presence of secondary spheres is thought to promote enhanced light scattering to disperse photons more effectively, allowing for more photons to be absorbed. In the case of ZnO nanowires, the low efficiency may have been due to 1) the random growth of the nanowires, 2) the variation in dimensions, and 3) the shorter length.

Additionally, it was found that 1) a higher concentration has a larger amount of dye molecules to saturate the surface quicker, where a longer immersion time may eventually cause surface dissolution, and 2) a lower concentration has a smaller amount of dye molecules for slower surface saturation, where a shorter or longer immersion time may result in incomplete surface coverage or better dye assembly, respectively.

Notes to Chapter 4

[136] D. Jezequel, J. Guenot, N. Jouini, and F. Fievet, "Preparation and Morphological Characterization of Fine, Spherical, Monodispersed Particles of ZnO," *Materials Science Forum* **339**, 152 (1994).

5 Future work

The previous chapters outlined the solar cell performance of 1) TiO_2 nanoparticle films with various particle sizes, 2) TiO_2-ITO nanocomposite films, and 3) ZnO nanoparticle and nanowire films. In addition, the dye loading effect on TiO_2 and ZnO nanoparticle films were studied.

In Chapter 2, by comparing the solar cell performance of TiO_2 nanoparticle films with varying particle sizes by way of varying the hydrothermal treatment temperature and time, it was found that the highest overall efficiency ~ 5.2% was obtained for TiO_2 film consisting of ~ 18nm diameter nanoparticles.

In Chapter 3, by comparing the solar cell performance of three types of TiO_2-ITO nanocomposite films, it was found that the addition of ITO nanoparticles to the TiO_2 nanoparticle film resulted in an increase in the overall efficiency from ~ 4.7% to ~ 5.6%, showing an ~ 19% improvement.

In Chapter 4, by comparing the solar cell performance of sol-gel-derived ZnO nanoparticle film with that of commercially-obtained ZnO nanoparticle film, it was found that the hierarchical structure of the sol-gel-derived ZnO nanoparticle film consisting of primary nanoparticle and secondary colloidal spheres, resulted in an increase in the overall efficiency from ~ 1.2% to ~ 3.5%.

Further studies to improve the solar cell performance were made by modifying the sensitizer concentration and the immersion time for TiO_2 and ZnO nanoparticle films. It was found that a higher sensitizer dye concentration required a shorter immersion time and a lower sensitizer dye concentration required a longer immersion time for complete surface coverage and better dye assembly.

In this chapter, further studies are outlined to continue the exploration of TiO_2 and ZnO nanoparticle films for use in dye-sensitized solar cells. In addition, hierarchically-structured nanowire arrays, nanocable arrays, and other nanocomposite structures for use in dye-sensitized solar cells are also detailed in the following sections.

5.1 Solar cell performance of TiO_2 nanoparticle film fabricated by way of combining hydrothermal crystallization and electrophoretic deposition

With the results from Chapter 2, it was found that hydrothermal crystallization of TiO_2 can vary the particle size from ~ 7nm up to ~ 18nm by varying the hydrothermal treatment temperature. In addition, the TiO_2 film with ~ 18nm diameter nanoparticles showed the highest overall efficiency. The process of hydrothermal crystallization, in conjunction with the electrophoretic deposition process[137,138], could be further studied in an effort to control the fabrication of TiO_2 nanoparticle film in order to improve the film quality and properties for use in dye-sensitized solar cells. Currently, the process of fabricating the nanoparticle films involves preparing a powder slurry and doctor-blading the film on a conductive substrate using 10μm-thick tape along the edges to control the thickness. This process can be time-consuming and the resulting films can vary in quality and thickness. In addition, the powder slurry can cause agglomeration and clustering of the individual nanoparticles during film formation.

By utilizing both hydrothermal crystallization and electrophoretic deposition[139,140], the fabrication of the film could be easier and the quality of the film could be improved. The dispersion of TiO_2 nanoparticles can be easily prepared by hydrothermal treatment and the resulting paste is easily dispersed in deionized water. The

deposition of the film on a conducting ITO or FTO substrate by electrophoretic deposition would only require the TiO_2 dispersion, a counter electrode, and an applied potential. With hydrothermal crystallization and electrophoretic deposition, there are a few advantages. These include: 1) simple tailoring of particle size by changing the hydrothermal treatment temperature, 2) easier control of film thickness by varying the deposition time, and 3) better potential for forming a more porous film by manipulating the migration and deposition of the nanoparticles to the conducting surface. Figure 5.1 shows the SEM images of TiO_2 nanoparticle film fabricated by way of hydrothermal treatment and electrophoretic deposition on an ITO substrate.

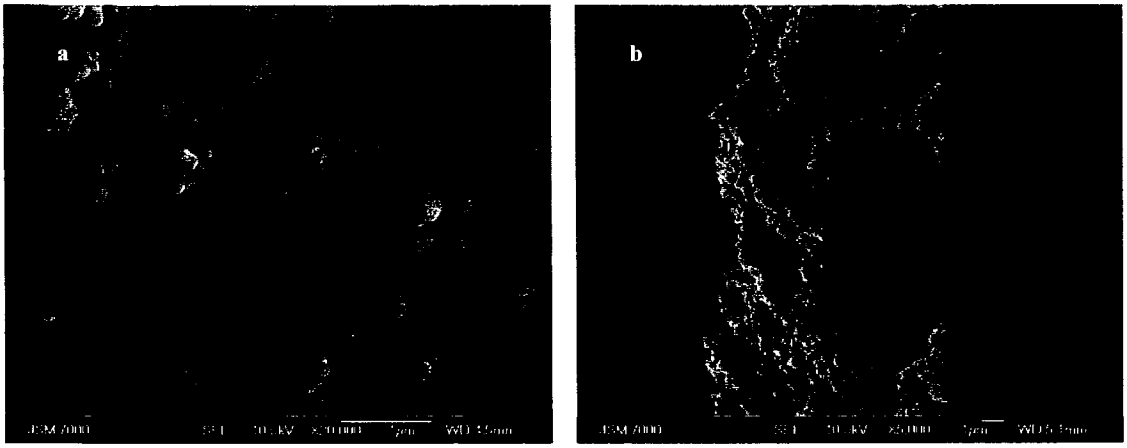

Figure 5.1. SEM images of TiO_2 nanoparticle film showing a) the top morphology, and b) the thickness of the film. The film was fabricated by combining hydrothermal crystallization and electrophoretic deposition.

These preliminary results show that the deposition of porous TiO_2 nanoparticle film is possible using electrophoretic deposition. The TiO_2 nanoparticle film in the SEM images was fabricated from an aqueous dispersion of hydrothermally treated TiO_2 at 250°C for 20 minutes and deposited onto an ITO substrate using a voltage of ~ 1V at an ~ 3mm distance for ~ 12 hours. It can be seen that the nanoparticle film is highly porous and that a film with thickness ~ 10μm is feasible.

Figure 5.2 shows the ideal process of film formation by electrophoretic deposition of a dispersion of TiO_2 nanoparticles obtained by hydrothermal treatment. In this manner, a solution-based method for growing thick porous film, as well as the possibility of single crystal growth, can be utilized for the formation of patterned microstructures[141]. This process to control the formation of thick porous film made of an arranged network of nanoparticles, and to promote homoepitaxial alignment of nanocrystals involves: 1) sol-gel processing of nanoclusters individually dispersed in liquid with desired stoichiometric composition, 2) hydrothermal crystallization in solution at relatively low temperatures, and 3) electrophoretic deposition to direct the migration and aggregation of nanocrystals[137,138] to form thick porous film.

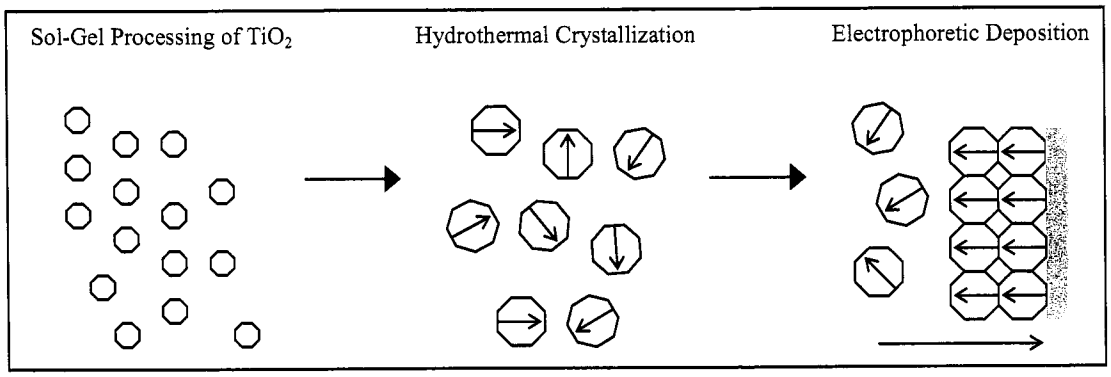

Figure 5.2. Schematic of TiO_2 film formation on a conducting substrate using sol-gel processing, hydrothermal crystallization, and electrophoretic deposition.

5.2 Comparison of solar cell performance of TiO_2 and ZnO nanoparticle films by incorporating various amounts of ITO

A more in-depth study of the results from Chapter 3 on the incorporation of ITO nanoparticles into TiO_2 nanoparticle film to fabricate nanocomposite films could be beneficial for further improvement in dye-sensitized solar cells by reducing the internal resistance[142]. The exploration into incorporating ITO nanoparticles into ZnO nanoparticle

film could also be advantageous. Since it was found that the addition of ITO nanoparticles into TiO_2 nanoparticle film increased the short-circuit current density from ~ 12.8mA/cm^2 to ~ 15.3mA/cm^2 and increased the overall efficiency from ~ 4.7% to ~ 5.6%, it would be interesting to see if the amount of ITO added would affect the solar cell performance. The increase in short-circuit current density and overall efficiency was obtained by adding a 20 wt% amount of ITO into the TiO_2 nanoparticle slurry before film formation. By varying the concentration of ITO added and comparing the solar cell performance of those films, the effect of ITO doping on the charge transport properties could be explored from variations in the short-circuit current density, open-circuit voltage, or overall light conversion efficiency. Since it is unknown what effect the addition of ITO has on the TiO_2 nanoparticle film, the solar cell performance of TiO_2 nanoparticle films with the addition of more or less than 20 wt% ITO could be compared. In addition, the same variation of ITO added to the ZnO nanoparticle film could also be utilized to enhance the solar cell performance of those films.

5.3 Fabrication of ITO-TiO_2 and ZnO-TiO_2 nanocomposite structures for dye-sensitized solar cells

The further exploration into nanocomposite films with nanoparticles or nanowires of two types of materials could also be advantageous. By utilizing ITO or ZnO, and combining one of those materials with TiO_2, there is a great potential for improving the solar cell performance of dye-sensitized solar cells. Since TiO_2 has been widely explored for dye-sensitized solar cells, but so far has not improved over ~ 10% efficiency for the past decade, the addition of ITO or ZnO with higher electron mobility[94,131] of ~ 40-70

cm^2/Vs and ~ 115-155cm^2/Vs, respectively, could improve the efficiency of TiO_2, which is limited to an electron mobility of ~ $10^{-5}cm^2/Vs$. Figure 5.3 shows the possible nanocomposite structures in the ideal case. These nanocomposite structures consist of a) ITO or ZnO nanoparticle film with a thin layer of TiO_2 coating, b) ITO or ZnO nanowire arrays with a thin layer of TiO_2 coating, and c) ITO or ZnO nanowire arrays with a thin layer of TiO_2, and the addition of mesoporous TiO_2 to fill the gaps between nanowires.

In the first nanocomposite structure, ITO or ZnO nanoparticle film is fabricated on transparent and conductive ITO or FTO substrates. The ITO film consists of nanoparticles with a diameter of ~ 9nm. The ZnO film consists of secondary colloidal spheres ~ 300nm in diameter and primary nanoparticles ~ 20nm in diameter. In the second nanocomposite structure, ITO or ZnO nanowire arrays are fabricated on ITO or FTO substrates by way of sol-gel processing and template-assisted electrophoretic deposition[143], as detailed in Chapter 3, or an aqueous solution method, as detailed in Chapter 4, respectively. The ITO nanowires are ~ 100nm in diameter and ~ 10μm in length. The ZnO nanowires are ~ 50-100nm in diameter and ~ 2-5μm in length, but the dimensions can vary depending on the growth time. In the third nanocomposite structure, an additional layer of mesoporous TiO_2 by way of sol-gel processing is incorporated into the ITO-TiO_2 or ZnO-TiO_2 nanocable array structure to fill in the space between each nanocable to form a complete film.

There are a few techniques that can be studied to incorporate a thin layer of TiO_2 onto the nanoparticle and nanowire structures. A relatively uniform coating < 10nm thick is difficult with conventional sol-gel coatings since these coatings are typically deposited from sols consisting of nanoclusters or nanoparticles a few nanometers in diameter in >

90% solvent that make it difficult to form a continuous film < 10nm. Therefore, induced pH deposition, electrochemical deposition, and monolayer adsorption through hydrolysis and condensation reactions would be studied.

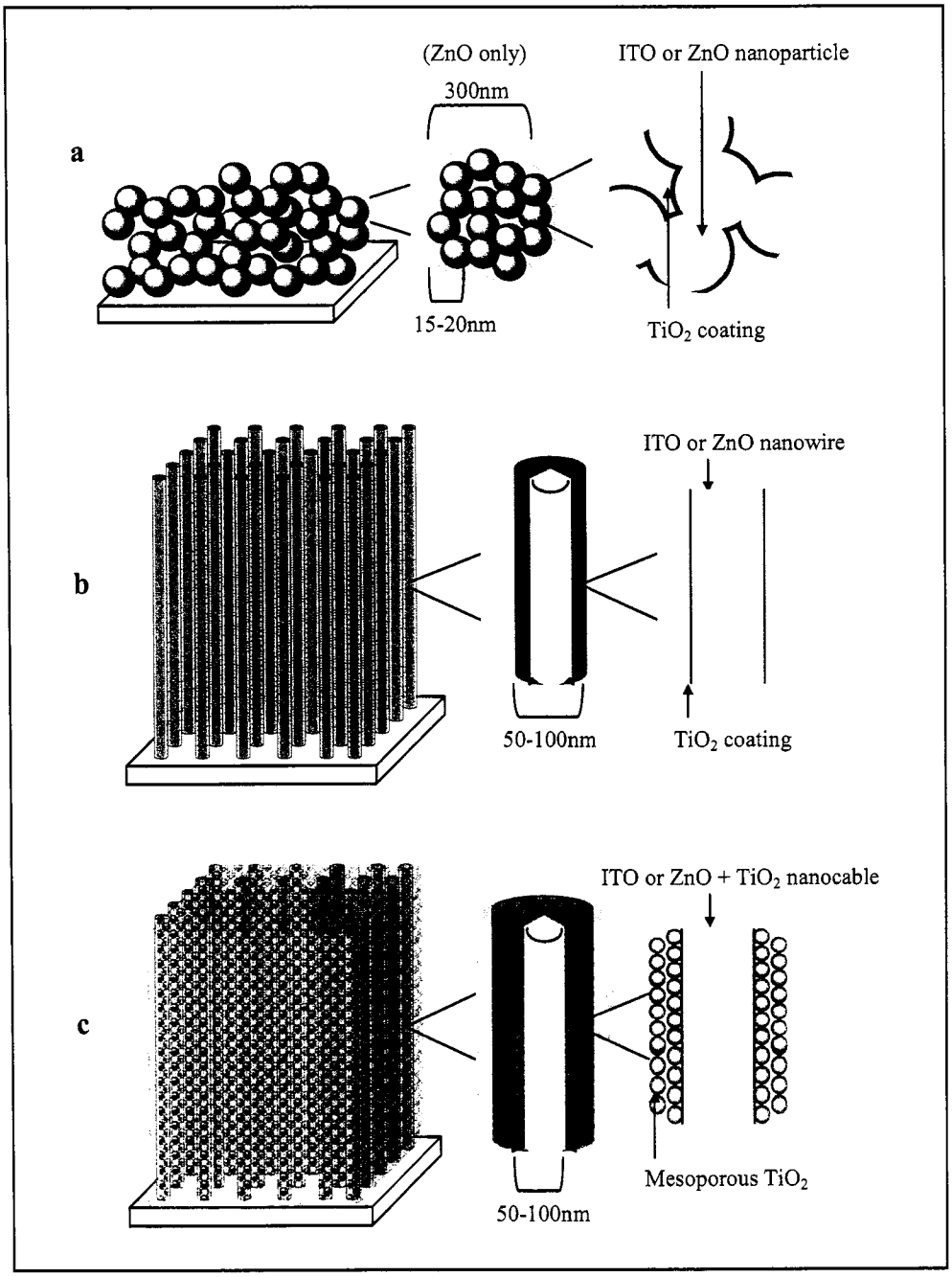

Figure 5.3. Schematic of the ideal nanocomposite structures, showing a) ITO or ZnO nanoparticle film with a layer of TiO_2, b) ITO or ZnO nanocable arrays consisting of an outer layer of TiO_2, and c) ITO or ZnO nanocable arrays with an additional mesoporous TiO_2 layer.

In the case of induced pH deposition[144] and electrochemical deposition[139,145], an electrolyte solution containing TiO ionic clusters would be used to electrodeposit TiO_2 potentiostatically. The TiO ionic clusters are stable only at a certain narrow range of pH so a change of pH often leads to precipitation of the solid oxide either through agglomeration and/or reduction-oxidation reaction. When ITO or ZnO are brought in contact with this ionic solution in an external electric field, hydrolysis of water would occur at the surface of ITO or ZnO, which results in a change of pH at the vicinity of the solid-liquid interface, leading to the deposition of TiO_2 on the surface. Since both induced pH deposition and direct electrochemical deposition have already been applied to the growth of V_2O_5 nanowires[144] and films, these two methods can be applicable to the TiO_2 system for the formation of a TiO_2 layer.

In the case of monolayer adsorption through hydrolysis and condensation reactions, a 0.01M non-aqueous stock solution consisting of either a titanium alkoxide or a titanium chloride precursor dissolved in ethanol would be utilized to form a monolayer of TiO_2 on the nanowire or nanoparticle surface. The surface of ITO or ZnO would be hydrolyzed with –OH groups by immersion in water at an elevated temperature, and the TiO_2 layer would be formed by reaction of the hydrolyzed surface to the Ti precursor solution. Further hydrolysis reactions would be induced on the surface by exposure to water for a long period of time.

The fabrication of ITO and ZnO nanowire arrays could also be optimized with continued efforts to improve the quality and electrical properties of those nanowire films. Further studies could be done in an attempt to improve the fabrication process to reduce the internal resistance and improve the quality of the nanowires. It is ideal to obtain

nanowires that are uniform, free-standing, and unidirectionally-aligned. This type of ordered arrangement would be ideal for use in dye-sensitized solar cells since the hierarchical structure would provide simple electron percolation pathways[146], so as to reduce the number of obstacles that can hinder electron transport. In addition, ordered nanowire arrays would be ideal for easier incorporation of a thin TiO_2 coating to the surface of the ITO or ZnO nanowires to form a nanocable structure.

5.4 Other considerations

In addition to ITO and ZnO as additional materials to TiO_2 that can be utilized in dye-sensitized solar cells, fluorine-doped tin-oxide (FTO) can also be considered as another material to explore. The electron mobility[135] of FTO is lower than that for ITO and ZnO with a value of ~ 9.3-11.8cm^2/Vs, but has better thermal stability at elevated temperatures. It has been shown that the conductivity of ITO is much lower after sintering to 500°C when preparing TiO_2 film, but the conductivity of FTO stays relatively the same even after sintering to 500°C. The stability of FTO would be advantageous for the nanowire structure, which has been shown to have higher internal resistance than that for thin films. In addition, FTO nanoparticles or nanowires can be utilized in coreshell and nanocable structures, where the inner core consists of FTO and the outer shell consists of TiO_2 in both types of structures.

In addition, single crystal nanowires[102,147,148] could also be explored. It has been reported that electron conduction in single crystal materials is higher than that in polycrystalline materials[52,149]. The conduction of electrons can be hindered by grain boundaries in polycrystalline materials. It has been shown that electrons migrating

through the TiO_2 nanocrystalline film are much slower than that through single crystal TiO_2. In addition, charge transport can be influenced by a high density of trap states associated with a large surface area in nanocrystalline films by affecting both mobility and recombination. With single crystal nanowires, there is great potential for faster electron conduction by combining the simple electron percolation pathway associated with the nanowire array structure and the nonexistent grain boundaries associated with single crystal material. The single-crystal nanowire structure can also be utilized in the nanocable array structure.

[137] O.O. Van der Biest and L.J. Vandeperre, "Electrophoretic Deposition of Materials," *Annual Review of Materials Science* **29**, 327 (1999).

[138] P. Sarker and P.S. Nicholson, "Electrophoretic Deposition (EPD): Mechanism, Kinetics, and Application to Ceramics," *Journal of the American Ceramic Society* **79**, 1987 (1996).

[139] C. Natarajan and G. Nogami, "Electrodeposition of Nanocrystalline Titanium Dioxide Thin Films," Journal of the *Electrochemical Society* **143**, 1547 (1996).

[140] R. Shacham, D. Avnir, and D. Mandler, "Electrodeposition of Dye-Doped Titania Thin Film," *Journal of Sol-Gel Science and Technology* **31**, 329 (2004).

[141] I. Zhitomirsky, "Cathodic Electrodeposition of Ceramic and Organoceramic Materials. Fundamental Aspects," *Advanced Colloid Interface Science* **97**, 277, (2002).

[142] L. Han, N. Koide, Y. Chiba, A. Islam, R. Komiya, N. Fuke, A. Fukui, and R. Yamanaka, "Improvement of efficiency of dye-sensitized solar cells by reduction of internal resistance," *Applied Physics Letters* **86**, 213501 (2005).

[143] G.Z. Cao, "Growth of Oxide Nanorod Arrays through Sol Electrophoretic Deposition," *Journal of Physical Chemistry B* **108**, 19921 (2004).

[144] K. Takahashi, S.J. Limmer, Y. Wang, and G.Z. Cao, "Synthesis and Electrochemical Properties of Single Crystal V_2O_5 Nanorod Arrays by Template-Based Electrodeposition," *Journal of Physical ChemistryB* **108**, 9795 (2004).

[145] S. Karuppuchamy, K. Nonomura, T. Yoshida, T. Sugiura, and H. Minoura, "Cathodic Electrodeposition of oxide semiconductor thin films and their application to dye-sensitized solar cells," *Solid State Ionics* **151**, 19 (2002).

[146] S. Chappel, L. Grinis, A. Ofir, and A. Zaban, "Extending the Current Collector into the Nanoporous Matrix of Dye Sensitized Electrodes," *Journal of Physical Chemistry B* **109**, 1643 (2005).

[147] Z. Miao, D. Xu, J. Ouyang, G. Guo, X. Zhao, and Y. Tang, "Electrochemically Induced Sol-Gel Preparation of Single-Crystalline TiO_2 Nanowires," *Nanoletters* **2**, 717 (2002).

[148] M. Adachi, Y. Murata, I. Okada, and S. Yoshikawa, "Formation of Titania Nanotubes and Applications for Dye-Sensitized Solar Cells," *Journal of the Electrochemical Society* **150**, G488 (2003).

[149] L. Kavan, M. Grätzel, S.E. Gilbert, C. Klemenz, and H.J. Scheel, "Electrochemical and Photoelectrochemical Investigation of Single-Crystal Anatase," *Journal of the American Chemical Society* **118**, 6716 (1996).

Bibliography

A. Hagfeldt and M. Grätzel, "Light-Induced Redox Reactions in Nanocrystalline Systems," *Chemical Reviews* **95**, 49 (1995).

A. Hagfeldt and M. Grätzel, "Molecular Photovoltaics," *Accounts of Chemical Research* **33**, 269 (2000).

A. Hagfeldt, G. Boschloo, H. Lindström, E. Figgemeier, A. Holmberg, V. Aranyos, E. Magnusson, and L. Malmqvist, "A system approach to molecular solar cells," *Coordination Chemistry Reviews* **248**, 1501 (2004).

A. Mills and S.L. Hunte, "An overview of semiconductor photocatalysis," *Journal of Photochemistry and Photobiology A: Chemistry* **108**, 1 (1997).

A.B. Kashyout, M. Soliman, M. El Gamal, and M. Fathy, "Preparation and characterization of nanoparticles ZnO films for dye-sensitized solar cells," *Materials Chemistry and Physics* **90**, 230 (2005).

A.E. Rakhshani, Y. Makdisi, and H.A. Ramazaniyan, "Electronic and optical properties of fluorine-doped tin oxide films," *Journal of Applied Physics* **83**, 1049 (1998).

A.J. Frank, N. Kopidakis, J. van de Lagemaat, "Electrons in nanostructured TiO_2 solar cells: transport, recombination and photovoltaic properties," *Coordination Chemistry Reviews* **248**, 1165 (2004).

A.M. Eppler, I.M. Ballard, and J. Nelson, "Charge transport in porous nanocrystalline titanium oxide," *Physica E* **14**, 197 (2002).

A.N.M. Green, E. Palomares, S.A. Haque, J.M. Kroon, and J.R. Durrant, "Charge Transport versus Recombination in Dye-Sensitized Solar Cells Employing Nanocrystalline TiO_2 and SnO_2 Films," *Journal of Physical Chemistry B* **109**, 12525 (2005).

ASTM International Standards 2006, <http://www.astm.org>

B. Kannan, K. Castelino, and A. Majumdar, "Design of Nanostructured Heterojunction Polymer Photovoltaic Devices," *Nanoletters* **3**, 1729 (2003).

B. Tan and Y. Wu, "Dye-Sensitized Solar Cells Based on Anatase TiO_2 Nanoparticle/Nanowire Composites," *Journal of Physical Chemistry B*, in press.

B.A. Gregg, "Excitonic Solar Cells," *Journal of Physical Chemistry B* **107**, 4688 (2003).

B.A. Gregg, "Interfacial processes in the dye-sensitized solar cell," *Coordination Chemistry Reviews* **248**, 1215 (2004).

B.D. Cullity. *Elements of X-Ray Diffraction*. 2nd ed. Reading, Mass: Addison-Wesley Publishing Co, 1956.

C. Guillard, B. Beaugiraud, C. Dutriez, J.M. Herrmann, H. Jaffrezic, N. Jaffrezic-Renault, and M. Lacroix, "Physicochemical properties and photocatalytic activities of TiO_2-films prepared by sol-gel methods," *Applied Catalysis B: Environmental* **39**, 331 (2002).

C. Natarajan and G. Nogami, "Electrodeposition of Nanocrystalline Titanium Dioxide Thin Films," Journal of the *Electrochemical Society* **143**, 1547 (1996).

C.H. Ku and J.J. Wu, "Aqueous Solution Route to High Aspect-Ratio Zinc Oxide Nanostructures on Indium Tin Oxide Substrates," *Journal of Physical Chemistry B* **110**, 12981 (2006).

C.J. Barbé, F. Arendse, P. Comte, M. Jirousek, F. Lenzmann, V. Shklover, and M. Grätzel, "Nanocrystalline Titanium Oxide Electrodes for Photovoltaic Applications," *Journal of the American Ceramic Society* **80**, 3157 (1997).

C.J. Brabec and N.S. Sariciftci, "Polymeric photovoltaic devices," *Materials Today*, 3 (2000).

D. Cahen and G. Hodes, "Nature of Photovoltaic Action in Dye-Sensitized Solar Cells," *Journal of Physical Chemistry B* **104**, 2053 (2000).

D. Gebeyehu, C.J. Brabec, and N.S. Sariciftci, "Solid-state organic/inorganic hybrid solar cells based on conjugated polymers and dye-sensitized TiO_2 electrodes," *Thin Solid Films* **403-404**, 271 (2002).

D. Jezequel, J. Guenot, N. Jouini, and F. Fievet, "Preparation and Morphological Characterization of Fine, Spherical, Monodispersed Particles of ZnO," *Materials Science Forum* **339**, 152 (1994).

D. Menzies, Q. Dai, Y.B. Cheng, G.P. Simon, and L. Spiccia, "Improvement of the Zirconia shell in nanostructured titania core-shell working electrodes for dye-sensitized solar cells," *Materials Letters* **59**, 1893 (2005).

D. Mergel, M. Schenkel, M. Ghebre, and M. Sulkowski, "Structural and electrical properties of In_2O_3:Sn films prepared by radio-frequency sputtering," *Thin Solid Films* **392**, 91 (2001).

D. Wöhrle and D. Meissner, "Organic Solar Cells," *Advanced Materials* **3**, 129 (1991).

D. Zhang, T. Yoshida, and H. Minoura, "Low Temperature Synthesis of Porous Nanocrystalline TiO_2 Thick Film for Dye-Sensitized Solar Cells by Hydrothermal Crystallization," *Chemistry Letters*, 874 (2002).

D. Zhang, T. Yoshida, K. Furuta, and H. Minoura, "Hydrothermal preparation of porous nano-crystalline TiO_2 electrodes for flexible solar cells," *Journal of Photochemistry and Photobiology A: Chemistry* **163**, 159 (2004).

D. Zhang, T. Yoshida, K. Furuta, and H. Minoura, "Hydrothermal preparation of porous nano-crystalline TiO_2 electrodes for flexible solar cells," *Journal of Photochemistry and Photobiology A: Chemistry* **164**, 159 (2004).

D.B. Menzies, L. Bourgeois, Y.B. Cheng, G.P. Simon, N. Brack, and L. Spiccia, "Characterization of nanostructured core-shell working electrodes for application in dye-sensitized solar cells," *Surface & Coatings Technology* **198**, 118 (2005).

D.E. Aspnes and A. Heller, "Photoelectrochemical Hydrogen Evolution and Water-Photolyzing Semiconductor Suspensions: Properties of Platinum Group Metal Catalyst-Semiconductor Contacts in Air and In Hydrogen," *Journal of Physical Chemistry* **87**, 4919 (1983).

E. Palomares, J.N. Clifford, S.A. Haque, T. Lutz, and J.R. Durrant, "Control of Charge Recombination Dynamics in Dye Sensitized Solar Cells by the Use of Conformally Deposited Metal Oxide Blocking Layers," *Journal of the American Chemical Society* **125**, 475 (2003).

E.M. Kaidashev, M. Lorenz, H. von Wenckstern, A. Rahm, H.C. Semmelhack, K.H. Han, G. Benndorf, C. Bundesmann, H. Hochmuth, and M. Grundmann, "High electron mobility of epitaxial ZnO thin films on c-plane sapphire grown by multistep pulsed-laser deposition," *Applied Physics Letters* **82**, 3901 (2003).

Evergreen Solar 2006, *Applications*, <http://evergreensolar.com/>

F. Gracia, J.P. Holgado, and A.R. González-Elipe, "Photoefficiency and Optical, Microstructural, and Structural Properties of TiO_2 Thin Films Used as Photoanodes," *Langmuir* **20**, 1688 (2004).

F. Pichot and B.A. Gregg, "The Photovoltage-Determining Mechanism in Dye-Sensitized Solar Cells," *Journal of Physical Chemistry B* **104**, 6 (2000).

F. Pichot, J.R. Pitts, and B.A. Gregg, "Low-Temperature Sintering of TiO_2 Colloids: Application to Flexible Dye-Sensitized Solar Cells," *Langmuir* **16**, 5626 (2000).

F. Fabregat-Santiago, J. Bisquert, G. Garcia-Belmonte, G. Boschloo, and A. Hagfeldt, "Influence of electrolyte in transport and recombination in dye-sensitized solar cells studied by impedance spectroscopy," *Solar Energy Materials & Solar Cells* **87**, 117 (2005).

G. Boschloo, H. Lindström, E. Magnusson, A. Holmberg, and A. Hagfeldt, "Optimization of dye-sensitized solar cells prepared by compression method," *Journal of Photochemistry and Photobiology A: Chemistry* **148**, 11 (2002).

G. Hodes, I.D.J. Howell, and L.M. Peter, "Nanocrystalline Photoelectrochemical Cells: A New Concept in Photovoltaic Cells," *Journal of the Electrochemical Society* **139**, 3136 (1992).

G. Yu, J. Gao, J.C. Hummelen, F. Wudl, and A.J. Heeger, "Polymer photovoltaic cells: enhanced efficiencies via a network of internal donor acceptor heterojunctions," *Science* **270**, 1789 (1995).

G.K. Mor, K. Shankar, M. Paulose, O.K. Varghese, C.A. Grimes, "Use of Highly-Ordered TiO_2 Nanotube Arrays in Dye-Sensitized Solar Cells," *Nanoletters* **6**, 215 (2006).

G.K. Mor, O.K. Varghese, M. Paulose, K. Shankar, and C.A. Grimes, "A review on highly ordered, vertically oriented TiO_2 nanotube arrays: Fabrication, material properties, and solar energy applications," *Solar Energy Materials and Solar Cells* **90**, 2011 (2006).

G.P. Smestad, "*Nanocrystalline Solar Cell Kit: Recreating Photosynthesis*," eds. A. Huseth and K. Shanks, ICE Publication, 1998.

G.R.A. Kumara, S. Kaneko, A. Konno, M. Okuya, K. Murakami, B. Onwona-agyeman, and K. Tennakone, "Large Area Dye-sensitized Solar Cells: Material Aspects of Fabrication," *Progress in Photovoltaics: Research and Applications*, in press.

G.Z. Cao, "Growth of Oxide Nanorod Arrays through Sol Electrophoretic Deposition," *Journal of Physical Chemistry B* **108**, 19921 (2004).

G.Z. Cao. Nanostructures & Nanomaterials: Synthesis, Properties, & Applications. London: Imperial College Press, 2004.

Green Car Congress, *Solar-Power-Augmented Prius Takes the Grid Out of "Plug-in"*, 15 August 2005, <http://www.greencarcongress.com/>

H. Hoppe and N.S. Sariciftci, "Organic solar cells: An overview," *Journal of Materials Research* **19**, 1924 (2004).

H. Tributsch, "Dye sensitization solar cells: a critical assessment of the learning curve," *Coordination Chemistry Reviews* **248**, 1511 (2004).

I. Kartini, D. Menzies, D. Blake, J.C.D. da Costa, P. Meredith, J.D. Riches, and G.Q. Lu, "Hydrothermal seeded synthesis of mesoporous titania for application in dye-sensitised solar cells (DSSCs)," *Journal of Materials Chemistry* **14**, 2917 (2004).

I. Zhitomirsky, "Cathodic Electrodeposition of Ceramic and Organoceramic Materials. Fundamental Aspects," *Advanced Colloid Interface Science* **97**, 277, (2002).

J. Bandara, U.W. Pradeep, and R.G.S.J. Bandara, "The role of n-p junction electrodes in minimizing the charge recombination and enhancement of photocurrent and photovoltage in dye sensitized solar cells," *Journal of Photochemistry and Photobiology A: Chemistry* **170**, 273 (2005).

J. Bisquert, A. Zaban, and P. Salvador, "Analysis of the Mechanisms of Electron Recombination in Nanoporous TiO_2 Dye-Sensitized Solar Cells. Nonequilibrium Steady-State Statistics and Interfacial Electron Transfer via Surface States," *Journal of Physical Chemistry B* **106**, 8774 (2002).

J. Bisquert, D. Cahen, G. Hodes, S. Rühle, and A. Zaban, "Physical Chemical Principles of Photovoltaic Conversion with Nanoparticulate, Mesoporous Dye-Sensitized Solar Cells," *Journal of Physical Chemistry B* **108**, 8106 (2004).

J. Jiu, F. Wang, M. Sakamoto, J. Takao, and M. Adachi, "Performance of dye-sensitized solar cell based on nanocrystals of TiO_2 film prepared with mixed template method," *Solar Energy Materials & Solar Cells* **87**, 77 (2005).

J. Jiu, S. Isoda, F. Wang, M. Adachi, "Dye-Sensitized Solar Cells Based on a Single-Crystalline TiO_2 Nanorod Film," *Journal of Physical Chemistry B* **110**, 2087 (2006).

J. Krüger, R. Plass, M. Grätzel, P.J. Cameron, and L.M. Peter, "Charge Transport and Back Reaction in Solid-State Dye-Sensitized Solar Cells: A Study Intensity-Modulated Photovoltage and Photocurrent Spectroscopy," *Journal of Physical Chemistry B* **107**, 7536 (2003).

J. Nelson, "Continuous-time random-walk model of electron transport in nanocrystalline TiO_2 electrodes," *Physical Review B* **59**, 153 74 (1999).

J. Nelson, S.A. Haque, D.R. Klug, and J.R. Durrant, "Trap-limited recombination in dye-sensitized nanocrystalline metal oxide electrodes," *Physical Review B* **63**, 205321-1 (2001).

J. Zhao, A. Wang, P. Altermatt, and M.A. Green, "Twenty-four percent efficient silicon solar cells with double layer antireflection coatings and reduced resistance loss," *Applied Physics Letters* **66**, 3636 (1995).

J.B. Baxter and E.S. Aydil, "Dye-sensitized solar cells based on semiconductor morphologies with ZnO nanowires," *Solar Energy Materials and Solar Cells* **90**, 607 (2006).

J.B. Baxter and E.S. Aydil, "Nanowire-based dye-sensitized solar cells," *Applied Physics Letters* **86**, 053114 (2005).

J.H. Yoon, S.R. Jang, R. Vittal, J. Lee, and K.J. Kim, "TiO_2 nanorods as additive to TiO_2 film for improvement in the performance of dye-sensitized solar cells," *Journal of Photochemistry and Photobiology A: Chemistry* **180**, 184 (2006).

J.H. Yum, S.S. Kim, D.Y. Kim, and Y.E. Sung, "Electrophoretically deposited TiO_2 photo-electrodes for use in flexible dye-sensitized solar cells," *Journal of Photochemistry and Photobiology A: Chemistry* **173**, 1 (2005).

J.J.M. Halls, K. Pickler, R.H. Friend, S.C. Morati, and A.B. Holmes, "Efficient photodiodes from interpenetrating polymer networks," *Nature* **376**, 498 (1995).

J.L. Segura, N. Martin, and D.M. Guldi, "Materials for organic solar cells: the C60/p-conjugated oligomer approach," *Chemical Society Reviews* **34**, 31 (2005).

J.M. Kroon, N.J. Bakker, H.J.P. Smit, P. Liska, K.R. Thampi, P. Wang, S.M. Zakeeruddin, M. Grätzel, A. Hinsch, S. Hore, U. Würfel, R. Sastrawan, J.R. Durrant, E. Palomares, H. Pettersson, T. Gruszecki, J. Walter, K. Skupien, and G.E. Tulloch, "Nanocrystalline Dye-sensitized Solar Cells Having Maximum Performance," *Progress in Photovoltaics: Research and Applications*, in press.

J.R. Durrant, S.A. Haque, and E. Palomares, "Towards optimization of electron transfer processes in dye sensitized solar cells," *Coordination Chemistry Review* **248**, 1247 (2004).

K. Fredin, J. Nissfolk, and A. Hagfeldt, "Brownian dynamics simulations of electrons and ions in mesoporous films," *Solar Energy Materials & Solar Cells* **86**, 283 (2005).

K. Kakiuchi, E. Hosono, and S. Fujihara, "Enhanced photoelectrochemical performance of ZnO electrodes sensitized with N-719," *Journal of Photochemistry and Photobiology A: Chemistry* **179**, 81 (2006).

K. Keis, C. Bauer, G. Boschloo, A. Hagfeldt, K. Westermark, H. Rensmo, and H. Siegbahn, "Nanostructured ZnO electrodes for dye-sensitized solar cell applications," *Journal of Photochemistry and Photobiology A: Chemistry* **148**, 57 (2002).

K. Schwarzburg and F. Willig, "Origin of Photovoltage and Photocurrent in the Nanoporous Dye-Sensitized Electrochemical Solar Cell," *Journal of Physical Chemistry B* **103**, 5743 (1999).

K. Srikanth, V.R. Marathe, and M.K. Mishra, "Role of Electronic Structure of Ruthenium Polypyridyl Dyes in the Photoconversion Efficiency of Dye-Sensitized Solar Cells: Semiempirical Investigation," *International Journal of Quantum Chemistry* **89**, 535 (2002).

K. Takahashi, S.J. Limmer, Y. Wang, and G.Z. Cao, "Synthesis and Electrochemical Properties of Single Crystal V_2O_5 Nanorod Arrays by Template-Based Electrodeposition," *Journal of Physical ChemistryB* **108**, 9795 (2004).

K. Tennakone, P.K.M. Bandaranayake, P.V.V. Jayaweera, A. Konno, and G.R.R.A. Kumara, "Dye-sensitized composite semiconductor nanostructures," *Physica E* **14**, 190 (2002).

K. Triyana, T. Yasuda, K. Fujita, and T. Tsutsui, "Tandem-type organic solar cells by stacking different heterojunction materials," *Thin Solid Films* **477**, 198 (2005).

K.J. Jiang, T. Kitamura, H. Yin, S. Ito, and S. Yanagida, "Dye-sensitized Solar Cells Using Brookite Nanoparticle TiO_2 Films as Electrodes," *Chemistry Letters*, 872 (2002).

K.M.P. Bandaranayake, M.K. Indika Senevirathna, P.M.G.M. Prasad Weligamuwa, and K. Tennakone, "Dye-sensitized solar cells made from nanocrystalline TiO_2 films coated with outer layers of different oxide materials," *Coordination Chemistry Reviews* **248**, 1277 (2004).

L. Han, H. Koide, Y. Chiba, A. Islam, R. Komiya, N. Fuke, A. Fukui, and R. Yamanaka, "Improvement of efficiency of dye-sensitized solar cells by reduction of internal resistance," *Applied Physics Letters* **86**, 213501 (2005).

L. Kavan, M. Grätzel, S.E. Gilbert, C. Klemenz, and H.J. Scheel, "Electrochemical and Photoelectrochemical Investigation of Single-Crystal Anatase," *Journal of the American Chemical Society* **118**, 6716 (1996).

L.M. Peter, A.B. Walker, G. Boschloo, and A. Hagfeldt, "Interpretation of Apparent Activation Energies for Electron Transport in Dye-sensitized Nanocrystalline Solar Cells," *Journal of Physical Chemistry B* **110**, 13694 (2006).

Live Science Technology, *Personal Power: Bendable Organic Solar Cells*, 24 December 2004, <http://www.livescience.com>

M. Adachi, M. Sakamoto, J. Jiu, Y. Ogata, and S. Isoda, "Determination of Parameters of Electron Transport in Dye-Sensitized Solar Cells Using Electrochemical Impedance Spectroscopy," *Journal of Physical Chemistry B* **110**, 13872 (2006).

M. Adachi, Y. Murata, I. Okada, and S. Yoshikawa, "Formation of Titania Nanotubes and Applications for Dye-Sensitized Solar Cells," *Journal of the Electrochemical Society* **150**, G488 (2003).

M. Adachi, Y. Murata, J. Takao, J. Jiu, M. Sakamoto, and F. Wang, "Highly Efficient Dye-Sensitized Solar Cells with a Titania Thin-Film Electrode Composed of a Network Structure of Single-Crystal-like TiO_2 Nanowires Made by the "Oriented Attachment" Mechanism," *Journal of the American Chemical Society* **126**, 14943 (2004).

M. Grätzel, "Conversion of sunlight to electric power by nanocrystalline dye-sensitized solar cells," *Journal of Photochemistry and Photobiology A: Chemistry* **164**, 3 (2004).

M. Grätzel, "Dye-sensitized solar cells," Journal of Photochemistry and Photobiology C: Photochemistry Reviews **4**, 145 (2003).

M. Grätzel, "Mesoscopic Solar Cells for Electricity and Hydrogen Production from Sunlight," *Chemistry Letters* **34**, 8 (2005).

M. Grätzel, "Perspectives for Dye-sensitized Nanocrystalline Solar Cells," *Progress in Photovoltaics: Research and Applications* **8**, 171 (2000).

M. Grätzel, "Photoelectrochemical Cells," *Nature* **414**, 338 (2001).

M. Grätzel, "The artificial leaf, bio-mimetic photocatalysis," *Catalyst Technology* **3**, 4 (1999).

M. Law, L.E. Greene, J.C. Johnson, R. Saykally, and P. Yang, "Nanowire dye-sensitized solar cells," *Nature Materials* **4**, 455 (2005).

M. Nishida, "A theoretical treatment of charge transfer via surface states at a semiconductor-electrolyte interface: Analysis of the water photoelectrolysis process," *Journal of Applied Physics* **51**, 1669 (1980).

M. Thelakkat, C. Schmitz, and H.W. Schmidt, "Fully Vapor-Deposited Thin-Layer Titanium Dioxide Solar Cells," *Advanced Materials* **14**, 577 (2002).

M.A. Contreras, B. Egaas, K. Ramanathan, J. Hiltner, A. Swartzlander, F. Hasoon, and R. Noufi, "Towards 20% efficiency in $Cu(In,Ga)Se_2$ polycrystalline solar cells," *Progress in Photovoltaic Research Applications* **7**, 311 (1999).

M.A. Green, "Third Generation Photovoltaics: Ultra-high Conversion Efficiency at Low Cost," *Progress in Photovoltaics: Research and Applications* **9**, 123 (2001).

M.A. Green, K. Emery, D.L. King, Y. Hishikawa, and W. Warta, "Solar cell efficiency tables," *Progress in Photovoltaics: Research and Applications* **14**, 455 (2006).

M.D. Archer and R. Hill. Series on Photoconversion of Solar Energy: Clean Electricity from Photovoltaics. Vol. 1. London: Imperial College Press, 2001.

M.K. Nazeeruddin, A. Kay, I. Rodicio, R. Humphry-Baker, E. Mueller, P. Liska, N. Vlachopoulos, and M. Graetzel, "Conversion of light to electricity by cis-X_2bis(2,2'-bipyridyl-4,4'-dicarboxylate)ruthenium(II) charge-transfer sensitizers (X = Cl-, Br-, I-, CN-, and SCN-) on nanocrystalline titanium dioxide electrodes," *Journal of the American Chemical Society* **115**, 6382 (1993).

M.Y. Song, D.K. Kim, K.J. Ihn, S.M. Jo, and D.Y. Kim, "Electrospun TiO_2 electrodes for dye-sensitized solar cells," *Nanotechnology* **15**, 1861 (2004).

M.Y. Song, Y.R. Ahn, S.M. Jo, D.Y. Kim, and J.P. Ahn, "TiO_2 single-crystalline nanorod electrode for quasi-solid-state dye-sensitized solar cells," *Applied Physics Letters* **87**, 113113 (2005).

N. Koide and L. Han, "Measuring methods of cell performance of dye-sensitized solar cells," *Review of Scientific Instruments* **75**, 2828 (2004).

N. Ozer, F. Tepehan, and N. Bozkurt, "An 'all-gel' electrochromic device," *Thin Solid Films* **219**, 193 (1992).

N.G. Park, M.G. Kang, K.M. Kim, K.S. Ryu, S.H. Chang, D.K. Kim, J. van de Lagemaat, K.D. Benkstein, and A.J. Frank, "Morphological and Photoelectrochemical Characterization of Core-Shell Nanoparticle Films for Dye-Sensitized Solar Cells: Zn-O Type Shell on SnO_2 and TiO_2 Cores," *Langmuir* **20**, 4246 (2004).

National Aeronautics and Space Administration 2006, *International Space Station*, <http://search.nasa.gov/home/index.html>

National Aeronautics and Space Administration 2006, *Mariner 5 Satellite*, <http://search.nasa.gov/home/index.html>

National Aeronautics and Space Administration 2006, *Sojourner Vehicles*, <http://search.nasa.gov/home/index.html>

O. Khaselev and J.A. Turner, "A Monolithic Photovoltaic-Photoelectrochemical Device for Hydrogen Production via Water Splitting," *Science* **280**, 425 (1998).

O.O. Van der Biest and L.J. Vandeperre, "Electrophoretic Deposition of Materials," *Annual Review of Materials Science* **29**, 327 (1999).

P. Peumans, A. Yakimov, and S.R. Forrest, "Small molecular weight organic thin-film photodetectors and solar cells," *Journal of Applied Physics* **93**, 3693 (2003).

P. Sarker and P.S. Nicholson, "Electrophoretic Deposition (EPD): Mechanism, Kinetics, and Application to Ceramics," *Journal of the American Ceramic Society* **79**, 1987 (1996).

P. Wang, S.M. Zakeeruddin, R. Humphry-Baker, J.E. Moser, and M. Grätzel, "Molecular-Scale Interface Engineering of TiO_2 Nanocrystals: Improving the Efficiency and Stability of Dye-Sensitized Solar Cells," *Advanced Materials* **15**, 2101 (2003).

P.J. Cameron and L.M. Peter, "How Does Back-Reaction at the Conducting Glass Substrate Influence the Dynamic Photovoltage Response of Nanocrystalline Dye-Sensitized Solar Cells?," *Journal of Physical Chemistry B* **109**, 7392 (2005).

P.K.M. Bandaranayake, P.V.V. Jayaweera, and K. Tennakone, "Dye-sensitization of magnesium-oxide-coated cadmium sulfide," *Solar Energy Materials & Solar Cells* **76**, 57 (2003).

Parr Instrument Company 2006, *General Purpose Acid Digestion Bombs*, <http://www.parrinst.com/>

R. Shacham, D. Avnir, and D. Mandler, "Electrodeposition of Dye-Doped Titania Thin Film," *Journal of Sol-Gel Science and Technology* **31**, 329 (2004).

R. Tena-Zaera, A. Katty, S. Bastide, C. Lévy-Clément, B. O'Regan, and V. Muñoz-Sanjosé, "ZnO/CdTe/CuSCN, a promising heterostructure to act as inorganic *eta*-solar cell," *Thin Solid Films* **483**, 372 (2005).

R.H. Bube. Photoelectronic Properties of Semiconductors. Cambridge: Cambridge University Press, 1992.

S. Chappel and A. Zaban, "Nanoporous SnO_2 electrodes for dye-sensitized solar cells: improved cell performance by the synthesis of 18 nm SnO_2 colloids," *Solar Energy Materials & Solar Cells* **71**, 141 (2002).

S. Chappel, L. Grinis, A. Ofir, and A. Zaban, "Extending the Current Collector into the Nanoporous Matrix of Dye Sensitized Electrodes," *Journal of Physical Chemistry B Letters* **109**, 1643 (2005).

S. Chappel, S.G. Chen, and A. Zaban, "TiO_2-coated Nanoporous SnO_2 Electrodes for Dye-Sensitized Solar Cells," *Langmuir* **18**, 3336 (2002).

S. Karuppuchamy, K. Nonomura, T. Yoshida, T. Sugiura, and H. Minoura, "Cathodic Electrodeposition of oxide semiconductor thin films and their application to dye-sensitized solar cells," *Solid State Ionics* **151**, 19 (2002).

S. Licht, "Multiple Band gap Semiconductor/Electrolyte Solar Energy Conversion," *Journal of Physical Chemistry B* **105**, 6281 (2001).

S. Licht, "Solar Water Splitting To Generate Hydrogen Fuel: Photothermal Electrochemical Analysis," *Journal of Physical Chemistry B* **107**, 4254 (2003).

S. Nakada, Y. Saito, W. Kubo, T. Kitamura, Y. Wada, and S. Yanagida, "Influence of TiO_2 Nanoparticle Size on Electron Diffusion and Recombination in Dye-Sensitized TiO_2 Solar Cells," *Journal of Physical Chemistry B* **107**, 8607 (2003).

S. Nakade, M. Matsuda, S. Kambe, Y. Saito, T. Kitamura, T. Sakata, Y. Wada, H. Mori, and S. Yanagida, "Dependence of TiO_2 Nanoparticle Preparation Methods and Annealing Temperature on the Efficiency of Dye-Sensitized Solar Cells," *Journal of Physical Chemistry B* **106**, 10004 (2002).

S. Ngamsinlapasathian, S. Sakulkhaemaruethai, S. Pavasupree, A. Kitiyanan, T. Sreethawong, Y. Suzuki, and S. Yoshikawa, "Highly efficient dye-sensitized solar cell using nanocrystalline titania containing nanotube structure," *Journal of Photochemistry and Photobiology A: Chemistry* **164**, 145 (2004).

S. Rühle and D. Cahen, "Electron Tunneling at the TiO_2/Substrate Interface Can Determine Dye-Sensitized Solar Cell Performance," *Journal of Physical Chemistry B* **108**, 17946 (2004).

S.C. Lee, J.H. Lee, T.S. Oh, and Y.H. Kim, "Fabrication of tin oxide film by sol-gel method for photovoltaic solar cell system," *Solar Energy Materials & Solar Cells* **75**, 481 (2003).

S.G. Chen, S. Chappel, Y. Diamant, and A. Zaban, "Preparation of Nb_2O_5 Coated TiO_2 Nanoporous Electrodes and Their Application to Dye-Sensitized Solar Cells," *Chemistry of Materials* **13**, 4629 (2001).

S.J. Limmer, S. Seraji, M.J. Forbess, Y. Wu, T.P. Chou, C. Nguyen, and G.Z. Cao, "Template-Based Growth of Various Oxide Nanorods by Sol-Gel Electrophoresis," *Advanced Functional Materials* **12**, 59-64 (2002).

S.J. Limmer, S.V. Cruz, and G.Z. Cao, "Films and nanorods of transparent conducting oxide ITO by a citric acid sol route," *Applied Physics A* **79**, 421 (2004).

S.J. Limmer, T.P. Chou, and G.Z. Cao, "A study on the growth of TiO_2 nanorods using sol electrophoresis," *Journal of Materials Science* **39**, 895 (2004).

S.R. Kurtz, P. Faine, and J.M. Olson, "Modeling of two-junction, series-connected tandem solar cells using top-cell thickness as an adjustable parameter," *Journal of Applied Physics* **68**, 1890 (1990).

Silicon Solar Inc 2006, *Commercial Solar Cells,* <http://www.siliconsolar.com>

Solar Light Company 2006, *Products*, < http://www.solar.com/>

Solaronix SA 2006, *Ruthenium 620 – 1H3TBA (Black-dye)*, <http://www.solaronix.com>

Solterra Fotovoltaica SA 2006, *Photosensitive Dyes: N3"red" dye*, <http://www.solterra.ch>

T. Miyasaka and Y. Kijitori, "Low-Temperature Fabrication of Dye-Sensitized Plastic Electrodes by Electrophoretic Preparation of Mesoporous TiO_2 Layers," *Journal of the Electrochemical Society* **151**, A1767 (2004).

T. Oekermann, D. Zhang, T. Yoshida, and H. Minoura, "Electron Transport and Back Reaction in Nanocrystalline TiO_2 Films Prepared by Hydrothermal Crystallization," *Journal of Physical Chemistry B* **108**, 2227 (2004).

T. Renouard, R.A. Fallahpour, Md.K. Nazeeruddin, R. Humphry-Baker, S.I. Gorelsky, A.B.P. Lever, and M. Grätzel, "Novel Ruthenium Sensitizers Containing Functionalized Hybrid Tetradentate Ligands: Synthesis, Characterization, and INDO/S Analysis," *Inorganic Chemistry* **41**, 367 (2002).

T. Stergiopoulos, I.M. Arabatzis, M. Kalbac, I. Lukes, and P. Falaras, "Incorporation of innovative compounds in nanostructured photoelectrochemical cells," *Journal of Materials Processing Technology* **161**, 107 (2005).

T. Takamoto, E. Ikeda, H. Kurita, and M. Ohmori, "Over 30% efficient InGaP/GaAs tandem solar cells," *Applied Physics Letters* **70**, 381 (1997a).

T. Zhang, W. Dong, M. Keeter-Brewer, K. Sanjit, R.N. Njabon, and Z.R. Tian, "Site-Specific Nucleation and Growth Kinetics in Hierarchical Nanosyntheses of Branched ZnO Crystallites," *Journal of the American Chemical Society*, in press.

T.L. Wen, J. Zhang, T.P. Chou, S.J. Limmer, and G.Z. Cao, "Template-Based Growth of Oxide Nanorod Arrays by Centrifugation," *Journal of Sol-Gel Science and Technology* **33**, 193 (2005).

T.S. Kang, S.H. Moon, and K.J. Kim, "Enhanced Photocurrent-Voltage Characteristics of Ru(II)-Dye Sensitized TiO_2 Solar Cells with TiO_2-WO_3 Buffer Layers Prepared by a Sol-Gel Method," *Journal of the Electrochemical Society* **149**, E155 (2002).

Th. Dittrich, E.A. Lebedev, and J. Weidmann, "Electron Drift Mobility in Porous TiO_2 (Anatase)," *Rapid Research Notes* **165**, R5 (1998).

U. Bach, D. Lupo, P. Comte, J.E. Moser, F. Weissörtel, J. Salbeck, H. Spreitzer, and M. Grätzel, "Solid-state dye-sensitized mesoporous TiO_2 solar cells with high photon-to-electron conversion efficiencies," *Nature* **395**, 583 (1998).

U.S. Department of Energy 2006, *Energy Efficiency and Renewable Energy*, <http://eere.energy.gov/>

W.U. Huynh, J.J. Dittmer, and A.P. Alivisatos, "Hybrid Nanorod-Polymer Solar Cells," *Science* **295**, 2425 (2002).

W.U. Huynh, X. Peng, and A.P. Alivisatos, "CdSe Nanocrystal Rods/Poly(3-hexylthiophene) Composite Photovoltaic Devices," *Advanced Materials* **11**, 923 (1999).

Wikipedia: The Free Encyclopedia 2006, *Solar Radiation*, <http://en.wikipedia.org>

Y. Diamant, S. Chappel, S.G. Chen, O. Melamed, and A. Zaban, "Core-shell nanoporous electrode for dye sensitized solar cells: the effect of shell characteristics on the electronic properties of the electrode," *Coordination Chemistry Reviews* **248**, 1271 (2004).

Y. Tachibana, K. Hara, S. Takano, K. Sayama, and H. Arakawa, "Investigation on anodic photocurrent loss processes in dye sensitized solar cells: comparison between nanocrystalline SnO_2 and TiO_2 films," *Chemical Physics Letters* **364**, 297 (2002).

Y. Tachibana, M.K. Nazeeruddin, M. Grätzel, D.R. Klug, and J.R. Durrant, "Electron injection kinetics for the nanocrystalline TiO_2 films sensitized with the dye $(Bu_4N)_2Ru(dcbpyH)_2(NCS)_2$," *Chemical Physics* **285**, 127 (2002).

Y.C. Hsu, H. Zheng, J.T. Lin, and K.C. Ho, "On the structural variations of Ru(II) complexes for dye-sensitized solar cells," *Solar Energy Materials & Solar Cells* **87**, 357 (2005).

Y.H. Tak, K.B. Kim, H.G. Park, K.H. Lee, and J.R. Lee, "Criteria for ITO (indium-tin-oxide) thin film as the bottom electrode of an organic light emitting diode," *Thin Solid Films* **411**, 12 (2002).

Y.V. Zubavichus, Y.L. Slovokhotov, M.K. Nazeeruddin, S.M. Zakeeruddin, M. Grätzel, and V. Shklover, "Structural Characterization of Solar Cell Prototypes Based on Nanocrystalline TiO_2 Anatase Sensitized with Ru Complexes. X-ray Diffraction, XPS, and XAFS Spectroscopy Study," *Chemistry of Materials* **14**, 3556 (2002).

Z. Miao, D. Xu, J. Ouyang, G. Guo, X. Zhao, and Y. Tang, "Electrochemically Induced Sol-Gel Preparation of Single-Crystalline TiO_2 Nanowires," *Nanoletters* **2**, 717 (2002).

Z.S. Wang, H. Kawauchi, T. Kashima, and H. Arakawa, "Significant influence of TiO_2 photoelectrode morphology on the energy conversion efficiency of N719 dye-sensitized solar cell," *Coordination Chemistry Reviews* **248**, 1381 (2004).

Appendix A: Other Pertinent Information

The following figures depict the transmission spectrum of TiO_2 nanoparticle film obtained by hydrothermal treatment at 250°C for 20 minutes after N3 dye sensitization for ~ 12 hours, and the plot of the incident-photon-to-current conversion efficiency as a function of wavelength for the TiO_2 nanoparticle film obtained by hydrothermal treatment at 250°C for 20 minutes after N3 dye sensitization for ~ 12 hours.

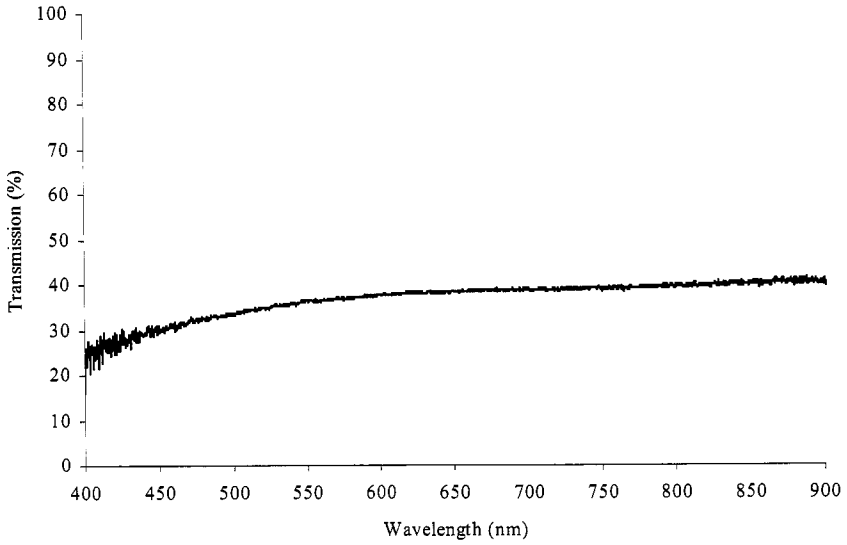

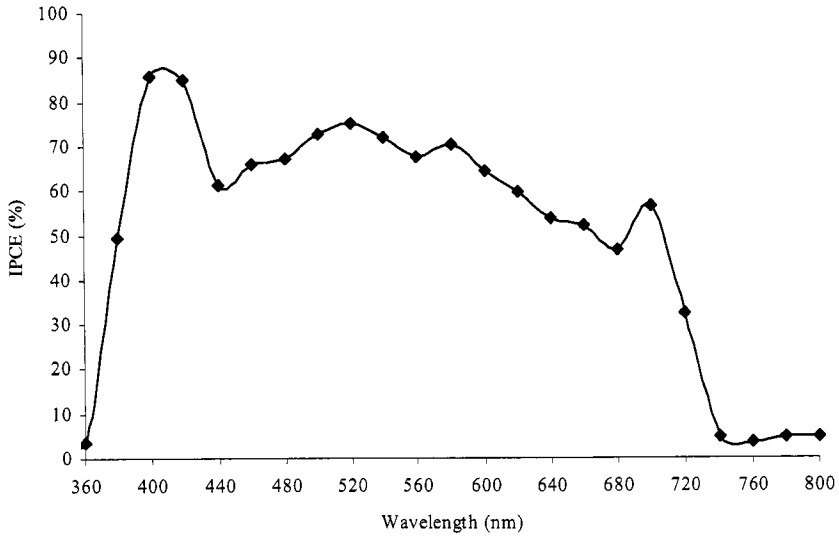

The following figure compares the absorbance spectrum of TiO_2 nanoparticle film obtained by hydrothermal treatment at 250°C for 20 minutes before N3 dye sensitization with the absorbance spectrum of TiO_2 nanoparticle film obtained by hydrothermal treatment at 250°C for 20 minutes after N3 dye sensitization for ~ 12 hours.

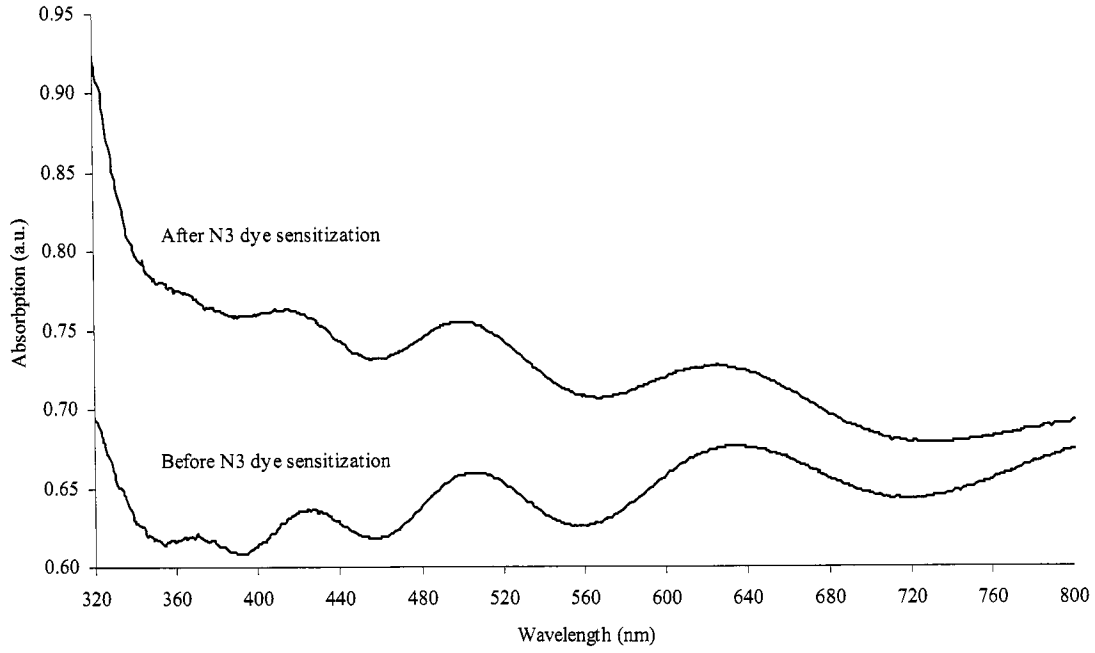

Appendix B: Corrosion Resistance of Sol-Gel-Derived Organic-Inorganic Hybrid Coatings on Stainless Steel

Various oxide coatings by sol-gel processing have been studied extensively for corrosion protection of stainless steel, but the development of dense sol-gel oxide coatings without post-deposition heat-treatment at elevated temperatures has been limited. In this study, the corrosion resistance of sol-gel-derived, silica-based, organic-inorganic hybrid coatings on stainless steel was analyzed. Hybrid sols with 5, 10, and 20 mol% organic content were prepared by copolymerizing a silica precursor (tetraethylorthosilicate, TEOS) and an organic component (3-methacryloxypropyltrimethoxysilane, MPS) using an acid-catalyzed, two-step, hydrolysis-condensation process. Hybrid coatings were deposited onto 304 and 316L stainless steel substrates by method of dip-coating, after surface hydroxylation (wet chemical etching), and heat-treated at 300°C for 30 minutes. Such prepared hybrid coatings were studied using optical microscopy, atomic force microscopy (AFM), ellipsometry, and scanning electron microscopy (SEM). Tape tests, biological tests, and electrochemical (potentiodynamic) tests were also performed to examine the adhesion, the biocompatibility, and the corrosion properties of the hybrid coatings.

Optical microscopy, AFM, and SEM imaging found that these coatings were found to be relatively dense, uniform and defect-free. Ellipsometry analysis indicated that the coating thickness increased as the amount of organic content increased, ranging from 190nm to 240nm. In addition, initial tape tests showed that these hybrid coatings showed excellent adhesion to the metal substrates, which could be attributed to the formation of chemical bonds at the interface, and biological tests verified the biocompatibility of

silica. Electrochemical analysis showed that the relatively dense hybrid coatings provided excellent corrosion protection by forming a physical barrier on the surface of the stainless steel substrates and showed further enhancement of corrosion protection after increasing the number of coatings, but the corrosion properties of these hybrid coatings were highly influenced by the aging of the sol used for deposition. It was also found that the corrosion protection of 10 and 20 mol% MPS coatings was not affected by flexural load, resulting in similar corrosion behavior before and after flexure of the stainless steel substrates. However, the 5 mol% MPS coating did not possess the desired flexibility as demonstrated by both 10 and 20 mol% MPS coatings, where the excellent flexibility could be attributed to the incorporation of a higher content of the organic component.

A comparison of the hybrid coatings on 304 and 316L stainless steel by way of SEM analysis revealed that the corrosion patterns were strongly dependent on the nature of the stainless steel substrates. Interface corrosion was the likely mechanism of breakdown in both cases, where corrosive ions were still able to diffuse through micropores in the coatings and react with the metal elements at the coating-metal interface after the electric potential exceeded the breakdown potential, but the mechanism of corrosion breakdown differed. The hybrid coating on 304 stainless steel cracked, delaminated, and debonded from the substrate, whereas, the hybrid coating on 316L stainless steel did not show any signs of appreciable delamination or extensive coating separation from the substrate. Based on these results, it is assumed that additional amounts of molybdenum and chromium associated with 316L stainless steel further assists in corrosion protection by forming a uniform oxide layer on the surface underneath the hybrid coating. Further details and results of this study can be found in the

following references:

[B1] T.P. Chou, C. Chandrasekaran, Y. Wu, M.J. Forbess, S. Seraji, S.J. Limmer, and G.Z. Cao, "Organic-Inorganic Hybrid Coatings for Corrosion Protection," *Journal of Non-Crystalline Solids* **290**, 153-162 (2001).

[B2] T.P. Chou, C. Chandrasekaran, S.J. Limmer, C. Nguyen, and G.Z. Cao, "Organic-Inorganic Sol-Gel Coating for Corrosion Protection of Stainless Steel," *Journal of Materials Science Letters* **21**, 251-255 (2002).

[B3] T.P. Chou, C. Chandrasekaran, and G.Z. Cao, "Sol-Gel-Derived Hybrid Coatings for Corrosion Protection," *Journal of Sol-Gel Science and Technology* **26**, 321-327 (2003).

Appendix C: Adhesion of Sol-Gel-Derived Organic-Inorganic Hybrid Coatings on Polyester

Ceramic coatings have shown to provide polymer surfaces with excellent abrasion and wear resistance, and protection against environmental degradation, but the adhesion characteristics have shown to be inadequate at the ceramic-polymer interface. Two methods were explored for enhancing the adhesion of ceramic coatings on polymer substrates: (1) formation of chemical bonds through surface condensation reactions, and (2) development of interlocking ceramic and polymeric networks through diffusion of alkoxide precursors. The adhesion of sol-gel-derived, silica-based, organic-inorganic hybrid coatings on polyester, either by forming chemical bonds between the polymer substrate and the hybrid coating or by developing interlocking polymeric and inorganic networks at the interface, was studied. Hybrid sols with 10 mol% organic content were prepared by copolymerizing a silica precursor (tetraethylorthosilicate, TEOS) and an organic component (3-methacryloxypropyltrimethoxysilane, MPS) using an acid-catalyzed, two-step, hydrolysis-condensation process. Coatings with 10 mol% MPS were deposited onto optical-grade polyester substrates by method of dip-coating, after surface modification, and heat-treated at 150°C for 30 minutes up to 3 hours. Surface modification consisted of either oxygen plasma etching or wet chemical etching to hydrolyze the polymer surface, or silicon alkoxide diffusion to form an interpenetrating silica network within the polymer structure. Contact angle tests and wettability tests were done on polyester substrates modified by oxygen plasma or wet chemical etching, and electron spectroscopy for chemical analysis (ESCA) was performed on polyester substrates modified by silicon alkoxide diffusion to verify the effectiveness of the

deposition of the coatings. Microscopy examination was used to analyze the adhesion behavior of the coatings on both modified polyester surfaces after dry and wet thermal cycling tests were performed.

Initial contact angle and wettability tests verified that both oxygen plasma etching and wet chemical etching were effective methods to introduce hydroxyl groups onto the polymer surface, which can readily react with the sol through surface condensation to form chemical bonds between the coating and the polymer substrate. ESCA confirmed that silicon alkoxide diffusion by way of solution treatment in tetramethylorthosilicate (TMOS) at elevated temperatures was an effective method to incorporate silicon alkoxide within the polymer structure, as evidenced by the presence of silicon within the top 100 angstroms of the polyester substrate. Dry thermal cycling and tape tests showed that both surface modification techniques resulted in excellent adhesion between the coating and the polyester substrate, where the coating remained stable and neither cracking nor delamination was observed. On the other hand, it was found that the adhesion of the coatings on polyester was strongly dependent on the bonding characteristics at the ceramic-polymer interface, as dictated by the surface modification techniques, during wet thermal cycling. The adhesion between the coating and the polyester substrate with interlocking ceramic and polymeric networks was far better than that with chemical bonds in the presence of water at elevated temperatures. Delamination and cracking occurred in the coatings deposited on oxygen-plasma- or wet-chemical-etched polyester substrates when subjected to wet thermal cycling, which could be attributed to the hydrolyzable nature of the chemical bonds at the interface. In contrast, the adhesion behavior of the coatings deposited on polyester substrates modified by silicon alkoxide

diffusion was found to be unchanged with stable adhesion when subjected to wet thermal cycling, which could be attributed to the interlocking silica network fused into the polymer structure of the polyester substrate, not found in hydroxylated polyester. Therefore, it is more desirable to achieve stable, unhydrolyzable bonding at the ceramic-polymer interface, where any possible hydrolysis reactions at the interface would be hindered, preventing the dissociation of the coating at the surface. Further details and results of this study can be found in the following reference:

[C1] T.P. Chou and G.Z. Cao, "Adhesion of Sol-Gel-Derived Organic-Inorganic Hybrid Coatings on Polyester," Journal of Sol-Gel Science and Technology **27**, 31-41 (2003).

Appendix D: TiO_2 Nanoparticle Film

BET analysis

BET analysis of the TiO_2 nanoparticle powder, obtained from 500°C calcination of the same prepared TiO_2 sol used to form TiO_2 nanorods, was performed to determine the surface area and pore size of prepared TiO_2 by way of sol-gel processing. Figure D.1 shows the BET nitrogen adsorption/desorption isotherms and the pore size distribution of TiO_2 powder, respectively. The internal surface area was found to be ~ $89m^2/g$ with a porosity of ~ 43% and a primary pore diameter of ~ 4nm. Based on this information, the density of the film was found to be ~ $2.17g/cm^3$, and the total internal surface area of the prepared TiO_2 nanoparticle film with ~ 10μm thickness was calculated to be ~ $3863cm^2$ for an analyzed surface area of ~ $1cm^2$.

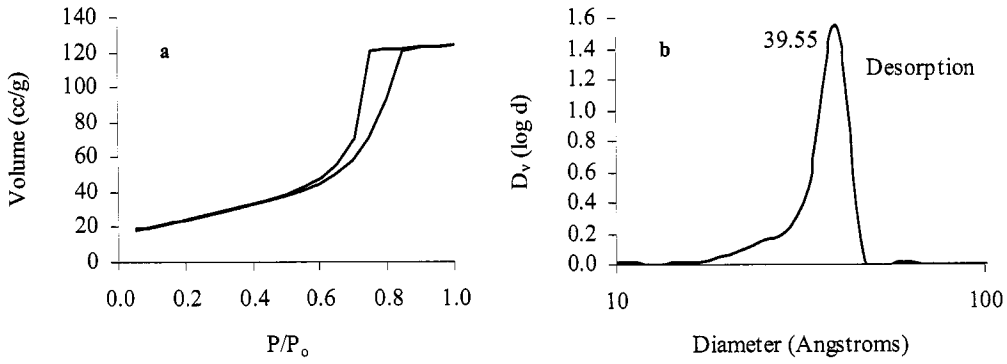

Figure D.1. BET analysis of TiO_2 nanoparticle powder showing a) the nitrogen adsorption and desorption isotherms, and b) the pore size distribution with a primary pore diameter ~ 4nm in size.

Stability under continuous light exposure

One of the important reasons for the decrease in performance in dye-sensitized solar cells is the degradation of the dye [D1] due to prolonged light exposure. Figure D.2 compares the I-V curves obtained from the same electrode after exposure to air and light

for various amounts of time. Table D.1 summarizes the measured and calculated values obtained from taking voltage and current measurements of each solar cell with a 10μm-thick TiO_2 film electrode after exposure to air and light for various amounts of time.

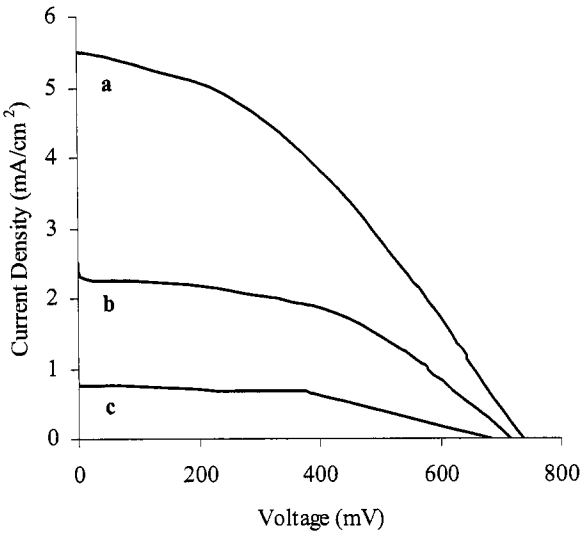

Figure D.2. Comparison of the measured I-V behavior of TiO_2 nanoparticle film after a) 0 days, b) 1 day, and c) 2 days of air and light exposure.

Table D.1. Measured and calculated values of TiO_2 nanoparticle film associated with increasing exposure time to air and light.

Curve (I-V)	Exposure (# days)	V_{oc} (mV)	J_{sc} (mA/cm^2)	V_{max} (mV)	J_{max} (mA/cm^2)	FF (%)	η (%)
a	0	736	5.50	404	3.80	37.9	1.02
b	1	718	2.50	467	1.63	42.4	0.51
c	2	683	0.80	387	0.65	46.0	0.17
	6	650	0.53	250	0.41	29.8	0.068
	7	637	0.35	169	0.27	20.4	0.030

From Figure D.2, it can be seen that the I-V curve for the solar cell with the 10μm-thick TiO_2 film electrode immediately after dye immersion had a much higher short-circuit current density and overall efficiency. As exposure time of these films to air

and light increased, the TiO_2 electrode became more unstable, indicating that dye oxidation and degradation occurred. The overall performance of the same TiO_2 film decreased with increasing exposure time in air and light. It can be seen that the behavior changed dramatically and the performance of the TiO_2 film decreased by ~ 50% after 1 day of air and light exposure. Eventually, the behavior became unstable and the current began to fluctuate after the electrode was exposed to air and light for 2 days before analysis. Additional analysis after 6 and 7 days of air and light exposure (not shown in the figure) also showed that the TiO_2 electrode produced very low current and voltage and was highly unstable. Figure D.3 shows the open-circuit voltage and short-circuit current trends, and the decline in efficiency associated with the performance of the solar cell relative to the amount of days exposed to air and light.

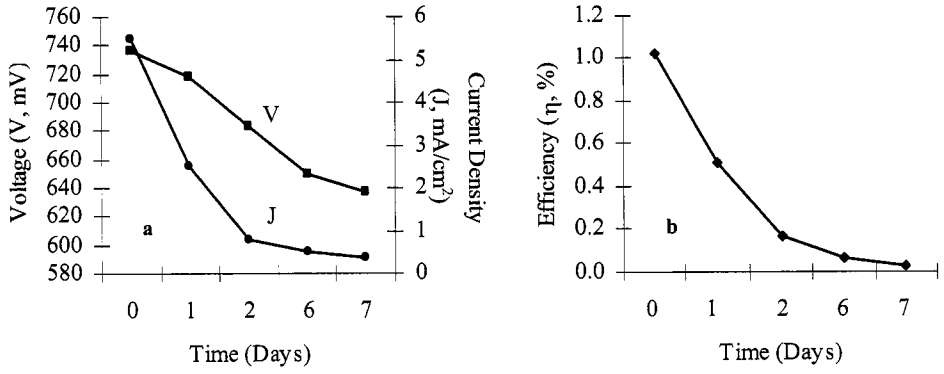

Figure D.3. Plots showing the decrease in a) open-circuit voltage and short-circuit current, and b) overall light conversion efficiency of TiO_2 nanoparticle film after 0, 1, 2, 6, and 7 days of air and light exposure.

Based on these trends, the amount of time the TiO_2 film was exposed to air and light had an effect on both the V_{oc} and the J_{sc}. The J_{sc} decreased by ~ 50% after 1 day and continued to decrease by about the same margin after 2 days. Eventually the J_{sc} decreased by a ~ 30% margin from 2 days to 6-7 days. The V_{oc}, on the other hand, decreased by

only ~ 2 % after 1 day and continued to slowly decrease by about the same margin after 2 days. From this data, it can be seen that the oxidation and degradation of the dye had a greater influence on the J_{sc}, as shown by the larger drop in current after 1-2 days. Figure D.3 also shows that the overall light conversion efficiency is highly influenced by the oxidation of the dye. The η also decreased by ~ 50% after 1 day from 1.02% to 0.51%, and continued to decrease by about the same margin to 0.17% after 2 days, 0.07% after 6 days, and 0.03% after 7 days. These results show that it is important to prevent dye oxidation in air and light to maintain the performance of the solar cell and that maintaining the stability of the dye-sensitized electrode is one area of importance that needs further exploration.

Effect of surface area

It has been widely shown that the amount of surface area for dye adsorption is an important factor, in which the amount of surface coverage or the presence of any visible surface defects in the TiO_2 film electrode can influence the efficiency of a solar cell. To demonstrate this effect, the I-V behavior of a solar cell with reduced surface coverage by removal of a large area of film was analyzed. Figure D.4 shows the I-V curves of two solar cells, one with complete surface coverage of TiO_2 and one with 50% less surface overage of the first sample.

By comparing the two curves, it can be seen that the performance of the solar cell with less TiO_2 film coverage was much lower than that of the solar cell with complete surface coverage. Table D.2 summarizes the output values obtained and calculated from the two I-V curves. The J_{sc} decreased by ~ 50% and the V_{oc} decreased by only ~ 3%,

resulting in a decrease in η by ~ 50% from 1.02% to 0.59%. The amount of surface coverage, or surface area, had a greater influence on J_{sc} relative to V_{oc}, where the V_{oc} of both electrodes were comparable. This is very reasonable in that a lower surface area of TiO_2 results in less dye adsorbed on the surface and a lower light absorption capability. The large difference in I-V behavior between the two prepared TiO_2 electrodes showed that the higher the surface area, the better the current and voltage output, resulting in higher conversion efficiency.

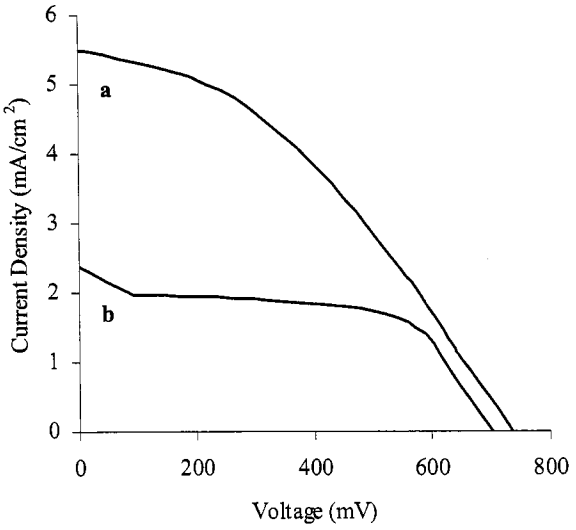

Figure D.4. Comparison of the measured I-V behavior of TiO_2 nanoparticle film a) with complete surface coverage, and b) with 50% less surface coverage.

Table D.2. Measured and calculated values of TiO_2 nanoparticle film associated with a difference in surface coverage of TiO_2.

Curve (I-V)	V_{oc} (mV)	J_{sc} (mA/cm^2)	V_{max} (mV)	J_{max} (mA/cm^2)	FF (%)	η (%)
a	736	5.50	404	3.80	37.9	1.02
b	703	2.36	532	1.67	53.6	0.59

Effect of film thickness

Another factor that can greatly influence the I-V behavior of solar cells is the thickness of the TiO_2 film. Based on literature reports [D2], the optimal performance of dye-sensitized solar cells so far has been shown in TiO_2 films between 8-12μm in thickness. Films having lower or higher thicknesses than this range have shown to have lower I-V output and lower efficiency. It is assumed that thicker films would have better performance because of its larger surface area and greater light absorption capabilities, but it has not been shown to follow that assumption. Figure D.5 shows the I-V behavior of TiO_2 film with varying thicknesses. It can be seen that the thicker the film, the more unstable the film becomes and the lower the overall light conversion efficiency. Table D.3 summarizes the output values obtained and calculated from the I-V curves.

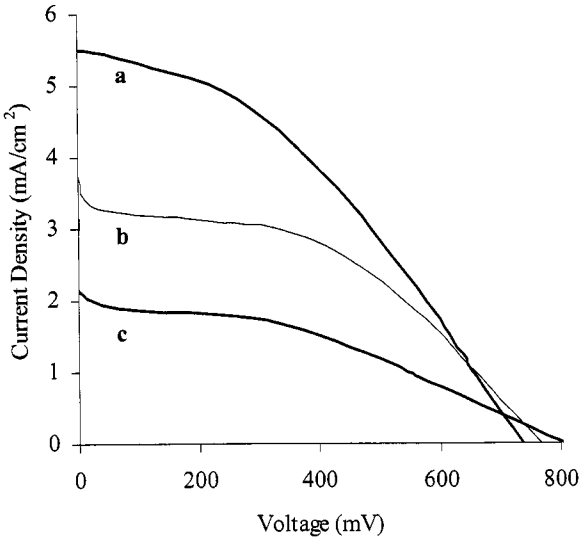

Figure D.5. The measured I-V behavior of TiO_2 nanoparticle film with a) 10μm, b) 20μm, and c) 40μm thickness.

Table D.3. Measured and calculated values of TiO_2 nanoparticle film with changing film thickness.

Curve (I-V)	Thickness (μm)	V_{oc} (mV)	J_{sc} (mA/cm^2)	V_{max} (mV)	J_{max} (mA/cm^2)	FF (%)	η (%)
a	10	736	5.50	476	2.75	37.9	1.02
b	20	767	4.18	442	2.61	36.0	0.77
c	40	808	3.15	430	1.43	24.2	0.41

By comparing the I-V curves, it can be seen that the I-V behavior of the thicker films became more unstable and eventually showing a more linear I-V curve with the thickest film, indicating that a higher internal resistance is present. The less-than-ideal I-V behavior in thicker films could have been due to the fact that the electrons have to migrate through a longer pathway, to the point where many obstacles hinder the conduction and extend the migration time of the electrons from the point of electron injection from the dye through the TiO_2 film to the underlying conducting substrate, reducing the overall efficiency. In addition, a longer electron percolation pathway allows for a higher probability and more chances for electron-hole recombination, which can cause a greater current loss.

[D1] G.P. Smestad, "*Nanocrystalline Solar Cell Kit: Recreating Photosynthesis*," eds. A. Huseth and K. Shanks, ICE Publication, 1998.

[D2] M. Grätzel, "Mesoscopic Solar Cells for Electricity and Hydrogen Production from Sunlight," *Chemistry Letters* **34**, 8 (2005).

Appendix E: TiO_2 Nanorods

Growth of TiO_2 nanorods

Nanorods grown from TiO_2 sol were formed from a technique combining sol-gel processing and template-assisted electrophoretic deposition (EPD). Track-etched hydrophilic polycarbonate membranes (PCM, Millipore, Bedford, MA) with a thickness of approximately 10μm and anodic alumina membranes (AAM, Millipore, Bedford, MA) with a thickness of approximately 60μm were used as the templates. The pore density of the PCM and the AAM templates was roughly estimated to be ~ 10^9 pores/cm^2 and ~ 10^{12} pores/cm^2, respectively, with a pore diameter of ~ 200 nm for both templates. It is also important to note that centrifugation [E1] can also be performed to obtain TiO_2 nanorods.

During the EPD process in PCM templates, an aluminum cathode was used as the contact on one side of the template, and the other side of the template was in contact with the sol, which was also in contact with a platinum anode. The sol was initially drawn into the pores of the template by capillary action, and the applied potential directed the sol particles to deposit within the pore channels of the template, filling the pores completely after a certain amount of time. For the growth of TiO_2 nanorods in PCM, an applied potential of ~ 1.67 V/cm was performed for ~ 30 minutes. After EPD, each template was dried in air at 100°C for 24 hours. For AAM templates, EPD used for the growth of TiO_2 nanorods was performed by contacting one end of the template (dull side with tortuous pore channels) to either ITO glass or a small titanium sheet and immersing this cathode in TiO_2 sol with a platinum mesh anode in parallel, thus exposing the aligned pore channels (polished side) of the template to the sol. A potential of ~ 1.67 V/cm was applied for ~ 3 hours with the sol requiring replenishing every 30 minutes. The sol was initially drawn

into the pores by capillary action and the applied potential directed the sol particles to deposit within the pore channels of the template, partially filling the pores. After the EPD process, each template was dried in air at 100°C for 24 hours and then sintered at 500°C for 1 hour with a heating rate of 2°C/min to densify the nanorods.

Attachment of TiO_2 nanorods

One important step is the attachment of these grown nanorods onto substrates that are both transparent and conductive for use in solar cell devices. Nanorods grown from both PCM and AAM were attached by various methods. For nanorods grown in PCM templates, the attachment of the nanorods required a two-step process. The first step utilized ITO sol to attach the PCM with completely filled pores. The second step required the use of high temperature to pyrolyze the PCM to remove the template while densifying the nanorods and maintaining the attachment of the nanorods to the substrate surface. A drop of ITO sol was placed on each conductive substrate, a filled PCM was placed on top of the sol, and the entire sample was placed in a 100°C drying oven for 24 hours. The template was then removed by sintering the sample at 500°C for 1 hour. In the case of AAM templates with partially filled pores and sintered at 500°C for 1 hour, the side in contact with the conducting cathode during EPD was attached to a glass substrate using a transparent epoxy adhesive after high temperature sintering. This adhesive functioned as a type of "glue" to attach the membrane and nanorods to the substrate surface, where the membrane was adequately imbedded into the epoxy. The membranes were then chemically etched using a 40% sodium hydroxide (NaOH) or potassium hydroxide

(KOH) solution to dissolve the alumina while simultaneously keeping the nanorods intact. However, only partial removal of the membrane resulted, as discussed later.

Fabrication of TiO_2 nanorod film

Samples containing a powder of TiO_2 nanorods were also prepared on conductive substrates. Powder containing TiO_2 nanorods was obtained by attaching 10 completely-filled membranes to glass using drops of ITO sol and then sintering at 500°C for 1 hour at a heating rate of 2°C/min after drying at 100°C for 24 hours. A small amount of nanorod powder was obtained from directly scraping off the nanorods from the glass substrate. The dispersion of nanorod powder was prepared by adding ethanol to an amount of nanorod powder to obtain a 20-30 wt% TiO_2 powder solution. This dispersion was then sonicated for ~ 10 minutes to separate any agglomerated nanorods. To form the film, a few drops of the TiO_2 nanorod dispersion was placed on the substrate surface and allowed to dry at room temperature. Each sample was then dried in air at 100°C for 1 hour, and sintered at 500°C for 1 hour at a heating rate of 2°C/min.

TiO_2 nanorod arrays

By way of template-based sol electrophoresis and centrifugation, TiO_2 nanorods can easily be grown in both PC membranes and AAM templates. Figure E.1 shows SEM images of TiO_2 nanorods grown in PC membranes using sol electrophoresis and centrifugation. It can be seen that solid, dense rods with good uniformity were obtained with ~ 150nm diameters and ~ 10μm lengths for the rods grown in PC and ~ 30μm lengths for the rods grown in AAM. In each case, the nanorods were all measured to have roughly the same diameter and length.

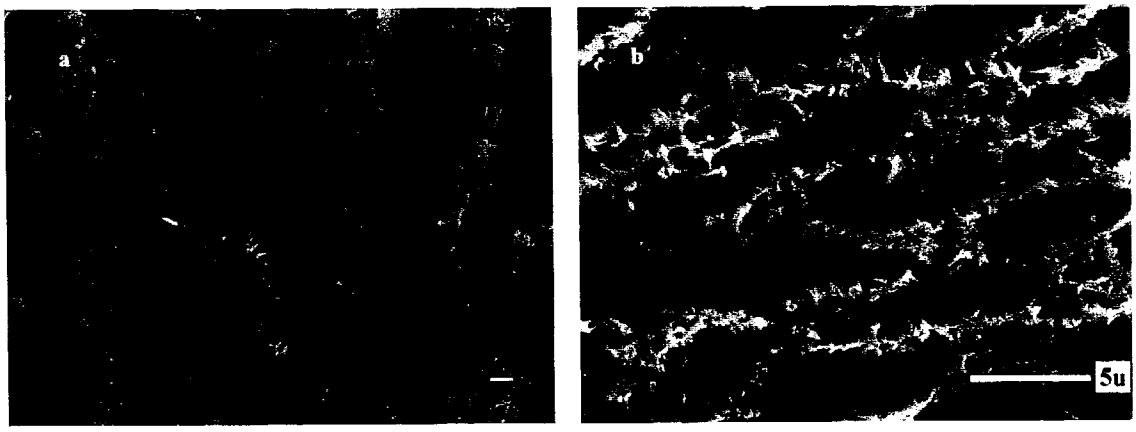

Figure E.1. SEM images of TiO_2 nanorods grown in PCM by way of a) EPD at 5V for 1 hour and b) centrifugation at 1400RPM for 1 hour.

Based on the measured diameters of the nanorods as compared to the 200nm pore size of the templates, an estimated 25% lateral shrinkage was observed, most likely caused by organic burnout and densification during high temperature sintering. XRD analysis, as reported [E2] previously, verified that sintering to 500°C maintained the anatase phase of the TiO_2 nanorods; sintering TiO_2 over 500°C would cause phase transformation from anatase to rutile.

Initial attempts to attach TiO_2 nanorods arrays onto conducting substrates

One of the initial ideas that facilitated the use of TiO_2 nanorods as the working electrode in solar cell devices is the potential of directly growing nanorods on conducting ITO glass by way of template-based sol electrophoresis. Since TiO_2 nanorods could be easily grown in PC membranes and ITO glass is conductive and transparent, which are important property requirements as the back-contact in solar cell devices, direct growth of an array of nanorods on conducting glass was attempted.

Initial attempts to directly grow nanorods on a conducting substrate were unsuccessful due to problems at the contact interface between the PC membrane and the ITO substrate during EPD. The high flexibility, as well as the low temperature pyrolysis, of the PC membrane was problematic for the direct attachment of the nanorods to the substrate surface. It was found that the flexibility of the PC membrane made it difficult to maintain complete contact between the membrane and the substrate during EPD. As a result, partial contact could only be achieved between the membrane and the conducting substrate during the EPD process, leading to incomplete nanorod growth.

Separating the growth process and the attachment of nanorods was the next step. The nanorods were grown in the membrane first and then attached to an ITO substrate using a thin layer of TiO_2 film at the contact interface. The films were deposited by either 1) dip-coating in sol or 2) EPD overgrowth forming an excess layer on the membrane from prolonged growth time. In this case, it was thought to improve the adhesion of the nanorods at the interface when in contact after drying and remain intact during membrane removal. However, the membrane remained attached to the substrate during drying but detached entirely during the heating process, subsequently removing the nanorods completely. The advantage of using PC is the simultaneous pyrolysis of the membrane and the densification of the nanorods at 500°C, resulting in the removal of the membrane leaving dense nanorods. But in this case, it was proved to be difficult in obtaining an array of free-standing nanorods after membrane removal since the heating process caused membrane deformation and detachment.

In an attempt to eliminate the aggressive nature of heating, wet chemical etching was used in place of pyrolysis. Chloroform solution was found to be an effective way to

dissolve PC. In this manner, the membrane can be slowly etched away after nanorod growth, substrate attachment, and drying. However, the etching of the membrane was also too aggressive to maintain membrane and nanorod attachment. In this case, the detachment was assumed to be due to 1) poor adhesion of the membrane to the substrate, 2) weak bonding of the nanorods to the substrate, and 3) lack of structural integrity of the nanorods by removing the membrane before densification at 500°C. With wet chemical etching, the structural support provided by the membrane would be removed before complete densification of the nanorods since high-temperature heating would not be used. It is assumed that the nanorods are structurally more stable and rigid after densification.

One of the advantages of using AAM templates is its ability to withstand and maintain stability at high-temperatures. Due to this advantage, the use of AAM provided the option of heating the nanorods without removing the membrane to improve the structural integrity of the nanorods before membrane removal. In this case, the densification and strengthening of the nanorods would occur within a rigid support structure provided by the channel walls of the membrane during high-temperature sintering, and the removal of the membrane would occur afterwards by wet chemical etching to eliminate deformation. The issue with using AAM is its rigidity, making it difficult to effectively attach the membrane to a substrate surface. Similar thin film techniques previously used was proved to be ineffective due to the stiffness and thickness of AAM. The only method of attaching AAM to a substrate required the use of epoxy adhesive, which functioned as a type of "glue" to adequately imbed the membrane and attach the nanorods to the substrate surface. The membranes were then chemically etched to dissolve the alumina membrane while simultaneously keeping the nanorods intact

since high temperature burnout was not necessary. The AAM templates without pore filling were easily dissolved in NaOH or KOH solution, indicating that the etching solution was very reactive with alumina, but after pore filling and substrate attachment, the etching solution was not as effective. It was thought that after pore filling, the channel walls of the membrane would be difficult to access with solution etching since the pores in the membranes are tightly packed with a very high pore density. In addition, the epoxy adhesive also prevented the membrane from complete exposure to the etching solution, allowing only a few top layers of the AAM to etch away. With this technique, only partial etching of AAM could be achieved.

Figure E.2 shows the SEM images of TiO_2 nanorods grown in AAM perpendicular to the substrate, indicating that the nanorods grown are approximately 200nm in diameter and 30-40μm in length. It can be seen that the growth and attachment of TiO_2 nanorods was achieved using AAM, with nanorods in an ordered array, but only partial etching of the alumina membrane was accomplished. The nanorods are shown to be uniform, dense, and aligned unidirectionally, normal to the substrate surface. It can also be noted that the high pore density of the AAM has the potential to provide substrates with high surface coverage. Furthermore, the nanorods are shown to be either very closely packed or possibly adhered to one another, which could be due to the high pore density of the membrane. Although the nanorods shown in the SEM images are ideal candidates for use in solar cells, there are a few problems to note: 1) the epoxy adhesive used to attach the AAM and nanorods to the substrate is non-conductive, and 2) wet chemical etching cannot completely dissolve AAM. There is great potential for the use of these TiO_2 nanorods because of the unidirectional alignment and uniform

structure, but the use of non-conductive epoxy adhesive to attach the filled alumina membranes and incomplete membrane removal by wet chemical etching is not favorable.

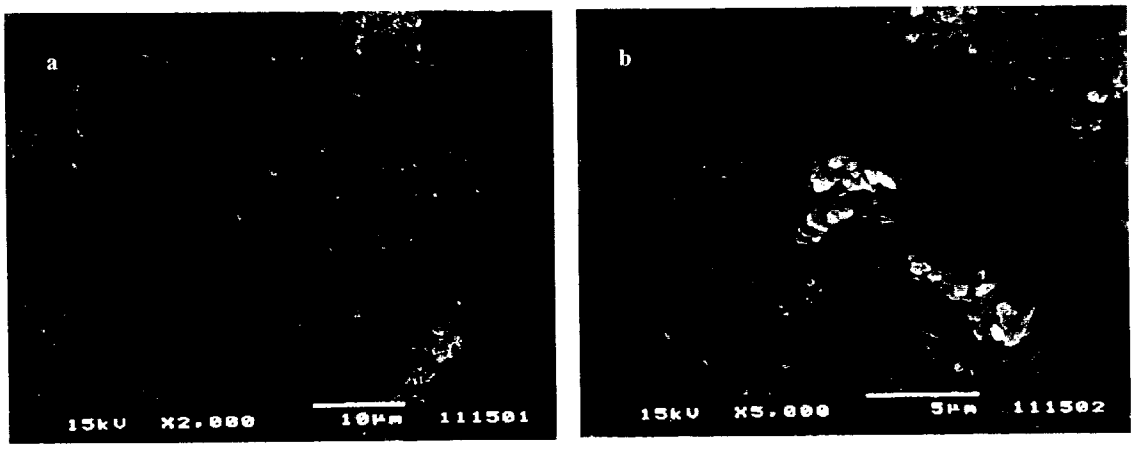

Figure E.2. SEM images of TiO_2 nanorods grown in AAM using EPD at 5V for 3 hours and attached to glass substrates using epoxy, shown at a) lower and b) higher magnifications.

Attachment of TiO_2 nanorod arrays using ITO sol

The successful development of a processing technique for ITO sol enabled the formation of ITO film for membrane attachment. Although the AAM templates allowed for high temperature sintering to densify the nanorod structure before membrane removal and offered excellent potential for obtaining nanorod arrays with extensive surface coverage on substrates, the attachment of AAM was difficult using ITO sol due to its rigidity. On the other hand, the attachment of PC membranes using ITO sol was successful because of its flexibility. Figure E.3 shows an array of TiO_2 nanorods attached to an ITO substrate after 500°C sintering, indicating that an array of nanorods can be attached onto a substrate by utilizing ITO sol.

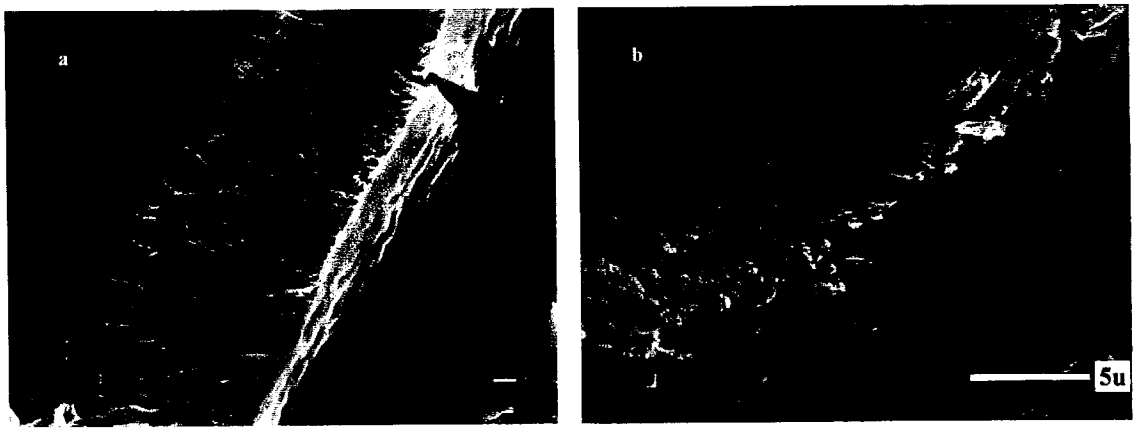

Figure E.3. SEM images of TiO_2 nanorods grown in PCM by way of a) EPD at 5V for 1 hour and b) centrifugation at 1400RPM for 1 hour, and attached to ITO substrates using ITO sol.

The nanorods were first grown in a PC membrane, dried at 100°C, attached to a substrate using a drop of ITO sol, and then dried at 100°C for 24 hours, followed by 500°C sintering. It can be seen that solid, dense nanorods with unidirectional alignment and good uniformity was achieved. In each case, the nanorods were all measured to have roughly the same diameter and length. The diameter of the nanorods was measured to be ~ 150nm and the length was measured to be about 10μm, similar to the thickness of the PC template. An estimated 25% lateral shrinkage was observed after organic burnout and densification at 500°C.

[E1] T.L. Wen, J. Zhang, T.P. Chou, S.J. Limmer, and G.Z. Cao, "Template-Based Growth of Oxide Nanorod Arrays by Centrifugation," *Journal of Sol-Gel Science and Technology* **33**, 193 (2005).

[E2] S.J. Limmer, T.P. Chou, and G.Z. Cao, "A study on the growth of TiO_2 nanorods using sol electrophoresis," *Journal of Materials Science* **39**, 895 (2004).

Vita

Tammy Ping-Chun Chou was born in Taipei, Taiwan. She immigrated to the U.S. with her parents and brother when she was 9 months old. The family eventually settled in Seattle, Washington where her paternal grandparents traveled her back and forth between Seattle and Taiwan until she was 2 years old. She became a U.S. Citizen at the age of 5, under her parents, and attended various schools in the Seattle area, where she learned the English language. Eventually, Bellevue, Washington became her home during the majority of her elementary, middle, and high school years. She continued to reside in Bellevue with her parents while studying at the University of Washington. In 2000, she received her Bachelor of Science degree in Materials Science and Engineering, with emphasis in Ceramics, from the University of Washington. She followed her parents to Sammamish, Washington while pursuing her doctorate in the same field. During her studies, she was awarded three Joint Institute for Nanoscience and Nanotechnology (JIN) Fellowships and one Intel Foundation PhD Fellowship. She published over 28 scientific papers in various technical journals. In 2006, she earned her Doctor of Philosophy degree at the University of Washington in Materials Science and Engineering.